

Modeling the passive mechanical response of soft tissues: constitutive modeling approaches, efficient parameter selection and subsequent adjustments due to residual stresses.

Von der Fakultät für Ingenieurwissenschaften,
Abteilung Bauwissenschaften
der Universität Duisburg-Essen
zur Erlangung des akademischen Grades
Doktor-Ingenieur
genehmigte Dissertation

von

Markus von Hoegen, M.Sc.

1. Gutachter: Prof. Dr.-Ing. habil. J. Schröder
2. Gutachter: Prof. Oliver Röhrle, PhD

Tag der Einreichung: 30. Juli 2018
Tag der mündlichen Prüfung: 08. Februar 2019

Fakultät für Ingenieurwissenschaften,
Abteilung Bauwissenschaften
der Universität Duisburg-Essen
Institut für Mechanik
Prof. Dr.-Ing. habil. J. Schröder

Herausgeber:

Prof. Dr.-Ing. habil. J. Schröder

Organisation und Verwaltung:

Prof. Dr.-Ing. habil. J. Schröder
Institut für Mechanik
Fakultät für Ingenieurwissenschaften
Abteilung Bauwissenschaften
Universität Duisburg-Essen
Universitätsstraße 15
45141 Essen
Tel.: 0201 / 183 - 2682
Fax.: 0201 / 183 - 2680

© Markus von Hoegen
Institut für Mechanik
Abteilung Bauwissenschaften
Fakultät für Ingenieurwissenschaften
Universität Duisburg-Essen
Universitätsstraße 15
45141 Essen

Alle Rechte, insbesondere das der Übersetzung in fremde Sprachen, vorbehalten. Ohne Genehmigung des Autors ist es nicht gestattet, dieses Heft ganz oder teilweise auf fotomechanischem Wege (Fotokopie, Mikrokopie), elektronischem oder sonstigen Wegen zu vervielfältigen.

Drucktechnisch überarbeitete Version

ISBN-10 3-9818074-7-2
ISBN-13 978-3-9818074-7-9
EAN 9783981807479

Vorwort

Die vorliegende Arbeit entstand während meiner Tätigkeit als wissenschaftlicher Mitarbeiter am Institut für Mechanik (Abt. Bauwissenschaften, Fak. Ingenieurwissenschaften) an der Universität Duisburg-Essen. Sie wurde unter anderem durch die finanzielle Unterstützung der Deutschen Forschungsgemeinschaft (DFG) im Rahmen des Projektes SCHR 570/16-1 ermöglicht. Für diese Unterstützung möchte ich mich herzlich bedanken. Darüber hinaus möchte ich im folgenden einigen Menschen meinen tiefen Dank aussprechen, die wesentlich zum Gelingen dieser Arbeit beigetragen haben.

Meinem geschätzten Doktorvater, Prof. Jörg Schröder, danke ich für die Betreuung meiner Arbeit in den vergangenen Jahren. Von dem entgegengebrachten Vertrauen und der Möglichkeit zur Umsetzung eigener Ideen mit internationalen Kollegen habe ich in besonderem Maße profitiert. In diesem Zusammenhang gilt mein großer Dank Dr. Michele Marino, Prof. Patrizio Neff und Sebastian Skatulla, PhD, die mich an ihren wissenschaftlichen Arbeiten und Einsichten teilhaben ließen und mich fachlich wie persönlich förderten.

Des weiteren bedanke ich mich bei Dr. Dominik Brands für die engagierte Unterstützung, gerade in der Frühphase meiner Promotion. Für die gute Zusammenarbeit im Bereich der Lehre gilt mein Dank Prof. Joachim Bluhm und Dr. Alexander Schwarz, die mir stets konstruktiv zur Seite standen.

Ich habe mich am Institut, sowohl während als auch nach meiner Anstellung als Wissenschaftlicher Mitarbeiter, immer sehr wohl gefühlt. Maßgeblich dafür verantwortlich waren die vielen Kollegen, die die positive und motivierende Atmosphäre in den vergangenen Jahren geprägt haben: Solveigh Averweg, Daniel Balzani, Julia Bergmann, Simon Fausten, Ashutosh Gandhi, Maximilian Igelbüscher, Veronika Jorisch, Simon Kugai, Veronica Lemke, Matthias Labusch, Petra Lindner-Roullé, Sascha Maassen, Simon Maike, Rainer Niekamp, Paulo Nigro, Carina Nisters, Sabine Ressel, Mohammad Sarhil, Lisa Scheunemann, Thomas Schmidt, Alexander Schwarz, Steffen Specht, Karl Steeger, Masato Tanaka, Huy Ngoc Thai, Sonja Uebing und Nils Viebahn. Besonderes bedanke ich mich bei Mangesh Pise und Serdar Serdaş, die meinen kulturellen Horizont erweiterten und für die notwendige Unterhaltung und Ablenkung abseits der Mechanik sorgten.

Yasemin Özmen danke ich herzlich für ihre Lebenslust, Geduld und Hilfsbereitschaft, die mich in den letzten Monaten erfüllten und zum Abschluss des Promotionsverfahrens getragen haben.

Zuletzt danke ich meiner Familie für die fortwährende, bedingungslose Unterstützung, die mir mein Leben lang zuteil wurde. Die Ermutigungen und das ehrliche Vertrauen in mich wenn Selbstzweifel aufkamen haben mir sehr geholfen und mich in meinem Weg bestärkt. Gerade die Eröffnung eines anderen Blickwinkels auf die Dinge war für mich rückblickend betrachtet immer sehr wertvoll.

Abstract

The present thesis focuses on modeling and simulation of soft biological tissues with a special focus on considering residual stresses. First, it is necessary to choose a suitable model for each simulation. Due to the heterogenous and complex structure of the considered tissues, particular effort in the development of constitutive material laws which accurately predict the macroscopic material response is required. In this respect, different approaches of varying complexity will be compared by means of numerical examples in the course of this thesis. Besides well-established methods, formulations for anisotropic material laws based on the logarithmic *Hencky* strain measure $\log \mathbf{U}$ and micromorphic continua of higher order are discussed. Apart from the suitability of the material law itself, the prediction quality of the material behavior depends to a large extent on the choice of the involved material parameters. In this context a novel approach is discussed. It relates the parameters of macroscopic, transversely isotropic, constitutive materials, which are in the first place of a phenomenological nature, to structural properties that can be associated with collagen fibers. The derivation of such correlations opens the door for patient-specific parameter selection. In the final part of the thesis, a numerical approach to estimate residual stresses in three-dimensional arterial walls is presented. This supplements the before discussed foundations of soft tissue modeling, applying the hypothesis that the in-vivo stress gradient of suitable invariants in radial direction is smaller than what can be expected from pure mechanical considerations. These circumstances can not be account for when testing tissue samples in uni- or biaxial tension tests.

Zusammenfassung

Die vorliegende Arbeit befasst sich mit der Simulation biologischer Weichgewebe mit einem besonderen Augenmerk auf sogenannte Eigenspannungen. Jede Simulation erfordert zunächst die Auswahl eines geeigneten Modells. Bedingt durch die heterogene und komplexe Struktur der betrachteten Gewebe erfordert dies besondere Anstrengungen in der Entwicklung konstitutiver Materialgesetze, die das makroskopische Verhalten zutreffend beschreiben. Hierzu werden im Rahmen der Arbeit Ansätze unterschiedlicher Komplexität anhand numerischer Beispiele miteinander verglichen. Neben etablierten Modellen wird die mögliche Formulierung von anisotropen Materialgesetzen basierend auf dem logarithmischen *Hencky* Maß $\log \mathbf{U}$ und micromorpher Kontinua höherer Ordnung erörtert. Abgesehen von der Eignung des gewählten Materialgesetzes selbst, hängt die Qualität des numerisch vorhergesagten Materialverhaltens maßgeblich von der Wahl der involvierten Materialparameter ab. Hierzu wird ein Ansatz diskutiert, der die vordergründig phenomenologische Natur der Parameter von makroskopischen, transversal-isotropen, konstitutiven Materialgleichungen mit Struktureigenschaften, die Kollagenfasern zugeordnet werden können, in Verbindung bringt. Durch Ableitung solcher Korrelationen wird die Möglichkeit zur Patienten-spezifischen Parameterwahl geschaffen. Im letzten Teil der Arbeit wird ein Ansatz vorgestellt, um Eigenspannungen in dreidimensionalen Arterienwänden abzuschätzen. Dieser ergänzt die vorangestellten Grundlagen der Modellbildung unter der Hypothese, daß der radiale Spannungsgradient geeigneter Invarianten im Organismus merklich kleiner ist als aus rein mechanischer Sicht zu erwarten wäre. Diesem Umstand kann in der Parameterkalibrierung anhand von Probekörpern in ein- oder biaxialen Zugversuchen zunächst keine Rechnung getragen werden.

Contents

1	Introduction	1
2	Aspects of the Hierarchical Structure and Mechanical Properties of Soft Biological Tissues	9
2.1	Collagen Reinforcement	9
2.2	Relative Deformations in Soft Tissues	11
2.3	Residual Stresses	13
3	Continuum Mechanical Framework	17
3.1	Kinematics of Classical Continua	17
3.2	Definition of Traction Vectors and Stress Tensors	20
3.3	Balance Laws	21
3.3.1	Conservation of Mass	21
3.3.2	Balance of Linear Momentum	21
3.3.3	Balance of Angular Momentum	22
3.3.4	First Law of Thermodynamics	23
3.3.5	Second Law of Thermodynamics	24
3.4	Additional Restrictions of the Constitutive Equation for the Stress	25
3.4.1	Principle of Objectivity	25
3.4.2	Principle of Material Symmetry	26
3.5	Isotropic and Anisotropic Invariants of Strain and Stretch Tensors	27
3.6	Kinematics of Micromorphic Continua	34
3.6.1	Micromorphic Constitutive Model	37
3.6.2	Additional Micro-Deformation Constraint	38
4	Finite Element Method	41
4.1	Definition of a Boundary Value Problem	41
4.2	Weak Form of Balance of Momentum	42
4.3	Discretization Strategy	44
4.4	Discretization of the Micromorphic Variational Principle	48
4.4.1	Discretization of $\delta \mathbf{E}^{(0)}$ and $\Delta \delta \mathbf{E}^{(0)}$	50
4.4.2	Discretization of $\delta \mathbf{E}^{(1)}$ and $\Delta \delta \mathbf{E}^{(1)}$	50
4.4.3	Discretization of $\delta \mathbf{E}^{(2)}$ and $\Delta \delta \mathbf{E}^{(2)}$	51
4.4.4	Discretization of $\delta \mathbf{H}^{(0)}$ and $\Delta \delta \mathbf{H}^{(0)}$	51
4.4.5	Discretization of $\delta \mathbf{H}^{(1)}$ and $\Delta \delta \mathbf{H}^{(1)}$	52

4.4.6	Discretization of $\delta\mathbf{H}^{(2)}$ and $\Delta\delta\mathbf{H}^{(2)}$	52
5	Comparison of Anisotropic Constitutive Approaches	55
5.1	Impact of the Initial Fiber Orientation	57
5.2	Non-Affine Fiber Reorientation	59
5.2.1	Example: Perforated Plate	59
5.2.2	Example: Tension Test	62
5.3	Uniaxial Stress-Strain Behavior	64
5.4	Influence of Dispersed Fiber Distributions	66
6	Micromechanical Motivated Constitutive Modeling	69
6.1	Correlations of Micro-Structural Features Under Uniaxial Tension	72
6.1.1	Benchmark Data	73
6.1.2	Parameter Identification	75
6.1.3	Regression Analysis of Discrete Data Sets	76
6.1.4	Linear Interpolation of Discrete Data Sets	77
6.1.5	Results: Parameter Identification	78
6.1.6	Results: Regression Analysis	80
6.1.7	Results: Interpolation	81
6.2	Correlations of Planar Collagen Arrangements Under Biaxial Tension	83
6.2.1	Benchmark Data	85
6.2.2	Parameter Identification	87
6.2.3	Regression Function for the Variance	89
6.2.4	Results: Inverse Identification of the Fiber Mean Angle	89
6.2.5	Results: Inverse Identification of the Variance as a Measure of Fiber Dispersion	91
7	Incorporation of Residual Stress/Strain	95
7.1	Material Models for Arterial Walls	95
7.2	Adjustment to Experiments of Excised Tissue Samples	96
7.3	Fiber Stress Invariants	100
7.4	Residual Stress Approach	101
7.5	Results of the Residual Stress Approach	104
7.5.1	Numerical Simulation of an Ideal Tube	104
7.5.2	Numerical Simulation of a Patient-Specific Arterial Segment	110
7.5.3	Application of an Inverse Form Finding Algorithm	113
7.6	Residual Strain Approach	114

7.6.1	Incorporation of Residual Strains in the Framework of Open System Thermodynamics	116
7.6.2	Volumetric Growth Tensor	119
7.6.3	Novel Anisotropic Growth Tensor	119
7.7	Results of the Residual Strain Approach	120
7.7.1	Numerical Simulation of an Ideal Tube	120
8	Conclusion & Outlook	125
A	Notes on the Notation	129
B	Notes on Elasticity Models in Terms of the <i>Hencky</i> Strain	131
C	The Concept of Generalized Structural Tensors (GST)	133
D	Micromechanical Correlations	134
D.1	Selected Plots of the Parameter Identification Results and Set $\mathcal{K}(\mathcal{F})$	134
D.2	Regression Coefficients	139
D.3	Collection of Coefficients Used to Generate the Fiber-Density Distributions $v_C^g(\theta)$ for the Biaxial Tension Tests	139
E	Consistent Material Tangents of Growth Algorithms	142
E.1	Volumetric Growth Tangent	142
E.2	Anisotropic Growth Tangent	143
	List of Figures	145
	List of Tables	150
	References	153

1 Introduction

In “Biomechanics” the thermodynamical processes triggered by mechanical, biochemical or electrical exposures are investigated. These processes couple the physiology and anatomy. This covers all aspects of the behavior from whole organs to cells and right up to molecules. The interest in biomechanical simulations of biological tissues increased steadily during the last decades. Numerical analysis of biological structures, inter alia, offers the potential for

- usage as a pathological diagnostic indicator
- gaining scientific knowledge on biological physiology and structure
- confirming/discarding biological hypotheses
- performing case studies to quantify influencing factors
- efficient optimization of implants and medical treatment.

Concerning the first bullet point above, already today modern imaging techniques allow for patient specific simulations of organs, see for instance the review of TAYLOR AND FIGUEROA [179] regarding cardiovascular applications. However, the actual usage of simulations for clinical purposes has been seldom in the past and remains a highly interdisciplinary topic of current research, involving multiple aspects in the fields of mathematics, computational mechanics, bioengineering and medicine. An ambitious project well describing the progress, goals and possible potential in cardiovascular simulation is currently carried out by the *VASCOPS* company. The developed software combines imaging, segmentation, meshing and mechanical analysis in order to gauge the risk of rupture of abdominal aortic aneurysms based on mechanical and geometrical criteria. Thus, present rough failure prediction methods are to be replaced by more accurate and individual prediction techniques, see also GASSER [49] among many other scientific contributions making use of *VASCOPS* products. To realize a broad, prospective medical usage of numerical simulations, which allow for risk assessment of possible injuries, diseases, tissue alterations, etc. or may predict the progression of a disease, it is necessary to link several challenging key points.

The basis assuredly lies in the development and validation of models that are able to describe reliably and comprehensively the specific material behavior. Problems in this field arise due to the highly heterogeneous structure and complexity of biological tissues in general, making it necessary to find individual approaches for specific organs. Popular transversely isotropic strain-energy functions, describing the highly nonlinear and anisotropic passive mechanical response, may be found in VAISHNAV ET AL. [182], CHUONG AND FUNG [23] or HOLZAPFEL ET AL. [77] and a concise review can be found in HOLZAPFEL AND OGDEN [74]. Orthotropic formulations for the passive response of the myocardium were for instance proposed in [28, 56, 73, 121, 148].

These comparatively simple phenomenological models compete with so-called multiscale models which in turn display the material in more depth across different scales. Challenges and potentials of biomechanical multiscale algorithms are for instance discussed

in TAWHAI ET AL. [178]. In this regard it is crucial to balance time consuming high-resolution micro-scale simulations containing a lot of information on the one hand and efficient phenomenological models on the other hand. In view of a clinical application, the importance of time consumption of numerical analysis is not to be underestimated. Therefore, parallel solution strategies as well as (non-linear) model order reduction methods are of high interest. Lastly, also the robustness of the material formulation at hand is of utmost interest. Especially with regard to quasi-incompressible and strongly anisotropic materials, elegant and locking-free formulations in the context of finite elements have been topics of research for several years [156, 165, 192, 198].

The present doctoral thesis aims to contribute to the process of developing reliable, numerical tools for biomechanical simulations, touching the fields of accurate material behavior description and parameter estimation. A special focus lies on the accurate and alternative description of anisotropic fiber reinforced solids.

First of all, any material model needs to be proven to be accurate from a mathematical point of view. In this regard BALL [8] developed the polyconvexity inequality. A strain-energy which is polyconvex in the sense of Ball is automatically *Legendre-Hadamard* elliptic, quasi-convex, rank-one convex and sequential weakly lower semi-continuous. The existence of minimizers is further guaranteed if at least one additive part of the strain-energy is coercive. SCHRÖDER AND NEFF [152] were the first to successfully apply the polyconvexity concept to anisotropic invariants and strain-energy functions. Subsequently, transversely isotropic, polyconvex strain-energies were studied extensively in complementary contributions [9, 35, 154, 155] and additionally in [86, 87, 174]. However, polyconvexity alone can not be seen as an exclusive evaluation criterion to decide whether a strain-energy is suitable to simulate a soft biological tissue. Generally, the involved parameters should be clearly identifiable from experiments, have an intrinsic physical meaning and the number should be as few as possible. In case of biological tissues, such a function specifically needs to be able to predict the material nonlinearities, observed especially in the large-strain domain. A promising isotropic function in mathematical respects was recently developed and analyzed in a series of papers: NEFF AND GHIBA [122], NEFF ET AL. [124; 125]. It can be seen as a modification of the well established *Hencky* strain-energy function introduced in HENCKY [67], which is based on the logarithmic *Hencky* strain tensor $\log \mathbf{U}$. The far majority of constitutive models use the right *Cauchy-Green* tensor \mathbf{C} or *Green*-strain tensor \mathbf{E} as the deformation-measure of choice while usage of other measures of the generalized *Seth-Hill* strain tensor family, comprising the *Hencky* tensor as a special case, is relatively rare. The eponymous authors for this class of tensors are SETH [161] and HILL [68]. From a theoretical point of view there is no reason to favor a specific finite strain in constitutive modeling since any material law can be equivalently reformulated in terms of any other strain tensor. Nevertheless, compared to the rest of the *Seth-Hill*-type measures the principal logarithmic strains for instance exhibit the remarkable property to tend to infinity for both finite compression and finite extension. Further, very recently it has been discovered by NEFF ET AL. [126] that the contributions $\|\text{dev } \log \mathbf{U}\|$ and $\|\text{tr } \log \mathbf{U}\|$ incorporated in the *Hencky* strain-energy function measure the geodesic distance of the isochoric and volumetric part of the deformation gradient to the special orthogonal group $\text{SO}(n)$, respectively. Moreover, the *Hencky* tensor has gained particular interest in the context of finite strain plasticity, since the general small strain concept of an additive split of the strain tensor can be maintained, see SIMO [164] or MIEHE ET AL. [116] for implementation details. Within this thesis the application of

logarithmic strain measures for transversely isotropic problems is discussed according to the recent findings in SCHRÖDER ET AL. [157].

The directional dependency of the mechanical behavior of solids is caused by the microstructure. In case of biological tissues, the primary reason for this is fiber reinforcement, orientated in a certain direction. In addition, distinct, direction-dependent porosity or a lamellar structure with sliding planes may give rise to anisotropic effects. Anisotropic material laws which are restricted to the macro-scale make use of so-called structural tensors, see BOEHLER [15; 16], which take into account the direction-dependent character of the microstructure by means of preferred directions. Together with the strain-measure, these form the foundation to define scalar invariants with respect to associated material-symmetry-groups. In that regard the deformation of the associated microstructure is rigidly coupled to the macroscopic deformation which represents an affine mapping of a fiber bundle for instance. In experimental studies, however, it has been observed that relative motions of microstructure components may have considerable impact on the overall material behavior. Therefore, the assumption of affine kinematics is not always justified. The myocardium, for instance, is a stacked laminae of myocytes which are loosely interconnected. SPOTNITZ ET AL. [173] supposed that slippage along cleavage planes has significant influence on wall thickening and cavity volume during heart contraction. This is presumed to be accompanied by myofiber rearrangement resulting in a denser packing. In KRASNY ET AL. [91] it was experimentally shown that deformation of blood vessels may trigger fiber rearrangement and spatial reorientation. In this context a constitutive framework bridging micro- and macro- deformations needs to be developed. Extended continuum mechanical approaches of higher order, also gathered under the name generalized continua, seem promising in this regard. In nature highly inhomogeneous solids can rather be regarded as being composed of fine deformable particles. In the aforementioned strategies this is taken into account by means of embedded sub-continua located at each macroscopic material point. In doing so, additional degrees of freedom can be introduced in order to distinguish between decoupled motions on different time or length scales. The *Cosserat*-continuum proposed at the beginning of the 20th century in the seminal paper by COSSERAT AND COSSERAT [27] was one of the earliest and most influencing contributions regarding the associated class of material models. Three independent degrees of freedom to account for pure micro-rotations were introduced. Subsequently, many models have been proposed. First to mention are MINDLIN [117] and ERINGEN AND SUHUBI [37]. The latter introduced three deformable directors involving nine additional, independent degrees of freedom. This micromorphic continuum was later modified to define the special case of microstretch continua which are free of micro-rotations and the special case of micropolar continua which are solely based on micro-rotations similar to the *Cosserat* approach. A particular focus was devoted to these kind of formulations in ERINGEN [38], providing extensive theoretical background. Generalized continua serve to incorporate size effects through a length scale parameter L_a determining the size of the associated micro-continuum. Further, a concise review on the history and current fields of research in higher order continuum theories is also provided in the introduction in NEFF ET AL. [123]. A second-order gradient model specifically dealing with relative deformations in fiber reinforced structures may be found in FERRETTI ET AL. [40]. This thesis contains a discussion on the potential of micromorphic formulations for fiber reinforced soft tissues based on the recent findings in VON HOEGEN ET AL. [185].

Even if the additional degrees of freedom in higher order theories can be directly associated to the microstructure, the generalized continuum material description is also an approach of phenomenological nature as all of the above mentioned formulations. Any phenomenological, biomechanical model will rely on material parameters which need to be calibrated or estimated and suitable constitutive laws involving preferably few material parameters appear to be attractive. However, in case of biological tissues this is a very difficult task due to the absence of data and the huge amount of complex factors influencing the mechanical response. This is aggravated by the fact that tissue properties may not only vary between organs but also between patients and also during lifetime for the same patient. As reported in literature aging and diseases may have significant influence on tissue micro-structure such as changes in collagen fiber thickness and number, initial crimp, intermolecular cross-link density or molecular flexibility. Furthermore, the fiber orientation distribution is subject to alterations, for instance in myocardial scar tissue after infarction, see WICKLINE ET AL. [188], or abdominal aortic aneurysms, see NIESTRAWKA ET AL. [127]. Age dependency of the macroscopic response measured in experimental material tests was demonstrated in VANDE GEEST ET AL. [183] and ÅSTRAND ET AL. [5] for human abdominal aorta. The authors concluded that tissues generally become stiffer with age. Classically, parameters may be fitted to ex-vivo, experimentally determined, stress-deformation curves of tissue samples. However, a validation of designed models for patient-specific applications is problematic because the required measurements are highly invasive and due to lack of available experimental data. Ultimately, the mechanical characteristic of the tissue can be attributed to the micro-structure which is remodeling. For a clinical application phenomenological strain-energies are generally favorable due to their simplicity, robustness and low computational cost. Undoubtedly, there must be a correlation between micro-structural features on the one hand and the optimal choice for material model parameters on the other hand. It seems highly attractive to uncover these relations, since physiological changes due to remodeling can be partially measured in a non-invasive way or estimated according to age, gender, health and pre-existing conditions of the patient. Because of the complex structure of soft tissues in general and the limited availability of samples for mechanical testing it appears very unlikely to ever generate the required amount of reference data which would allow for a meaningful statistical evaluation. To overcome this problem, it seems reasonable to replace the experiments by accurate multi-scale simulations that have a high information content in terms of microscopic features and are restricted to input parameters identified with a clear physical/physiological meaning. This enables the opportunity to determine the effects of a certain feature on the stress-strain behavior. An interesting approach was recently developed in MACERI ET AL. [106], MARINO AND VAIRO [110; 111] and MARINO AND WRIGGERS [112]. The final goal is to estimate the variance of the required parameters in order to minimize the degree of uncertainty with regard to the accuracy of the predicted results. Recently, in MARINO ET AL. [113] a method was proposed to effectively find correlations between collagen-related structural features of soft tissues and constitutive parameters of classical strain-energy functions which are based on a phenomenological description of collagen non-linearities. The procedure uses a multi-scale algorithm to produce numerical-experiments and applies parameter optimization strategies. The method is discussed in detail within the present thesis.

Nevertheless, for a lot of biological tissues several predominant dispersed fiber families are present as, for example, for arterial tissues. In these cases the fiber density distri-

tribution needs to be considered as an additional unknown. Since stretched collagen fibers are primarily attributable for the strain stiffening in the higher strain regime, knowledge about the fiber orientation and distribution is of utmost interest in modeling biological tissues. The derivation of relationships between constitutive material parameters associated with the fiber orientation and the histological data may significantly contribute to increased reliability of numerical predictions. On the other hand, experimental testing protocols may be designed based on that knowledge such that the mechanical material characterization becomes more effective. Biaxial material testing appears to be suitable for the characterization of the fiber distribution. Firstly, because the grade of anisotropy can be directly estimated from the ratio of the measured stresses in the loading directions. Secondly, the testing conditions are relatively close to the *in vivo* mechanical exposure. Thirdly, because it is one of the standard tests for biological soft tissues and a comparatively large amount of data is available in literature for different organs which is a basic prerequisite to fit constitutive functions. Therefore, also the influence of the fiber orientation distribution will be studied along with the correlation to structural features according to VON HOEGEN ET AL. [186].

However, even if the parameters could be clearly determined from mechanical measurements or correlations, considerable uncertainty remains in how far *ex-vivo* experiments appropriately and sufficiently reflect the *in-vivo* conditions. One factor which is ignored during testing of excised tissue samples are the so-called residual stresses. The existence of these load independent occurring stresses is manifest in the so-called opening angle experiment. This was carried out first by VAISHNAV AND VOSSOUGH [181], where an arterial segment was sliced in longitudinal direction. Although no external loads are applied, the artery deforms into a horseshoe-shaped configuration. The release of the residual stresses acting in the non stress-free zero blood-pressure configuration is responsible for that. In recent years, several scientist have performed similar investigations on tissues removed from various species and locations along the vascular tree. As a logical consequence, testing of excised tissue samples in uniaxial or biaxial tests are free of residual stresses. A material model fitted to those kind of measurements is suitable to only a limited extent to describe the *in-vivo* material behavior. Of particular importance for the development of mechanical approaches to account for residual stresses were the works of CHUONG AND FUNG [24] and TAKAMIZAWA AND HAYASHI [177]. Regarding arteries all subsequently proposed models are based on the idea that either the transmural *in-vivo* (circumferential) stresses or (elastic) strains are more uniform than what can be expected from classical mechanics and *ex-vivo* experiments. The superposed residual stresses/strains are then of a compressive nature on the inner layers and of a tensile nature on the outer layers resulting in the bending like opening effect discovered in the experiments.

Several different strategies to incorporate residual stresses in computational models were developed in the past. Within this context, the different methods can be roughly divided into three categories. In the first one deformation independent residual stress tensors are defined that may also be coupled with strains to form invariants. These in turn can be incorporated in strain-energy functions maintaining the usual constitutive framework of solid mechanics. Examples may be found in SHAMS ET AL. [162], WANG ET AL. [187] and CIARLETTA ET AL. [25]. As pointed out in the latter contribution, the coupling of an initial stress tensor and a strain can be regarded as a mechanism of adaption on a larger time scale. The second category comprises of methods that characterize the residual stresses in terms of the assumed stress-free configuration after slicing. Analytical, incompressible

stretches from the opening angle experiment and longitudinal pre-stretch were derived for cylinders in HOLZAPFEL AND OGDEN [75], BUSTAMANTE AND HOLZAPFEL [20] or ZHENG AND REN [194]. The approach described in BALZANI ET AL. [10] also uses the opened, approximately stress-free configuration and applies deformation driven boundary conditions in order to close the gap after slicing. Another basic approach belonging to the second class is to introduce a multiplicative split of the deformation gradient, where one part is an initial, incompressible and incompatible strain-field approximating the opening experiment and the elastic strain-energy is formulated in terms of the second part. This guideline was followed in PEÑA ET AL. [134], ALASTRUÉ ET AL. [2] and ALASTRUÉ ET AL. [3]. Several times in literature it has been suggested that residual stresses originate from incompatible growth of different constituents. Therefore, in the third principal procedure a multiplicative split of the deformation gradient is introduced, where the first part is a compressible growth tensor mapping the reference configuration to a pre-grown stress-free configuration. The second part is the elastic deformation gradient which is decisive for the constitutive stress response. This approach goes back to the ideas of RODRIGUEZ ET AL. [142], see also SKALAK ET AL. [166]. It implies open system thermodynamics, cf. EPSTEIN AND MAUGIN [36]. A review on computational growth models and growth driving sources in this framework is provided in MENZEL AND KUHL [115]. Residual stress computations involving this basic theory were performed, inter alia, in TABER AND HUMPHREY [176], OLSSON AND KLARBRING [131], REN [138], POLZER ET AL. [136] or ZAHN AND BALZANI [191]. Apart from these simple growth models, there also exists the constrained mixture model introduced by HUMPHREY AND RAJAGOPAL [84]. Considering mass production of individual constituents with a multiplicative split of the individual deformation gradient, this scheme was applied to account for residual stresses in CARDAMONE ET AL. [21]. Exceptions from these three main classes can also be found in literature. In CHEN AND EBERTH [22], for instance, the actual consideration of residual stresses was neglected and instead the constitutive framework was optimized in such a way that the transmural circumferential stress is close to being homogeneous. However, many of the introduced models work on an academic basis by making use of cylindrical coordinate systems and subsequent analytical derivations that are not transferable to patient-specific geometries. A commonly accepted method for patient-specific problems has not yet become established. Within this thesis, the promising method recently proposed by SCHRÖDER AND BRINKHUES [150] and SCHRÖDER AND VON HOEGEN [153] is discussed in detail. It is modified and extended to account for residual strains in the framework of open system thermodynamics.

In this doctoral thesis a framework from constitutive modeling of fiber reinforced, anisotropic solids to parameter estimation for biomechanical purposes and in-vivo adaptation due to arising residual stresses is presented. The outline is as follows:

Chapter 2 gives a rough survey on the mechanobiological phenomena that are addressed in a computational framework. Starting from an exemplary discussion on the hierarchical structure of soft biological tissues, the general mechanical properties of collagen fibers are elucidated. The already mentioned characteristics of relative deformations and residual stresses in soft tissues are outlined in more detail. This forms the basis for the subsequently discussed material models and numerical examples.

Chapter 3 deals with the continuum mechanical preliminaries. Classical as well as micromorphic continuum kinematics are introduced. The basic conservation laws and the constitutive equation for the stresses based on varying strain measures are given. Special

attention is paid to transversely isotropic invariants that are capable to predict the characteristics of fiber reinforced solids in view of the *Hencky* strain tensor.

Chapter 4 contains a brief summary of the Finite Element Method (FEM). The balance of momentum introduced in chapter 3 is a differential equation that can be effectively, numerically solved for with help of this well-established method. All numerical examples in the further course of the thesis are computed based on this strategy.

Chapter 5 is meant to compare three different constitutive models based on the right *Cauchy-Green* tensor, the *Hencky* strain tensor and the introduced micromorphic concept. Therefore, different academic boundary value problems are studied in order to compare and assess the potential of the discussed approaches, specifically in view of biomechanical application.

Chapter 6 is on the estimation of suitable parameters of phenomenological material laws as they are studied in chapter 5. A principal strategy is established in order to correlate the parameters of transversely isotropic constitutive laws to structurally/physically motivated parameters. A powerful multiscale simulation tool based on solely meaningful parameters is used to generate a reference data set in terms of uniaxial and biaxial stress-strain curves. The comparatively simpler phenomenological parameters are then in turn fitted to these strain-curves to obtain a discrete set of data including the information of the intrinsic relationship between the different types of parameters. It is shown that a continuous regression function can be obtained which approximates the relationship.

Chapter 7 finally aims to compare different simulation techniques to incorporate residual stresses and strains based on the homogeneous transmural in-vivo stress hypothesis. Both reconstructed patient-specific arteries as well as idealized tubes are considered in numerical examples. Stress-strain plots of the transmural stress and strain distributions as well as simulations of the opening-angle experiment are shown to demonstrate the effectiveness of the specific method. Since the residual stresses/strains are incorporated subsequently, the calibration of material laws based on residual stress free samples remains essential in this context. Accordingly, even though accounting for residual stresses/strains, no modifications are required to the general rationale proposed in the previous chapter.

Chapter 8 concludes the thesis and gives some perspectives on possible aspects of future work.

2 Aspects of the Hierarchical Structure and Mechanical Properties of Soft Biological Tissues

Without any doubt, the intrinsic structure of a certain material is decisive for the mechanical behavior. Especially in the case of living tissues the composition of the material and the response to physiological mechanical exposure mutually influence each other. The following section is meant to provide some foundations which are helpful to understand the different material modeling approaches presented in the following chapters. Detailed overviews on structural/functional and computational aspects can be found in FUNG [46], HUMPHREY [83], SHERMAN ET AL. [163] or the articles published in FRATZL [42]. Material properties and data for many different biological tissues were gathered in BLACK AND HASTINGS [13].

Soft tissues can be subdivided into muscle tissues, connective tissues or fatty tissues. These include blood vessels, ligaments, tendons or nerves. Despite their many similarities bones are classified as hard tissues. The two building blocks of soft tissues are cells and the extracellular matrix (ECM) which is of interest in the further course. The ECM essentially consists of ground substance, collagen fibers, elastic fibers such as elastin and bound or unbound water. Albeit the structural differences and specific peculiarities, all soft tissues share common features to be explained in the following on concise examples. Microstructural features are discussed in view of the macroscopic-mechanical behavior which is briefly outlined.

2.1 Collagen Reinforcement

Collagen fibers are fibrous proteins and their long chains of molecules form a triple-helical structure. To date, 28 different types of collagen are distinguished. Most interesting with regard to the mechanical behavior are the fibrillar collagen-types such as collagen-types I and III. They are present in fibrous connective tissues such as tendons, ligaments, bones, skin and blood vessels and are of major importance in load carrying structures. A detailed description on different types of collagen can be found in HULMES [82]. The intrinsic differences of the above-mentioned tissues in terms of mechanical exposure already demonstrate the ability of soft tissues to adapt their composition to different environments. The main reason for this lies in the associated hierarchical structure. Through lifetime or diseases this structure may undergo considerable changes and the collagen provides the required adaptability. Furthermore, the collagen orientation for instance is a crucial cause for anisotropic material behavior. Thus, rearrangement may easily, considerably alter the mechanical properties.

A schematic representation of the hierarchical structure of a tendon is depicted in Fig. 2.1. A tendon consists of several bundles of fascicles that are in turn made up of several collagen fibrils (labeled with 'F'). Adjacent fibrils are interconnected through the protein proteoglycan ('pg'). The fibrils are built of triple helical molecule chains (labeled with 'M'). These tropocollagen molecules are connected through inter-molecular covalent cross-links. The proportions of the different scales are indicated in the figure. As also indicated in Fig. 2.1 the total strain of the tendon ε_T , the strain of the fibril ε_F and the molecular strain ε_M vary widely. X-Ray scattering facilitates to measure fibril and tendon elongation separately. The stretch of the fibrils is usually much smaller than that of the tendon.

CRIBB AND SCOTT [30] suggested that the interaction of fibrils and proteoglycan filaments is responsible for that. FRATZL ET AL. [44] reported that “only 40% of the strain on the rat tail tendon is actually transmitted to the fibrils”.

Both, fibrils and molecules, are aligned mutually parallel forming the basis for a stiff material response if the tissue is elongated in direction of the fibers. Compared to that, extension transverse to the fiber axis will result in a less stiff material response. Under compression the fibers tend to buckle. A schematic stress-strain curve of a reinforced tissue under tensile forces is shown in Fig. 2.2 in order to highlight the significance of the fiber contribution. Clearly, strain stiffening is visible, subdivided into toe region, heel region and linear region. A detailed description of the deformation mechanisms acting in tendons is given in FRATZL ET AL. [44] and FRATZL AND WEINKAMER [43] and summarized in the following. For the first phase the initially crimped fibrils don’t carry any load which is why the stiffness is low. In MARTUFI AND GASSER [114] a distribution function of the initial waviness of the fibrils forming a fiber bundle was assumed. Experimental measurements regarding collagen waviness can be for example found in REZAKHANIHA ET AL. [139] and the references given therein. In the heel region the molecular kinks are straightened in an entropic process and thermal fluctuations progressively disappear. Subsequently, all kinks are straightened in the linear region, where the molecule chains and cross-links are further stretched including intermolecular sliding. Sliding and stretching can be seen to act in series from a mechanical point of view.

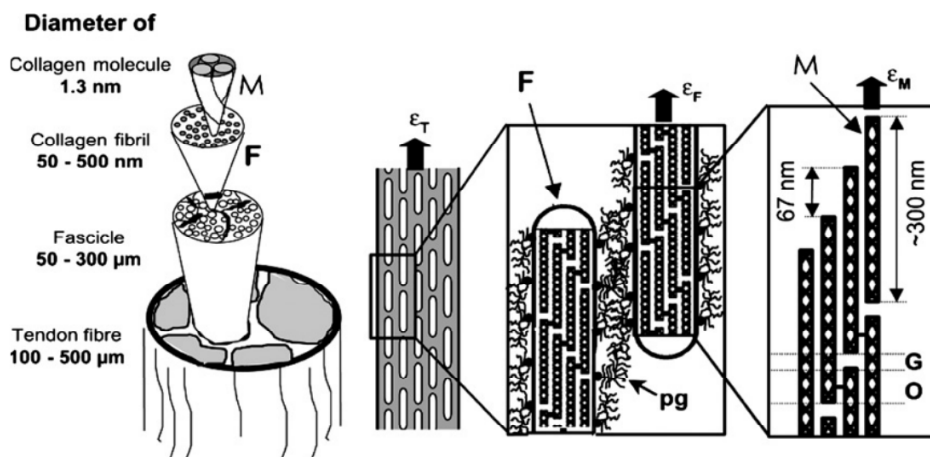


Figure 2.1: Hierarchical structure of a tendon across different scales. Taken from FRATZL [41] with permission.

Moreover, the material can be generally characterized as viscoelastic, i.e. the material response depends on the strain rate [46, 83]. The reason for that lies in internal friction, for instance of fluids under motion. As already mentioned above, the density distribution regarding the orientation can be very different depending on the specific tissue. In tendons and ligaments most of the fibers are aligned in one direction while in arterial tissue there is a fiber density distribution. The transmural orientation may also vary within lamellar subunits, see O’CONNELL ET AL. [128]. Empirical evidence on collagen dispersion of human and animal arteries may also be found for instance in REZAKHANIHA ET AL. [139], SCHRIEFL ET AL. [149] or SUGITA AND MATSUMOTO [175]. Measurements indicate that the dispersion in healthy arteries is first of all two-dimensional in the plane spanned by the circumferential and longitudinal direction and orientated approxi-

mately symmetrically with regard to two or more prominent fiber family directions. In NIESTRAWKA ET AL. [127], it was discovered that the out of plane dispersion significantly increases for abdominal aortic aneurysms compared to healthy abdominal aorta. In accordance with this observation, RAGHAVAN ET AL. [137] showed that the stress-strain behavior of uniaxial tension tests of excised samples performed in longitudinal and circumferential direction was very similar indicating an increased level of dispersion. Age dependency of the mechanical response of human tissues in biaxial tests was shown in VANDE GEEST ET AL. [183] and the changes due to the appearance of aneurysms are discussed in VANDE GEEST ET AL. [184].

Dispersed fiber distributions may be modeled with help of histomechanical constitutive models, integrating fiber distribution functions. In particular, the approaches developed by LANIR [95] and GASSER ET AL. [50] need to be mentioned. In the first case the strain-energy is weighted with a fiber-density distribution and integrated over all possible fiber directions which corresponds to the surface of a unit sphere. In the second case only the set of all structural tensors is weighted with a fiber-density distribution and integrated over the surface of a unit sphere. This yields the so-called generalized structural tensor that is used to compute the anisotropic mixed invariants. Many additional and subsequent approaches were reported in the recent past [26, 51, 76, 81, 133].

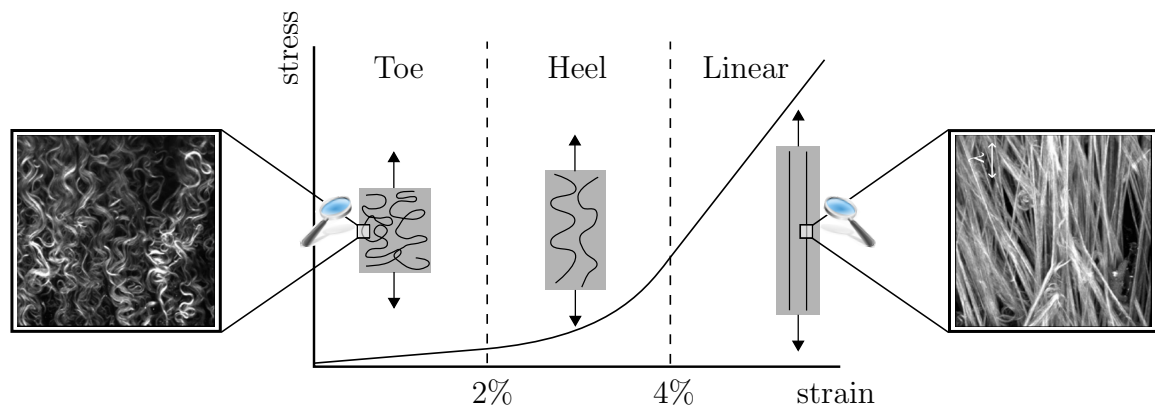


Figure 2.2: Schematic stress-strain relationship of a fiber reinforced uniaxial tension test and associated microscopic images of the collagen network (taken from KRASNY ET AL. [91] with permission). The fibers are initially crimped (left) and straighten with increasing load (right). The fiber distribution is dispersed which means that not all fibers are aligned.

2.2 Relative Deformations in Soft Tissues

Due to the complicated hierarchical structure of biological tissues in general relative deformations may occur on different scales. This already became apparent in the previous section when comparing the deformation mechanisms on different scales, introducing individual strains for the tendon, fibrils and molecules. A schematic example for relative deformations under simple shear is illustrated in Fig. 2.3. On the left a cube is shown defining the initial configuration. While the black edges belong to the macroscopic domain a micro-plane is highlighted in blue. Instead of a plane also a fiber may have been considered without loss of generality. The middle and right images show deformed configurations. The macroscopic deformation in both cases is the same referring to simple shear.

However, in the middle picture the deformation of the microscopic plane is exactly following the macroscopic deformation which is nothing else than an affine mapping. Therefore, the micro-plane and the outer surface of the cube are still parallel. In this case the microstructure is firmly embedded. In contrast to that, in the right image the surfaces are obviously not parallel to each other, i.e. there is an additional non-affine deformation of the micro-plane going beyond the macroscopic deformation. In conclusion, the highly inhomogeneous composition of soft tissues including interaction between different constituents raises numerous questions with regard to the mechanical behavior. Some of the hypotheses in the below-mentioned literature references still need to be proven. Pursuing the aim to unveil the micro-mechanical processes will require additional experiments in the future.

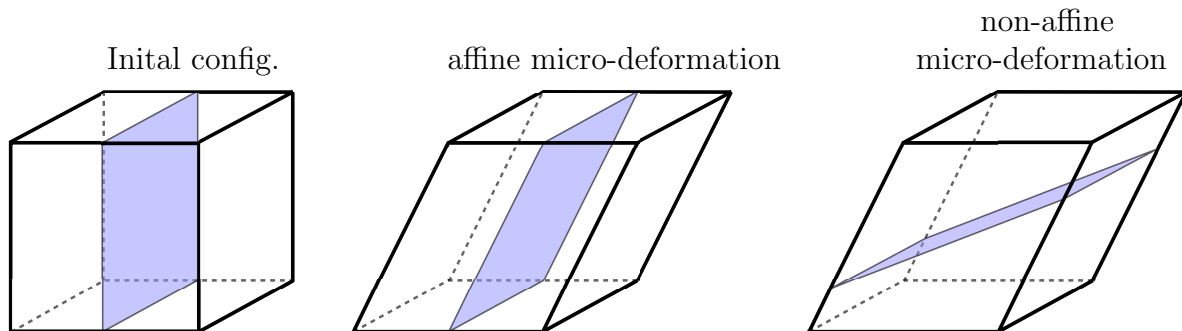


Figure 2.3: Theoretical comparison of affine and non-affine scale dependent deformations of a (microscopic) plane.

In experimental studies it has however been observed that relative motions of microstructure components may have considerable impact on the overall material behavior. For instance in KRASNY ET AL. [91; 92] it was experimentally shown that deformation of blood vessels triggers fiber rearrangement and spatial reorientation. The authors used multiphoton microscopy imaging to track the fiber orientation during mechanical deformation and compared the measurements to the computed, theoretical orientation from affine reorientation. Rabbit carotid arteries were tested and significant non-affine reorientation was revealed to occur in the adventitia. In uniaxial tension tests the fibers, generally speaking, reorientated faster towards the loading direction than what could be expected from affine kinematics. In contrast to that, the fiber rearrangement was overestimated by the affine model for inflation tests. Interaction between fibers and matrix material as well as interaction between individual fibers may be responsible for that. Very recently LYNCH ET AL. [105] hypothesized that internal sliding of collagen fibers is an important mechanism in skin mechanics and reported non-affine fiber reorientation. Earlier, SCREEN ET AL. [159] showed that adjacent collagen units in rat tail tendons may slide.

To give a last example for internal deformation mechanisms, cardiac tissue exhibits a complex hierarchical structure involving different fibrous constituents. A schematic representation of the myocardium of the left ventricle across different scales is shown in Fig. 2.4. As explained by LEGRICE ET AL. [98], the myocardium is a laminated structure. Each of the stacked layers or sheets is four to six cells thick. These sheets are relatively weakly interconnected by perimysial collagen fibers. Therefore, relative sliding of adjacent sheets is possible and LEGRICE ET AL. [99] reported the resistance against this to

be low, resulting in considerable relative motions. The first to notice the effect of internal slippage were probably SPOTNITZ ET AL. [173]. They stated that the slippage of laminae along the cleavage plane is an important factor in wall thickening during passive filling causing considerable myofiber rearrangement at the same time. Also the uncoiling of initially crimped fibers during the systole of the cardiac cycle (cf. MACKENNA ET AL. [107], ROBINSON ET AL. [141]) can be regarded as a processes involving deformations relative to the surrounding matrix material. Apart from heart tissue, this likewise applies for soft tissues in general.

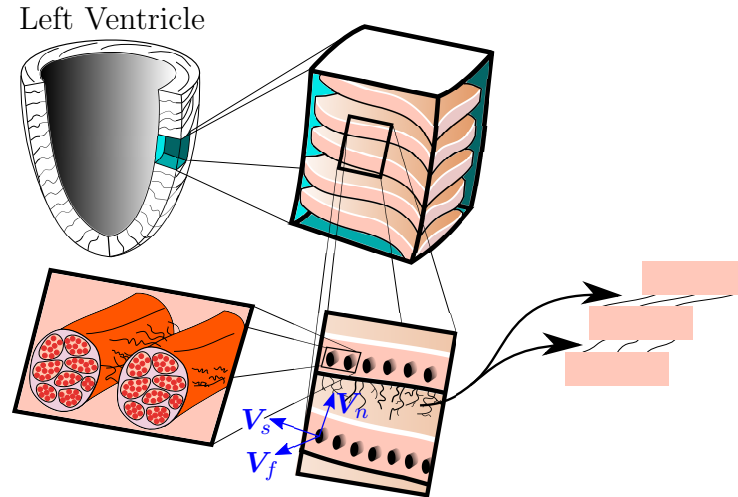


Figure 2.4: Schematic hierarchical structure of the myocardium allowing for relative slippage of adjacent sheets. The fiber fiber direction is labeled with \mathbf{V}_f , sheet direction with \mathbf{V}_s and the sheet normal direction with \mathbf{V}_n .

2.3 Residual Stresses

Considerable residual stresses are present in a number of biological tissues such as the myocardium (OMENS AND FUNG [132]), white matter of the brain (XU ET AL. [190]), tendons (ABRAHAMS [1]) or arteries (BERGEL [12], VAISHNAV AND VOSSOUGH [181], FUNG [45]). For all of these tissues, it is characteristic that the residual stresses are released when the non-loaded body is sliced. This thesis will specifically deal with residual stresses in arteries.

Various methods to characterize residual stresses are conceivable. The most prominent approach is to measure the opening angle of an arterial segment. A radial slice causes the artery to spring open. This is schematically illustrated in the lower half of Fig. 2.5. In experimental studies like HOLZAPFEL ET AL. [80], it was shown that the layer specific opening angles are individually different. This is also indicated in Fig. 2.5 by the definition of the arterial opening angle θ_{Art} and the layer specific opening angles θ_{Med} and θ_{Adv} of the media and the adventitia, respectively. An artery is made up of basically three main layers. The inner layer is called intima and is very thin, the middle layer is called media and carries most of the mechanical load and the softer, outermost layer is called adventitia. Here and in what follows, the comparatively thin intima will be neglected. The opening angle is a sensitive measure implying many difficulties. The residual stresses are released slowly,

see HAN AND FUNG [64]. Therefore, in the literature measurements of the approximately stress-free configuration are usually taken 20 to 30 minutes after cutting of the segments. Moreover, even the opened configuration may only be seen as an approximation of the stress-free configuration since after cutting the arterial segment a second time the pieces will continue to deform. This and the fact that the opening angle increases with age support the assumption that incompatible growth of different constituents is the main origin of the phenomenon. Apart from the opening angle, the residual stress release may also be quantified in terms of the deformation of excised tissue strips as indicated in the upper right part of Fig. 2.5. Again this can be done individually for different layers. These kind of experiments were also performed by HOLZAPFEL ET AL. [80]. However, the opening angle and comparable indicators can only be seen as average estimates of the residual stress release. The information content regarding the transmural distribution is limited. An alternative experimental measurement procedure was proposed in BADEL ET AL. [7] in order to overcome this shortcoming. They used optical full field measurements to facilitate the inclusion of local information.

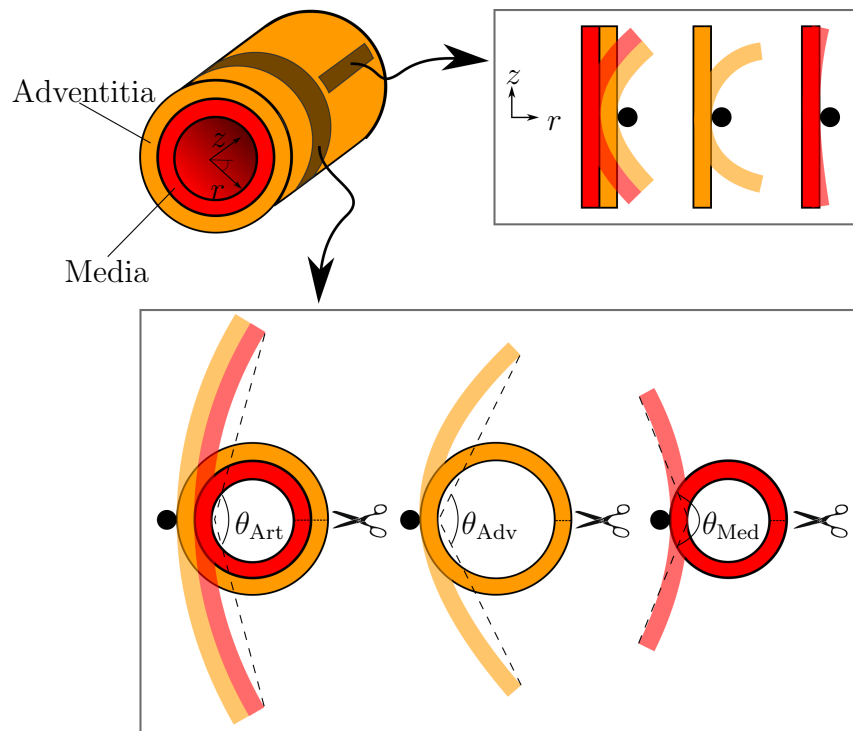


Figure 2.5: Different experiments to release residual stresses. The top row shows excised tissue stripes while rings are tested in the bottom row. The images indicate the different opening angles of the artery, the media and the adventitia, respectively. The intima is neglected in this case.

In an experimental context, the opening angle is still the measure of first choice to quantify residual stresses, since it allows for easy comparison. It is frequently used to study varying factors influencing the residual stress level in order to reveal the origins of the discussed phenomenon. According to FUNG AND LIU [47] and LIU AND FUNG [103], the opening angle is subject to considerable differences along the vascular tree and changes due to progressing hypertrophy and blood pressure. For intact arteries extensive experi-

ments along the human vascular tree were performed in SOKOLIS ET AL. [168], showing an enormous range of the opening angle between 90° and 250° . Layer specific observations regarding the position can be found in PEÑA ET AL. [135]. The influence of aging based on human specimens was investigated in SAINI ET AL. [143]. It was found that the opening angle increases with age. In AZELOGLU ET AL. [6] the dependence of the opening angle on bathing solution concentrations of sodium chloride (NaCl) was studied. The authors concluded that the fixed-charge density of transmurally distributed proteoglycan might play a key role in residual stress generation. The effects of osmotic swelling were also studied in LANIR ET AL. [96] for myocardial tissue and in GUO ET AL. [61] for arterial tissue. In GREENWALD ET AL. [59] the contributions of elastin, collagen and smooth muscle cells to the opening angle were studied. The components were chemically disabled and the authors concluded that elastin has the greatest impact, i.e. the opening angle reduced significantly when dissolving elastin.

However, the opening angle basically approximates the stress release in circumferential direction. The existing pre-stretch in the axial direction cannot be estimated from that parameter. Generally speaking, an artery will be longer under in-vivo conditions than under ex-vivo conditions. In DOBRIN ET AL. [33] it was found that the pre-stretch linearly increases with age and in DOBRIN ET AL. [34] that the elastin is responsible for the axial pre-stretch. The range of pre-stretch may be considerably different. In DELFINO ET AL. [31], for example, an average in-situ longitudinal pre-stretch of 1.1 was measured for human carotid, while HOLZAPFEL ET AL. [79] reported a mean in-situ pre-stretch of 1.044 of a human coronary artery.

Besides of the quantification of the residual stresses, the material parameter calibration of the passive response remains a key problem. Usually, these are estimated from mechanical material tests. In that respect, it is crucial to note that mechanical tests of excised arterial stripes in uniaxial or biaxial tests will be approximately free of any residual stress. This is naturally different for inflation tests. In that case the artery is not sliced and the (circumferential) residual stress component is still active which affects the measured pressure-volume curve. A selection of available experiments for possible material calibration in the literature is given in Tab. 2.1. To approximate the in-vivo conditions in material testing it is necessary to initially consider the pre-stretch in the experimental setting, see LEAROYD AND TAYLOR [97]. Generally the change in axial stretch or length during the cardiac cycle can be assumed to be very small, cf. CARDAMONE ET AL. [21], and the circumferential and radial arterial stiffness is more or less independent of the axial pre-stretch, cf. COX [29]. The vast majority of computational models to predict the effects of residual stresses mentioned in the introduction included these subsequently. Thus, the calibration of material laws based on residual stress-free samples remains essential in this context. However, it appears particularly attractive to perform parameter optimizations, which are based on both in-vivo experiments from inflation tests and uniaxial or biaxial ex-vivo experiments. This might give some insight on the quantitative influence of residual stresses. The major challenge is to find comprehensible and comparable data in the literature which also becomes obvious from Tab. 2.1 and seems to be impossible at present. Only one contribution (LILLIE ET AL. [101]) provides uniaxial and inflation tests at the same time. The results of different studies are usually not readily comparable since different specimens and locations along the vascular tree are tested using varying testing protocols.

Table 2.1: Summary of available mechanical experiments on arterial tissue in the literature.

Source	Test	species	location
SCHMID ET AL. [147]	uniaxial	human	aorta
HOLZAPFEL ET AL. [78]	uniaxial	human	iliac artery
HOLZAPFEL ET AL. [79]	uniaxial	human	coronary artery
GARCÍA ET AL. [48]	uniaxial	porcine	carotid artery
SOKOLIS [167]	uniaxial	porcine	thoracic/abdominal aorta
ZEMÁNEK ET AL. [193]	uniaxial & biaxial	porcine	thoracic aorta
LALLY ET AL. [94]	uniaxial & biaxial	porcine	coronary artery
OKAMOTO ET AL. [130]	uniaxial & biaxial	human	ascending aortic
VANDE GEEST ET AL. [184]	biaxial	human	abdominal aorta
ZHOU AND FUNG [195]	biaxial	canine	thoracic aorta
LILLIE ET AL. [101]	uniaxial & inflation	porcine	thoracic aorta
SOMMER ET AL. [169]	inflation	human	carotid artery
SCHULZE-BAUER ET AL. [158]	inflation	human	iliac artery
SARAVANAN ET AL. [146]	inflation	porcine	coronary artery
MONSON ET AL. [119]	inflation	human	cerebral artery
MOHAN AND MELVIN [118]	inflation	human	thoracic aorta
GENOVESE [53]	inflation	porcine	unspecified
KIM AND BAEK [89]	inflation	porcine	thoracic aorta
GUINEA ET AL. [60]	inflation	human	carotid artery
SOMMER ET AL. [170]	shear	human	thoracic aorta

3 Continuum Mechanical Framework

The classical basis for the macroscopic, phenomenological modeling of materials is formed by continuum mechanics. In continuum mechanics, field quantities, such as deformation, velocity, temperature or density, are described as continuous functions over the considered body. Thus, any field quantity is then given at every material point in space and time. A detailed description of the microstructure is omitted in such a phenomenological description. Due to the inherent stronger or weaker non-homogenous characteristic of a material at lower scales this approach can be seen as a simplification. Higher order continua, such as a micromorphic continuum, introduce additional sub-continua located at each macroscopic material point, including additional degrees of freedom which can be associated with micro-structural features. In the following some fundamentals of continuum mechanics are summarized, including the motion of material points, also known as kinematics, the concept of stress, balance laws, material frame indifference and material symmetry. Comprehensive textbooks dealing with continuum mechanical foundations and principals can be, among many others, found in SPENCER [172], GURTIN [62], OGDEN [129] or HOLZAPFEL [71].

3.1 Kinematics of Classical Continua

Let a solid body \mathcal{B}_0 comprise the set of material points in the undeformed reference configuration at time $t = t_0$ as a subset of the *Euclidean* vector space \mathbb{R}^3 . Each of these material points $P(\mathbf{X}) \in \mathcal{B}_0$ is defined through the continuous position vector function $\mathbf{X}(\vartheta^1, \vartheta^2, \vartheta^3)$ with the curvilinear coordinates $\vartheta^i | i = 1, 2, 3$. The motion function $\varphi(\mathbf{X}, t)$ transforms the position vector field of the material points P to the actual, continuous position vector field

$$\mathbf{x}(\mathbf{X}, t) = \varphi(\mathbf{X}, t) \quad \in \mathcal{B} \subset \mathbb{R}^3 \quad (3.1)$$

at a certain time t . Then $\varphi : \mathcal{B} \mapsto \mathbb{R}^3$ defines a one-to-one mapping of each material point $P(\mathbf{X}) \in \mathcal{B}_0$ to the domain \mathcal{B} in the *Euclidean* vector space \mathbb{R}^3 . Here, \mathcal{B} denotes the body comprising of the material points $p(\mathbf{x}) \in \mathcal{B}$ in the actual configuration at time t . Then the inverse motion function will yield

$$\mathbf{X}(t_0) = \varphi^{-1}(\mathbf{x}, t) \quad \in \mathcal{B}_0 \subset \mathbb{R}^3. \quad (3.2)$$

Linking the referential and actual position vector through the time-dependent deformation vector \mathbf{u} results in

$$\mathbf{x}(\mathbf{X}, t) = \mathbf{X}(t_0) + \mathbf{u}(\mathbf{X}, t) \quad \text{with} \quad \mathbf{u}(\mathbf{X}, t_0) = \mathbf{0}. \quad (3.3)$$

The motion due to forces and prescribed deformations of an arbitrary continuous body \mathcal{B}_0 defined as a set of material points will be discussed in the following and basic kinematic relations are captured. In Fig. 3.1 the aforementioned vectors and configurations are illustrated schematically for an arbitrary body in its reference and deformed configuration.

The covariant tangent base vectors are defined as the partial derivatives of the placement vectors in the reference and actual configuration with respect to the curvilinear coordinates $\vartheta^i | i = 1, 2, 3$:

$$\mathbf{G}_i = \frac{\partial \mathbf{X}}{\partial \vartheta^i} \quad \text{and} \quad \mathbf{g}_i = \frac{\partial \mathbf{x}}{\partial \vartheta^i}. \quad (3.4)$$

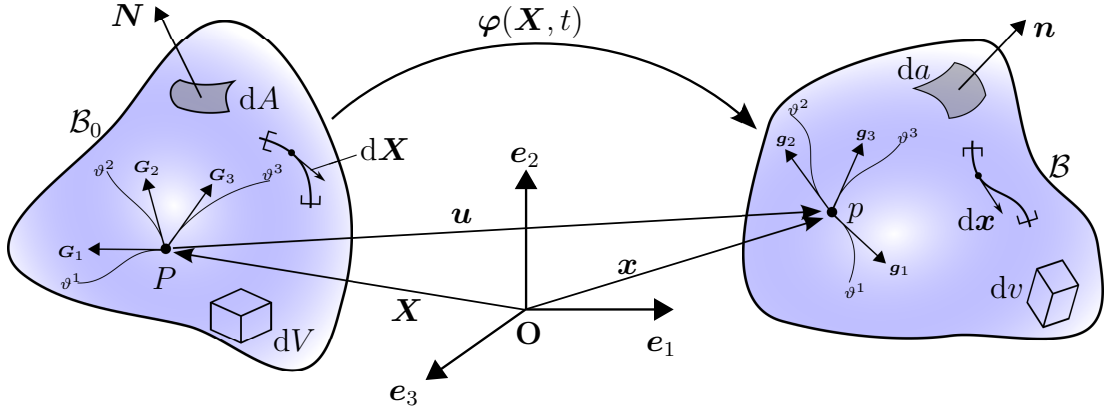


Figure 3.1: Arbitrary body in the undeformed and deformed configuration \mathcal{B}_0 and \mathcal{B} , respectively. Corresponding base vectors as well as infinitesimal volume-, surface- and line-elements are indicated.

The dual base system is defined in terms of the relations

$$\mathbf{G}^i \cdot \mathbf{G}_j = \delta_j^i \quad \text{and} \quad \mathbf{g}^i \cdot \mathbf{g}_j = \delta_j^i, \quad (3.5)$$

where \mathbf{G}^i and \mathbf{g}^i denote the contravariant referential and actual tangent vectors

$$\mathbf{G}^i = \frac{\partial \vartheta^i}{\partial \mathbf{X}} \quad \text{and} \quad \mathbf{g}^i = \frac{\partial \vartheta^i}{\partial \mathbf{x}}. \quad (3.6)$$

The Kronecker-symbol δ_j^i is defined as $\delta_j^i = 1$ if $i = j$ and $\delta_j^i = 0$ if $i \neq j$. The tensor function

$$\mathbf{F}(\mathbf{X}, t) := \text{Grad } \mathbf{x} = \frac{\partial \mathbf{x}}{\partial \mathbf{X}} = \frac{\partial \mathbf{x}}{\partial \vartheta^i} \otimes \frac{\partial \vartheta^i}{\partial \mathbf{X}} = \mathbf{g}_i \otimes \mathbf{G}^i \quad (3.7)$$

is called deformation gradient, playing a key role in continuum mechanics and material modeling. Further, the so-called spatial velocity gradient is defined through

$$\mathbf{l} := \text{grad } \dot{\mathbf{x}} = \frac{\partial \dot{\mathbf{x}}}{\partial \mathbf{x}} = \frac{\partial \dot{\mathbf{x}}}{\partial \vartheta^i} \otimes \frac{\partial \vartheta^i}{\partial \mathbf{x}} = \dot{\mathbf{g}}_i \otimes \mathbf{g}^i = \dot{\mathbf{F}}\mathbf{F}^{-1} = \mathbf{d}^{\text{sym}} + \mathbf{w}^{\text{skew}}, \quad (3.8)$$

where \mathbf{d}^{sym} and \mathbf{w}^{skew} denote the symmetric and skew-symmetric part of \mathbf{l}

$$\mathbf{d}^{\text{sym}} := \frac{1}{2}(\mathbf{l} + \mathbf{l}^T) \quad \text{and} \quad \mathbf{w}^{\text{skew}} := \frac{1}{2}(\mathbf{l} - \mathbf{l}^T), \quad (3.9)$$

respectively. The deformation gradient may be rewritten with help of a polar multiplicative decomposition

$$\mathbf{F} = \mathbf{R}\mathbf{U} = \mathbf{v}\mathbf{R}. \quad (3.10)$$

It is split into the orthogonal rotation tensor $\mathbf{R} \in \text{SO}(3)$ with $\mathbf{R}^{-1} = \mathbf{R}^T$ and the symmetrical, positive definite right or left stretch tensors $\mathbf{U} \in \text{Sym}^+(3)$ and $\mathbf{v} \in \text{Sym}^+(3)$, respectively. The tensor \mathbf{R} refers to a rigid body rotation. The deformation gradient locally maps infinitesimal line elements of the reference configuration to the actual configuration. Hence, the so-called transport theorem of infinitesimal line elements reads as follows:

$$d\mathbf{x} = \mathbf{F} d\mathbf{X}. \quad (3.11)$$

In the same fashion arbitrary, infinitesimal surface elements $d\mathbf{a}$ and $d\mathbf{A}$ in the actual and reference configuration are mapped with help of the transport theorem

$$d\mathbf{a} = \mathbf{n} da = J\mathbf{F}^{-T}\mathbf{N} dA = \text{Cof } \mathbf{F} \mathbf{N} dA = \text{Cof } \mathbf{F} d\mathbf{A}, \quad (3.12)$$

where \mathbf{n} and \mathbf{N} are normal vectors of the specific surfaces (cf. Fig. 3.1) and $J = \det \mathbf{F}$. Finally, the change of arbitrary, infinitesimal volume elements dv and dV in the actual and reference configuration is represented by the transport theorem

$$dv = J dV \quad (3.13)$$

and only depends on J . Strain measures excluding rigid body motions are derived by considering the quadratic distance of the differential vectors connected via the linear mapping in Eq. (3.11). Then, the *Green*-strain \mathbf{E} and *Almansi*-strain \mathbf{z} are defined by means of the relation

$$\begin{aligned} ds^2 - dS^2 &= \|\mathbf{d}\mathbf{x}\|^2 - \|\mathbf{d}\mathbf{X}\|^2 = \mathbf{d}\mathbf{x} \cdot \mathbf{d}\mathbf{x} - \mathbf{d}\mathbf{X} \cdot \mathbf{d}\mathbf{X} \\ &= 2\mathbf{d}\mathbf{X} \cdot (\mathbf{E} \mathbf{d}\mathbf{X}) = 2\mathbf{d}\mathbf{x} \cdot (\mathbf{z} \mathbf{d}\mathbf{x}). \end{aligned} \quad (3.14)$$

Straight forward conversions yield the expressions

$$\begin{aligned} \mathbf{E} &= \frac{1}{2}(\mathbf{C} - \mathbf{1}), \quad \text{with } \mathbf{C} = \mathbf{F}^T \mathbf{F}, \\ \mathbf{z} &= \frac{1}{2}(\mathbf{1} - \mathbf{b}^{-1}), \quad \text{with } \mathbf{b} = \mathbf{F} \mathbf{F}^T. \end{aligned} \quad (3.15)$$

The tensors \mathbf{C} and \mathbf{b} denote the so-called right and left *Cauchy-Green* tensor, respectively. Taking into account Eq. (3.10), we obtain that

$$\mathbf{C} = \mathbf{U}^2 \quad \text{and} \quad \mathbf{b} = \mathbf{v}^2 \quad (3.16)$$

and consequently these symmetric tensors, as well as the above introduced strain measures, are independent of rigid body motions \mathbf{R} .

An eigenvector \mathbf{N}^k of an arbitrary symmetric tensor \mathbf{C} is defined as a vector that keeps the same direction when the linear and symmetric transformation \mathbf{C} is applied and therefore

$$\mathbf{C} \mathbf{N}^k = \lambda_k \mathbf{N}^k \quad \text{for} \quad \mathbf{C} \neq \mathbf{0}, \quad (3.17)$$

where λ_k defines the corresponding eigenvalue of the eigenvector \mathbf{N}^k . Due to the premise $\mathbf{N}^k \neq \mathbf{0}$ we obtain the linear equation system

$$(\mathbf{C} - \lambda_k \mathbf{1}) \mathbf{N}^k = \mathbf{0} \quad (3.18)$$

which is possible to solve if

$$\det(\mathbf{C} - \lambda_k \mathbf{1}) = 0. \quad (3.19)$$

In case of $\mathbf{C} \in \mathbb{R}^{3 \times 3}$, the latter equation leads to a polynomial of third order in λ_k and therefore three possible solutions $\{\lambda_1, \lambda_2, \lambda_3\}$ with corresponding eigenvectors $\{\mathbf{N}^1, \mathbf{N}^2, \mathbf{N}^3\}$ and $\mathbf{N}^k \perp \mathbf{N}^j$, $k \neq j$. Based on the aforementioned definitions it is possible to express deformation tensors in the so-called spectral decomposition. The right

Cauchy-Green tensor \mathbf{C} , left *Cauchy-Green* tensor \mathbf{b} and deformation gradient \mathbf{F} may be written as

$$\mathbf{C} = \sum_{k=1}^3 \lambda_k^2 \mathbf{N}^k \otimes \mathbf{N}^k, \quad \mathbf{b} = \sum_{k=1}^3 \lambda_k^2 \mathbf{n}^k \otimes \mathbf{n}^k, \quad \mathbf{F} = \sum_{k=1}^3 \lambda_k \mathbf{n}^k \otimes \mathbf{N}^k, \quad (3.20)$$

where $\lambda_k^2, k = 1, 2, 3$ denote the eigenvalues of \mathbf{C} and \mathbf{b} . The eigenvectors are expressed through \mathbf{N}^k and \mathbf{n}^k associated to \mathbf{C} and \mathbf{b} , respectively. Generalized *Lagrangian* strain measures of the *Seth-Hill* family, are defined according to SETH [161] and HILL [68] as

$$\mathbf{E}^{(m)} = \begin{cases} \frac{1}{m} (\mathbf{C}^{m/2} - \mathbf{1}) & m \neq 0 \\ \frac{1}{2} \log \mathbf{C} = \log \mathbf{U} & m = 0 \end{cases}. \quad (3.21)$$

For the case $m = 2$ we obtain the *Green-strain* $\mathbf{E}^{(2)} = \mathbf{E}$ which was already introduced in Eq. (3.15). The tensor $\mathbf{E}^{(0)} = \log \mathbf{U}$ for $m = 0$ is called *Hencky* strain tensor, see HENCKY [67], and $\mathbf{E}^{(1)} = \mathbf{U} - \mathbf{1}$ denotes the so-called *Biot*-strain. In consideration of the spectral decomposition and the relation $\mathbf{1} = \sum_{k=1}^3 \mathbf{N}^k \otimes \mathbf{N}^k$ we obtain

$$\mathbf{E}^{(m)} = \begin{cases} \frac{1}{m} \sum_{k=1}^3 (\lambda_k^m - 1) \mathbf{N}^k \otimes \mathbf{N}^k & m \neq 0 \\ \sum_{k=1}^3 \log \lambda_k \mathbf{N}^k \otimes \mathbf{N}^k & m = 0 \end{cases}. \quad (3.22)$$

3.2 Definition of Traction Vectors and Stress Tensors

Stresses may be defined either referring to the reference or the spatial configuration. In that sense, let the vectors \mathbf{t}_0 and \mathbf{t} define referential and spatial traction vectors acting on the surfaces $\partial \mathcal{B}_0$ and $\partial \mathcal{B}$ with surface normals \mathbf{N} and \mathbf{n} , respectively. Applying *Cauchy's* theorem, one may find the relation

$$\int_{\partial \mathcal{B}_0} \underbrace{\mathbf{P} \mathbf{N}}_{\mathbf{t}_0} dA = \int_{\partial \mathcal{B}} \underbrace{\boldsymbol{\sigma} \mathbf{n}}_{\mathbf{t}} da, \quad (3.23)$$

involving the the spatial *Cauchy*-stress tensor $\boldsymbol{\sigma}$ and the first *Piola-Kirchhoff*-stress \mathbf{P} . The deformation gradient as well as \mathbf{P} are two-point tensors with one base vector in the actual and one in the referential configuration. Considering the transport theorem regarding surface elements in Eq. (3.12), we may easily find the relation

$$\boldsymbol{\sigma} = \frac{1}{J} \mathbf{P} \mathbf{F}^T. \quad (3.24)$$

Auxiliary stress measures allowing for alternative numerical treatments of the later discussed partial differential equations are given by the *Kirchhoff*-stress

$$\boldsymbol{\tau} = J \boldsymbol{\sigma}, \quad (3.25)$$

which weights the *Cauchy*-stress with the determinant J of the deformation gradient and by the second *Piola-Kirchhoff*-stress

$$\mathbf{S} = \mathbf{F}^{-1} \mathbf{P} = J \mathbf{F}^{-1} \boldsymbol{\sigma} \mathbf{F}^{-T}, \quad (3.26)$$

which is defined in terms of a push-backward operation.

3.3 Balance Laws

The balance laws are axioms serving as the starting point for developing material models in computational mechanics, which need to obey the fundamental equations. In the following the balance of mass, the balance of linear and angular momentum, the balance of energy and the entropy inequality are discussed.

3.3.1 Conservation of Mass

In a closed system, i.e. no mass flux is considered, the mass

$$M = \int_{\mathcal{B}} \rho(\mathbf{X}, t) \, dv = \int_{\mathcal{B}_0} \rho_0(\mathbf{X}) \, dV \quad (3.27)$$

of a body is computed through the integration of the spatial density ρ or the referential density ρ_0 over the corresponding domain. From Eq. (3.27) it becomes apparent that the mass M is conserved in the deformed configuration and is independent of the time. Consequently, the time derivative of the constant mass yields

$$\dot{M} = \frac{dM}{dt} = 0. \quad (3.28)$$

Making use of the transport theorem $JdV = dv$, the expression above can be converted to read as follows:

$$\dot{M} = \frac{d}{dt} \int_{\mathcal{B}_0} \rho J \, dV = \int_{\mathcal{B}_0} (\dot{\rho} J + \rho \dot{J}) \, dV = 0. \quad (3.29)$$

In consideration of the relation $\dot{J} = J \operatorname{div} \dot{\mathbf{x}} = J \operatorname{tr} \mathbf{l}$, we may further find that

$$\dot{M} = \int_{\mathcal{B}_0} (\dot{\rho} + \rho \operatorname{tr} \mathbf{l}) J \, dV = \int_{\mathcal{B}} (\dot{\rho} + \rho \operatorname{tr} \mathbf{l}) \, dv = 0, \quad (3.30)$$

comprising the local form

$$\dot{\rho} + \rho \operatorname{tr} \mathbf{l} = 0 \quad \forall \mathbf{x} \in \mathcal{B} \quad (3.31)$$

under the assumption that a continuous integrand is present in Eq. (3.30). A direct consequence of the balance of mass is that the determinant of the deformation gradient

$$J = \frac{\rho_0}{\rho} \quad (3.32)$$

may be expressed as the quotient of the initial and actual density.

3.3.2 Balance of Linear Momentum

The axiom of balance of momentum states that the change in time of the momentum vector \mathbf{l}_M equals the vector of external forces \mathbf{f} , meaning

$$\dot{\mathbf{l}}_M = \mathbf{f}. \quad (3.33)$$

The momentum \mathbf{l}_M and the vector of external forces \mathbf{f} acting on a body are given by

$$\mathbf{l}_M = \int_{\mathcal{B}} \rho \dot{\mathbf{x}} \, dv \quad \text{and} \quad \mathbf{f} = \int_{\mathcal{B}} \rho \mathbf{b}_a \, dv + \int_{\partial \mathcal{B}} \mathbf{t} \, da. \quad (3.34)$$

The latter mentioned vector is additively composed of external body and surface forces. The body force is caused by the product of the actual density ρ and the acceleration \mathbf{b}_a acting on a volume and the surface force results from external traction vectors $\mathbf{t} = \boldsymbol{\sigma}\mathbf{n}$ subjected to the surface of the body, cf. Eq. (3.23). In consideration of the transport theorem of infinitesimal volume elements, see Eq. (3.13), and the local statement of the balance of mass, see (3.31), the time derivative yields

$$\dot{\mathbf{i}}_M = \frac{d}{dt} \int_{\mathcal{B}_0} \rho \dot{\mathbf{x}} J \, dV = \int_{\mathcal{B}_0} (\dot{\rho} \dot{\mathbf{x}} + \rho \ddot{\mathbf{x}} + \rho \dot{\mathbf{x}} \operatorname{tr} \mathbf{l}) J \, dV = \int_{\mathcal{B}} [\rho \ddot{\mathbf{x}} + \underbrace{(\dot{\rho} + \rho \operatorname{tr} \mathbf{l})}_{=0} \dot{\mathbf{x}}] \, dv. \quad (3.35)$$

Making use of *Cauchy's* divergence theorem $\int_{\partial \mathcal{B}} \boldsymbol{\sigma} \mathbf{n} \, da = \int_{\mathcal{B}} \operatorname{div} \boldsymbol{\sigma} \, dv$ the fundamental balance equation in Eq. (3.33) takes the form

$$\int_{\mathcal{B}} \rho (\mathbf{b}_a - \ddot{\mathbf{x}}) + \operatorname{div} \boldsymbol{\sigma} \, dv = \mathbf{0}. \quad (3.36)$$

Alternatively, the equation above can be rewritten in the reference configuration as

$$\int_{\mathcal{B}_0} \rho_0 (\mathbf{b}_a - \ddot{\mathbf{x}}) + \operatorname{Div} \mathbf{P} \, dV = \mathbf{0} \quad (3.37)$$

with help of the Eqs. (3.12), (3.24) and (3.32) as well as the divergence theorem. The corresponding local statements are then given by

$$\rho (\mathbf{b}_a - \ddot{\mathbf{x}}) + \operatorname{div} \boldsymbol{\sigma} = \mathbf{0} \quad \text{and} \quad \rho_0 (\mathbf{b}_a - \ddot{\mathbf{x}}) + \operatorname{Div} \mathbf{P} = \mathbf{0}. \quad (3.38)$$

3.3.3 Balance of Angular Momentum

The axiom of balance of angular momentum

$$\dot{\mathbf{h}}_{(\mathbf{O})} = \mathbf{m}_{(\mathbf{O})} \quad (3.39)$$

grounds on the statement that the material time derivative of the moment of momentum $\mathbf{h}_{(\mathbf{O})}$ equals the momentum induced by the external forces $\mathbf{m}_{(\mathbf{O})}$ with respect to an arbitrary but fixed origin \mathbf{O} . The moment of momentum is defined through the cross products of the actual position vector \mathbf{x} with the internal and external forces Eq. (3.34):

$$\mathbf{h}_{(\mathbf{O})} = \int_{\mathcal{B}} \mathbf{x} \times \rho \dot{\mathbf{x}} \, dv \quad \text{and} \quad \mathbf{m}_{(\mathbf{O})} = \int_{\mathcal{B}} \mathbf{x} \times \rho \mathbf{b}_a \, dv + \int_{\partial \mathcal{B}} \mathbf{x} \times \mathbf{t} \, da. \quad (3.40)$$

In consideration of the transport theorem in Eq. (3.13) and the balance of mass in Eq. (3.31), the time rate $\dot{\mathbf{h}}_{(\mathbf{O})}$ can be written in the condensed version

$$\dot{\mathbf{h}}_{(\mathbf{O})} = \frac{d}{dt} \int_{\mathcal{B}} \mathbf{x} \times \rho \dot{\mathbf{x}} \, dv = \int_{\mathcal{B}} \mathbf{x} \times \rho \ddot{\mathbf{x}} \, dv. \quad (3.41)$$

Further taking into account the divergence theorem for the part involving the surface traction vector yields

$$\int_{\partial \mathcal{B}} \mathbf{x} \times \mathbf{t} \, da = \int_{\partial \mathcal{B}} \mathbf{x} \times \boldsymbol{\sigma} \mathbf{n} \, da = \int_{\mathcal{B}} (\mathbf{x} \times \operatorname{div} \boldsymbol{\sigma} + \mathbf{1} \times \boldsymbol{\sigma}) \, dv \quad (3.42)$$

and one may convert Eq. (3.39) according to

$$\int_{\mathcal{B}} \mathbf{x} \times [\rho(\mathbf{b}_a - \ddot{\mathbf{x}}) + \operatorname{div} \boldsymbol{\sigma}] dv + \int_{\mathcal{B}} \mathbf{1} \times \boldsymbol{\sigma} dv = \mathbf{0}, \quad (3.43)$$

where the balance equation of linear momentum is identified and therefore the first part vanishes. After additional mathematical conversions the balance equation

$$\boldsymbol{\sigma}^T = \boldsymbol{\sigma} \quad (3.44)$$

in the local form reveals the well known symmetry of the *Cauchy* stress. Inserting the transformation rule referring to Eq. (3.24), the equation above is equivalent to

$$\mathbf{P}\mathbf{F}^T = \mathbf{F}\mathbf{P}^T \quad (3.45)$$

in terms of the generally non-symmetric first *Piola-Kirchhoff* stress.

3.3.4 First Law of Thermodynamics

The balance of energy

$$\dot{E} + \dot{K} = W + Q \quad (3.46)$$

states that the material time derivative of the total energy, additively split into the kinetic energy K and the internal energy E , is equal to the sum of the mechanical work W and the thermal work Q which result from mechanical and thermal external loads, respectively. The single terms used above are defined as

$$\dot{E} = \frac{d}{dt} \int_{\mathcal{B}} \rho \varepsilon dv = \int_{\mathcal{B}_0} [\dot{\varepsilon} \rho + \varepsilon (\dot{\rho} + \rho \operatorname{tr} \mathbf{l})] J dV = \int_{\mathcal{B}} \rho \dot{\varepsilon} dv, \quad (3.47)$$

$$\dot{K} = \frac{d}{dt} \int_{\mathcal{B}} \frac{1}{2} \rho \dot{\mathbf{x}} \cdot \dot{\mathbf{x}} dv = \int_{\mathcal{B}_0} \frac{1}{2} [\dot{\mathbf{x}} \cdot \dot{\mathbf{x}} (\dot{\rho} + \rho \operatorname{tr} \mathbf{l}) + 2\rho \dot{\mathbf{x}} \cdot \dot{\mathbf{x}}] J dV = \int_{\mathcal{B}} \rho \dot{\mathbf{x}} \cdot \dot{\mathbf{x}} dv, \quad (3.48)$$

$$W = \int_{\mathcal{B}} \dot{\mathbf{x}} \cdot \rho \mathbf{b}_a dv + \int_{\partial \mathcal{B}} \dot{\mathbf{x}} \cdot \mathbf{t} da = \int_{\mathcal{B}} \dot{\mathbf{x}} \cdot \rho \mathbf{b}_a + \operatorname{div} \boldsymbol{\sigma} \cdot \dot{\mathbf{x}} + \boldsymbol{\sigma} : \mathbf{d}^{\text{sym}} dv, \quad (3.49)$$

$$Q = \int_{\mathcal{B}} \rho r dv - \int_{\partial \mathcal{B}} \mathbf{q} \cdot \mathbf{n} da = \int_{\mathcal{B}} \rho r - \operatorname{div} \mathbf{q} dv. \quad (3.50)$$

Herein, $r(\mathbf{X}, t)$ denotes a spatial external heat source per reference mass element, $\mathbf{q}(\mathbf{X}, t)$ denotes the heat flux acting on the boundary $\partial \mathcal{B}$ and $\varepsilon(\mathbf{X}, t)$ denotes the specific internal energy per reference mass element. Inserting Eqs. (3.47)–(3.50) in Eq. (3.46) and considering the balance equation of momentum, see Eq. (3.38), yields the expression

$$\int_{\mathcal{B}} \rho \dot{\varepsilon} - \boldsymbol{\sigma} : \mathbf{d}^{\text{sym}} - \rho r + \operatorname{div} \mathbf{q} - [\operatorname{div} \boldsymbol{\sigma} + \rho(\mathbf{b}_a - \ddot{\mathbf{x}})] \cdot \dot{\mathbf{x}} dv = 0. \quad (3.51)$$

Thus, the local statement of the balance of energy is given by

$$\rho \dot{\varepsilon} - \boldsymbol{\sigma} : \mathbf{d}^{\text{sym}} - \rho r + \operatorname{div} \mathbf{q} = 0. \quad (3.52)$$

3.3.5 Second Law of Thermodynamics

According to the entropy inequality or *Clausius-Duhem* inequality the entropy in a closed system without mass or heat exchange can never decrease. Therefore, processes releasing entropy are irreversible and involve energy dissipation. As a consequence, the entropy change in time, $\dot{\mathcal{H}}$, is always equal or greater than the temperature weighted difference of the contributions of the internal heat source and the heat flux, denoted by Q_Θ :

$$\dot{\mathcal{H}} \geq Q_\Theta \quad \text{with} \quad (3.53)$$

$$\frac{d}{dt} \mathcal{H} = \frac{d}{dt} \int_{\mathcal{B}} \rho \eta \, dv = \int_{\mathcal{B}} \rho \dot{\eta} \, dv \quad \text{and} \quad Q_\Theta = \int_{\mathcal{B}} \frac{\rho r}{\Theta} \, dv - \int_{\partial \mathcal{B}} \frac{1}{\Theta} \mathbf{q} \cdot \mathbf{n} \, da. \quad (3.54)$$

Here, η defines the specific entropy and Θ the temperature. Considering the divergence theorem, inserting the local form of the balance of energy, see Eq. (3.52), and introducing the free Helmholtz Energy $\psi = \varepsilon - \eta \Theta$, the local form of the entropy inequality takes the form

$$\boldsymbol{\sigma} : \mathbf{d}^{\text{sym}} - \rho(\dot{\psi} + \dot{\Theta}\eta) - \frac{1}{\Theta} \mathbf{q} \cdot \text{grad } \Theta \geq 0. \quad (3.55)$$

In the following we will restrict ourselves to isothermal processes where Θ is constant and $\mathbf{q} = \mathbf{0}$. Bearing these conditions in mind, the equation above simplifies to

$$\boldsymbol{\sigma} : \mathbf{d}^{\text{sym}} - \rho \dot{\psi} \geq 0. \quad (3.56)$$

The second law of thermodynamics is essential to formulate constitutive relations for the stresses introduced in Sec. 3.2 and the heat flux for non-isothermal processes. This is necessary since the set of mechanical equations does not match the number of variables included. Therefore, the stress function is expressed as a constitutive law in terms of a scalar valued tensor function ψ , rendering the concept of hyperelasticity. With regard to the different stress tensors already introduced, it is helpful to keep in mind the equivalents

$$J \boldsymbol{\sigma} : \mathbf{d}^{\text{sym}} = \boldsymbol{\tau} : \mathbf{d}^{\text{sym}} = \mathbf{S} : \dot{\mathbf{E}} = \mathbf{P} : \dot{\mathbf{F}}, \quad (3.57)$$

of the so-called stress-power. In view of Eq. (3.56) one may then convert the local statement to

$$\left(\mathbf{S} - \rho_0 \frac{\partial \psi}{\partial \mathbf{E}} \right) : \dot{\mathbf{E}} \geq 0 \quad \text{or} \quad \left(\mathbf{P} - \rho_0 \frac{\partial \psi}{\partial \mathbf{F}} \right) : \dot{\mathbf{F}} \geq 0 \quad (3.58)$$

and define the constitutive equations

$$\mathbf{S} = \rho_0 \frac{\partial \psi}{\partial \mathbf{E}} \quad \text{and} \quad \mathbf{P} = \rho_0 \frac{\partial \psi}{\partial \mathbf{F}}, \quad (3.59)$$

which ensures the entropy inequality to be zero, i.e. no dissipation is present, and form the foundation of elastic material modeling. In order to further simplify the equation above, one may introduce the strain-energy density function $W = \rho_0 \psi$. Equivalent constitutive equations based on different strain measures can then be found analogously, yielding

$$\begin{aligned} \boldsymbol{\tau} &= \frac{\partial \check{W}(\log \mathbf{v})}{\partial \log \mathbf{v}} = \mathbf{R} \frac{\partial \widehat{W}(\log \mathbf{U})}{\partial \log \mathbf{U}} \mathbf{R}^T = \mathbf{R} \frac{\partial W^\#(\mathbf{U})}{\partial \mathbf{U}} \mathbf{U} \mathbf{R}^T \\ &= 2 \mathbf{F} \frac{\partial \overline{W}(\mathbf{C})}{\partial \mathbf{C}} \mathbf{F}^T = 2 \mathbf{b} \frac{\partial W^+(\mathbf{b})}{\partial \mathbf{b}} = \frac{\partial W(\mathbf{F})}{\partial \mathbf{F}} \mathbf{F}^T \end{aligned} \quad (3.60)$$

in the isotropic case. However, if anisotropic material behavior is to be considered only the relations

$$\boldsymbol{\tau} = 2\mathbf{F} \frac{\partial \overline{W}(\mathbf{C})}{\partial \mathbf{C}} \mathbf{F}^T = \frac{\partial W(\mathbf{F})}{\partial \mathbf{F}} \mathbf{F}^T \quad (3.61)$$

remain valid. In view of a material law $\widehat{W}(\log \mathbf{U})$ formulated with help of the Hencky tensor $\log \mathbf{U}$, for instance, this demands the application of a projection tensors $\partial_{\mathbf{C}} \log \mathbf{U}$ according to

$$\boldsymbol{\tau} = 2\mathbf{F} \left[\frac{\partial \widehat{W}(\log \mathbf{U})}{\partial \log \mathbf{U}} : \frac{\partial \log \mathbf{U}}{\partial \mathbf{C}} \right] \mathbf{F}^T. \quad (3.62)$$

Explicit projection tensors for the evaluation of the stresses and the consistent material tangent are given in Appendix B.

3.4 Additional Restrictions of the Constitutive Equation for the Stress

In order to formulate physically meaningful constitutive laws, the principles of objectivity and material symmetry need to be obeyed. These are to be explained in the following and form the basis for the choice of adequate strain invariants to be introduced in Sec. 3.5.

3.4.1 Principle of Objectivity

Material frame indifference requires the constitutive equations found in Sec. 3.3.5 to be invariant to a change of the position of the observer. The latter can also be interpreted as a rigid body motion of the deformed configuration according to $\mathbf{x}^+ = \mathbf{Q}\mathbf{x}$ and $\varphi^{-1}(\mathbf{x}, t) = (\varphi^+)^{-1}(\mathbf{x}^+, t)$. Then the mapping

$$\mathbf{F}^+ = \frac{\partial \mathbf{x}^+}{\partial \mathbf{X}} = \mathbf{Q}\mathbf{F} \quad \text{with} \quad \mathbf{Q} : \mathcal{B} \mapsto \mathcal{B}^+ \quad (3.63)$$

applies and regarding isothermal elasticity it is necessary to obey the restrictions

$$\left. \begin{aligned} W(\mathbf{Q}\mathbf{F}) &= W(\mathbf{F}) \\ \mathbf{S}(\mathbf{Q}\mathbf{F}) &= \mathbf{S}(\mathbf{F}) \\ \mathbf{P}(\mathbf{Q}\mathbf{F}) &= \mathbf{Q}\mathbf{P}(\mathbf{F}) \\ \boldsymbol{\sigma}(\mathbf{Q}\mathbf{F}) &= \mathbf{Q}\boldsymbol{\sigma}(\mathbf{F})\mathbf{Q}^T \\ \boldsymbol{\tau}(\mathbf{Q}\mathbf{F}) &= \mathbf{Q}\boldsymbol{\tau}(\mathbf{F})\mathbf{Q}^T \end{aligned} \right\} \forall \mathbf{Q} \in \text{SO}(3) \quad (3.64)$$

regarding the constitutive equation. Since the tensor \mathbf{Q} is orthogonal and thus $\mathbf{Q}^T = \mathbf{Q}^{-1}$, one may easily show that

$$\mathbf{C}^+ = (\mathbf{F}^+)^T \mathbf{F}^+ = (\mathbf{Q}\mathbf{F})^T (\mathbf{Q}\mathbf{F}) = \mathbf{F}^T \underbrace{\mathbf{Q}^T \mathbf{Q}}_{\mathbf{1}} \mathbf{F} = \mathbf{C}. \quad (3.65)$$

Therefore, using the right *Cauchy-Green* tensor as the variable of choice implies that $W := \overline{W}(\mathbf{C}) = \overline{W}(\mathbf{C}^+)$ and $\mathbf{S}(\mathbf{C}) = \mathbf{S}(\mathbf{C}^+)$ and the requirements are automatically fulfilled. Recalling the multiplicative split of the deformation gradient into a stretch tensor and a rotation tensor in Eq. (3.10) and further considering that $\mathbf{C} = \mathbf{U}^2$, see Eq. (3.10), it also becomes obvious that \mathbf{C} is independent of rigid body rotations. The same naturally applies for $\mathbf{b} = \mathbf{v}^2$.

3.4.2 Principle of Material Symmetry

The construction of suitable material strain-energies additionally requires to obey the set of material symmetry groups \mathcal{G} . In that case a rigid body rotation of the reference configuration $\mathbf{X}^* = \mathbf{Q}\mathbf{X}$ with $\varphi(\mathbf{X}, t) = \varphi^*(\mathbf{X}^*, t)$ should leave the constitutive response unaffected. The associated deformation gradient in view of the rotated reference configuration then reads

$$\mathbf{F}^* = \frac{\partial \mathbf{x}}{\partial \mathbf{X}^*} = \mathbf{F}\mathbf{Q}^T \quad \text{with} \quad \mathbf{Q} : \mathcal{B}_0 \mapsto \mathcal{B}_0^*. \quad (3.66)$$

In contrast to \mathbf{C}^+ , \mathbf{C}^* is not identical to \mathbf{C} since

$$\mathbf{C}^* = (\mathbf{F}^*)^T \mathbf{F}^* = \mathbf{Q}\mathbf{C}\mathbf{Q}^T \neq \mathbf{C}. \quad (3.67)$$

Therefore the fundamental principle of isotropic material symmetry

$$\mathbf{Q}\mathbf{S}(\mathbf{C})\mathbf{Q}^T = \mathbf{S}(\mathbf{Q}\mathbf{C}\mathbf{Q}^T) \quad \forall \quad \mathbf{Q} \in \mathcal{G}_{\text{iso}} \quad (3.68)$$

is not automatically fulfilled. The latter equation represents the restriction for an isotropic material with the symmetry group

$$\mathcal{G}_{\text{iso}} := \text{SO}(3). \quad (3.69)$$

However, as will be shown in Sec. 3.5 there exist scalar invariant functions solely depending on \mathbf{C} that are able to accomplish the necessary prerequisite in Eq. (3.68).

For materials exhibiting a transversely isotropic material characteristic, the constitutive equation is not only linked to the stretch but also depends on one or more predefined material directions incorporated in a so-called structural tensor \mathbf{M} . Then, the fundamental principle of material symmetry for a transversely isotropic material reads

$$\mathbf{Q}\mathbf{S}(\mathbf{C}, \mathbf{M})\mathbf{Q}^T = \mathbf{S}(\mathbf{Q}\mathbf{C}\mathbf{Q}^T, \mathbf{Q}\mathbf{M}\mathbf{Q}^T) \quad \forall \quad \mathbf{Q} \in \mathcal{G}_{\text{ti}}. \quad (3.70)$$

Let \mathbf{A} , with $\|\mathbf{A}\| = 1$, be the preferred material direction vector of the transversely isotropic material, then the material symmetry group is defined by

$$\mathcal{G}_{\text{ti}} := \{ \pm \mathbf{1}; \mathbf{Q}(\alpha, \mathbf{A}) \mid 0 < \alpha < 2\pi \}, \quad (3.71)$$

where $\mathbf{Q}(\alpha, \mathbf{A})$ is the set of all admissible rotations about the \mathbf{A} -axis. The orthogonal tensor \mathbf{Q} may also be written as

$$\mathbf{Q}(\alpha, \mathbf{A}) = \begin{pmatrix} A_1^2(1-c) + c & A_1A_2(1-c) - A_3s & A_1A_3(1-c) + A_2s \\ A_1A_2(1-c) + A_3s & A_2^2(1-c) + c & A_2A_3(1-c) - A_1s \\ A_1A_3(1-c) - A_2s & A_2A_3(1-c) + A_1s & A_3^2(1-c) + c \end{pmatrix} \quad (3.72)$$

with the abbreviations $c = \cos \alpha$, $s = \sin \alpha$ and $A_i \mid i = 1, 2, 3$ denoting the specific vector entries of \mathbf{A} . The structural tensor \mathbf{M} , whose invariance group preserves the material symmetry group \mathcal{G}_{ti} , is given by the rank-one tensor

$$\mathbf{M} = \mathbf{A} \otimes \mathbf{A}, \quad (3.73)$$

see BOEHLER [14; 15] regarding the concept of structural tensors. Making use of Eq. (3.72) and (3.73) it is possible to show that

$$\mathbf{Q}\mathbf{M}\mathbf{Q}^T = \mathbf{M} \quad \forall \quad \mathbf{Q} \in \mathcal{G}_{\text{ti}} \quad (3.74)$$

such that the concept of structural tensors recovers isotropic like quantities regarding the symmetry group \mathcal{G}_{ti} .

Orthotropic material behavior is symmetric regarding three mutually orthogonal planes and thus the extended principle

$$QS(C, M_1, M_2, M_3)Q^T = S(QCQ^T, QM_1Q^T, QM_2Q^T, QM_3Q^T) \quad \forall Q \in \mathcal{G}_o \quad (3.75)$$

holds. These three planes are spanned by the three preferred directions \mathbf{A}_1 , \mathbf{A}_2 and \mathbf{A}_3 which are orthogonal unit vectors. The material symmetry group is then defined by

$$\mathcal{G}_o := \{\pm \mathbf{1}; \mathbf{R}_1, \mathbf{R}_2, \mathbf{R}_3\}, \quad (3.76)$$

where \mathbf{R}_1 , \mathbf{R}_2 and \mathbf{R}_3 are the reflections with respect to the planes spanned by $(\mathbf{A}_2, \mathbf{A}_3)$, $(\mathbf{A}_1, \mathbf{A}_3)$ and $(\mathbf{A}_1, \mathbf{A}_2)$, respectively. The three preferred directions $\mathbf{A}_i | i = 1, 2, 3$ form the three structural tensors $\mathbf{M}_i = \mathbf{A}_i \otimes \mathbf{A}_i | i = 1, 2, 3$ which satisfy the orthogonality conditions $\mathbf{M}_i : \mathbf{M}_j = \delta_{ij}$. However, it is sufficient to formulate orthotropic strain-energies with only two structural tensors \mathbf{M}_1 and \mathbf{M}_2 and additional isotropic principal or main invariants. It is possible to show that

$$QM_1Q^T = M_1, \quad QM_2Q^T = M_2, \quad QM_3Q^T = M_3 \quad \forall Q \in \mathcal{G}_o \quad (3.77)$$

such that the concept of structural tensors recovers isotropic like quantities regarding the symmetry group \mathcal{G}_o .

3.5 Isotropic and Anisotropic Invariants of Strain and Stretch Tensors

Building on the aforementioned construction principles of free-energy functions, it is common to use invariants that automatically fulfill the requirements. Regarding the right *Cauchy-Green* tensor \mathbf{C} , the principal isotropic invariants are given by

$$\begin{aligned} I_1^C &= \text{tr}[\mathbf{C}] = \lambda_1^2 + \lambda_2^2 + \lambda_3^2, & I_2^C &= \text{tr}[\text{Cof } \mathbf{C}] = \lambda_1^2\lambda_2^2 + \lambda_1^2\lambda_3^2 + \lambda_2^2\lambda_3^2 \quad \text{and} \\ I_3^C &= \det \mathbf{C} = \lambda_1^2\lambda_2^2\lambda_3^2, \end{aligned} \quad (3.78)$$

where the cofactor is defined as $\text{Cof}(\bullet) = \det(\bullet)(\bullet)^{-T}$. As can be seen above, the principal invariants may be exclusively expressed in terms of the eigenvalues $\lambda_i^2 | i = 1, 2, 3$ of \mathbf{C} . The transformation

$$\mathbf{C}^* = \mathbf{C}\mathbf{C}\mathbf{C}^T = \sum_{k=1}^3 \lambda_k^2 \mathbf{Q}\mathbf{N}^k \otimes \mathbf{Q}\mathbf{N}^k \quad (3.79)$$

reveals that the eigenvalues of \mathbf{C}^* and \mathbf{C} are the same, since $\mathbf{Q}\mathbf{N}^i \perp \mathbf{Q}\mathbf{N}^j$ if $i \neq j$ and $\|\mathbf{Q}\mathbf{N}^k\| = 1$. Therefore, $\mathbf{Q}\mathbf{N}^k$ are the eigenvectors of \mathbf{C}^* . Thus, the invariants $I_1 = I_1^*$, $I_2 = I_2^*$ and $I_3 = I_3^*$ remain unaltered after transformation with an element of the symmetry group \mathcal{G}_{iso} , even though $\mathbf{C} \neq \mathbf{C}^*$. Taking into account the spectral decomposition in Eq. (3.20), one may easily see that also the eigenvalues of \mathbf{b} and therefore also the principal invariants must be identical. According to RICHTER [140], let us further

introduce the basic isotropic invariants

$$\begin{aligned}
J_1^{\text{H}} &= \text{tr}(\log \mathbf{U}) = \log(\det \mathbf{U}) = \sum_{k=1}^3 \log \lambda_k, \\
J_2^{\text{H}} &= \text{tr}[(\log \mathbf{U})^2] = \|\log \mathbf{U}\|^2 = \sum_{k=1}^3 (\log \lambda_k)^2 \quad \text{and} \\
J_3^{\text{H}} &= \text{tr}[(\log \mathbf{U})^3] = \sum_{k=1}^3 (\log \lambda_k)^3
\end{aligned} \tag{3.80}$$

of the *Hencky* strain tensor $\log \mathbf{U}$. Anisotropic invariants, sometimes also call mixed invariants, involving structural tensors as defined in Eq. (3.73) may be defined according to

$$\begin{aligned}
I_4^{\text{C}^i} &= \mathbf{C}^i : \mathbf{M}, & J_5^{\text{C}} &= \text{Cof } \mathbf{C} : \mathbf{M}, \\
I_4^{\text{H}^i} &= (\log \mathbf{U})^i : \mathbf{M}, & J_5^{\text{H}} &= \log(\text{Cof } \mathbf{U}) : \mathbf{M},
\end{aligned} \tag{3.81}$$

where $i \in \mathbb{N}$, $i > 0$, denotes an exponent. The invariant $I_4^{\text{C}^1}$ has gained special attention in the modeling of biological tissues in recent years due to its clear physical interpretation as the squared stretch in fiber direction \mathbf{A} . In J_5^{H} the positive definite tensor $\text{Cof } \mathbf{U} \in \text{Sym}^+(3)$ is used. In contrast, $\text{Cof}(\log \mathbf{U})$ would lack of this property and further has no physical meaning. The logarithmic cofactor function

$$\begin{aligned}
\log(\text{Cof } \mathbf{U}) &= \log [(\det \mathbf{U}) \mathbf{U}^{-T}] = \sum_{k=1}^3 \log \left(\frac{\det \sqrt{\mathbf{C}}}{\lambda_k} \right) \mathbf{N}^k \otimes \mathbf{N}^k \\
&= \sum_{k=1}^3 \left[\log(\det \sqrt{\mathbf{C}}) - \log \lambda_k \right] \mathbf{N}^k \otimes \mathbf{N}^k \\
&= (\log \lambda_2 + \log \lambda_3) \mathbf{N}^1 \otimes \mathbf{N}^1 + (\log \lambda_1 + \log \lambda_3) \mathbf{N}^2 \otimes \mathbf{N}^2 \\
&\quad + (\log \lambda_1 + \log \lambda_2) \mathbf{N}^3 \otimes \mathbf{N}^3 \\
&= \text{tr}(\log \mathbf{U}) \mathbf{1} - \log \mathbf{U}
\end{aligned} \tag{3.82}$$

yields the transversely isotropic invariant

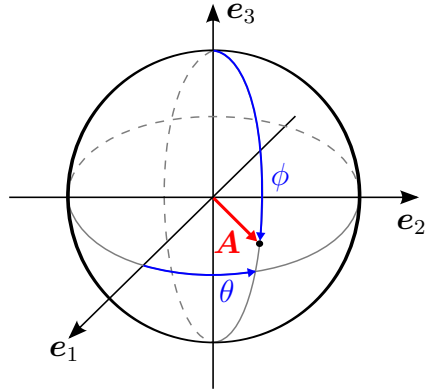
$$J_5^{\text{H}} = \log(\text{Cof } \mathbf{U}) : \mathbf{M} = \text{tr}(\log \mathbf{U}) \underbrace{\mathbf{M} : \mathbf{1}}_1 - \log \mathbf{U} : \mathbf{M} = J_1^{\text{H}} - I_4^{\text{H}^1}, \tag{3.83}$$

which is added to the set of invariants. Generally, when a strain-energy function is formulated only in terms of isotropic invariants the stretch tensor \mathbf{b} and the stress tensor $\boldsymbol{\sigma}$ will be coaxial, i.e. they share the same eigenvectors. As soon as mixed invariants come into play this observation is no longer valid.

The set of all possible preferred material directions may be formulated in the spherical coordinates

$$\begin{aligned}
x_1 &= r \sin \phi \cos \theta, \\
x_2 &= r \sin \phi \sin \theta, \\
x_3 &= r \cos \phi.
\end{aligned} \tag{3.84}$$

The radius r is chosen equal to one, while $\theta \in [-\pi, \pi]$ and $\phi \in [0, \pi]$ denote the azimuth and polar angle, respectively. This results in the unit vector



$$\mathbf{A} = \begin{pmatrix} \sin \phi \cos \theta \\ \sin \phi \sin \theta \\ \cos \phi \end{pmatrix}. \quad (3.85)$$

Further, let us define the angles θ_j between the eigenvectors \mathbf{N}_j and the preferred material directions \mathbf{A} as

$$\cos \theta_1 = \mathbf{A} \cdot \mathbf{N}_1, \quad \cos \theta_2 = \mathbf{A} \cdot \mathbf{N}_2, \quad \cos \theta_3 = \mathbf{A} \cdot \mathbf{N}_3.$$

Then we obtain the alternative representations of the above defined invariants

$$I_4^{C^i} = (\lambda_1^2)^i \cos^2 \theta_1 + (\lambda_2^2)^i \cos^2 \theta_2 + (\lambda_3^2)^i \cos^2 \theta_3, \quad (3.86)$$

$$I_4^{H^i} = (\log \lambda_1)^i \cos^2 \theta_1 + (\log \lambda_2)^i \cos^2 \theta_2 + (\log \lambda_3)^i \cos^2 \theta_3. \quad (3.87)$$

In a first step the anisotropic invariants of the right *Cauchy-Green* tensor are to be compared to the anisotropic invariants of the *Hencky* tensor for the exponents $i = 1, 2, 3, 4$ on a simple example for one specific state of strain. In order to do so let us assume the tensor

$$\mathbf{C} = \sum_{k=1}^3 \lambda_k^2 \mathbf{N}_k \otimes \mathbf{N}_k, \quad \text{with}$$

$$\lambda_1^2 = 1.35, \quad \lambda_2^2 = 0.9, \quad \lambda_3^2 = 0.7 \quad \text{and}$$

$$\mathbf{N}_1 = \begin{pmatrix} 1 \\ 0 \\ 0 \end{pmatrix}, \quad \mathbf{N}_2 = \begin{pmatrix} 0 \\ 1 \\ 0 \end{pmatrix}, \quad \mathbf{N}_3 = \begin{pmatrix} 0 \\ 0 \\ 1 \end{pmatrix}, \quad (3.88)$$

represented in spectral decomposition. Based on that, invariant plots for all possible preferred directions \mathbf{A} are shown in Fig. 3.2 according to Eq. (3.86) for the right *Cauchy-Green* tensor and in Fig. 3.3 according to Eq. (3.87) for the *Hencky* tensor. Every point of the plotted unit spheres represents one specific orientation $\mathbf{A}(x_1, x_2, x_3)$ with x_1, x_2 and x_3 coordinates and $r = 1$, compare Eqs. (3.84) and (3.85). The associated invariant values are displayed by the color scale. Please note that a value of one is subtracted from the invariants based on \mathbf{C} in order to be able to compare stretches ($I_4^{C^i}$) and strains ($I_4^{H^i}$). Furthermore, please also note that a different choice of the orthogonal vectors $\mathbf{N}_1, \mathbf{N}_2$ and \mathbf{N}_3 would merely result in a rotation of the sphere with the eigenvector-axes. Therefore, for this kind of plot arbitrary eigenvectors could be assumed without loss of generality such that the eigenvalues remain as the only variables.

First of all it becomes apparent from the contour plots that all the direction dependent distributions of $I_4^{C^i}$ are very similar. This also applies for $I_4^{H^1}$ and to some extent for $I_4^{H^3}$. For $I_4^{H^2}$ and $I_4^{H^4}$ however a different picture emerges. As can be seen the maximum is shifted from the \mathbf{N}_1 direction to the \mathbf{N}_3 direction while the minimum in turn is shifted from the \mathbf{N}_3 direction to the \mathbf{N}_2 direction. In view of Eq. (3.85) the fiber directions may also be uniquely expressed in terms of the polar and azimuth angles ϕ and θ . This alternative representation was exploited in the right column of the discussed figures next to the spheres, where the signum functions of the invariants at hand are plotted. These are helpful in explaining the above recognized discrepancies of the plotted spheres, especially for $I_4^{H^2}$ and $I_4^{H^4}$. For these two invariants (and for any other invariant $I_4^{H^i}$ with an even exponent i) the invariant will always be positive or zero. If i takes an even number both $(\log \mathbf{U})^i$ and the structural tensor \mathbf{M} are semi-positive definite and therefore $I_4^{H^i} = (\log \mathbf{U})^i : \mathbf{M} \geq 0$. Then the shift of the maximum and minimum invariant values can easily be explained since the logarithmic invariant function in Eq. (3.87) weights the (compressive) eigenvalues $\lambda_k < 1$ stronger than the (tensile) eigenvalues $\lambda_k > 1$.

The second important aspect included in the signum plots deals with the distinction of compressive and tensile fiber strains/stretchers. In view of modeling biological collagen reinforced tissues it is important to exclude fibers under compression from the constitutive model due to the waviness of the fibers. In that sense the plotted signum functions of the invariants are tested as a distinguishing criterion. As discussed above, every function $\text{sign}[(\log \mathbf{U})^i : \mathbf{M}]$ with an even value of i is inappropriate to serve as a criterion since they will always be positive, thus making a distinction impossible. For the other invariants in Fig. 3.2 and Fig. 3.3 the green areas would represent active zones of stretched fibers while the gray areas denote compressed fibers where the constitutive response should be switched off. As can be seen for $\mathbf{C}^i : \mathbf{M}$ the tensile area tends to increase with i . The plots of $\mathbf{C}^1 : \mathbf{M} - 1$ and $(\log \mathbf{U})^1 : \mathbf{M}$ appear to be very similar. Due to the clear physical interpretation of $\mathbf{C}^1 : \mathbf{M}$ it is very effective to compare those two different measures in more detail. As shown in SCHRÖDER ET AL. [157], the fundamental relation

$$\mathbf{C} : \mathbf{M} - 1 \geq \frac{1}{2} \log \mathbf{C} : \mathbf{M} = \log \mathbf{U} : \mathbf{M} \quad \text{for } \mathbf{C} : \mathbf{M} \geq 1 \quad (3.89)$$

can be derived. As a conclusion of these considerations, a switching criterion based on $\log \mathbf{U} : \mathbf{M}$ will always exclude physically stretched fibers within the framework of affine fiber deformations. Analytical proof of Eq. (3.89) is obtained by considering that

$$\begin{aligned} \mathbf{C} : \mathbf{M} - 1 - \log \mathbf{C} : \mathbf{M} &= (\mathbf{C} - 1) : \mathbf{M} - \log \mathbf{C} : \mathbf{M} \\ &= \sum_k^3 \underbrace{[\lambda_k^2 - 1 - \log(\lambda_k^2)]}_{\geq 0} \underbrace{\cos^2 \theta_k}_{\geq 0} \geq 0. \end{aligned}$$

Consequently, we obtain

$$\mathbf{C} : \mathbf{M} - 1 \geq \log \mathbf{C} : \mathbf{M} \quad (3.90)$$

and thus Eq. (3.89) follows for the special case that $\mathbf{C} : \mathbf{M} \geq 1$. Knowing about this inequality, Fig. 3.4 shows three different zones. Areas where both $\mathbf{C} : \mathbf{M} - 1$ and $(\log \mathbf{U}) : \mathbf{M}$ are positive are shown in green and zones where both are negative are depicted in dark gray. However, there exists a transition zone, colored in light gray where $\mathbf{C} : \mathbf{M} - 1$ is positive while $(\log \mathbf{U}) : \mathbf{M}$ is negative. The opposite case, i.e. $\mathbf{C} : \mathbf{M} - 1 < 0$ and $(\log \mathbf{U}) : \mathbf{M} > 0$, is precluded by Eq. (3.90).

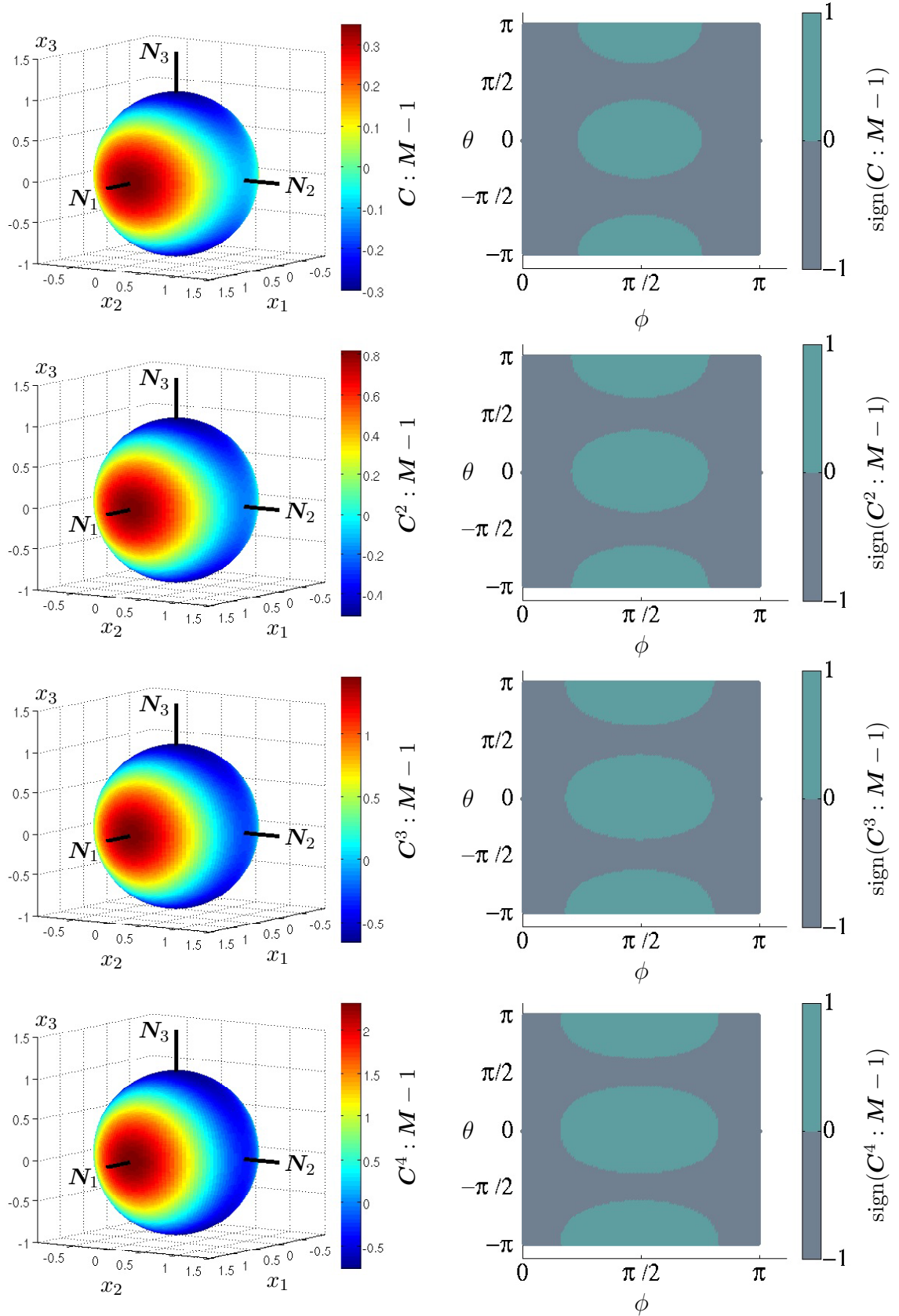


Figure 3.2: Contour plots of transversely isotropic invariants (left column) based on $C = \text{diag}[1.35; 0.9; 0.7]$, see Eq. (3.88), and corresponding plots of the signum function (right column). Each point on the spheres is associated with a specific preferred direction $A(x_1, x_2, x_3)$.

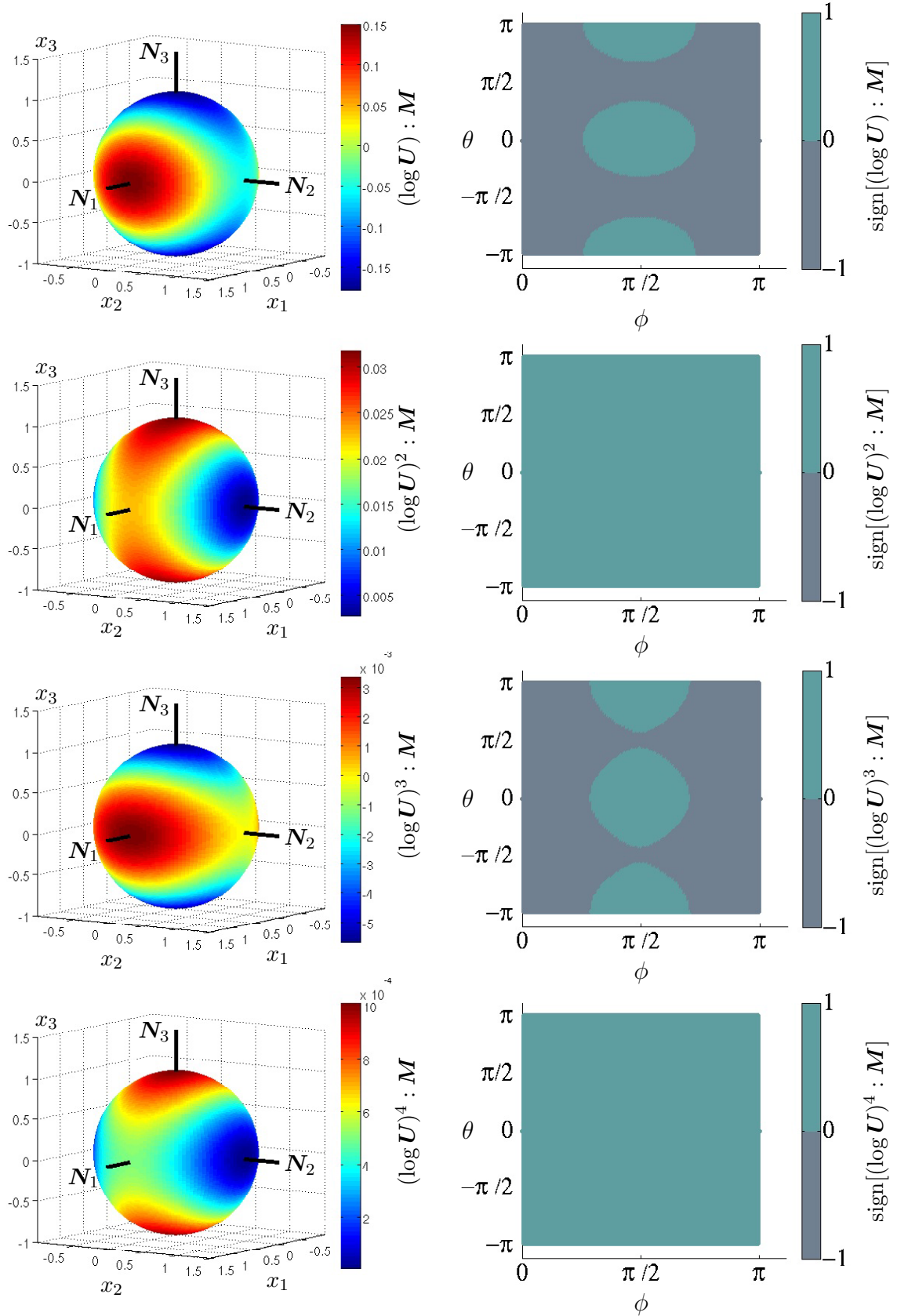


Figure 3.3: Contour plot of transversely isotropic invariants (left column) based on $\log U = 1/2 \log C$ with $C = \text{diag}[1.35; 0.9; 0.7]$, see Eq. (3.88), and corresponding plots of the signum function (right column). Each point on the spheres is associated with a specific preferred direction $\mathbf{A}(x_1, x_2, x_3)$.

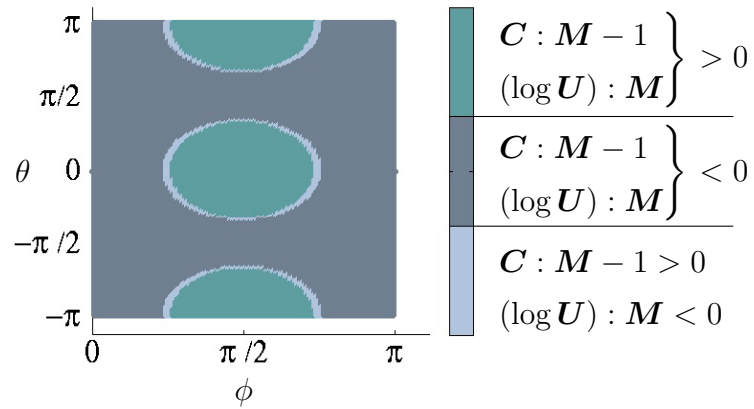


Figure 3.4: Comparison of the signum function of $\mathbf{C} : \mathbf{M} - 1$ and $(\log \mathbf{U}) : \mathbf{M}$. Only three different cases are to be distinguished, the transition zone with different sign is colored in light gray. Again, the right *Cauchy-Green* tensor is set to $\mathbf{C} = \text{diag}[1.35; 0.9; 0.7]$, see Eq. (3.88).

3.6 Kinematics of Micromorphic Continua

The generalized micromorphic continuum consists of a macro-space $\mathcal{B}_0 \subset \mathbb{R}^3$ according to Sec. 3.1 which is combined with an underlying micro-space \mathcal{S}_0 , enriched with additional degrees of freedom. Then the generalized continuum space in the undeformed state

$$\mathcal{M}_0 := \mathcal{B}_0 \times \mathcal{S}_0 := \{(\mathbf{X}, \boldsymbol{\Xi}) | \mathbf{X} \in \mathcal{B}_0 \text{ and } \boldsymbol{\Xi} \in \mathcal{S}_0\} \in \mathbb{E}(3+n) \quad (3.91)$$

is defined with help of the *Cartesian* product as the set of all ordered pairs $(\mathbf{X}, \boldsymbol{\Xi})$. Here, \mathbf{X} still denotes the reference placement vector in \mathcal{B}_0 while $\boldsymbol{\Xi}$ denotes the reference vector of order n which is associated to \mathcal{S}_0 . Assuming an additive nature of the generalized space, the generalized placement vector is given by

$$\tilde{\mathbf{X}}(\vartheta^k, \zeta^\alpha) = \mathbf{X}(\vartheta^k) + \boldsymbol{\Xi}(\vartheta^k, \zeta^\alpha), \quad \tilde{\mathbf{X}} \in \mathcal{M}_0. \quad (3.92)$$

While the macro-coordinates $\vartheta^k | k = 1, 2, 3$ are still limited to the three-dimensional space, the micro-coordinates $\zeta^\alpha | \alpha = 1, 2, \dots, n$ are generally n -dimensional. A formal representation of the placement vectors in the reference domain \mathcal{M}_0 and in the actual domain \mathcal{M} is depicted in Fig. 3.5. In analogy to the base vectors of the macro-space, cf. Eq. (3.4), one may define the curvilinear generalized base vectors

$$\tilde{\mathbf{G}}_k = \frac{\partial \tilde{\mathbf{X}}}{\partial \vartheta^k} \quad \text{and} \quad \tilde{\mathbf{g}}_k = \frac{\partial \tilde{\mathbf{x}}}{\partial \vartheta^k} \quad (3.93)$$

as well as

$$\tilde{\mathbf{I}}_\alpha = \frac{\partial \tilde{\mathbf{X}}}{\partial \zeta^\alpha} \quad \text{and} \quad \tilde{\mathbf{i}}_\alpha = \frac{\partial \tilde{\mathbf{x}}}{\partial \zeta^\alpha}. \quad (3.94)$$

Then the dual base system is defined by

$$\tilde{\mathbf{G}}^k = \frac{\partial \vartheta^k}{\partial \tilde{\mathbf{X}}} \quad \text{and} \quad \tilde{\mathbf{g}}^k = \frac{\partial \vartheta^k}{\partial \tilde{\mathbf{x}}} \quad (3.95)$$

as well as

$$\tilde{\mathbf{I}}^\alpha = \frac{\partial \zeta^\alpha}{\partial \tilde{\mathbf{X}}} \quad \text{and} \quad \tilde{\mathbf{i}}^\alpha = \frac{\partial \zeta^\alpha}{\partial \tilde{\mathbf{x}}}. \quad (3.96)$$

Analogously to Eqs. (3.91) and (3.92), the actual generalized domain is defined in terms of the *Cartesian* product

$$\mathcal{M} := \mathcal{B} \times \mathcal{S} := \{(\mathbf{x}, \boldsymbol{\xi}) | \mathbf{x} \in \mathcal{B} \text{ and } \boldsymbol{\xi} \in \mathcal{S}\} \in \mathbb{E}(3+n) \quad (3.97)$$

of the actual macro- and micro-space \mathcal{B} and \mathcal{S} and the actual generalized placement vector is again additively split into

$$\tilde{\mathbf{x}}(\vartheta^k, \zeta^\alpha, t) = \mathbf{x}(\vartheta^k, t) + \boldsymbol{\xi}(\vartheta^k, \zeta^\alpha, t), \quad \tilde{\mathbf{x}} \in \mathcal{M}. \quad (3.98)$$

The vectors $\mathbf{x} \in \mathcal{B}$ and $\boldsymbol{\xi} \in \mathcal{S}$ denote the macro- and micro-placement vectors after deformation at a certain time-step t .

In order to complete the description of the generalized continuum it is essential to choose an ansatz for the micro-motion depending on the additional degrees of freedom associated to the micro-space. In the simplest case this is

$$\boldsymbol{\Xi} = \zeta^\alpha \mathbf{A}_\alpha(\vartheta^k, \zeta^\alpha) \quad \text{and} \quad \boldsymbol{\xi} = \zeta^\alpha \mathbf{a}_\alpha(\vartheta^k, \zeta^\beta, t), \quad (3.99)$$

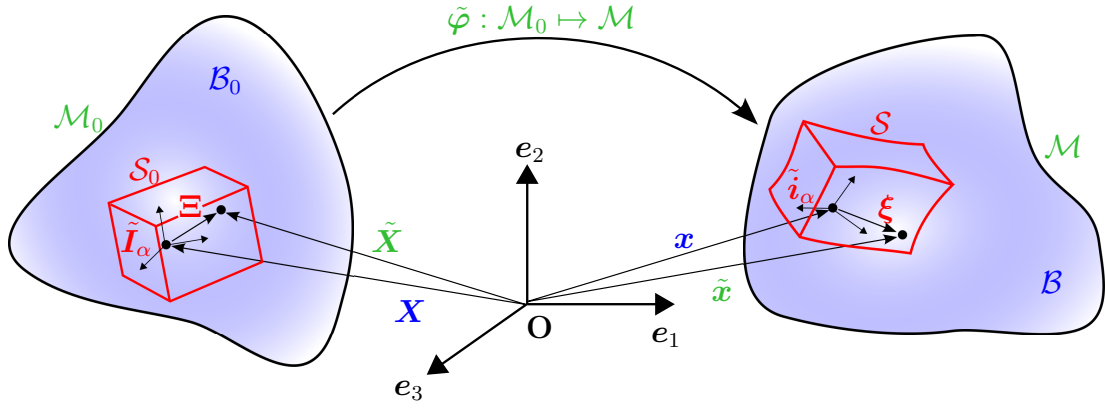


Figure 3.5: Micromorphic continuum spaces. Taken from VON HOEGEN ET AL. [185].

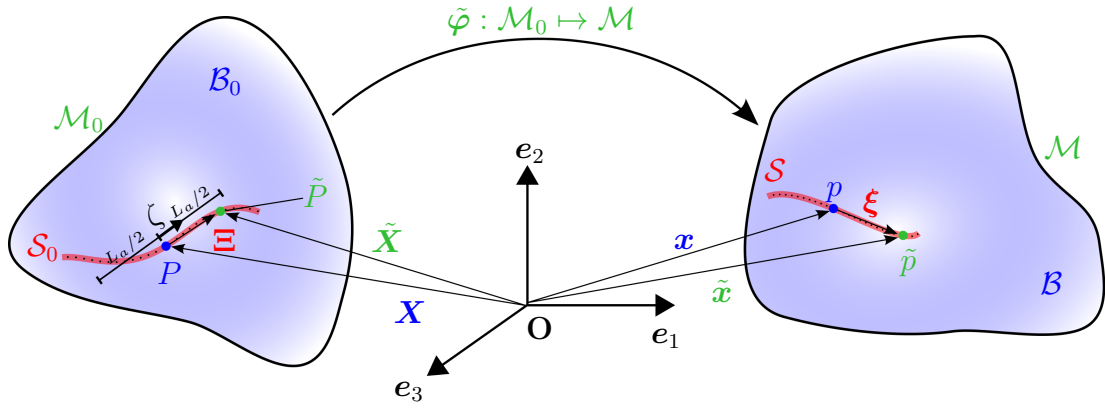


Figure 3.6: Micromorphic continuum with a micro-continuum of first order.

see also ERINGEN [38]. In the following the a priori choice

$$\Xi = \zeta^\alpha \mathbf{A}_\alpha(\vartheta^k, \zeta^\alpha) \quad \text{and} \quad \xi = \zeta^\alpha (1 + \zeta^\beta \chi^\beta(\vartheta^k, t)) \mathbf{a}_\alpha(\vartheta^k, \zeta^\beta, t), \quad (3.100)$$

made by SANSOUR ET AL. [145] will be utilized. This refers to a quadratic formulation of full-rank as will become apparent in the definition of strain-measures performed later. Further, the following considerations and results are restricted to a micromorphic continuum of first order, i.e. only one director \mathbf{A} is present and $n = \alpha = \beta = 1$. Therefore, Greek superscripts are neglected in the further course. The predefined director $\mathbf{A}(\vartheta^k, \zeta)$ essentially determines the orientation of the 1-D micro-continuum \mathcal{S}_0 along ζ . A micromorphic continuum of order one is schematically depicted in Fig. 3.6, where the origin of the one-dimensional micro-coordinate ζ is associated with the macroscopic material point P . The chord length of the micro-continuum of order one is denoted with the length-scale parameter L_a and $\zeta \in [L_a/2; -L_a/2]$. The director represents an initial orientation vector which could be associated to a fiber bundle. The orientation may vary in both spaces \mathcal{B}_0 and \mathcal{S}_0 or in other words it may be a function of both the macro-coordinates ϑ^k and the micro-coordinate ζ . The director is deformed independently of the macro-deformations according to Tab. 3.1 by the micro-deformation vector \mathbf{w} . Further, the scalar quantity χ in Eq. (3.100) forms an additional degree of freedom that linearly scales the strain in

direction of Ξ and was introduced to achieve the quadratic characteristic while reducing the number of degrees of freedom, see SANSOUR ET AL. [145].

\mathcal{B}/\mathcal{S}	$\mathcal{B}_0/\mathcal{S}_0$	$Defo.$	Dof
\mathbf{x}	$= \mathbf{X}$	$+ \mathbf{u}$	3
\mathbf{a}_α	$= \mathbf{A}_\alpha$	$+ \mathbf{w}_\alpha$	$3 \cdot n$
χ_α	$= 0$	$+ \chi_\alpha$	$1 \cdot n$
			$3 + 4 \cdot n$

Table 3.1: Definition of the degrees of freedom of the micromorphic continuum of order n . Taken from VON HOEGEN ET AL. [185].

Having completed the description of the generalized kinematics it is necessary to derive the strain measures to be used in constitutive material models. As a first step, considering the placement vectors according to Eq. (3.100) as well as the base vectors according to Eqs. (3.95) and (3.96) the generalized deformation gradient reads as

$$\begin{aligned} \tilde{\mathbf{F}} &= \frac{\partial \tilde{\mathbf{x}}}{\partial \tilde{\mathbf{X}}} = \frac{\partial \tilde{\mathbf{x}}}{\partial \vartheta^k} \otimes \frac{\partial \vartheta^k}{\partial \tilde{\mathbf{X}}} + \frac{\partial \tilde{\mathbf{x}}}{\partial \zeta} \otimes \frac{\partial \zeta}{\partial \tilde{\mathbf{X}}} \\ &= [\mathbf{x}_{,k} + \zeta^2 \chi_{,k} \mathbf{a} + \zeta(1 + \zeta \chi) \mathbf{a}_{,k}] \otimes \tilde{\mathbf{G}}^k \\ &\quad + (1 + 2\zeta \chi) \mathbf{a} \otimes \tilde{\mathbf{I}} + (\zeta + \zeta^2 \chi) \mathbf{a}_{,\zeta} \otimes \tilde{\mathbf{I}} \end{aligned} \quad (3.101)$$

in analogy to Eq. (3.7). Here, the abbreviations $(\bullet)_{,k} := \frac{\partial(\bullet)}{\partial \vartheta^k}$ and $(\bullet)_{,\zeta} := \frac{\partial(\bullet)}{\partial \zeta}$ are used. In the later presented finite element framework the micro-deformations \mathbf{w} and χ are independent of ζ , i.e. $\mathbf{w}_{,\zeta} = \mathbf{0}$ and $\chi_{,\zeta} = 0$. Further, the generalized right *Cauchy-Green* tensor

$$\tilde{\mathbf{C}} = \tilde{\mathbf{F}}^T \tilde{\mathbf{F}} \approx \hat{\mathbf{C}} + \zeta \mathbf{K} \quad (3.102)$$

may be additively split into a part $\hat{\mathbf{C}}$, independent of ζ and one part \mathbf{K} which is multiplied with ζ . Quadratic terms in ζ are neglected, assuming the length of the micro-space to be small. In more detail these two parts comprise of the expressions provided in Tab. 3.2. Both, $\hat{\mathbf{C}}$ and \mathbf{K} are again additively split into three tensors $\hat{\mathbf{C}}^{(i)}$ and $\mathbf{K}^{(i)} | i = 0, 1, 2$, separating the specific tensor according to different base vectors.

$\hat{\mathbf{C}}$	$= \mathbf{C}^{(0)} + \mathbf{C}^{(1)} + \mathbf{C}^{(2)}$	\mathbf{K}	$= \mathbf{K}^{(0)} + \mathbf{K}^{(1)} + \mathbf{K}^{(2)}$
$\mathbf{C}^{(0)}$	$= (\mathbf{x}_{,k} \cdot \mathbf{x}_{,l}) \tilde{\mathbf{G}}^k \otimes \tilde{\mathbf{G}}^l$	$\mathbf{K}^{(0)}$	$= (\mathbf{a}_{,k} \cdot \mathbf{x}_{,l} + \mathbf{x}_{,k} \cdot \mathbf{a}_{,l}) \tilde{\mathbf{G}}^k \otimes \tilde{\mathbf{G}}^l$
$\mathbf{C}^{(1)}$	$= (\mathbf{x}_{,k} \cdot \mathbf{a})$ $\quad \left(\tilde{\mathbf{G}}^k \otimes \tilde{\mathbf{I}} + \tilde{\mathbf{I}} \otimes \tilde{\mathbf{G}}^k \right)$	$\mathbf{K}^{(1)}$	$= (\mathbf{a}_{,k} \cdot \mathbf{a} + 2\chi \mathbf{x}_{,k} \cdot \mathbf{a} + \mathbf{x}_{,k} \cdot \mathbf{a}_{,\zeta})$ $\quad \left(\tilde{\mathbf{G}}^k \otimes \tilde{\mathbf{I}} + \tilde{\mathbf{I}} \otimes \tilde{\mathbf{G}}^k \right)$
$\mathbf{C}^{(2)}$	$= (\mathbf{a} \cdot \mathbf{a}) \tilde{\mathbf{I}} \otimes \tilde{\mathbf{I}}$	$\mathbf{K}^{(2)}$	$= (4\chi \mathbf{a} \cdot \mathbf{a} + 2\mathbf{a} \cdot \mathbf{a}_{,\zeta}) \tilde{\mathbf{I}} \otimes \tilde{\mathbf{I}}$

Table 3.2: Split of the generalized right *Cauchy-Green* tensor, neglecting higher-order terms in ζ .

The inherent anisotropic characteristic of the discussed generalized strain measure becomes apparent when considering an initial director $\mathbf{A}(\vartheta^k, \zeta) = \mathbf{A}(\vartheta^k)$ which is independent of the micro-coordinate. In this special case it immediately follows from Eqs. (3.94) and (3.100) that $\tilde{\mathbf{I}} = \mathbf{A}$ and $\mathbf{a}_{,\zeta} = \mathbf{0}$. Hence, $\mathbf{C}^{(1)}$ describes stretch and shear between the macro- and microscopical tangent space while $\mathbf{C}^{(2)}$ represents a pure micro-strain. In contrast, $\mathbf{C}^{(0)}$ is always identical with the classical right *Cauchy-Green* tensor \mathbf{C} . The higher-order strain contributions $\mathbf{K}^{(0)}$, $\mathbf{K}^{(1)}$ and $\mathbf{K}^{(2)}$ are meant to include scale-dependent non-local fluctuations of the material response. A constitutive material law, accounting for non-affine as well as for affine motions of fiber bundles in comparison to the surrounding matrix material incorporates all six separated strains. In view of the higher order micro-strain $\mathbf{K}^{(2)}$ the tensor would vanish if the additional degree of freedom χ would be inactive and $\mathbf{A}_{,\zeta} = \mathbf{0}$. The placement vector would reduce to the one described in Eq. (3.99). This is specifically precluded by the followed assumption for the micro-placement $\boldsymbol{\xi}$.

For constitutive purposes let the lower- and higher-order strain measures

$$\mathbf{E}^{(i)} = \frac{1}{2} \left(\mathbf{C}^{(i)} - \mathbf{C}_0^{(i)} \right) \quad \text{and} \quad \mathbf{H}^{(i)} = \frac{1}{2} \left(\mathbf{K}^{(i)} - \mathbf{K}_0^{(i)} \right), \quad i = 0, 1, 2 \quad (3.103)$$

be given which are equal to $\mathbf{0}$ in the reference configuration. Consequently, $\mathbf{C}_0^{(i)}$ and $\mathbf{K}_0^{(i)}$ denote the strains evaluated at the reference configuration with $\tilde{\mathbf{x}} = \tilde{\mathbf{X}}$, $\mathbf{a} = \mathbf{A}$ and $\chi = 0$. Maintaining the concept of separating the strains with respect to the specific base vectors one may add the corresponding lower- and higher-order contributions

$$\tilde{\mathbf{E}}^{(i)} = \mathbf{E}^{(i)} + \zeta \mathbf{H}^{(i)}. \quad (3.104)$$

3.6.1 Micromorphic Constitutive Model

Let us define a generic free-energy function

$$\widetilde{W} := \widetilde{W}(\tilde{\mathbf{E}}^{(0)}, \tilde{\mathbf{E}}^{(1)}, \tilde{\mathbf{E}}^{(2)}) \quad (3.105)$$

based on the generalized strains in order to develop a hyperelastic material model. Consequently, in view of the second law of thermodynamics the generalized second *Piola-Kirchhoff* stress tensor

$$\tilde{\mathbf{S}} = \tilde{\mathbf{S}}^{(0)} + \tilde{\mathbf{S}}^{(1)} + \tilde{\mathbf{S}}^{(2)}$$

is additively split with respect to the specific strain contributions:

$$\tilde{\mathbf{S}}^{(0)} = \frac{\partial \widetilde{W}}{\partial \tilde{\mathbf{E}}^{(0)}}, \quad \tilde{\mathbf{S}}^{(1)} = \frac{\partial \widetilde{W}}{\partial \tilde{\mathbf{E}}^{(1)}}, \quad \tilde{\mathbf{S}}^{(2)} = \frac{\partial \widetilde{W}}{\partial \tilde{\mathbf{E}}^{(2)}}. \quad (3.106)$$

The separation of the strain measures with regard to the base vectors is effective in order to distinguish contributions related to the bulk material, to the interaction mechanisms between macro and micro-strains as well as to the single micro-strains. Then the balance of momentum in its weak form may be written in the form of a variational principle

$$\int_{\mathcal{B}_0} \int_{\mathcal{S}_0} \left\{ \tilde{\mathbf{S}}^{(0)} : \delta \tilde{\mathbf{E}}^{(0)} + \tilde{\mathbf{S}}^{(1)} : \delta \tilde{\mathbf{E}}^{(1)} + \tilde{\mathbf{S}}^{(2)} : \delta \tilde{\mathbf{E}}^{(2)} \right\} dS dV - \mathcal{W}_{ext} = 0. \quad (3.107)$$

Due to the additive decomposition of the generalized space \mathcal{M}_0 it is feasible to integrate separately over the macro- and micro-space domains \mathcal{B}_0 and \mathcal{S}_0 . According to the definition

of the generalized space in terms of the *Cartesian* product in Eq. (3.91), the generalized boundary space is split into

$$\begin{aligned} \partial\mathcal{B} \times \mathcal{S} &= \partial\mathcal{B}_D \times \mathcal{S} \cup \partial\mathcal{B}_N \times \mathcal{S} & \text{and} & & \partial\mathcal{B}_D \times \mathcal{S} \cap \partial\mathcal{B}_N \times \mathcal{S} &= \emptyset, \\ \mathcal{B} \times \partial\mathcal{S} &= \mathcal{B} \times \partial\mathcal{S}_D \cup \mathcal{B} \times \partial\mathcal{S}_N & \text{and} & & \mathcal{B} \times \partial\mathcal{S}_D \cap \mathcal{B} \times \partial\mathcal{S}_N &= \emptyset, \\ \partial\mathcal{B} \times \partial\mathcal{S} &= \partial\mathcal{B}_D \times \partial\mathcal{S}_D \cup \partial\mathcal{B}_N \times \partial\mathcal{S}_N & \text{and} & & \partial\mathcal{B}_D \times \partial\mathcal{S}_D \cap \partial\mathcal{B}_N \times \partial\mathcal{S}_N &= \emptyset. \end{aligned}$$

While subscript “D” indicates a boundary of Dirichlet-type, subscript “N” indicates a boundary space associated to Neumann boundary conditions. Accounting for the different boundary spaces, the variation of the external body and surface forces in \mathcal{W}_{ext} can be expressed as

$$\mathcal{W}_{ext} = \int_{\mathcal{B}_0} \mathbf{b}_a \cdot \delta \mathbf{u} \, dV + \int_{\mathcal{B}_0} \mathbf{l}_a \cdot \delta \mathbf{w} \, dV + \int_{\partial\mathcal{B}_N} \mathbf{t}^{(n)} \cdot \delta \mathbf{u} \, dA + \int_{\partial\mathcal{B}_N} \mathbf{q}^{(n)} \cdot \delta \mathbf{w} \, dA, \quad (3.108)$$

where the vectors \mathbf{b}_a , \mathbf{l}_a , $\mathbf{t}^{(n)}$ and $\mathbf{q}^{(n)}$ have already been integrated over the corresponding micro-space domain \mathcal{S} or $\partial\mathcal{S}_N$, respectively. Specifically, the first two vectors \mathbf{b}_a and \mathbf{l}_a are the lower- and higher order body forces given by

$$\begin{aligned} \mathbf{b}_a(\vartheta^k) &= \int_{\mathcal{S}_0} \tilde{\mathbf{b}}(\vartheta^k, \zeta) \, dS + \int_{\partial\mathcal{S}_N} \tilde{\mathbf{b}}^{(\nu)}(\vartheta^k, \iota) \, d\Sigma, \\ \mathbf{l}_a(\vartheta^k) &= \int_{\mathcal{S}_0} \zeta \tilde{\mathbf{b}}(\vartheta^k, \zeta) \, dS + \int_{\partial\mathcal{S}_N} \zeta \tilde{\mathbf{b}}^{(\nu)}(\vartheta^k, \iota) \, d\Sigma. \end{aligned} \quad (3.109)$$

Here, $\tilde{\mathbf{b}}$ is acting on $\mathcal{B} \times \mathcal{S}$ and $\tilde{\mathbf{b}}^{(\nu)}$ is a normal vector on $\mathcal{B} \times \partial\mathcal{S}_N$, whereby ι is the coordinate chart on $\partial\mathcal{S}$. In analogy to the body forces the external lower- and higher order traction vectors are given by

$$\begin{aligned} \mathbf{t}^{(n)}(\eta^k) &= \int_{\mathcal{S}_0} \tilde{\mathbf{t}}^{(n)}(\eta^k, \zeta) \, dS + \int_{\partial\mathcal{S}_N} \tilde{\mathbf{t}}^{(\nu)}(\eta^k, \iota) \, d\Sigma, \\ \mathbf{q}^{(n)}(\eta^k) &= \int_{\mathcal{S}_0} \zeta \tilde{\mathbf{t}}^{(n)}(\eta^k, \zeta) \, dS + \int_{\partial\mathcal{S}_N} \zeta \tilde{\mathbf{t}}^{(\nu)}(\eta^k, \iota) \, d\Sigma. \end{aligned} \quad (3.110)$$

Here, $\tilde{\mathbf{t}}^{(n)}$ is a normal vector on $\partial\mathcal{B}_N \times \mathcal{S}$ and $\tilde{\mathbf{t}}^{(\nu)}$ is a normal vector on $\partial\mathcal{B}_N \times \partial\mathcal{S}_N$, where $\eta^k|_{k=1,2}$ denotes the coordinate chart on the surface $\partial\mathcal{B}_N$.

3.6.2 Additional Micro-Deformation Constraint

For the numerical simulations presented in the further course it appears useful to limit the independent fiber reorientation on the micro-scale to a certain extent in order to draw meaningful comparisons and to characterize the material behavior. This consideration motivates to include essential micro-boundary conditions in the variational principle that enforce affine mappings of micro- and macro-deformations. The micro-deformation $\boldsymbol{\gamma}$ can easily be formulated based on the already introduced reference and actual micro-placement vectors $\boldsymbol{\Xi}$ and $\boldsymbol{\xi}$ according to

$$\boldsymbol{\xi}(\vartheta^k, \zeta, t) = \boldsymbol{\Xi}(\vartheta^k, \zeta) + \boldsymbol{\gamma}(\vartheta^k, \zeta, t), \quad (3.111)$$

where

$$\Xi = \zeta \mathbf{A} \quad \text{and} \quad \xi = \zeta(1 + \zeta\chi)(\mathbf{A} + \mathbf{w}), \quad (3.112)$$

see Eq. (3.100), and thus

$$\gamma = \zeta (1 + \zeta\chi) \mathbf{w} + \zeta^2 \chi \mathbf{A}. \quad (3.113)$$

A rigid coupling of macro- and micro-deformations would be present, if the affine mapping

$$\xi = \mathbf{F}\Xi \quad \text{on } \partial\mathcal{S}_D \quad (3.114)$$

controlled by the deformation gradient $\mathbf{F}(\vartheta^k, t) = \mathbf{1} + \text{Grad } \mathbf{u}$ would be present. Taking Eq. (3.111) into account this corresponds to a prescribed micro-deformation

$$\hat{\gamma} = \zeta (\mathbf{F} - \mathbf{1}) \mathbf{A} \quad \text{on } \partial\mathcal{S}_D. \quad (3.115)$$

As proposed in VON HOEGEN ET AL. [185], the constraint $\hat{\gamma} \approx \gamma$ can be enforced by adding a penalty to the micromorphic variational principle (Eq. (3.107)) resulting in

$$\begin{aligned} & \int_{\mathcal{B}_0} \int_{\mathcal{S}_0} \left\{ \tilde{\mathbf{S}}^{(0)} : \delta \tilde{\mathbf{E}}^{(0)} + \tilde{\mathbf{S}}^{(1)} : \delta \tilde{\mathbf{E}}^{(1)} + \tilde{\mathbf{S}}^{(2)} : \delta \tilde{\mathbf{E}}^{(2)} \right\} dS dV \\ & + \int_{\mathcal{B}_0} \int_{\partial\mathcal{S}_D} F (\hat{\gamma} - \gamma) \cdot \delta \gamma \, d\Sigma dV - \mathcal{W}_{ext} = 0. \end{aligned} \quad (3.116)$$

This penalty term provides the means to directly influence the distribution of the micro-placement $\xi(\vartheta^k, \zeta)$ throughout the micro-space \mathcal{S} although the specific condition is only enforced on \mathcal{S}_D . In this way, the deformed configuration of the bulk material constrains the micro-deformation γ associated to the fiber. However, this approach provides a certain degree of flexibility at the same time such that the extra degrees of freedom \mathbf{w} and χ , respectively, can be influenced differently if $\mathbf{A}(\vartheta^k, \zeta)$ is not constant in \mathcal{S}_0 . The strength of the coupling is essentially determined and controlled by the magnitude of the penalty parameter F . It is to be chosen large for a strong coupling and low for a weak coupling.

4 Finite Element Method

The finite element method (FEM) was developed starting from the middle of the 20th century. With increasing computer power it became an established tool in industry and science to solve partial differential equations numerically. In the mechanical description of solids it is particularly used in cases when the structure of the problem at hand does not allow for an efficient analytical solution of the balance laws discussed in the previous chapter. In the field of biological tissues, first and foremost, the complex geometries, the heterogeneous material composition and the general non-linearity of the material response are to mention.

The basic concept of the method is described in the following. Within the framework of this work, several different finite elements are used. In the light of the various existing types, the method is presented in general terms. The selection of textbooks about the FEM is large and varies considerably between theoretical and rather practical elaborations, sometimes with a certain specification on a special application field. Exhaustive descriptions may be found in ZIENKIEWICZ AND TAYLOR [197] or WRIGGERS [189] to mention only two examples.

The finite element method consists of three basic parts which are to be explained step by step. These include the formulation of a boundary value problem, the reformulation of the partial differential equation in its weak form and finally the discretization in a finite number of subspaces. Only the balance law of momentum is considered (Eq. (3.38)) with a constant temperature field $\theta(\mathbf{X}, t)$. Thus thermal effects are neglected.

4.1 Definition of a Boundary Value Problem

Once more let us consider the depicted body in Fig. 4.1 in the undeformed and deformed domains \mathcal{B}_0 and \mathcal{B} , respectively. The boundary domain $\partial\mathcal{B}_0$ of \mathcal{B}_0 in the reference configuration with

$$\partial\mathcal{B}_0 = \partial\mathcal{B}_{0,u} \cup \partial\mathcal{B}_{0,\sigma} \quad \text{and} \quad \partial\mathcal{B}_{0,u} \cap \partial\mathcal{B}_{0,\sigma} = \emptyset \quad (4.1)$$

and analogously the boundary domain $\partial\mathcal{B}$ of \mathcal{B} in the actual configuration with

$$\partial\mathcal{B} = \partial\mathcal{B}_u \cup \partial\mathcal{B}_\sigma \quad \text{and} \quad \partial\mathcal{B}_u \cap \partial\mathcal{B}_\sigma = \emptyset \quad (4.2)$$

are additively decomposed. The so-called *Dirichlet* boundary conditions

$$\mathbf{u}(\mathbf{X}, t) = \hat{\mathbf{u}}(\mathbf{X}, t) \quad \text{on} \quad \partial\mathcal{B}_{0,u} \quad (4.3)$$

predefine the displacement vector \mathbf{u} with a user-defined vector $\hat{\mathbf{u}}$. Please note that instead of predefining the whole displacement vector it is also possible to prescribe only specific vector entries of \mathbf{u} . On the domain $\mathcal{B}_0 \setminus \partial\mathcal{B}_{0,u}$ the displacements remain as unknowns in the balance equations. These boundaries are complemented by the boundary conditions

$$\mathbf{P}(\mathbf{X}, t)\mathbf{N}(\mathbf{X}) = \hat{\mathbf{t}}_0(\mathbf{X}, t) \quad \text{on} \quad \partial\mathcal{B}_{0,\sigma} \quad (4.4)$$

of *Neumann*-type, predefining a traction vector $\hat{\mathbf{t}}_0$ acting on the associated surface $\partial\mathcal{B}_{0,\sigma}$ with a normal vector \mathbf{N} . Please recall Eq. (3.23) for the definition of traction and normal vectors. The set of balance equations then needs to be solved according to the above defined boundary conditions. The function $\mathbf{u}(\mathbf{X}, t)$ on $\mathcal{B}_0 \setminus \partial\mathcal{B}_{0,u}$ needs to be found.

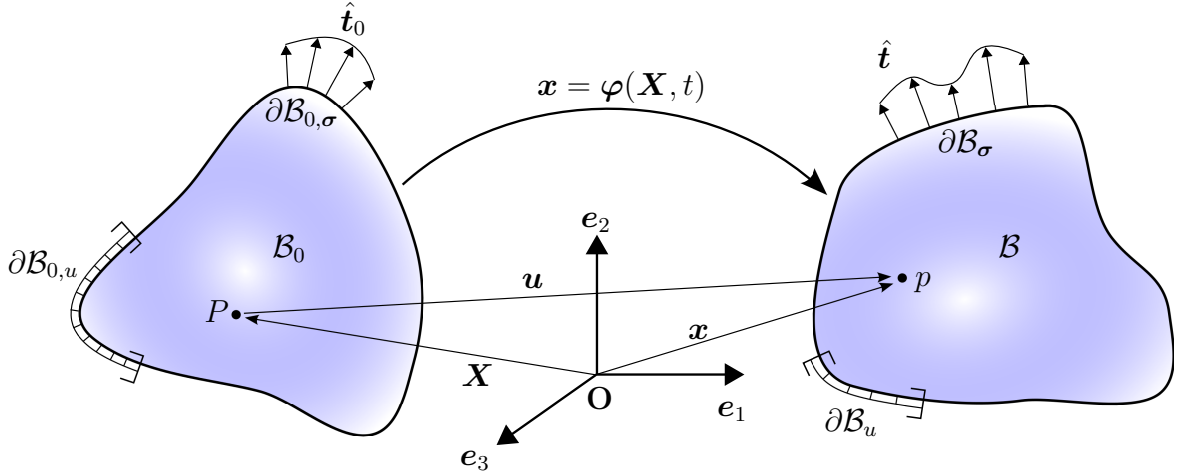


Figure 4.1: Boundary conditions of a continuum in the reference and actual configuration.

4.2 Weak Form of Balance of Momentum

The strong form of balance of momentum

$$\text{Div } \mathbf{P} + \rho_0(\mathbf{b}_a - \ddot{\mathbf{x}}) = \mathbf{0} \quad (4.5)$$

will be in most cases impossible to solve for the displacement function $\mathbf{u}(\mathbf{X}, t)$. A so-called weak form will be solved instead with aid of the finite element method. This in turn can be formulated with help of *Galerkin's* method. Neglecting the acceleration $\ddot{\mathbf{x}}$, the strong form in Eq. (4.5) is multiplied with a test function $\delta \mathbf{u}$ with $\delta \mathbf{u} = \mathbf{0}$ on $\partial \mathcal{B}_{0,u}$ and is integrated over the domain of interest:

$$G(\varphi, \delta \mathbf{u}) := \int_{\mathcal{B}_0} \text{Div } \mathbf{P} \cdot \delta \mathbf{u} + \rho_0 \mathbf{b}_a \cdot \delta \mathbf{u} \, dV = 0. \quad (4.6)$$

Thus, the dimension of the basic equation reduces from a vector to a scalar. The weak form is then reformulated by applying

$$\text{Div } \mathbf{P} \cdot \delta \mathbf{u} = \mathbf{P} : \text{Grad } \delta \mathbf{u} - \text{Div}(\mathbf{P}^T \delta \mathbf{u}) \quad (4.7)$$

and subsequently making use of *Gauss's*-divergence theorem

$$\int_{\mathcal{B}_0} \text{Div}(\mathbf{P}^T \delta \mathbf{u}) \, dV = \int_{\partial \mathcal{B}_{0,\sigma}} (\mathbf{P}^T \delta \mathbf{u}) \cdot d\mathbf{A} = \int_{\partial \mathcal{B}_{0,\sigma}} \hat{\mathbf{t}}_0 \cdot \delta \mathbf{u} \, dA, \quad (4.8)$$

where the volume integral is replaced by a surface integral. This results in the reformulated weak form of balance of momentum in the reference configuration

$$G(\varphi, \delta \mathbf{u}) = \underbrace{\int_{\mathcal{B}_0} \mathbf{P} : \text{Grad } \delta \mathbf{u} \, dV}_{G_{\text{int}}} - \underbrace{\left(\int_{\mathcal{B}_0} \rho_0 \mathbf{b}_a \cdot \delta \mathbf{u} \, dV + \int_{\partial \mathcal{B}_{0,\sigma}} \hat{\mathbf{t}}_0 \cdot \delta \mathbf{u} \, dA \right)}_{G_{\text{ext}}} = 0. \quad (4.9)$$

Alternatively, one may find that

$$G_{\text{int}} = \int_{\mathcal{B}_0} \mathbf{P} : \text{Grad } \delta \mathbf{u} \, dV = \int_{\mathcal{B}_0} \mathbf{S} : \delta \mathbf{E} \, dV \quad (4.10)$$

and it is worth noting that the variation of a potential energy functional

$$\Pi = \underbrace{\int_{\mathcal{B}_0} W(\mathbf{F}) \, dV}_{\Pi_{\text{int}}} - \underbrace{\left(\int_{\mathcal{B}_0} \rho_0 \mathbf{b}_a \cdot \mathbf{u} \, dV + \int_{\partial \mathcal{B}_{0,\sigma}} \hat{\mathbf{t}}_0 \cdot \mathbf{u} \, dA \right)}_{\Pi_{\text{ext}}} \quad (4.11)$$

yields the identical result, i.e. $\delta \Pi = G$. An equivalent expression in the actual configuration requires the transformation rule $\boldsymbol{\sigma} = \frac{1}{J} \mathbf{P} \mathbf{F}^T$ according to Eq. (3.24) and consequently we may find that

$$\mathbf{P} : \text{Grad } \delta \mathbf{u} = J(\boldsymbol{\sigma} \mathbf{F}^{-T}) : \text{Grad } \delta \mathbf{u} = J \boldsymbol{\sigma} : \text{grad } \delta \mathbf{u}. \quad (4.12)$$

Inserting Eq. (4.12), as well as the transformation rule for the traction vectors according to Eq. (3.23) in Eq. (4.9) and additionally considering the transport theorems $dv = JdV$ and $\rho = J\rho_0$ then yields

$$g(\varphi, \delta \mathbf{u}) = \int_{\mathcal{B}} \boldsymbol{\sigma} : \text{grad } \delta \mathbf{u} \, dv - \int_{\mathcal{B}} \rho \mathbf{b}_a \cdot \delta \mathbf{u} \, dv - \int_{\partial \mathcal{B}_\sigma} \hat{\mathbf{t}} \cdot \delta \mathbf{u} \, da = 0. \quad (4.13)$$

Here, g is exclusively expressed in quantities which are associated to the current configuration. Alternatively, Eq. (4.13) can be recast into a formulation

$$g(\varphi, \delta \mathbf{u}) = \underbrace{\int_{\mathcal{B}_0} \boldsymbol{\tau} : \text{grad } \delta \mathbf{u} \, dV}_{g_{\text{int}}} - \underbrace{\left(\int_{\mathcal{B}_0} \rho_0 \mathbf{b}_a \cdot \delta \mathbf{u} \, dV + \int_{\partial \mathcal{B}_{0,\sigma}} \hat{\mathbf{t}}_0 \cdot \delta \mathbf{u} \, dA \right)}_{g_{\text{ext}}} = 0, \quad (4.14)$$

which is integrated over the reference domain and where $\boldsymbol{\tau} = J\boldsymbol{\sigma}$. This simplifies the numerical integration and the linearization

$$\text{Lin } g|_{\varphi=\bar{\varphi}} := g(\bar{\varphi}, \delta \mathbf{u}) + \Delta g(\bar{\varphi}, \delta \mathbf{u}, \Delta \mathbf{u}) = 0 \quad (4.15)$$

of the weak form of the equilibrium equation at a specific deformation state $\mathbf{u} = \bar{\mathbf{u}}$ with a motion function $\varphi = \bar{\varphi}$ and

$$\Delta g(\bar{\varphi}, \delta \mathbf{u}, \Delta \mathbf{u}) = \underbrace{\int_{\mathcal{B}_0} (\text{grad } \Delta \mathbf{u} \boldsymbol{\tau}) : \text{grad } \delta \mathbf{u} \, dV}_{\Delta g_{\text{geo}}} + \underbrace{\int_{\mathcal{B}_0} \nabla_{\text{sym}} \delta \mathbf{u} : \mathbb{C} : \nabla_{\text{sym}} \Delta \mathbf{u} \, dV}_{\Delta g_{\text{mat}}}. \quad (4.16)$$

The incremental displacement vector is denoted with $\Delta \mathbf{u}$ and $\nabla_{\text{sym}}(\bullet) = 1/2 [\text{grad}(\bullet) + \text{grad}^T(\bullet)]$. The term Δg in turn is required due to the non-linearity of the equation. The full derivation of Eq. (4.16) is omitted, but it can be obtained as a push forward of the linearized weak form in the reference configuration. It is split into a geometric part Δg_{geo} referring to the non-linearity of the strain measure and a material part Δg_{mat} referring to the possible non-linearity of the constitutive law. For a specific boundary value problem it is essential to determine the displacement vector \mathbf{u} such that the condition in Eq. (4.14) is (approximately) met. This corresponds to a numerical determination of roots, which is usually performed with help of a *Newton*. The displacements are updated according to $\bar{\mathbf{u}}_{n+1} = \bar{\mathbf{u}}_n + \Delta \mathbf{u}_{n+1}$ until a motion $\bar{\varphi} = \varphi$ is found which sufficiently minimizes the error in Eq. (4.14). The increment $\Delta \mathbf{u}_{n+1}$ is computed from the linear system of equations arising from $\text{Lin } g = 0$, see Eq. (4.15).

A consistent linearization is indispensable for ensuring good convergence properties. However, that doesn't mean that convergence is guaranteed at all. A push-forward of the *Lagrangian* tangent moduli \mathbf{C} yields the *Eulerian* tangent moduli \mathbf{c} , i.e.

$$\mathbf{c} = (\mathbf{F} \boxtimes \mathbf{F}) : \mathbf{C} : (\mathbf{F}^T \boxtimes \mathbf{F}^T) \Big|_{\varphi=\bar{\varphi}} \quad \text{with} \quad \mathbf{C} = 4 \frac{\partial^2 W}{\partial \mathbf{C} \partial \mathbf{C}} \Big|_{\varphi=\bar{\varphi}}, \quad (4.17)$$

where the operator \boxtimes is defined in detail in Appendix A. The increment of the second *Piola-Kirchhoff* stress may be written as $\Delta \mathbf{S} = \mathbf{C} : \Delta \mathbf{E}$.

4.3 Discretization Strategy

Within the finite element method the potentially complicated arbitrary geometry \mathcal{B}_0 in the reference configuration is approximated by a finite number of interconnected elements n_e with an individual domain \mathcal{B}_0^e . Then the approximation of the domain

$$\mathcal{B}_0 \approx \mathcal{B}_0^h = \bigcup_{e=1}^{n_e} \mathcal{B}_0^e \quad (4.18)$$

is formed by the union of all elements, whereby it is important to note that two elements may share common edges (in 2D) or surfaces (in 3D), but must not overlap. In that sense, the elements form a mesh. An example for such a mesh is depicted in Fig. 4.2, where the domains of interest \mathcal{B}_0 and \mathcal{B} , respectively, are subdivided into four-noded elements. In general, the quality of the approximation $\mathcal{B}_0 \approx \mathcal{B}_0^h$ increases with the number of elements n_e .

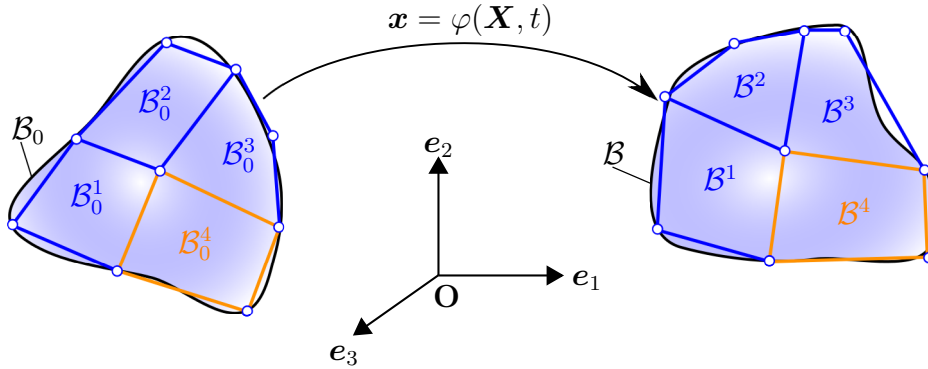


Figure 4.2: Exemplary mesh of a body in the deformed and undeformed configuration discretized with four quadrilateral elements. The nodes of the elements are shown as white dots. The element \mathcal{B}_0^4 is highlighted in orange for further consideration in the following figure.

Each element comprises a number of n_n nodes. Then the element geometry in the reference and actual placement

$$\mathbf{X} = \sum_{I=1}^{n_n} N_I(\boldsymbol{\xi}) \mathbf{X}_I \quad \text{and} \quad \mathbf{x} = \sum_{I=1}^{n_n} N_I(\boldsymbol{\xi}) \mathbf{x}_I \quad (4.19)$$

are sufficiently defined through the interpolation functions $N_I(\boldsymbol{\xi})$ associated to node number I . In the same manner the vectors \mathbf{X}_I and \mathbf{x}_I denote the placement vectors associated

to node number I . The interpolation or shape functions need to be constructed in such a way that they meet the conditions

$$N_I(\boldsymbol{\xi}(\mathbf{X}_J)) = \begin{cases} 1 & \text{if } I = J \\ 0 & \text{if } I \neq J \end{cases} \quad \text{and} \quad \sum_{I=1}^{n_n} N_I(\boldsymbol{\xi}) = 1. \quad (4.20)$$

The vector $\boldsymbol{\xi}$ denotes the local coordinates of a reference unit element domain $\mathcal{B}_{\text{unit}}$. This is shown in Fig. 4.3, where only the element $I = 4$, which was already highlighted in orange in the mesh of the previous figure, is considered. In this two-dimensional case the coordinates of the nodes in the unit element are given in the form $\{\xi, \eta\} = \{\pm 1 \mid \pm 1\}$ with $\xi \in [-1, 1]$ and $\eta \in [-1, 1]$. In analogy to the definition of the deformation gradient, the transformation mappings of the unit element with respect to the reference and actual configuration are given by

$$\begin{aligned} \mathbf{J}_e &= \frac{\partial \mathbf{X}}{\partial \boldsymbol{\xi}} = \sum_{I=1}^{n_n} \mathbf{X}_I \otimes \frac{\partial N_I(\boldsymbol{\xi})}{\partial \boldsymbol{\xi}}, & \mathbf{J}_e : \mathcal{B}_{\text{unit}} &\mapsto \mathcal{B}_0^e, \\ \mathbf{j}_e &= \frac{\partial \mathbf{x}}{\partial \boldsymbol{\xi}} = \sum_{I=1}^{n_n} \mathbf{x}_I \otimes \frac{\partial N_I(\boldsymbol{\xi})}{\partial \boldsymbol{\xi}}, & \mathbf{j}_e : \mathcal{B}_{\text{unit}} &\mapsto \mathcal{B}^e \end{aligned} \quad (4.21)$$

on each element. The main benefit of these mappings and the usage of a reference unit element is the unification of the fundamental computations for every element.

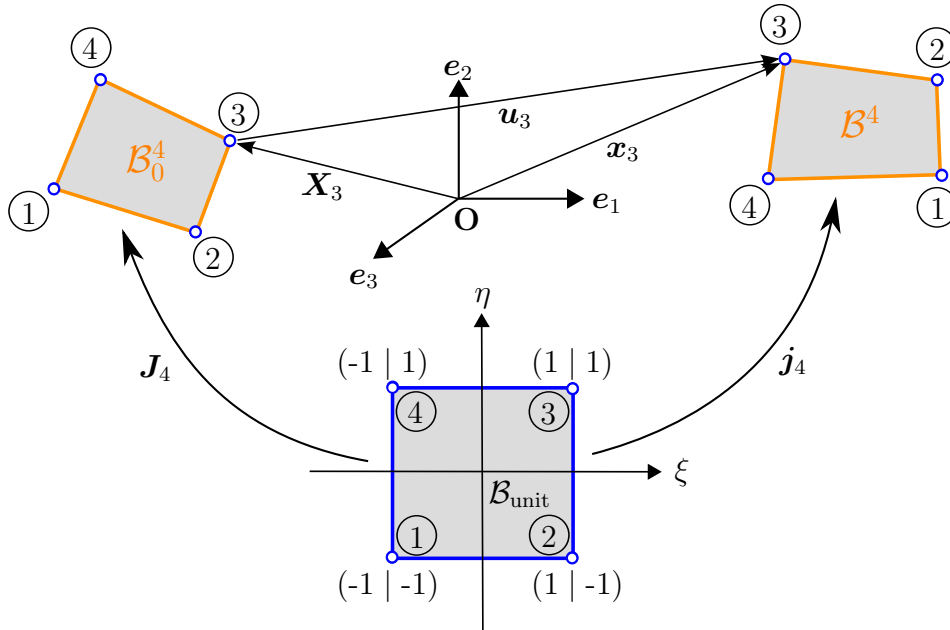


Figure 4.3: Exemplary deformation maps of element \mathcal{B}^4 to a reference unit element $\mathcal{B}_{\text{unit}}$. The nodes are numbered counter clockwise with the specific numbers $I = 1, 2, 3, 4$ are circled. Additionally, the placement and deformation vectors $\mathbf{X}_I, \mathbf{x}_I$ and \mathbf{u}_I for node three with $I = 3$ are shown.

If the so-called isoparametric concept is applied, the same shape functions for the field variables as for the geometry are used and thus

$$\mathbf{u}(\mathbf{X}) = \sum_{I=1}^{n_n} N_I(\boldsymbol{\xi}) \mathbf{u}_I, \quad \delta \mathbf{u}(\mathbf{X}) = \sum_{I=1}^{n_n} N_I(\boldsymbol{\xi}) \delta \mathbf{u}_I, \quad \Delta \mathbf{u}(\mathbf{X}) = \sum_{I=1}^{n_n} N_I(\boldsymbol{\xi}) \Delta \mathbf{u}_I. \quad (4.22)$$

Again, \mathbf{u}_I , $\delta \mathbf{u}_I$ and $\Delta \mathbf{u}_I$ represent vectors associated to node I . In the domain \mathcal{B}_0^h the field variables are C^0 continuous and in view of the linearized weak form, see Eqs. (4.14)–(4.16), it is crucial to define

$$\text{grad } \mathbf{u} = \sum_{I=1}^{n_n} \mathbf{u}_I \otimes \frac{\partial N_I(\boldsymbol{\xi})}{\partial \mathbf{x}}. \quad (4.23)$$

Within the discretization scheme the gradient of the shape functions are then given by

$$\frac{\partial N_I(\boldsymbol{\xi})}{\partial \mathbf{x}} = \frac{\partial N_I(\boldsymbol{\xi})}{\partial \boldsymbol{\xi}} \frac{\partial \boldsymbol{\xi}}{\partial \mathbf{x}} = \frac{\partial N_I(\boldsymbol{\xi})}{\partial \boldsymbol{\xi}} \mathbf{j}_e^{-1}. \quad (4.24)$$

In *Voigt*-notation the symmetric part of the gradient may also be written in vector form

$$\nabla_{\text{sym}} \mathbf{u} = \frac{1}{2} (\text{grad } \mathbf{u} + \text{grad}^T \mathbf{u}) = \sum_{I=1}^{n_n} \mathbf{B}_I \mathbf{u}_I, \quad (4.25)$$

where the matrix

$$\mathbf{B}_I = \begin{pmatrix} N_{I,x_1} & 0 & 0 \\ 0 & N_{I,x_2} & 0 \\ 0 & 0 & N_{I,x_3} \\ N_{I,x_2} & N_{I,x_1} & 0 \\ 0 & N_{I,x_3} & N_{I,x_2} \\ N_{I,x_3} & 0 & N_{I,x_1} \end{pmatrix} \quad (4.26)$$

includes the spatial shape function derivatives with the abbreviation $N_{I,j} = \partial_{x_j} N_I$, see also Eq. (4.24). The symmetric gradients of the variation $\nabla_{\text{sym}} \delta \mathbf{u}$ and the increment $\nabla_{\text{sym}} \Delta \mathbf{u}$ can then be computed by simply replacing \mathbf{u}_I with $\delta \mathbf{u}_I$ and $\Delta \mathbf{u}_I$, respectively. Further considering that $\boldsymbol{\tau} : \text{grad } \delta \mathbf{u} = \boldsymbol{\tau} : \nabla_{\text{sym}} \delta \mathbf{u}$ due to the symmetry of $\boldsymbol{\tau} = \boldsymbol{\tau}^T$, we may write the weak form in Eq. (4.14) for each element e as

$$g^e(\bar{\varphi}, \delta \mathbf{u}_e) = \sum_{I=1}^{n_n} (\delta \mathbf{u}_I)^T \left[\underbrace{\int_{\mathcal{B}_0^e} \mathbf{B}_I^T \boldsymbol{\tau} \, dV_e}_{\mathbf{r}_I^{\text{int}}} - \underbrace{\left(\int_{\mathcal{B}_0^e} N_I \rho_0 \mathbf{b}_a \, dV_e + \int_{\partial \mathcal{B}_{0,\sigma}^e} N_I \hat{\mathbf{t}}_0 \, dA_e \right)}_{\mathbf{r}_I^{\text{ext}}} \right], \quad (4.27)$$

where we identify the nodal internal and external residual vectors $\mathbf{r}_I^{\text{int}}$ and $\mathbf{r}_I^{\text{ext}}$. The latter may be recast into

$$g^e = \delta \mathbf{u}_e^T \mathbf{r}_e \quad \text{with} \quad \mathbf{r}_e = \begin{pmatrix} \mathbf{r}_1^{\text{int}} + \mathbf{r}_1^{\text{ext}} \\ \mathbf{r}_2^{\text{int}} + \mathbf{r}_2^{\text{ext}} \\ \vdots \\ \mathbf{r}_{n_n}^{\text{int}} + \mathbf{r}_{n_n}^{\text{ext}} \end{pmatrix}, \quad \delta \mathbf{u}_e = \begin{pmatrix} \delta \mathbf{u}_1 \\ \delta \mathbf{u}_2 \\ \vdots \\ \delta \mathbf{u}_{n_n} \end{pmatrix} \quad \text{and} \quad \delta \mathbf{u}_I = \begin{pmatrix} \delta u_I^{x_1} \\ \delta u_I^{x_2} \\ \delta u_I^{x_3} \end{pmatrix},$$

where \mathbf{r}_e is the total element residual vector and $\delta \mathbf{u}_e$ is a vector containing all nodal variations of the degrees of freedom of the specific element, while the vector $\delta \mathbf{u}_I$ contains

all variations associated to one specific node $I \in \{1, 2, \dots, n_n\}$. Applying the discretization scheme on Δg in Eq. (4.16) results in the element wise geometrical part

$$\Delta g_{\text{geo}}^e(\bar{\varphi}, \delta \mathbf{u}_e, \Delta \mathbf{u}_e) = \sum_{I=1}^{n_n} \sum_{J=1}^{n_n} (\delta \mathbf{u}_I)^T \underbrace{\int_{\mathcal{B}_0^e} (\partial_{\mathbf{x}} N_I)^T \boldsymbol{\tau} (\partial_{\mathbf{x}} N_J) dV_e}_{\mathbf{k}_{IJ}^{\text{geo}}} \Delta \mathbf{u}_J \quad (4.28)$$

as well as the material part

$$\Delta g_{\text{mat}}^e(\bar{\varphi}, \delta \mathbf{u}_e, \Delta \mathbf{u}_e) = \sum_{I=1}^{n_n} \sum_{J=1}^{n_n} (\delta \mathbf{u}_I)^T \underbrace{\int_{\mathcal{B}_0^e} \mathbf{B}_I^T \mathbb{c}^V \mathbf{B}_J dV_e}_{\mathbf{k}_{IJ}^{\text{mat}}} \Delta \mathbf{u}_J, \quad (4.29)$$

where we identify the nodal stiffness matrices $\mathbf{k}_{IJ}^{\text{geo}}$ and $\mathbf{k}_{IJ}^{\text{mat}}$. Here, \mathbb{c}^V denotes the *Voigt*-notation of the material tangent \mathbb{c} . In analogy to the element residual vector \mathbf{r}_e also the stiffness matrix can be recast in an element wise representation \mathbf{k}_e according to

$$\Delta g^e = \Delta g_{\text{geo}}^e + \Delta g_{\text{mat}}^e = \delta \mathbf{u}_e^T \mathbf{k}_e \Delta \mathbf{u}_e. \quad (4.30)$$

The element stiffness matrix is symmetric, quadratic and of order $(n_n \cdot \text{ndof}) \times (n_n \cdot \text{ndof})$, where *ndof* denotes the degrees of freedom per node. The integration of the linearized weak form is typically accomplished with help of a *Gaussian* quadrature rule. This numerical procedure uses a weighted sum of function values and is exact for polynomials if a sufficient number of evaluation points is considered. The integration may easily be performed on the unit element domain, considering that $\int_{\mathcal{B}_0^e} (\bullet) dV_e = \int_{\mathcal{B}_{\text{unit}}^e} (\bullet) \det \mathbf{J}_e dV_{\text{unit}}$.

The element wise defined residual vectors and stiffness matrices finally need to be assembled to form the global counterparts

$$\mathbf{R} := \mathbf{A} \begin{matrix} n_e \\ \mathbf{r}_e \end{matrix} \quad \text{and} \quad \mathbf{K} := \mathbf{A} \begin{matrix} n_e \\ \mathbf{k}_e \end{matrix}. \quad (4.31)$$

The assembly operator \mathbf{A} sorts all entries over all elements n_e such that we obtain the final discretized version

$$(\delta \mathbf{D})^T (\mathbf{K} \Delta \mathbf{D} + \mathbf{R}) = 0 \quad \text{with} \quad \delta \mathbf{D} = \begin{pmatrix} \delta \mathbf{u}_{1^*} \\ \delta \mathbf{u}_{2^*} \\ \vdots \\ \delta \mathbf{u}_{n_{\text{tot}}} \end{pmatrix}, \quad \Delta \mathbf{D} = \begin{pmatrix} \Delta \mathbf{u}_{1^*} \\ \Delta \mathbf{u}_{2^*} \\ \vdots \\ \Delta \mathbf{u}_{n_{\text{tot}}} \end{pmatrix} \quad (4.32)$$

of the linearized weak form. Here, the vectors $\delta \mathbf{D}$ and $\Delta \mathbf{D}$ contain all nodal variations and increments of the complete mesh, whereby n_{tot} is the total number of nodes of the mesh. The index is labeled with a star to differentiate the global node number I^* associated to the complete mesh from the local element node number I , as it was used in Eq. (4.3) in order to define $\delta \mathbf{u}_e$.

Then $\mathbf{K} \Delta \mathbf{D} + \mathbf{R} = \mathbf{0}$ is nothing else than a linear equation system, which needs to be solved for the nodal increments in $\Delta \mathbf{D}$. As already explained in the previous subsection a *Newton* iteration facilitates to iterate a global displacement vector \mathbf{D} , which fulfills the

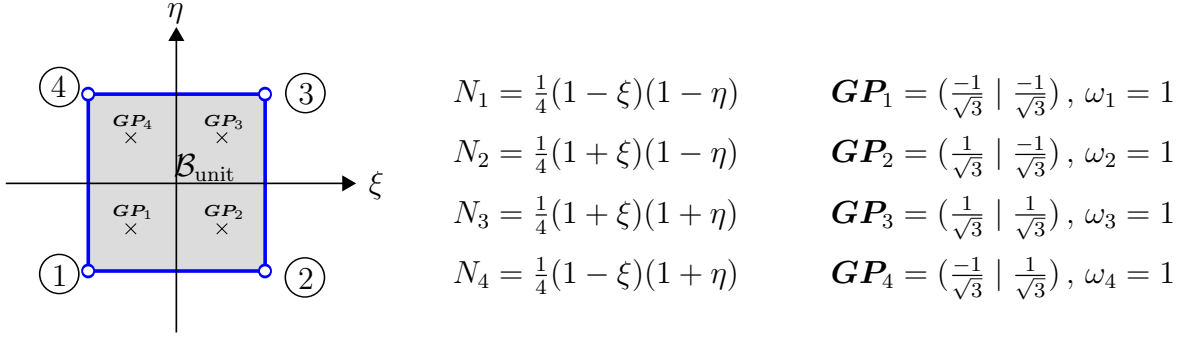


Figure 4.4: Shape functions N_I , Gauss-points \mathbf{GP}_K and corresponding integration weights ω_K of a linear four-noded quadrilateral element.

weak form sufficiently accurate, i.e. $\|\mathbf{R}\| \approx 0$, while updating $\mathbf{D} \leftarrow \mathbf{D} + \Delta\mathbf{D}$. The precise indication of shape functions, associated integrations points and weighting functions has been left open so far. In the course of this thesis different element types will be used. In Fig. 4.4 only the shape functions N_I , Gauss-points \mathbf{GP}_K and the corresponding weights ω_K are given for a linear quadrilateral element. With help of the Gaussian quadrature we may then approximate the above presented volume integrals of the linearized weak form according to

$$\int_{\mathcal{B}_0^e} f(\boldsymbol{\xi}) V_e \approx \sum_{K=1}^{n_{GP}} f(\mathbf{GP}_K) \omega_K \det \mathbf{J}_e(\mathbf{GP}_K), \quad (4.33)$$

where n_{GP} is the number of Gauss-points per element (four for the depicted quadrilateral element) and $f(\boldsymbol{\xi})$ is an arbitrary function which is evaluated at the coordinates \mathbf{GP}_K . Shape functions for different elements in different dimensions and integration data regarding common finite elements are for instance listed in ZIENKIEWICZ [196] and the appendix of ZIENKIEWICZ AND TAYLOR [197].

4.4 Discretization of the Micromorphic Variational Principle

Let the micromorphic energy potential

$$\Pi = \underbrace{\int_{\mathcal{B}_0^e} \int_{\mathcal{S}_0} \widetilde{W}(\delta \tilde{\mathbf{E}}^{(0)}, \delta \tilde{\mathbf{E}}^{(1)}, \delta \tilde{\mathbf{E}}^{(2)}) \, dS \, dV}_{\Pi_{\text{int}}} - \Pi_{\text{ext}}, \quad (4.34)$$

similar to Eq. (4.11), be given. Then the variation of the internal part Π_{int} results in the element wise weak form

$$G_{\text{int}}^e(\bar{\varphi}, \delta \mathbf{u}_e) = \sum_{i=0}^2 \int_{\mathcal{B}_0^e} \int_{\mathcal{S}_0} \tilde{\mathbf{S}}^{(i)} : \delta \tilde{\mathbf{E}}^{(i)} \, dS \, dV_e. \quad (4.35)$$

and the required increment

$$\begin{aligned} \Delta G^e(\bar{\varphi}, \delta \mathbf{u}_e, \Delta \mathbf{u}_e) &= \sum_{i=0}^2 \int_{\mathcal{B}_0^e} \int_{\mathcal{S}_0} \tilde{\mathbf{S}}^{(i)} : \Delta \delta \tilde{\mathbf{E}}^{(i)} \, dS \, dV_e \\ &+ \sum_{i=0}^2 \int_{\mathcal{B}_0^e} \int_{\mathcal{S}_0} \delta \tilde{\mathbf{E}}^{(i)} : \tilde{\mathbf{C}}^{(i)} : \Delta \tilde{\mathbf{E}}^{(i)} \, dS \, dV_e \end{aligned} \quad (4.36)$$

for the linearization. Please note that the micro-space \mathcal{S}_0 is not discretized. All seven degrees of freedom per node

$$\mathbf{u}_I = \begin{pmatrix} u_I^{x_1} \\ u_I^{x_2} \\ u_I^{x_3} \\ w_I^{x_1} \\ w_I^{x_2} \\ w_I^{x_3} \\ \chi_I \end{pmatrix} \quad \text{with} \quad \delta \mathbf{u}_I = \begin{pmatrix} \delta u_I^{x_1} \\ \delta u_I^{x_2} \\ \delta u_I^{x_3} \\ \delta w_I^{x_1} \\ \delta w_I^{x_2} \\ \delta w_I^{x_3} \\ \delta \chi_I \end{pmatrix} \quad \text{and} \quad \Delta \mathbf{u}_I = \begin{pmatrix} \Delta u_I^{x_1} \\ \Delta u_I^{x_2} \\ \Delta u_I^{x_3} \\ \Delta w_I^{x_1} \\ \Delta w_I^{x_2} \\ \Delta w_I^{x_3} \\ \Delta \chi_I \end{pmatrix} \quad (4.37)$$

are defined on the meshed macro-space. Therefore, \mathbf{u}_I is independent of the micro-coordinate ζ . All nodes together form the element displacement, variation and increment vectors

$$\mathbf{u}_e = \begin{pmatrix} \mathbf{u}_1 \\ \mathbf{u}_2 \\ \vdots \\ \mathbf{u}_{n_n} \end{pmatrix}, \quad \delta \mathbf{u}_e = \begin{pmatrix} \delta \mathbf{u}_1 \\ \delta \mathbf{u}_2 \\ \vdots \\ \delta \mathbf{u}_{n_n} \end{pmatrix} \quad \text{and} \quad \Delta \mathbf{u}_e = \begin{pmatrix} \Delta \mathbf{u}_1 \\ \Delta \mathbf{u}_2 \\ \vdots \\ \Delta \mathbf{u}_{n_n} \end{pmatrix}. \quad (4.38)$$

However, still one needs to integrate over both the discretized element domain \mathcal{B}_0^e and the non-discretized micro-space \mathcal{S}_0 . This is simply done by using *Gaussian* quadrature and applying a second integration loop.

In the following the required discretizations of $\delta \mathbf{E}^{(i)}|_{i=0,1,2}$ and $\Delta \delta \mathbf{E}^{(i)}|_{i=0,1,2}$ in a finite element framework are captured. In that context it is worth mentioning that following from Eqs. (3.103) and (3.104)

$$\delta \tilde{\mathbf{E}}^{(i)} = \delta \mathbf{E}^{(i)} + \zeta \delta \mathbf{H}^{(i)} = \frac{1}{2} \delta \mathbf{C}^{(i)} + \frac{1}{2} \zeta \delta \mathbf{K}^{(i)}. \quad (4.39)$$

Therefore, the discretized pairs $\delta \mathbf{E}^{(i)}$ and $\delta \Delta \mathbf{E}^{(i)}$ as well as $\delta \mathbf{H}^{(i)}$ and $\delta \Delta \mathbf{H}^{(i)}$ are presented in tensor notation. The increments $\Delta \mathbf{E}^{(i)}$ and $\Delta \mathbf{H}^{(i)}$ are omitted, but can be simply be obtained by replacing $\delta \mathbf{u}_e$ with $\Delta \mathbf{u}_e$ in the corresponding variation. In all presented examples in the following section it is assumed that the initial direction \mathbf{A} is constant in the macro-space. In that case it is evident that $\tilde{\mathbf{G}}^k = \tilde{\mathbf{G}}_k = \mathbf{e}_k$, cf. Eqs. (3.93) and (3.95). If \mathbf{A} is additionally independent of ζ one may find that $\tilde{\mathbf{I}} = \mathbf{A}$. However, for small length scales L_a the vector $\tilde{\mathbf{I}} = \partial_\zeta \tilde{\mathbf{X}} = \mathbf{A} + \zeta \mathbf{A}_{,\zeta}$ is also approximately equal to \mathbf{A} , considering ζ to be small. The explicit description of the remaining assembly operations is omitted as they are formally identical to the already presented scheme.

4.4.1 Discretization of $\delta \mathbf{E}^{(0)}$ and $\Delta \delta \mathbf{E}^{(0)}$

Considering Tab. 3.2 and Eq. (3.103) the variation of $\mathbf{E}^{(0)}$ and its increment in tensor notation are given by

$$\delta \mathbf{E}^{(0)} = \frac{1}{2} (\delta \mathbf{x}_{,k} \cdot \mathbf{x}_{,l} + \mathbf{x}_{,k} \cdot \delta \mathbf{x}_{,l}) \mathbf{e}_k \otimes \mathbf{e}_l, \quad (4.40)$$

$$\Delta \delta \mathbf{E}^{(0)} = \frac{1}{2} (\delta \mathbf{x}_{,k} \cdot \Delta \mathbf{x}_{,l} + \Delta \mathbf{x}_{,k} \cdot \delta \mathbf{x}_{,l}) \mathbf{e}_k \otimes \mathbf{e}_l. \quad (4.41)$$

The variation $\delta \mathbf{x}_{,k}$ may be expressed as

$$(\delta \mathbf{x}_{,k})^T = \delta \mathbf{u}_e^T \mathbf{B}_{,k} \quad \text{with} \quad \mathbf{B}_{,k} = \begin{pmatrix} \mathbf{B}_{1,k} \\ \mathbf{B}_{2,k} \\ \vdots \\ \mathbf{B}_{n,k} \end{pmatrix}, \quad \mathbf{B}_{I,k} = \begin{pmatrix} N_{I,k} & 0 & 0 \\ 0 & N_{I,k} & 0 \\ 0 & 0 & N_{I,k} \\ 0 & 0 & 0 \\ 0 & 0 & 0 \\ 0 & 0 & 0 \\ 0 & 0 & 0 \end{pmatrix} \quad (4.42)$$

in a finite element scheme with a variational displacement vector $\delta \mathbf{u}_e$. According to that, it follows that

$$\delta \mathbf{E}^{(0)} = \frac{1}{2} \{ \delta \mathbf{u}_e^T (\mathbf{B}_{,k} \mathbf{x}_{,l} + \mathbf{B}_{,l} \mathbf{x}_{,k}) \} \mathbf{e}_k \otimes \mathbf{e}_l, \quad (4.43)$$

$$\Delta \delta \mathbf{E}^{(0)} = \frac{1}{2} \{ \delta \mathbf{u}_e^T (\mathbf{B}_{,k} \mathbf{B}_{,l}^T + \mathbf{B}_{,l} \mathbf{B}_{,k}^T) \Delta \mathbf{u}_e \} \mathbf{e}_k \otimes \mathbf{e}_l. \quad (4.44)$$

4.4.2 Discretization of $\delta \mathbf{E}^{(1)}$ and $\Delta \delta \mathbf{E}^{(1)}$

Considering Tab. 3.2 and Eq. (3.103) the variation of $\mathbf{E}^{(1)}$ and its increment in tensor notation are given by

$$\delta \mathbf{E}^{(1)} = \frac{1}{2} (\delta \mathbf{x}_{,k} \cdot \mathbf{a} + \mathbf{x}_{,k} \cdot \delta \mathbf{a}) (\mathbf{e}_k \otimes \tilde{\mathbf{I}} + \tilde{\mathbf{I}} \otimes \mathbf{e}_k), \quad (4.45)$$

$$\Delta \delta \mathbf{E}^{(1)} = \frac{1}{2} (\delta \mathbf{x}_{,k} \cdot \Delta \mathbf{a} + \Delta \mathbf{x}_{,k} \cdot \delta \mathbf{a}) (\mathbf{e}_k \otimes \tilde{\mathbf{I}} + \tilde{\mathbf{I}} \otimes \mathbf{e}_k). \quad (4.46)$$

The variation $\delta \mathbf{a}$ may be expressed as

$$\delta \mathbf{a}^T = \delta \mathbf{u}^T \mathbf{B}_a \quad \text{with} \quad \mathbf{B}_a = \begin{pmatrix} \mathbf{B}_a^1 \\ \mathbf{B}_a^2 \\ \vdots \\ \mathbf{B}_a^{n_n} \end{pmatrix}, \quad \mathbf{B}_a^I = \begin{pmatrix} 0 & 0 & 0 \\ 0 & 0 & 0 \\ 0 & 0 & 0 \\ N_I & 0 & 0 \\ 0 & N_I & 0 \\ 0 & 0 & N_I \\ 0 & 0 & 0 \end{pmatrix} \quad (4.47)$$

in a finite element scheme. According to that and recalling Eq. (4.42), it follows that

$$\delta \mathbf{E}^{(1)} = \frac{1}{2} \{ \delta \mathbf{u}_e^T (\mathbf{B}_{,k} \mathbf{a} + \mathbf{B}_a \mathbf{x}_{,k}) \} (\mathbf{e}_k \otimes \tilde{\mathbf{I}} + \tilde{\mathbf{I}} \otimes \mathbf{e}_k), \quad (4.48)$$

$$\Delta \delta \mathbf{E}^{(1)} = \frac{1}{2} \{ \delta \mathbf{u}_e^T (\mathbf{B}_{,k} \mathbf{B}_a^T + \mathbf{B}_a \mathbf{B}_{,k}^T) \Delta \mathbf{u}_e \} (\mathbf{e}_k \otimes \tilde{\mathbf{I}} + \tilde{\mathbf{I}} \otimes \mathbf{e}_k). \quad (4.49)$$

4.4.3 Discretization of $\delta \mathbf{E}^{(2)}$ and $\Delta \delta \mathbf{E}^{(2)}$

Considering Tab. 3.2 and Eq. (3.103) the variation of $\mathbf{E}^{(2)}$ and its increment in tensor notation are given by

$$\delta \mathbf{E}^{(2)} = \frac{1}{2} (2\delta \mathbf{a} \cdot \mathbf{a}) \tilde{\mathbf{I}} \otimes \tilde{\mathbf{I}}, \quad (4.50)$$

$$\Delta \delta \mathbf{E}^{(2)} = \frac{1}{2} (2\delta \mathbf{a} \cdot \Delta \mathbf{a}) \tilde{\mathbf{I}} \otimes \tilde{\mathbf{I}}. \quad (4.51)$$

With help of the already above defined matrix \mathbf{B}_a this can be reformulated to read as follows in tensor notation:

$$\delta \mathbf{E}^{(2)} = \frac{1}{2} \{ \delta \mathbf{u}_e^T (2\mathbf{B}_a \mathbf{a}) \} \tilde{\mathbf{I}} \otimes \tilde{\mathbf{I}}, \quad (4.52)$$

$$\Delta \delta \mathbf{E}^{(2)} = \frac{1}{2} \{ \delta \mathbf{u}_e^T (2\mathbf{B}_a \mathbf{B}_a^T) \Delta \mathbf{u}_e \} \tilde{\mathbf{I}} \otimes \tilde{\mathbf{I}}. \quad (4.53)$$

4.4.4 Discretization of $\delta \mathbf{H}^{(0)}$ and $\Delta \delta \mathbf{H}^{(0)}$

Considering Tab. 3.2 and Eq. (3.103) the variation of $\mathbf{H}^{(0)}$ and its increment in tensor notation are given by

$$\delta \mathbf{H}^{(0)} = \frac{1}{2} (\delta \mathbf{a}_{,k} \cdot \mathbf{x}_{,l} + \mathbf{a}_{,k} \cdot \delta \mathbf{x}_{,l} + \delta \mathbf{x}_{,k} \cdot \mathbf{a}_{,l} + \mathbf{x}_{,k} \cdot \delta \mathbf{a}_{,l}) \mathbf{e}_k \otimes \mathbf{e}_l, \quad (4.54)$$

$$\Delta \delta \mathbf{H}^{(0)} = \frac{1}{2} (\delta \mathbf{a}_{,k} \cdot \Delta \mathbf{x}_{,l} + \Delta \mathbf{a}_{,k} \cdot \delta \mathbf{x}_{,l} + \delta \mathbf{x}_{,k} \cdot \Delta \mathbf{a}_{,l} + \Delta \mathbf{x}_{,k} \cdot \delta \mathbf{a}_{,l}) \mathbf{e}_k \otimes \mathbf{e}_l. \quad (4.55)$$

The variation $\delta \mathbf{a}_{,k}$ may be expressed as

$$\delta \mathbf{a}_{,k}^T = \delta \mathbf{u}^T \mathbf{B}_{a,k} \quad \text{with} \quad \mathbf{B}_{a,k} = \begin{pmatrix} \mathbf{B}_{a,k}^1 \\ \mathbf{B}_{a,k}^2 \\ \vdots \\ \mathbf{B}_{a,k}^{n_n} \end{pmatrix}, \quad \mathbf{B}_{a,k}^I = \begin{pmatrix} 0 & 0 & 0 \\ 0 & 0 & 0 \\ 0 & 0 & 0 \\ N_{I,k} & 0 & 0 \\ 0 & N_{I,k} & 0 \\ 0 & 0 & N_{I,k} \\ 0 & 0 & 0 \end{pmatrix} \quad (4.56)$$

in a finite element scheme. According to that, it follows that

$$\delta \mathbf{H}^{(0)} = \frac{1}{2} \{ \delta \mathbf{u}^T (\mathbf{B}_{a,k} \mathbf{x}_{,l} + \mathbf{B}_{,l} \mathbf{a}_{,k} + \mathbf{B}_{,k} \mathbf{a}_{,l} + \mathbf{B}_{a,l} \mathbf{x}_{,k}) \} \mathbf{e}_k \otimes \mathbf{e}_l, \quad (4.57)$$

$$\Delta \delta \mathbf{H}^{(0)} = \frac{1}{2} \{ \delta \mathbf{u}_e^T (\mathbf{B}_{a,k} \mathbf{B}_{,l}^T + \mathbf{B}_{,l} \mathbf{B}_{a,k}^T + \mathbf{B}_{,k} \mathbf{B}_{a,l}^T + \mathbf{B}_{a,l} \mathbf{B}_{,k}^T) \Delta \mathbf{u}_e \} \mathbf{e}_k \otimes \mathbf{e}_l. \quad (4.58)$$

4.4.5 Discretization of $\delta\mathbf{H}^{(1)}$ and $\Delta\delta\mathbf{H}^{(1)}$

Considering Tab. 3.2 and Eq. (3.103) the variation of $\mathbf{H}^{(1)}$ and its increment in tensor notation are given by

$$\begin{aligned} \delta\mathbf{H}^{(1)} &= \frac{1}{2}(\delta\mathbf{a}_{,k} \cdot \mathbf{a} + \mathbf{a}_{,k} \cdot \delta\mathbf{a} + 2\delta\chi\mathbf{x}_{,k} \cdot \mathbf{a} + 2\chi\delta\mathbf{x}_{,k} \cdot \mathbf{a} + 2\chi\mathbf{x}_{,k} \cdot \delta\mathbf{a} \\ &\quad + \delta\mathbf{x}_{,k} \cdot \mathbf{a}_{,\zeta} + \mathbf{x}_{,k} \cdot \delta\mathbf{a}_{,\zeta})^{\mathbf{0}} \left(\mathbf{e}_k \otimes \tilde{\mathbf{I}} + \tilde{\mathbf{I}} \otimes \mathbf{e}_k \right), \end{aligned} \quad (4.59)$$

$$\begin{aligned} \Delta\delta\mathbf{H}^{(1)} &= \frac{1}{2}(\delta\mathbf{a}_{,k} \cdot \Delta\mathbf{a} + \Delta\mathbf{a}_{,k} \cdot \delta\mathbf{a} + 2\delta\chi\Delta\mathbf{x}_{,k} \cdot \mathbf{a} + 2\delta\chi\mathbf{x}_{,k} \cdot \Delta\mathbf{a} \\ &\quad + 2\Delta\chi\delta\mathbf{x}_{,k} \cdot \mathbf{a} + 2\chi\delta\mathbf{x}_{,k} \cdot \Delta\mathbf{a} + 2\Delta\chi\mathbf{x}_{,k} \cdot \delta\mathbf{a} + 2\chi\Delta\mathbf{x}_{,k} \cdot \delta\mathbf{a} \\ &\quad + \delta\mathbf{x}_{,k} \cdot \Delta\mathbf{a}_{,\zeta} + \Delta\mathbf{x}_{,k} \cdot \delta\mathbf{a}_{,\zeta})^{\mathbf{0}} \left(\mathbf{e}_k \otimes \tilde{\mathbf{I}} + \tilde{\mathbf{I}} \otimes \mathbf{e}_k \right). \end{aligned} \quad (4.60)$$

The variation $\delta\mathbf{a}_{,\zeta}$ and increment $\Delta\mathbf{a}_{,\zeta}$ vanish since $\mathbf{a}_{,\zeta}$ is independent of any degree of freedom. This becomes apparent when recalling that $\mathbf{a} = \mathbf{A}(\vartheta^k, \zeta) + \mathbf{w}(\vartheta^k, t)$ and therefore $\mathbf{a}_{,\zeta} = \partial_{\zeta}\mathbf{a} = \partial_{\zeta}\mathbf{A}(\vartheta^k, \zeta)$, which is constant in time. Further, the variation $\delta\chi$ may be expressed as

$$\delta\chi = \delta\mathbf{u}_e^T \mathbf{B}_{\chi} \quad \text{with} \quad \mathbf{B}_{\chi} = \begin{pmatrix} \mathbf{B}_{\chi}^1 \\ \mathbf{B}_{\chi}^2 \\ \vdots \\ \mathbf{B}_{\chi}^{n_n} \end{pmatrix}, \quad \mathbf{B}_{\chi}^I = \begin{pmatrix} 0 \\ 0 \\ 0 \\ 0 \\ 0 \\ 0 \\ N_I \end{pmatrix} \quad (4.61)$$

in a finite element scheme. According to that, it follows that

$$\begin{aligned} \delta\mathbf{H}^{(1)} &= \frac{1}{2} \left\{ \delta\mathbf{u}_e^T (\mathbf{B}_{a,k} \mathbf{a} + \mathbf{B}_a \mathbf{a}_{,k} + 2\mathbf{B}_{\chi} \mathbf{x}_{,k} \cdot \mathbf{a} + 2\chi \mathbf{B}_{,k} \mathbf{a} \right. \\ &\quad \left. + 2\chi \mathbf{B}_a \mathbf{x}_{,k} + \mathbf{B}_{,k} \mathbf{a}_{,\zeta}) \right\} \left(\mathbf{e}_k \otimes \tilde{\mathbf{I}} + \tilde{\mathbf{I}} \otimes \mathbf{e}_k \right), \end{aligned} \quad (4.62)$$

$$\begin{aligned} \Delta\delta\mathbf{H}^{(1)} &= \frac{1}{2} \left\{ \delta\mathbf{u}_e^T [\mathbf{B}_{a,k} \mathbf{B}_a^T + \mathbf{B}_a \mathbf{B}_{a,k}^T + 2\mathbf{B}_{\chi} \otimes (\mathbf{B}_{,k} \mathbf{a}) + 2\mathbf{B}_{\chi} \otimes (\mathbf{B}_a \mathbf{x}_{,k}) \right. \\ &\quad \left. + 2(\mathbf{B}_{,k} \mathbf{a}) \otimes \mathbf{B}_{\chi} + 2\chi \mathbf{B}_{,k} \mathbf{B}_a^T + 2(\mathbf{B}_a \mathbf{x}_{,k}) \otimes \mathbf{B}_{\chi} + 2\chi \mathbf{B}_a \mathbf{B}_{,k}^T] \right. \\ &\quad \left. \Delta\mathbf{u}_e \right\} \left(\mathbf{e}_k \otimes \tilde{\mathbf{I}} + \tilde{\mathbf{I}} \otimes \mathbf{e}_k \right). \end{aligned} \quad (4.63)$$

4.4.6 Discretization of $\delta\mathbf{H}^{(2)}$ and $\Delta\delta\mathbf{H}^{(2)}$

Considering Tab. 3.2 and Eq. (3.103) the variation of $\mathbf{H}^{(2)}$ and its increment in tensor notation are given by

$$\delta\mathbf{H}^{(2)} = \frac{1}{2} (4\delta\chi\mathbf{a} \cdot \mathbf{a} + 8\chi\delta\mathbf{a} \cdot \mathbf{a} + 2\delta\mathbf{a} \cdot \mathbf{a}_{,\zeta} + 2\mathbf{a} \cdot \delta\mathbf{a}_{,\zeta})^{\mathbf{0}} \tilde{\mathbf{I}} \otimes \tilde{\mathbf{I}}, \quad (4.64)$$

$$\begin{aligned} \Delta\delta\mathbf{H}^{(2)} &= \frac{1}{2} (8\delta\chi\Delta\mathbf{a} \cdot \mathbf{a} + 8\chi\delta\mathbf{a} \cdot \Delta\mathbf{a} + 8\Delta\chi\delta\mathbf{a} \cdot \mathbf{a} \\ &\quad + 2\delta\mathbf{a} \cdot \Delta\mathbf{a}_{,\zeta} + 2\Delta\mathbf{a} \cdot \delta\mathbf{a}_{,\zeta})^{\mathbf{0}} \tilde{\mathbf{I}} \otimes \tilde{\mathbf{I}}. \end{aligned} \quad (4.65)$$

With help of the already above defined \mathbf{B} -matrices one may reformulate the two equations to result in

$$\delta \mathbf{H}^{(2)} = \frac{1}{2} \{ \delta \mathbf{u}_e^T (4 \mathbf{B}_\chi \mathbf{a} \cdot \mathbf{a} + 8 \chi \mathbf{B}_a \mathbf{a} + 2 \mathbf{B}_a \mathbf{a}_{,\zeta}) \} \tilde{\mathbf{I}} \otimes \tilde{\mathbf{I}}, \quad (4.66)$$

$$\Delta \delta \mathbf{H}^{(2)} = \frac{1}{2} \{ \delta \mathbf{u}_e^T (8 \mathbf{B}_\chi \otimes \mathbf{B}_a \mathbf{a} + 8 \chi \mathbf{B}_a \mathbf{B}_a^T + 8 \mathbf{B}_a \mathbf{a} \otimes \mathbf{B}_\chi) \Delta \mathbf{u}_e \} \tilde{\mathbf{I}} \otimes \tilde{\mathbf{I}}. \quad (4.67)$$

5 Comparison of Anisotropic Constitutive Approaches

In the following, three different strain-energy functions which utilize different invariants are considered. In particular, a micromorphic strain-energy $\widetilde{W}_M(\tilde{\mathbf{E}}^{(0)}, \tilde{\mathbf{E}}^{(1)}, \tilde{\mathbf{E}}^{(2)})$, a *Hencky*-strain-energy $W_H(\log \mathbf{U})$ and an energy $W_C(\mathbf{C})$ based on the right *Cauchy-Green* tensor are to be compared. The resulting different behavior is demonstrated on several academic examples which are discussed in view of possible biomechanical applications. Each formulation's potential is specifically studied for distinct anisotropic problems. The latter is ensured by identifying appropriate sets of parameters. The micromorphic function

$$\begin{aligned} \widetilde{W}_M(\tilde{\mathbf{E}}^{(0)}, \tilde{\mathbf{E}}^{(1)}, \tilde{\mathbf{E}}^{(2)}) &= \tilde{\mu}_0 \operatorname{tr}[(\tilde{\mathbf{E}}^{(0)})^2] + \frac{\tilde{\lambda}_0}{2} (\operatorname{tr}[\tilde{\mathbf{E}}^{(0)}])^2 + \tilde{\mu}_1 \operatorname{tr}[(\tilde{\mathbf{E}}^{(1)})^2] + \frac{\tilde{\lambda}_2}{2} (\operatorname{tr}[\tilde{\mathbf{E}}^{(1)}])^2 \\ &+ \tilde{\mu}_2 \operatorname{tr}[(\tilde{\mathbf{E}}^{(2)})^2] + \frac{\tilde{\lambda}_2}{2} (\operatorname{tr}[\tilde{\mathbf{E}}^{(2)}])^2 \end{aligned} \quad (5.1)$$

is additively split with respect to the three derived strain measures. The structure of the individual parts is in line with the classical *Saint Venant-Kirchhoff* energy. Only the strain measure \mathbf{E} is replaced with $\tilde{\mathbf{E}}^{(0)}$, $\tilde{\mathbf{E}}^{(1)}$ and $\tilde{\mathbf{E}}^{(2)}$, respectively, and pairs of parameters $[\tilde{\mu}_0, \tilde{\lambda}_0]$, $[\tilde{\mu}_1, \tilde{\lambda}_1]$ and $[\tilde{\mu}_2, \tilde{\lambda}_2]$ are applied. Further, the logarithmic, transversely isotropic strain-energy

$$\begin{aligned} W_H(\log \mathbf{U}) &= \mu_T \operatorname{tr}[(\log \mathbf{U})^2] + \frac{\lambda}{2} [\operatorname{tr}(\log \mathbf{U})]^2 + \alpha \log \mathbf{U} : \mathbf{M} (\operatorname{tr} \log \mathbf{U}) \\ &+ \frac{1}{2} \beta (\log \mathbf{U} : \mathbf{M})^2 + 2(\mu_L - \mu_T) (\log \mathbf{U})^2 : \mathbf{M} \end{aligned} \quad (5.2)$$

is considered. It can be seen as an anisotropic extension of the classical *Hencky*-energy, see HENCKY [67]. While λ denotes the first infinitesimal *Lamé* parameter, μ_T and μ_L are associated to the infinitesimal shear moduli in the transverse isotropy plane and perpendicular to that. In addition, β is directly associated to the stiffness in fiber direction. Replacing the *Hencky* strain $\log \mathbf{U}$ with the linearized *Green*-strain $\boldsymbol{\varepsilon} = 1/2(\operatorname{Grad} \mathbf{u} + \operatorname{Grad}^T \mathbf{u})$ in the equation above would refer to transversely isotropic linear elasticity. In the same fashion one may replace $\log \mathbf{U}$ with \mathbf{E} . By means of additionally considering that $\mathbf{E} = 1/2(\mathbf{C} - \mathbf{1})$ one may formulate the function

$$\begin{aligned} W_C(\mathbf{C}) &= \mu_T \operatorname{tr}(\mathbf{E}^2) + \frac{\lambda}{2} (\operatorname{tr} \mathbf{E})^2 + \alpha \mathbf{E} : \mathbf{M} (\operatorname{tr} \mathbf{E}) \\ &+ \frac{1}{2} \beta (\mathbf{E} : \mathbf{M})^2 + 2(\mu_L - \mu_T) \mathbf{E}^2 : \mathbf{M} \\ &= \frac{1}{4} \mu_T (\operatorname{tr} \mathbf{C}^2 - 2 \operatorname{tr} \mathbf{C} + 3) + \frac{1}{8} \lambda (\operatorname{tr} \mathbf{C} - 3)^2 \\ &+ \frac{1}{4} \alpha (\mathbf{C} : \mathbf{M} - 1) (\operatorname{tr} \mathbf{C} - 3) + \frac{1}{8} \beta (\mathbf{C} : \mathbf{M} - 1)^2 \\ &+ \frac{1}{2} (\mu_L - \mu_T) (\mathbf{C}^2 : \mathbf{M} - 2 \mathbf{C} : \mathbf{M} + 1). \end{aligned} \quad (5.3)$$

All of the above given strain-energies share the property of being quadratic in the corresponding non-linear strain/stretch measure. However, the material tangent \mathbb{C} is only constant for W_C and the strain/stretch measures remain nonlinear in the deformation. For classical transversely isotropic materials of the form of W_H and W_C , the elasticity

tensor \mathbf{C} contains five independent material parameters. Without loss of generality, let the isotropic-plane be spanned by the \mathbf{e}_1 and \mathbf{e}_2 axes. Then the preferred direction is aligned with the \mathbf{e}_3 axis perpendicular to the isotropic plane and thus $\mathbf{M} = \text{diag}(0, 0, 1)$. Under these conditions the general notation of the material tangent in *Voigt*-notation^{1.)} is given by

$$\mathbf{C}^V = \begin{pmatrix} \mathbf{C}_{11}^V & \mathbf{C}_{12}^V & \mathbf{C}_{13}^V & 0 & 0 & 0 \\ \mathbf{C}_{12}^V & \mathbf{C}_{11}^V & \mathbf{C}_{13}^V & 0 & 0 & 0 \\ \mathbf{C}_{13}^V & \mathbf{C}_{13}^V & \mathbf{C}_{33}^V & 0 & 0 & 0 \\ 0 & 0 & 0 & \frac{1}{2}(\mathbf{C}_{11}^V - \mathbf{C}_{12}^V) & 0 & 0 \\ 0 & 0 & 0 & 0 & \mathbf{C}_{44}^V & 0 \\ 0 & 0 & 0 & 0 & 0 & \mathbf{C}_{44}^V \end{pmatrix}. \quad (5.4)$$

In case of W_H and W_C we obtain the identical result

$$\mathbf{C}^V|_{\mathbf{C}=\mathbf{1}} = \begin{pmatrix} \lambda + 2\mu_T & \lambda & \lambda + \alpha & 0 & 0 & 0 \\ \lambda & \lambda + 2\mu_T & \lambda + \alpha & 0 & 0 & 0 \\ \lambda + \alpha & \lambda + \alpha & \lambda - 2\mu_T + 2\alpha + 4\mu_L + \beta & 0 & 0 & 0 \\ 0 & 0 & 0 & \mu_T & 0 & \\ 0 & 0 & 0 & 0 & \mu_L & 0 \\ 0 & 0 & 0 & 0 & 0 & \mu_L \end{pmatrix}$$

in the reference configuration with $\mathbf{C} = \mathbf{U} = \mathbf{1}$. Then the material parameters incorporated in W_H and W_C are related to the five classical independent parameters, introduced in Eq. (5.4) as follows:

$$\begin{aligned} \mu_L &= \mathbf{C}_{44}^V, \\ \mu_T &= \frac{1}{2}(\mathbf{C}_{11}^V - \mathbf{C}_{12}^V), \\ \lambda &= \mathbf{C}_{12}^V, \\ \alpha &= \mathbf{C}_{13}^V - \mathbf{C}_{12}^V, \\ \beta &= \mathbf{C}_{11}^V + \mathbf{C}_{33}^V - 2\mathbf{C}_{13}^V - 4\mathbf{C}_{44}^V. \end{aligned} \quad (5.5)$$

The above parameter identification was performed in analogy to SCHRÖDER AND GROSS [151]. The identification for the function \widetilde{W}_M is omitted due to the added complexity caused by the additional degrees of freedom.

^{1.)}The *Voigt*-notation implies a condensed form, where the 4th order tensor \mathbf{C} is written in the matrix form \mathbf{C}^V . Here, and in what follows tensorial indices are allocated to the matrix indexes according to $\{11, 22, 33, 12, 23, 13\} \rightarrow \{1, 2, 3, 4, 5, 6\}$.

5.1 Impact of the Initial Fiber Orientation

The initial orientation of a preferred direction within a numerical simulation is a predefined parameter. Soft tissues are known to typically show increased stiffness in the direction of the collagen reinforcement. In order to study characteristic material features that can be traced back to the fiber reinforcement it is useful to consider a simple example and to vary the initial fiber direction. In the following we will consider a force-driven tension test. The material is reinforced with a single fiber and its orientation direction \mathbf{A} is defined by an angle β_f to the horizontal-axis according to Fig. 5.1a). The boundary value problem has been conceived in such a way that interfering effects from boundary conditions and mesh anisotropy are precluded. Thus, the symmetries

$$u_{h_2}(\beta_f) = u_{h_3}(-\beta_f), \quad u_{v_1}(\beta_f) = u_{v_4}(-\beta_f), \quad u_{v_2}(\beta_f) = u_{v_3}(-\beta_f) \quad (5.6)$$

regarding the nodal horizontal and vertical displacements hold true. Horizontal displacements are named with u_{h_i} and vertical displacements with u_{v_i} , where the index i corresponds to the node number. The nodes 1 to 4 are labeled in Fig. 5.1a) and will be used to evaluate the results of the numerical computations. In a first step, the parameters of the three different models are set according to Tab. 5.1. They are chosen identical for W_H and W_C . It is essential to note that for this specific choice only the invariants $\log \mathbf{U} : \mathbf{M} = I_4^{H1}$ and $\mathbf{E} : \mathbf{M} = 1/2(I_4^{C1} - 1)$ are of interest and the anisotropy exclusively arises from the parameter β . As already mentioned earlier the invariant I_4^{C1} has a clear physical interpretation as the squared fiber stretch and is therefore appropriate and favorable for a first comparison. Further, the parameters of \widetilde{W}_M were adjusted such that the horizontal displacement u_{h_2} at node 2 for $\beta_f = 0^\circ$ is identical for \widetilde{W}_M and W_C .

The results are plotted in Figs. 5.1b)–d). Due to the symmetries according to Eq. (5.6) it is sufficient to concentrate on u_{v_1} , u_{h_2} and u_{v_2} . It becomes apparent that the qualitative progression of all three constitutive laws is very similar. This confirms the expectation of a stiffening effect in direction of the fiber for both the logarithmic *Hencky* strain measure $\log \mathbf{U}$ as well as the micromorphic model. Therefore, the horizontal displacement u_{h_2} becomes minimal when the load is aligned with the reinforcement-direction, i.e. $\beta_f = 0^\circ$, indicating the distinct stiffening. However, as can be seen W_H behaves generally stiffer than W_C .

	μ_T	λ	α	μ_L	β		L_a	$\tilde{\mu}_0$	$\tilde{\lambda}_0$	$\tilde{\mu}_1$	$\tilde{\lambda}_1$	$\tilde{\mu}_2$	$\tilde{\lambda}_2$
W_H	15	10	0	15	575	\widetilde{W}_M	10^{-4}	15	10	300	470	500	350
W_C	15	10	0	15	575								

Table 5.1: Parameter set 1 for the uniaxial tension test in Fig. 5.1. All parameters are stated in $[\bullet] = \text{MPa}$ except of $[L_a] = \text{mm}$.

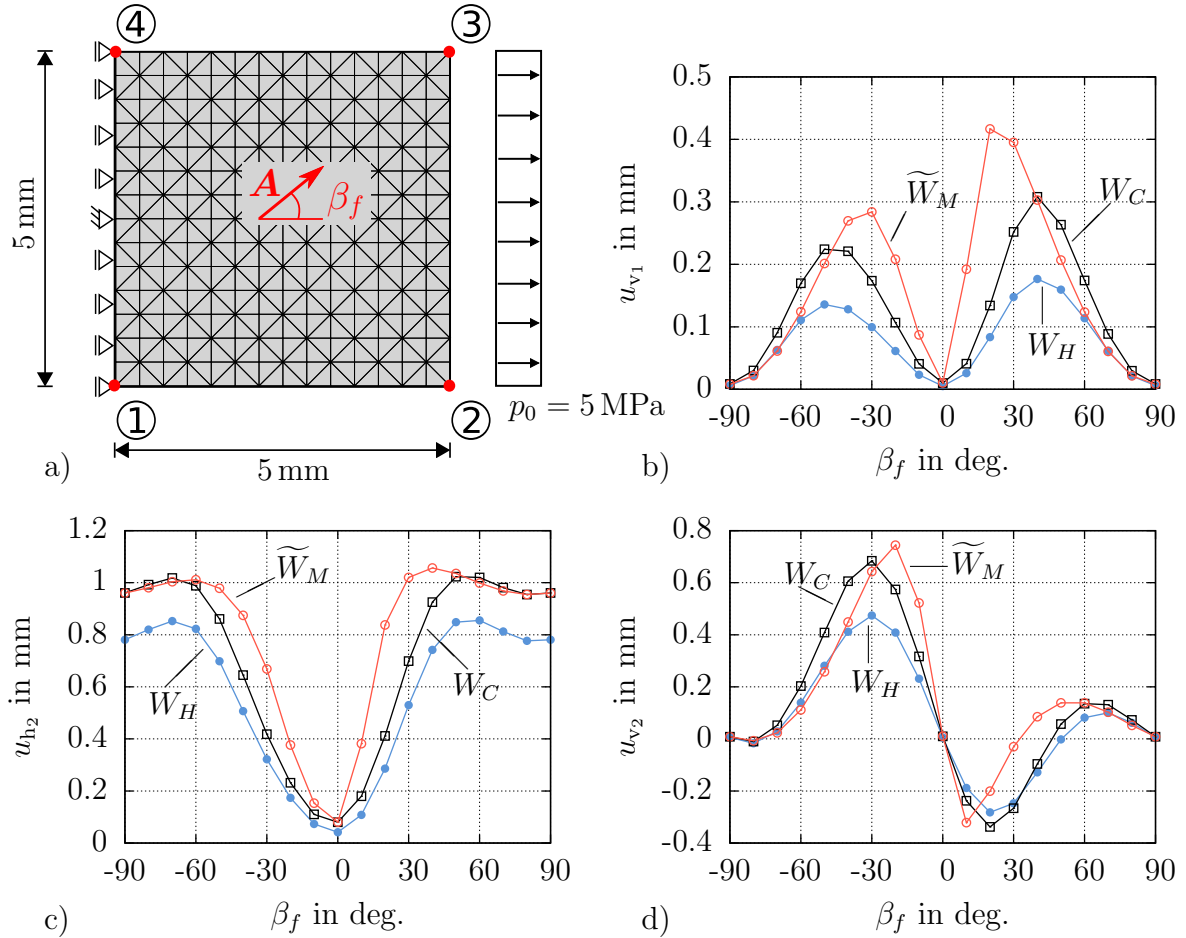


Figure 5.1: a) Boundary value problem with varying fiber orientation β_f . b)–d) Displacement plots over β_f for three different constitutive laws and parameter set 1.

The same example is repeated for the models W_H and W_C with parameter set 2 according to Tab. 5.2. In contrast to parameter set 1, all parameters are different from zero and thus all parts of the strain-energies are involved. Again, identical parameters are chosen for both constitutive models. The corresponding plots of the displacements over the fiber angle β_f are shown in Fig. 5.2. The qualitative progression is once again very similar with W_H showing a higher resistance against deformation than W_C . For the micromorphic model \widetilde{W}_M it appeared difficult to find a parameter set showing comparable macroscopic deformations.

	μ_T	λ	α	μ_L	β
W_H	15	10	10	60	10
W_C	15	10	10	60	10

Table 5.2: Parameter set 2 for the uniaxial tension test in Fig. 5.2. All parameters are stated in [•] = MPa.

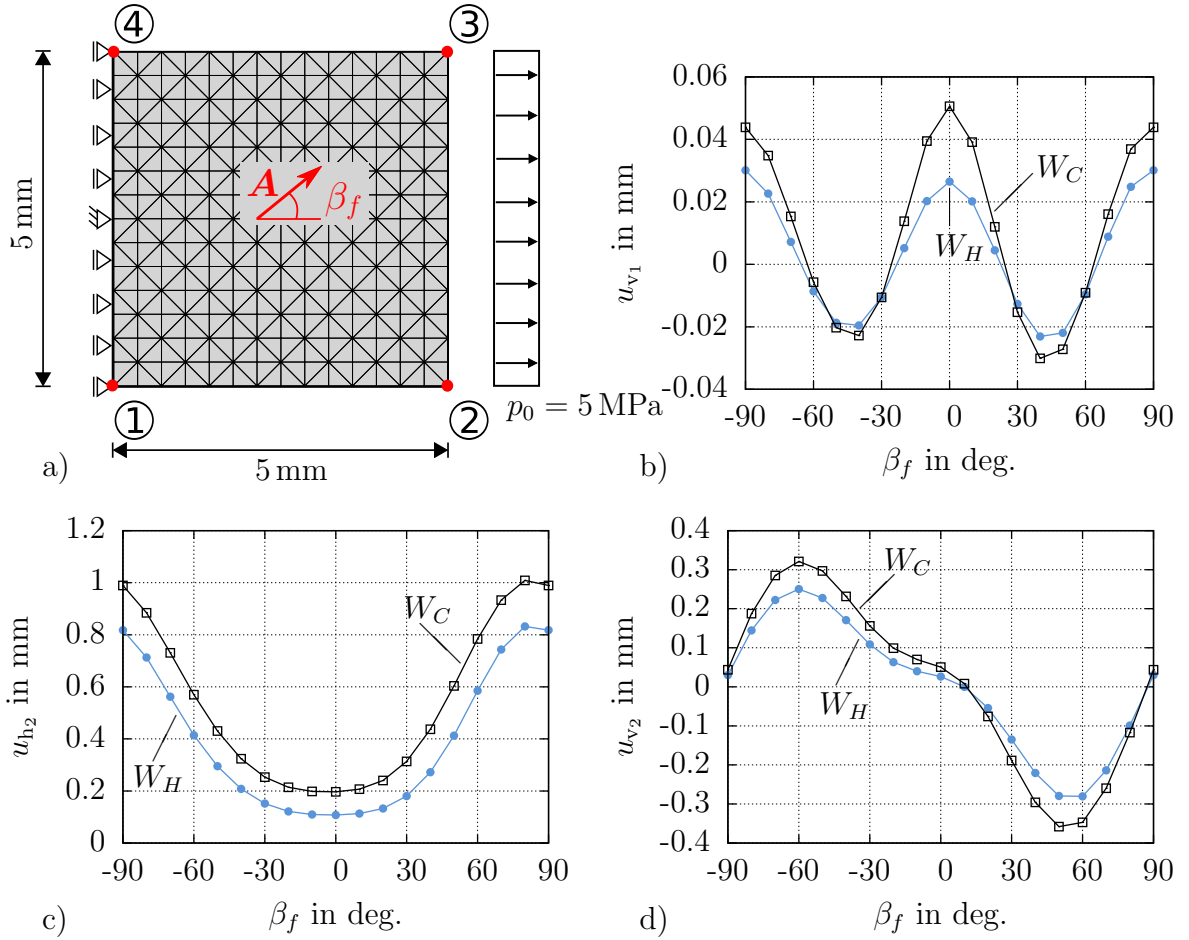


Figure 5.2: a) Boundary value problem with varying fiber orientation β_f . b)–d) Displacement plots over β_f for two different constitutive laws and parameter set 2.

5.2 Non-Affine Fiber Reorientation

As already explained in Sec. 2.2, matrix material and collagen fibers of soft biological tissues are not necessarily firmly connected. This in turn allows for relative deformations of individual components. With regard to that fact, two different examples are presented, especially in order to highlight the potential of the micromorphic material description and the involved additional degrees of freedom.

5.2.1 Example: Perforated Plate

As a first example we consider a rectangular plate with a rectangular perforation. The $40 \text{ mm} \times 40 \text{ mm}$ plate is exposed to equi-biaxial loading under the assumption of plane strain conditions and meshed with linear quadrilateral elements. Moreover, the plate is reinforced with a single fiber with an angle β_f of 45° to the horizontal direction. The boundary value problem depicted in Fig. 5.3a) is displacement driven with the condition $u = \bar{u}$ on the outer edges of the plate. No boundary conditions of *Dirichlet*-type are applied with respect to \boldsymbol{w} and χ . The boundary conditions as well as the geometry are chosen double-symmetric. Therefore, the anisotropy of the considered constitutive laws becomes apparent from the rotation of the symmetry axis of the deformed whole. In a first step, the micromorphic strain-energy \widehat{W}_M is considered with the parameters according to

Tab. 5.3. In Fig. 5.3b) the deformed plate is shown for several load steps. The dimensions along the axes \mathbf{e}_1 and \mathbf{e}_2 are also indicated. The initial anisotropy of the material is demonstrated by the shape of the whole. It is not double-symmetric regarding the \mathbf{e}_1 and \mathbf{e}_2 axes but rather regarding \mathbf{A} and its orthogonal direction in the drawing. However, the shape slowly turns into a rotationally symmetric circle with increasing deformation. The main reason for that is the reorientation of the director according to $\mathbf{a} = \mathbf{A} + \mathbf{w}$, where the degrees of freedom \mathbf{w} are independent from the macroscopic displacement \mathbf{u} . The non-affine rearrangement of fiber bundles relative to the bulk material remains fully elastic in contrast to different approaches as proposed by HARITON ET AL. [66], HIMPEL ET AL. [70] or FAUSTEN ET AL. [39].

The reorientation is depicted in Figs. 5.3c) and d) for $\bar{u} = 8$ mm and $\bar{u} = 20$ mm. The magnitude of the micro-deformation \mathbf{w} is indicated by the length of the plotted vectors at each node as well as by the contour. The micro-deformations are particularly striking at the corners of the initially rectangular shaped whole and are increasing with \bar{u} . In the variational principle in Eq. (3.107) the constitutive choice for \widetilde{W}_M is the driving source for the reorientation. Under the premise of the minimization of the potential it appears reasonable that the macroscopic deformation follows the symmetries arising from the geometry and the boundary conditions from an energetic perspective. It will be shown in the following example that this is also the case for isotropic examples. This behavior was also observed for a circular perforation in VON HOEGEN ET AL. [185].

	L_a	$\tilde{\mu}_0$	$\tilde{\lambda}_0$	$\tilde{\mu}_1$	$\tilde{\lambda}_1$	$\tilde{\mu}_2$	$\tilde{\lambda}_2$
\widetilde{W}_M	10^{-4}	15	10	2000	2000	2000	2000

Table 5.3: Parameter set for the equi-biaxial tension test in Fig. 5.3. All parameters are stated in $[\bullet] = \text{MPa}$ except of $[L_a] = \text{mm}$.

In order to draw a comparison with models using classical invariant theory we will consider the parameter sets according to Tab. 5.4 in the following. The parameters are chosen such that only one part of the anisotropic invariants in W_H and W_C is dominant and it is ensured that $\mathbb{C}|_{\mathcal{C}=1}$ is positive definite.

The deformed shapes of the plate at several deformation steps are depicted in Fig. 5.4 for each material. Here, the varieties of the shape of the hole emphasize that different anisotropic characteristics can be attributed to the respective invariant involved. This was also discussed in more detail in SCHRÖDER ET AL. [157].

	μ_T	λ	α	μ_L	β		μ_T	λ	α	μ_L	β
$W_H^{(\text{iso})}$	15	10	0	15	0	$W_C^{(\text{iso})}$	15	10	0	15	0
$W_H^{(\alpha)}$	15	10	50	20	0	$W_C^{(\alpha)}$	15	10	50	20	0
$W_H^{(\mu_L)}$	15	10	0	150	0	$W_C^{(\mu_L)}$	15	10	0	150	0
$W_H^{(\beta)}$	15	10	0	15	150	$W_C^{(\beta)}$	15	10	0	15	150

Table 5.4: Parameter sets for the equi-biaxial tension tests carried out in Fig. 5.4. All parameters are stated in $[\bullet] = \text{MPa}$.

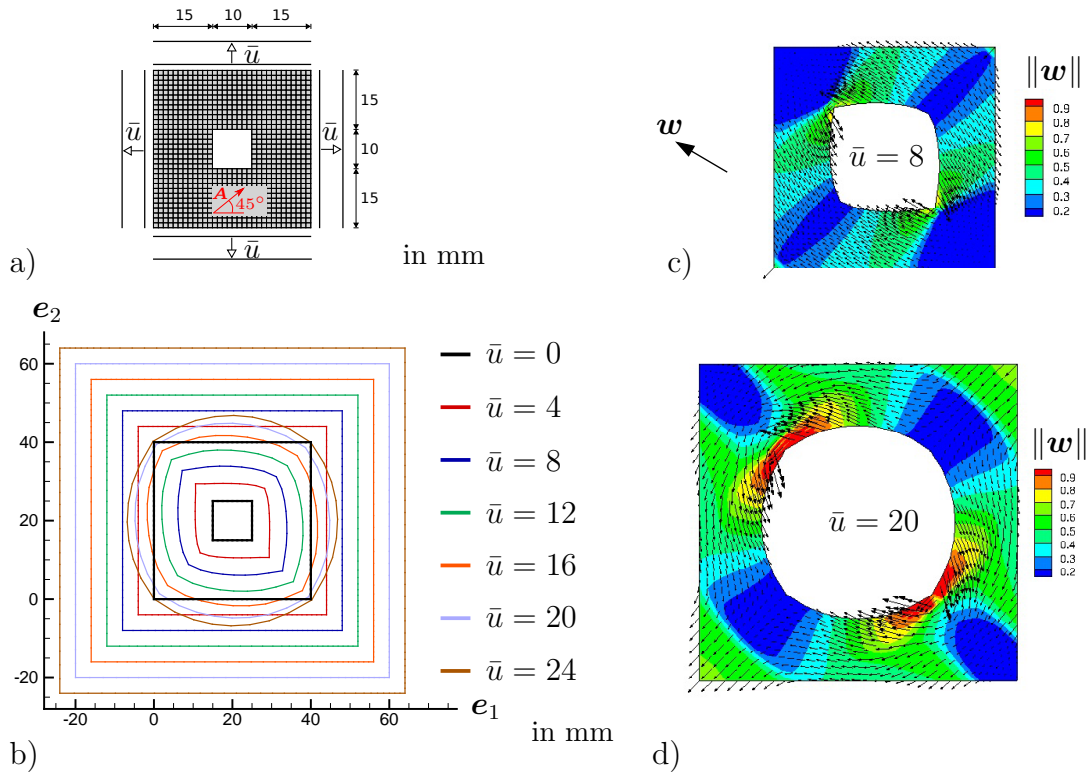


Figure 5.3: a) Displacement driven equi-biaxial test of a double-symmetric perforated plate. b) Deformed shapes after different applied deformations \bar{u} . c)–d) Deformed geometry and orientation of the director deformations w for $\bar{u} = 8$ mm and $\bar{u} = 20$ mm, respectively. All computations were carried out using the parameters of \widetilde{W}_M according to Tab. 5.3.

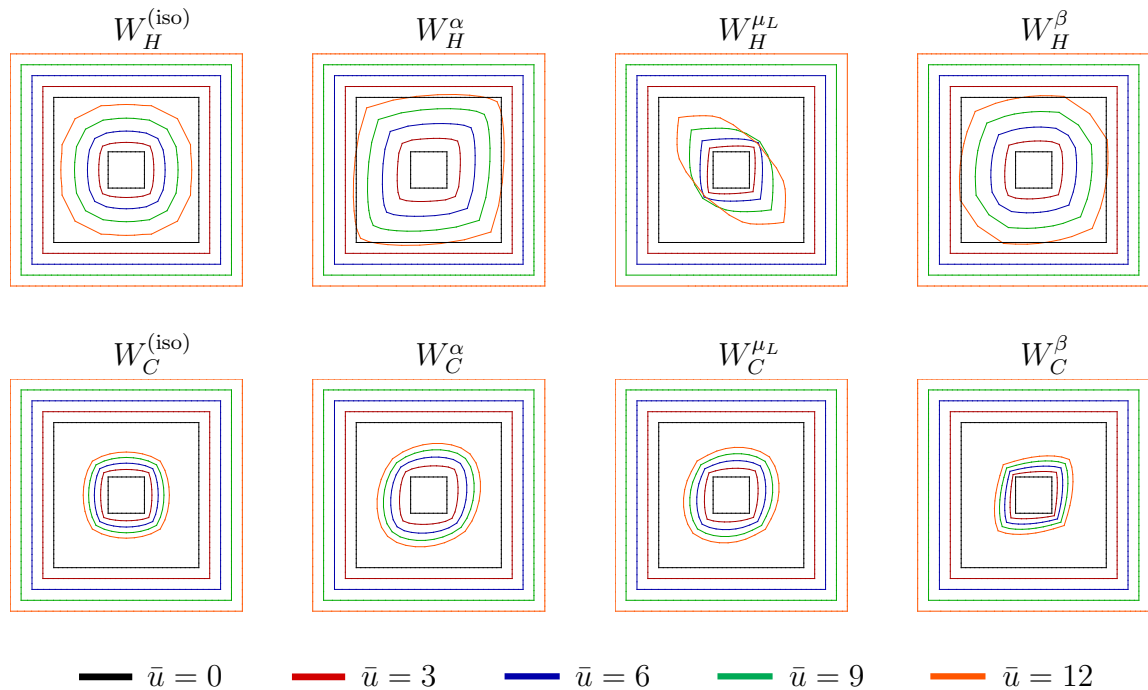


Figure 5.4: Deformed shapes of the perforated plates for different material parameters and deformations \bar{u} on the boundary. Strain-energies formulated in term of the *Hencky* strain are displayed on the top row and strain-energies formulated in terms of the *Green* strain on the bottom row. Computations were carried out using the parameters according to Tab. 5.4.

However, due to the incorporated affine mapping of the preferred direction the basic characteristic of the deformed body remains the same for each deformation \bar{u} and each material and is in that regard strictly different to the results in Fig. 5.3b).

5.2.2 Example: Tension Test

The boundary value problem presented in Fig. 5.5 is inspired by HIMPEL ET AL. [70]. They developed a model that accounts for fiber reorientation in terms of an evolution equation which is driven by the principal stretches. It was shown that in a deformation driven tension test with an initial fiber orientation different from the loading direction the time dependent reorientation process leads to a perfect rectangular deformed shape. In the present example the initial preferred direction has an angle β_f of 30° to the horizontal-axis over the whole domain. The basis for the calculation form the parameter sets defined in Tab. 5.5, including the models $W_H(\log \mathbf{U})$, $W_C(\mathbf{C})$ and the micromorphic alternative $\widetilde{W}_M(\widetilde{\mathbf{E}}^{(0)}, \widetilde{\mathbf{E}}^{(1)}, \widetilde{\mathbf{E}}^{(2)})$. It is worth mentioning, that for W_H and W_C large values for the parameter β are chosen. For that reason, the invariants $\mathbf{C} : \mathbf{M}$ and $\log \mathbf{U} : \mathbf{M}$, respectively, become dominant in the strain-energies. This was done in view of the improved comparability with model \widetilde{W}_M , as discovered in Sec. 5.1. Moreover, the invariant $\mathbf{C} : \mathbf{M}$ is always useful for a comparison due to its clear physical interpretation as the squared stretch in fiber direction. The deformed shapes of all three models at different time steps and associated boundary displacements \bar{u} at the right edge are shown in Fig. 5.5b)–d).

All deformed shapes at $\bar{u} = 0.3 \text{ mm}$ are very comparable. The vertical deflections arise due to the strong anisotropy of the materials. This anisotropic characteristic begins to disappear in case of \widetilde{W}_M with increasing \bar{u} . More and more the deformed body turns back into a rectangular shape as it would be expected for an isotropic material. That is the effect which was also observed for the reorientation model in HIMPEL ET AL. [70]. However, in contrast to that model, the presented micromorphic reorientation model is purely elastic. That means it is free of thermodynamical dissipation. In case of W_H and W_C the anisotropic characteristic and general shape remain similar when the body is further elongated.

	μ_T	λ	α	μ_L	β		L_a	$\tilde{\mu}_0$	$\tilde{\lambda}_0$	$\tilde{\mu}_1$	$\tilde{\lambda}_1$	$\tilde{\mu}_2$	$\tilde{\lambda}_2$
W_H	15	10	0	15	1000	\widetilde{W}_M	10^{-4}	15	10	3500	3500	3500	3500
W_C	15	10	0	15	1000								

Table 5.5: Parameter sets for the tension tests performed in Fig. 5.5. All parameters are stated in $[\bullet] = \text{MPa}$ except of $[L_a] = \text{mm}$.

The macroscopic relevance of the lower scale independent fiber deformation needs to be controlled on a constitutive level. This may be facilitated by applying the penalty formulation in Eq. (3.116) with regard to the additional constraint $\gamma \approx \hat{\gamma}$ on $\partial \mathcal{S}_D$. Results are shown in Fig. 5.6, where the same boundary value problem as before is considered and different penalty parameters F are chosen. The micro-space boundary domain $\partial \mathcal{S}_D$ is defined by the two points $\{\zeta = -L_a/2, \zeta = L_a/2\}$. As can be seen, the consideration of micro-macro interface conditions heavily influences the resulting macroscopic, deformed shape.

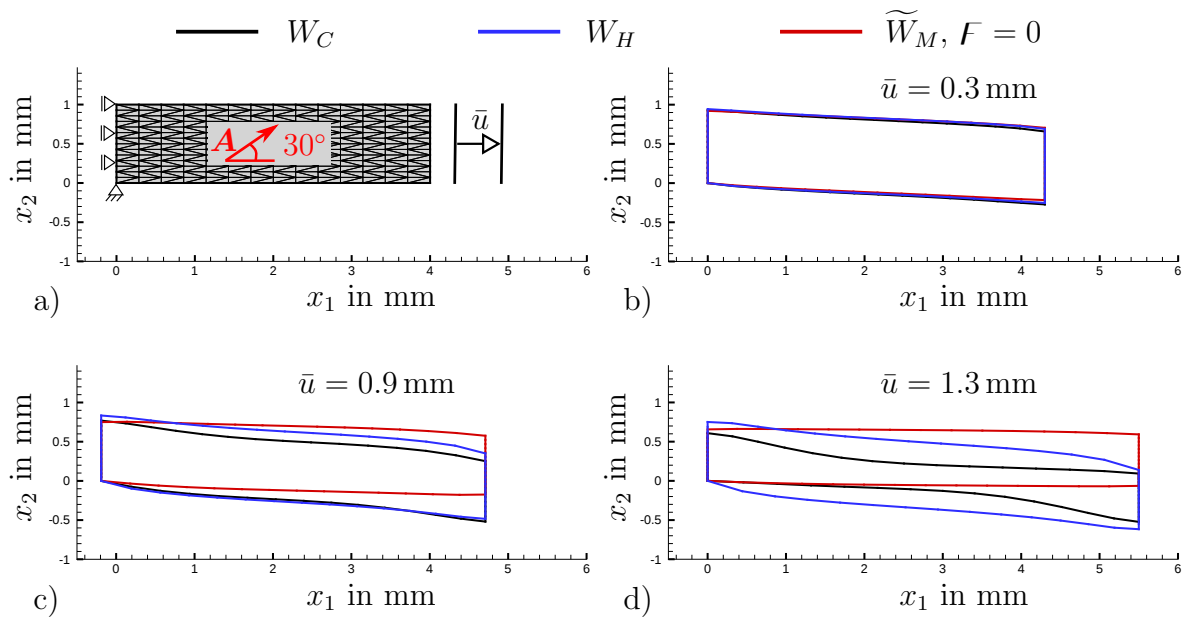


Figure 5.5: a) Considered boundary value problem and b)–d) deformed shapes after different applied deformations \bar{u} for W_H , W_C and \widetilde{W}_M and material parameters according to Tab. 5.5.

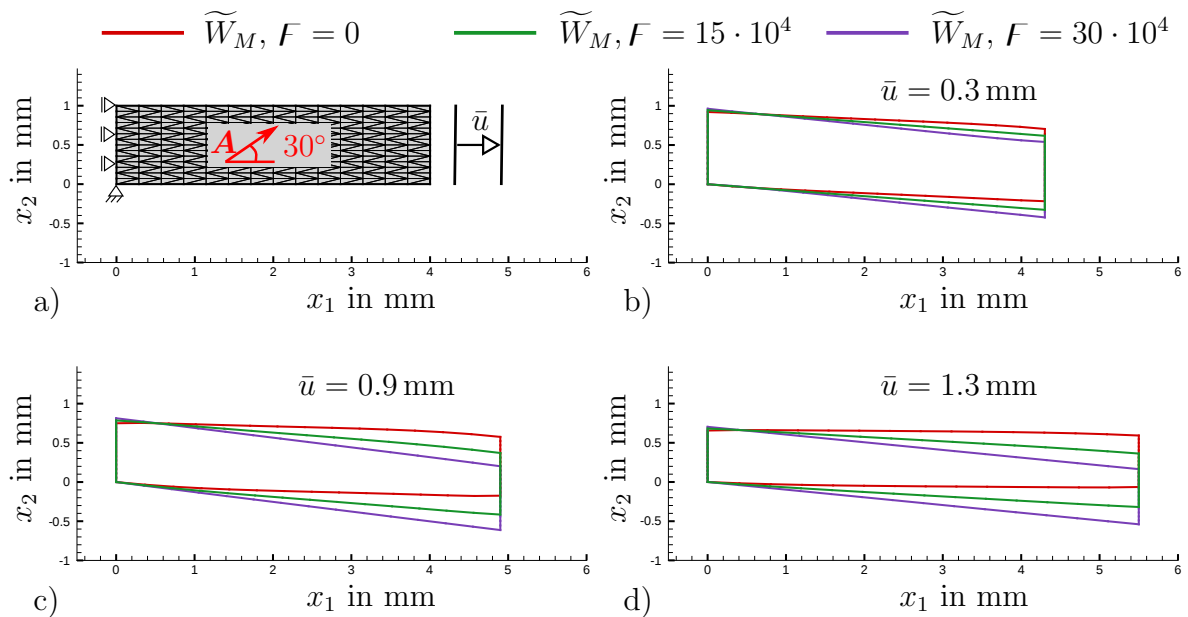


Figure 5.6: a) Considered boundary value problem and b)–d) deformed shapes after different applied deformations \bar{u} for the micromorphic model \widetilde{W}_M and penalty parameters according to the legend. The remaining parameters are listed in Tab. 5.5.

The previously described visible effects of non-affine reorientation vanish with an increasing penalty parameter, since affine kinematics are enforced. This becomes particularly apparent from the increased deflection of the body when increasing F .

Lastly, for completeness also the results in Fig. 5.7 are given. These are based on the parameter sets in Tab. 5.6, where μ_L is chosen large such that the influence of the invariants $\mathbf{E}^2 : \mathbf{M} = 1/4(I_4^{C^2} - 2I_4^{C^1} + 1)$ and $(\log \mathbf{U})^2 : \mathbf{M} = I_4^{H^2}$ become dominant. Especially the latter will gain special attention in the course of this thesis, see Sec. 7. Except of the different parameters the considered boundary value problem is the same like before. It is observed in Fig. 5.7 that these invariants seem to cause a significant increase in volume and the previous observation that they do not show considerable effects in terms of reorientation is confirmed.

	μ_T	λ	α	μ_L	β
W_H	15	10	0	500	0
W_C	15	10	0	500	0

Table 5.6: Parameter sets for the tension tests performed in Fig. 5.7. All parameters are stated in $[\bullet] = \text{MPa}$.

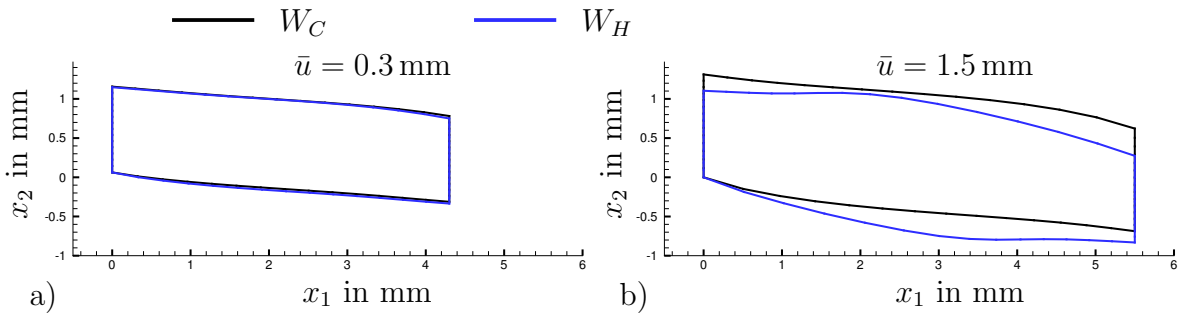


Figure 5.7: Deformed shapes after applied deformations $\bar{u} = 0.3 \text{ mm}$ and $\bar{u} = 1.5 \text{ mm}$ for W_H and W_C and material parameters according to Tab. 5.6.

5.3 Uniaxial Stress-Strain Behavior

In the previous examples the material response was mostly characterized and evaluated in terms of the resulting deformations. However, the selection of a constitutive law is frequently made based on the stress-strain behavior that is measured experimentally. The perhaps simplest case is thereby a homogenous, uniaxial tension and compression test as depicted in Fig. 5.8. Here, the fiber direction is aligned with the loading direction. The deformed configurations under tension and compression are shown on the right. Considering material parameters according to Tab. 5.7, the stress-stretch curves are shown in Fig. 5.9a). For a better comparison, the stress values are normalized with respect to the occurring maximal absolute stress. In the tensile regime the stresses are strictly increasing with the stretch λ_1 for all three materials. While W_C shows considerable strain stiffening, W_H and \tilde{W}_M show very slight strain softening behavior. The stress-strain curve of W_H reminds strongly of the logarithmic function. In case of compression, the stresses of the two latter energies tend to infinity as it would be expected from a physical point of view. In contrast W_C behaves strictly unphysical as the stress tends to zero for $\lambda_1 \rightarrow 0$ and therefore lacks of monotonicity. The strain stiffening of W_H under compression is

especially remarkable. Porous copper fabricated by unidirectional solidification behaves strongly anisotropic under compression and exhibits considerable stiffening under large strains up to 80% due to the alignment of the pores, cf. HYUN AND NAKAJIMA [85]. This could be modeled with help of logarithmic invariants.

In Fig. 5.8b) the identical lateral stretches $\lambda_2 = \lambda_3$ are plotted for each energy. All values are nearly the same for W_C and \widetilde{W}_M . This is due to the fact that $\widetilde{\mathbf{E}}^{(0)}$ contains the classical Green strain, see Eqs. (3.103) and (3.104), since $\mathbf{E}^{(0)} = \mathbf{E}$. In \widetilde{W}_M , $\widetilde{\mathbf{E}}^{(0)}$ constitutes the direction-independent part of the strain-energy. Because of the matching loading and fiber direction in the current example the anisotropic components only induce stresses in that direction. The lateral stresses σ_{22} and σ_{33} must be equal to zero due to the equilibrium conditions. Therefore, the isotropic part $\mu \text{tr}(\mathbf{E}^2) + \lambda/2(\text{tr} \mathbf{E})^2$ takes the decisive role in determining the lateral stretches λ_2 and λ_3 . Apparently, this is also the case for \widetilde{W}_M which confirms the made assumptions when splitting $\widetilde{\mathbf{E}} = \widetilde{\mathbf{E}}^{(0)} + \widetilde{\mathbf{E}}^{(1)} + \widetilde{\mathbf{E}}^{(2)}$ and demonstrates that isotropic and anisotropic effects are decoupled in the different strain measures. The lateral stretches of W_H are also very similar to those of W_C for stretches of λ_1 close to one. This is in accordance with the observation that $\mathbb{C}(W_C)|_{C=1} = \mathbb{C}(W_H)|_{C=1}$. For larger deformations W_C and W_H behave approximately antisymmetric regarding tension and compression.

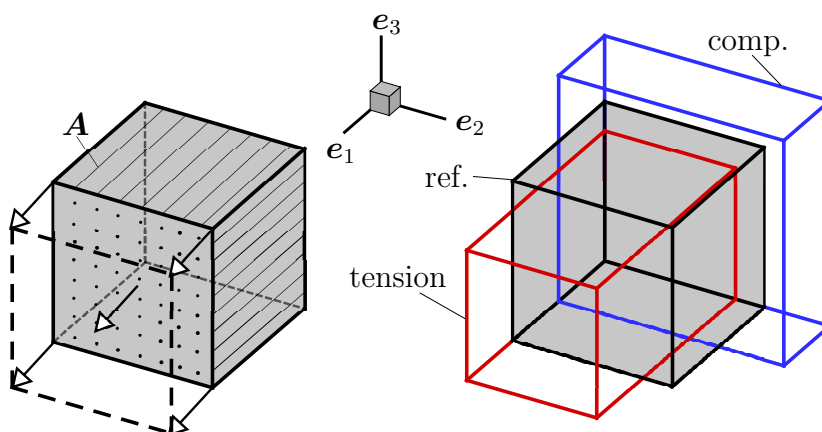


Figure 5.8: Uniaxial compression and tension test, where the preferred direction and the loading direction are aligned. Taken from SCHRÖDER ET AL. [157].

	μ_T	λ	α	μ_L	β		L_a	$\tilde{\mu}_0$	$\tilde{\lambda}_0$	$\tilde{\mu}_1$	$\tilde{\lambda}_1$	$\tilde{\mu}_2$	$\tilde{\lambda}_2$
W_H	15	10	0	15	575	\widetilde{W}_M	10^{-4}	15	10	300	470	500	350
W_C	15	10	0	15	575								

Table 5.7: Material parameters used to generate the uniaxial stress-strain responses shown in Fig. 5.9. All parameters are stated in $[\bullet] = \text{MPa}$ except of $[L_a] = \text{mm}$.

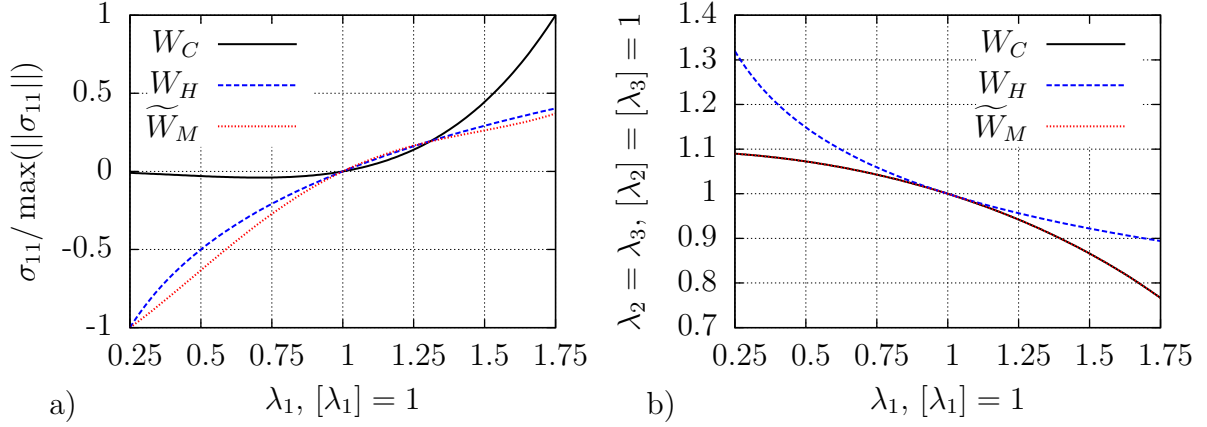


Figure 5.9: a) Normalized stress-stretch relationships under uniaxial loading and b) associated lateral stretches. Material parameters according to Tab. 5.7 were used.

5.4 Influence of Dispersed Fiber Distributions

In the so far presented examples, the fiber families have been assumed to be clearly orientated in one specific direction. However, histology of soft tissues rather reveals a collagen fiber distribution function than one specific orientation. A fairly simple approach was developed in GASSER ET AL. [50], where a so-called generalized structural tensor is derived by integration of a fiber density distribution. For two-dimensional dispersion, i.e. all fibers are orientated in one specific plane, the generalized structural tensor is given by

$$\mathbf{H} = \varsigma \mathbf{1}^* + (1 - 2\varsigma) \mathbf{A} \otimes \mathbf{A} \quad \text{with} \quad \mathbf{1}^* = \mathbf{e}_1 \otimes \mathbf{e}_1 + \mathbf{e}_2 \otimes \mathbf{e}_2 \quad \text{and} \quad \varsigma \in [0, 0.5]. \quad (5.7)$$

A full derivation including the integration of the fiber density distribution is provided in Appendix C. The parameter ς can be directly associated with the level of dispersion, whereby $\varsigma = 0$ refers to a non-dispersed fiber distribution with $\mathbf{H} = \mathbf{M}$. In contrast a value of $\varsigma = 0.5$ refers to a uniform distribution in the fibrous \mathbf{e}_1 - \mathbf{e}_2 plane. Thus, replacing the structural tensor \mathbf{M} in Eqs. (5.2) and (5.3) with the generalized representation \mathbf{H} results in the strain-energies

$$\begin{aligned} W_H^{GST}(\log \mathbf{U}) &= \mu_T \operatorname{tr}[(\log \mathbf{U})^2] + \frac{\lambda}{2} [\operatorname{tr}(\log \mathbf{U})]^2 + \alpha \log \mathbf{U} : \mathbf{H} (\operatorname{tr} \log \mathbf{U}) \\ &\quad + \frac{1}{2} \beta (\log \mathbf{U} : \mathbf{H})^2 + 2(\mu_L - \mu_T) (\log \mathbf{U})^2 : \mathbf{H}. \end{aligned} \quad (5.8)$$

and

$$\begin{aligned} W_C^{GST}(\mathbf{C}) &= \mu_T \operatorname{tr}(\mathbf{E}^2) + \frac{\lambda}{2} (\operatorname{tr} \mathbf{E})^2 + \alpha \mathbf{E} : \mathbf{H} (\operatorname{tr} \mathbf{E}) \\ &\quad + \frac{1}{2} \beta (\mathbf{E} : \mathbf{H})^2 + 2(\mu_L - \mu_T) \mathbf{E}^2 : \mathbf{H}. \end{aligned} \quad (5.9)$$

The micromorphic model generally allows to vary the orientation of the director explicitly over the micro-space \mathcal{S}_0 . Considering only one director $\mathbf{A}(\zeta)$ any function may be assumed and integrated over the microspace. The examples depicted in Fig. 5.10a) and c) show equibiaxial tension tests. The sample is loaded with a given displacement \bar{u} on the boundaries and the fibrous plane is identical to the drawing plane. It is chosen here because it is

ensured that every fiber will be stretched and the grade of dispersion can be estimated from the ratio of the stresses in the different loading directions. In a) the distribution of the initial micro-director is specified with help of

$$\alpha(\zeta) = -\frac{2\zeta}{L_a}\alpha' \quad \text{and} \quad \mathbf{A}(\zeta) = \begin{pmatrix} \cos \alpha(\zeta) \\ \sin \alpha(\zeta) \\ 0 \end{pmatrix}, \quad (5.10)$$

where $\alpha(\zeta)$ denotes the angle of the director to the horizontal-axis \mathbf{e}_1 at a micro-space coordinate $\zeta \in [-L_a/2, L_a/2]$. Obviously, α is assumed to be linearly distributed with a maximum value of $\alpha(\zeta = -L_a/2) = \alpha'$ and a minimum value of $\alpha(\zeta = L_a/2) = -\alpha'$, where α' is a user-defined value to be varied within the example. The mean angle of the linear distribution is equal to 0° . The micromorphic material response is to be compared to the above defined strain-energies W_C^{GST} and W_H^{GST} . In Fig. 5.10a) the same boundary conditions as in Fig. 5.10c) are chosen. The fiber direction \mathbf{A} is orientated in horizontal direction and the dispersion parameter ς is to be varied within the simulations in order to study different degrees of dispersion.

	μ_T	λ	α	μ_L	β		L_a	$\tilde{\mu}_0$	$\tilde{\lambda}_0$	$\tilde{\mu}_1$	$\tilde{\lambda}_1$	$\tilde{\mu}_2$	$\tilde{\lambda}_2$
W_H^{GST}	15	10	0	15	575	\tilde{W}_M	10^{-4}	15	10	300	470	500	350
W_C^{GST}	15	10	0	15	575								

Table 5.8: Material parameters used to generate the plots depicted in Fig. 5.10. All parameters are stated in $[\bullet] = \text{MPa}$ except of $[L_a] = \text{mm}$.

The results are shown in Fig. 5.10b) for the micromorphic model, in d) for ψ_C^{GST} and in e) for ψ_H^{GST} . In the corresponding graphs the stress ratio of the horizontal and vertical stresses is plotted over the predefined displacement \bar{u} . The involved material parameters are summarized in Tab. 5.8. Parameters triggering the anisotropic material behavior are chosen considerably larger such that the isotropic material response can be considered to be of minor importance. This allows for a meaningful comparison of the models. As can be seen, the stress ratio decreases with increasing α' which seems reasonable since the direction function has more vertical components with increasing α' . Similarly, the stress ratio also decreases if the dispersion parameter ς increases for both models in d) and e). Thus, varying the orientation of the initial director $\mathbf{A}(\zeta)$ over the micro-space intrinsically incorporates the possibility to integrate fiber density distributions and consequently to account for fiber dispersion. Integration is thereby performed very efficiently using *Gaussian* quadrature on a 1-D element.

A second aspect to be concluded from the plots is that again the fibers of the micromorphic model tend to reorient with increasing deformation such that the stress ratio decreases. The ratio tends to one which would be the ratio for an isotropic problem. This is substantially different for W_H^{GST} and W_C^{GST} , where the ratio is constant. In fact, the stress ratios for W_H^{GST} and W_C^{GST} are even identical in case of identical values of ς .

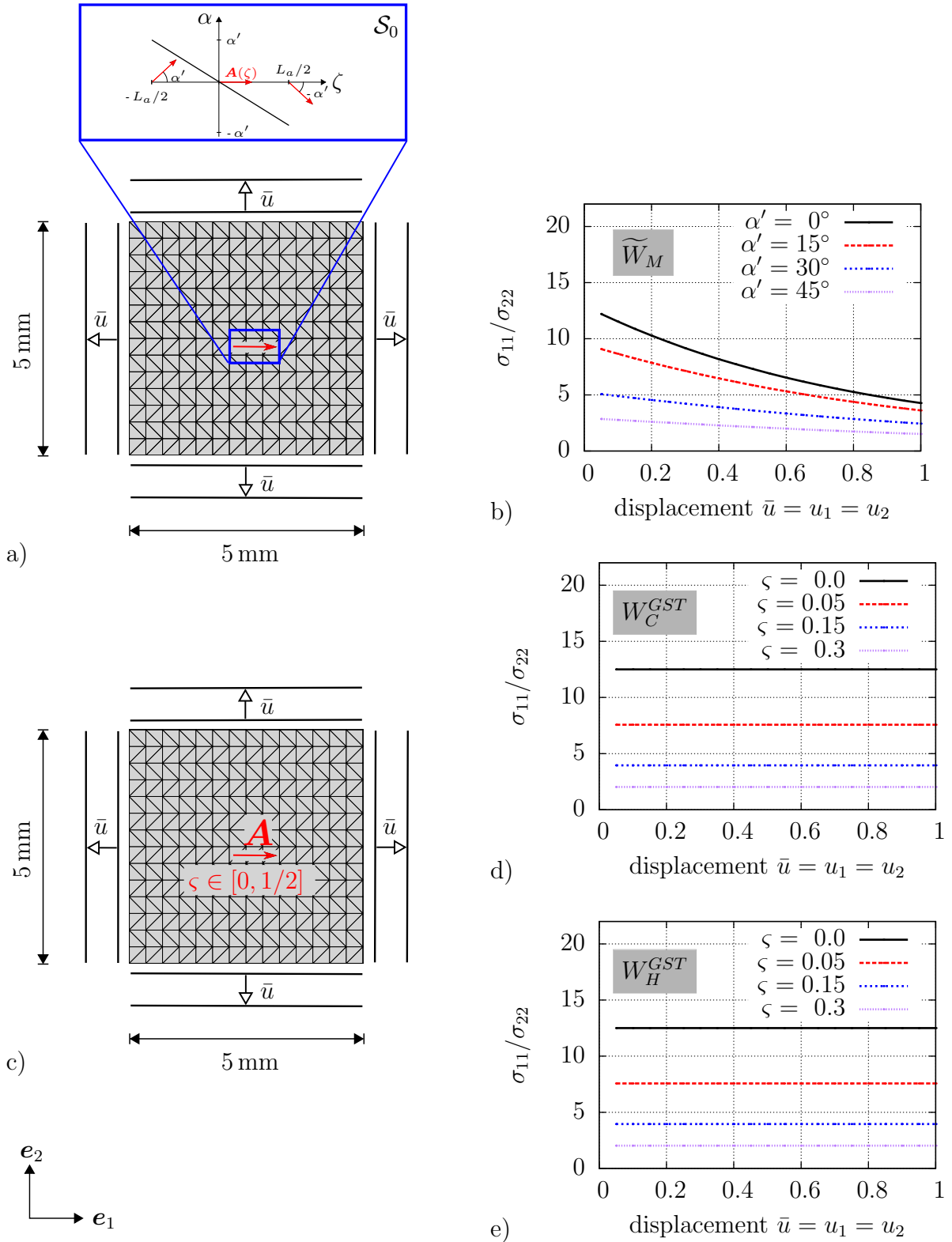


Figure 5.10: Equi-biaxial tension test with a) non-uniform director orientation over the micro-space \mathcal{S}_0 and c) generalized strain tensors. Corresponding results are shown in b), d) and e), where the stress-ratio of horizontal (σ_{11}) and vertical stresses (σ_{22}) is plotted over the displacement \bar{u} of the boundary condition. The example is adapted from VON HOEGEN ET AL. [185].

6 Micromechanical Motivated Constitutive Modeling

In order to obtain reliable results within a simulation, it is of utmost interest to choose suitable material parameters. In case of biological tissues this discipline is challenging because the material properties are subject to considerable fluctuations. The heterogeneous composition of a tissue changes throughout lifetime by aging, adaption to diseases, medication or training, which is gathered under the term “remodeling”. Furthermore, also gender has significant influence on the structural features. The material parameters of so-called phenomenological material laws, first of all, miss a clear physical meaning. However, for some, there exists an (often unknown) correlation between those parameters of a descriptive nature and measurable structural features. With no doubt, the underlying micro-structural composition and features determine the stress-strain response observed in mechanical measurements which in turn form the basis of parameter fitting procedures for finding the phenomenological parameters. To uncover this relationship it would be necessary to combine non-invasive measurements of the micro- and nanoscale features with invasive mechanical experiments.

The large number of required experiments, which would be necessary for the reliable determination of parameters, will most likely never be available. Therefore, it seems reasonable to replace the experiments with accurate multi-scale simulations of collagen fiber bundles, exclusively involving meaningful parameters in the governing equation. In the following, the constitutive response of a collagen fiber orientated in direction \mathbf{A} with a macroscopic stretch $\lambda_4 = \sqrt{I_4^{C^1}}$ is described by a strain energy

$$W_{\text{multi}}(\lambda_4) = \int_1^{(\lambda_4-1)+1} \int_1^{(\xi-1)+1} E_C(\eta, \mathcal{F}) d\eta d\xi. \quad (6.1)$$

The approach, summarized in Tab. 6.1, was developed in MACERI ET AL. [106], MARINO AND VAIRO [111] and MARINO AND WRIGGERS [112] and is utilized to generate a set of numerical experiments. In brief, the along-the-chord collagen fiber stiffness E_C is defined in terms of a homogenization scheme across three different scales:

1. The **nanoscale** represents the molecular level, where the molecular stretch

$$\lambda_m = \frac{\ell_m}{\ell_{m,o}} = \lambda_m^s + \lambda_m^h - 1. \quad (6.2)$$

is the result of the entropic stretch λ_m^s due to thermal fluctuations and the energetic stretch λ_m^h . The lengths ℓ_m and $\ell_{m,o}$ denote the actual and reference end-to-end lengths of the molecule. The tangent modulus E_m of the molecule in Eq. (6.6) is determined by means of the entropic *Young's* modulus E_m^s , see Eq. (6.7), and the energetic *Young's* modulus E_m^h , see Eq. (6.8), which are acting in series. Remaining parameters are explained in Tab. 6.2 and values from the literature are given while k_B is the *Boltzmann* constant.

2. The **mesoscale** describes the fibril mechanics. The fibril stretch

$$\lambda_f = \frac{\ell_m + \delta_c}{\ell_{m,o}} = \lambda_m + \frac{\delta_c}{\ell_{m,o}} \quad (6.3)$$

of a representative unit system is the sum of the molecular stretch λ_m and the stretch due to the sway of cross-links δ_c . Both mechanisms are acting in series. Let Λ_C be

a representative measure for the density of cross-links acting in parallel within the unit system, then the total cross-link stiffness is given by $\Lambda_K = \Lambda_C k_c$, where k_c is the constant, deformation independent stiffness of a single cross-link. The tangent modulus of fibrils is denoted by E_f in Eq. (6.5), where the deformation of Λ_c parallel cross-links act in series with molecular elongation. The remaining parameter A_m is explained in Tab. 6.2 and values for both A_m and Λ_K from the literature are given.

3. On the **microscale** a crimped fiber reference unit system is modeled within the framework of the *Euler-Bernoulli* beam theory for large deformations with an along-the-chord *Young's* modulus E_C according to Eq. (6.4). The beam is of a circular cross-section with a radius r_F , an actual fiber amplitude $H_F(\lambda_4)$ and an actual fiber period $L_F(\lambda_4)$. For convenience, the quarter of the period $\ell_F = L_F/4$ is introduced. The initial amplitude and period in the unloaded state are given by $H_{F,o} = H_F(\lambda_4 = 1)$ and $\ell_{F,o} = L_{F,o}/4 = \ell_F(\lambda_4 = 1)$.

Table 6.1: Computation of the along-the-chord collagen fiber stiffness E_C .

Microscale: crimped collagen fiber	
$E_C = \frac{E_f}{\lambda_4} \frac{\ell_F^2 + H_F^2}{\sqrt{\ell_{F,o}^2 + H_{F,o}^2}} \left[\ell_F + \frac{4H_F^2}{3r_F^2 \ell_F} (\ell_F^2 + H_F^2) \right]^{-1},$	$\frac{\partial \lambda_f}{\partial \lambda_4} = \frac{\lambda_4 \ell_{F,o}^2 + H_F \frac{\partial H_F}{\partial \lambda_4}}{\sqrt{(\lambda_4^2 \ell_{F,o}^2 + H_F^2)(\ell_{F,o}^2 + H_{F,o}^2)}}$
$\frac{\partial H_F}{\partial \lambda_4} = -\frac{\ell_F H_F [4(\ell_F^2 + H_F^2) - 3r_F^2]}{\lambda_4 [4H_F^2(\ell_F^2 + H_F^2) + 3\ell_F^2 r_F^2]} \quad (6.4)$	
Mesoscale: collagen fibril	
$E_f = \left[\frac{1}{E_m} + \frac{A_m}{\Lambda_c k_c \ell_{m,o}} \right]^{-1},$	$\frac{\partial \lambda_m}{\partial \lambda_f} = \frac{E_f(\lambda_m^s, \lambda_m^h)}{E_m(\lambda_m^s, \lambda_m^h)} \quad (6.5)$
Nanoscale: collagen molecule	
$E_m = \frac{E_m^s E_m^h}{E_m^s + E_m^h} \quad (6.6)$	
$E_m^s = \frac{k_B T \ell_{m,o}}{\ell_p \ell_c A_m} \left[\frac{\ell_c^3}{2(\ell_c - \ell_{m,o} \lambda_m^s)^3} + 1 \right],$	$\frac{\partial \lambda_m^s}{\partial \lambda_m} = \frac{E_m(\lambda_m^s, \lambda_m^h)}{E_m^s(\lambda_m^s)}$
$E_m^h = \frac{\ell_{m,o}}{\ell_c} \left[\frac{\hat{E}}{1 + \exp\{-\eta_m[\ell_{m,o}(\lambda_m^h - 1)/\ell_c - \varepsilon_o^h]\}} + \hat{E}_o \right],$	
$\frac{\partial \lambda_m^h}{\partial \lambda_m} = \frac{E_m(\lambda_m^s, \lambda_m^h)}{E_m^h(\lambda_m^h)} \quad (6.8)$	

The interscale conditions in Tab. 6.1 are sufficient to compute the derivatives

$$\frac{\partial \lambda_m^s}{\partial \lambda_4} = \frac{\partial \lambda_m^s}{\partial \lambda_m} \frac{\partial \lambda_m}{\partial \lambda_f} \frac{\partial \lambda_f}{\partial \lambda_4} \quad \text{and} \quad \frac{\partial \lambda_m^h}{\partial \lambda_4} = \frac{\partial \lambda_m^h}{\partial \lambda_m} \frac{\partial \lambda_m}{\partial \lambda_f} \frac{\partial \lambda_f}{\partial \lambda_4}, \quad (6.9)$$

which are required in the context of hyperelastic materials. Characteristic values for all parameters concerned are listed in Tab. 6.2 together with details of sources. The values are specifically meaningful for rat tail tendon, cf. MARINO AND WRIGGERS [112]. The

relatively large number of parameters is opposed by the increased information content. Results of atomic force microscopy measurements of collagen fibers, for instance, can be reproduced by the model, see MARINO AND VAIRO [110].

Table 6.2: Parameters of W_{multi} and considered basic values to compute the numerical experiments. Adapted from MARINO ET AL. [113].

	Value	Definition	References
$H_{F,o}$	13.04 μm	Fiber crimp amplitude	DIAMANT ET AL. [32], MARINO AND WRIGGERS [112]
r_F	1.63 μm	Fiber radius	ANGEL AND GHEORGHE [4], MARINO AND WRIGGERS [112]
Λ_K	7 nN/ μm	Cross-link stiffness density	SAITO ET AL. [144], MARINO [109]
ℓ_p	14.5 nm	Persistence length	BUEHLER AND WONG [19], MARINO [109]
$L_{f,o}$	240 μm	Reference collagen fiber period	HANSEN ET AL. [65]
$\ell_{m,o}$	273 nm	Reference molecular end-to-end length	BUEHLER AND WONG [19]
ℓ_c	287 nm	Molecular contour length	BOZEC AND HORTON [17]
A_m	1.41 nm ²	Molecular cross-sectional area	MARINO AND VAIRO [111]
\hat{E}_o	1 GPa	Low-strain triple-helix modulus	MARINO AND VAIRO [111]
\hat{E}	80 GPa	High-strain triple-helix modulus	MARINO AND VAIRO [111]
η_m	22.5	Triple-helix uncoiling resistance	MARINO AND VAIRO [111]
ε_o^h	0.1	Triple-helix uncoiling strain	MARINO AND VAIRO [111]
T	310 K	Body temperature	-
k_B	$\frac{1.38}{10^{23}}$ J/K	<i>Boltzmann</i> constant	-

In the further course of the thesis, it is desired to correlate physical and measurable parameters to “classical” phenomenological parameters. The numerical experiments based on W_{multi} , in turn, are fitted to a simpler phenomenological strain-energy function, where the anisotropic collagen fiber response is covered in

$$W_{\text{exp}} = \frac{k_1}{2k_2} \{ \exp[(k_2 \langle I_4^{C^1} - 1 - k_3 \rangle^2) - 1] \} \quad (6.10)$$

including the phenomenological parameters k_1 , k_2 and k_3 . For the modeling of collagen fibers it is assumed that the fiber reorientation of fibers during loading follows affine kinematics, i.e the embedded fibers are firmly connected to the surrounding matrix. For $k_3 = 0$ the function is identical to the *Holzappel-Gasser-Ogden* model, see HOLZAPFEL ET AL. [77]. For the chosen setups it will be ensured that each fiber is stretched, i.e. $I_4^{C^1} \geq 1$, which is why the tension-compression switch is neglected throughout this chapter without loss of generality. The main selection criterion is to apply a frequently used and validated model in literature that can be later on applied for the residual stress simulation. Furthermore, the matrix material is modeled in each case in terms of an isotropic *Mooney-Rivlin* type strain-energy

$$W_{\text{MR}} = c_1 I_1^C + c_2 I_2^C + c_3 I_3^C - \delta \log \sqrt{I_3^C}, \quad (6.11)$$

where c_1 , c_2 and c_3 are stress-like material parameters and $\delta = 2c_1 + 4c_2 + 2c_3$. The parameters are randomly set to $c_1 = c_2 = c_3 = 0.1$ MPa in order to focus on the collagenous constituents. Thus, in the further course the strain-energies

$$W_u^{\text{multi}}(\mathbf{C}, \mathbf{M}) = (1 - V_C) W_{\text{MR}}(\mathbf{C}) + V_C W_{\text{multi}}(\mathbf{C}, \mathbf{M}), \quad (6.12)$$

$$W_u^{\text{pheno}}(\mathbf{C}, \mathbf{M}) = (1 - V_C) W_{\text{MR}}(\mathbf{C}) + V_C W_{\text{exp}}(\mathbf{C}, \mathbf{M}) \quad (6.13)$$

are considered which are split into the isotropic contribution W_{MR} associated to the matrix material and the anisotropic contributions W_{multi} and W_{exp} associated to the collagen fibers. Here, $V_C = 0.57$ ([113]) denotes the collagen volume fraction. The material incompressibility is enforced by adding the *Lagrange*-multiplier p to the *Cauchy* stress

$$\boldsymbol{\sigma} = \frac{2}{J} \mathbf{F} \frac{\partial W}{\partial \mathbf{C}} \mathbf{F}^T - p \mathbf{1}. \quad (6.14)$$

In Sec. 6.1, a uniaxial tension test is assumed, where the loading and fiber direction are aligned. These assumptions are accurate to characterize the behavior of tendons for instance and allow to relatively easy find correlations between structural and phenomenological parameters.

Nevertheless, for a lot of biological tissues several predominant dispersed fiber families are present as for example for arterial tissues. In these cases, the fiber density distribution needs to be considered as an additional unknown. Biaxial material testing appears to be suitable for the characterization of the fiber distribution and is conducted in Sec. 6.2. Firstly, because the grade of anisotropy can be directly estimated from the ratio of the measured stresses in the loading directions. Secondly, the testing conditions are relatively close to the in vivo mechanical exposure. Thirdly, because it is one of the standard tests for biological soft tissues and a comparatively large amount of data is available in literature for different organs which is a basic prerequisite to fit constitutive functions.

6.1 Correlations of Micro-Structural Features Under Uniaxial Tension

The general approach followed in this subsection was described in MARINO ET AL. [113]. As depicted in Fig. 6.1, the collagen fiber direction \mathbf{A} in the uniaxial tension test is assumed to be aligned with the loading direction \mathbf{e}_1 and therefore the stretches orthogonal to the loading direction are identical and $\lambda_2 = \lambda_3 = 1/\sqrt{\lambda_1}$ can be computed from the incompressibility condition. Thus, the deformation gradient is given by

$$\mathbf{F} = \begin{pmatrix} \lambda_1 & 0 & 0 \\ 0 & \frac{1}{\sqrt{\lambda_1}} & 0 \\ 0 & 0 & \frac{1}{\sqrt{\lambda_1}} \end{pmatrix}. \quad (6.15)$$

Considering the constraint $\sigma_{22} = \sigma_{33} \stackrel{!}{=} 0$ in a uniaxial tension test and the specific fiber orientation $\mathbf{A} = \mathbf{e}_1$, the *Lagrange*-multiplier is given by

$$p = 2(1 - V_C) \frac{1}{\lambda_1} \left[c_1 + c_2 \left(\lambda_1^2 + \frac{1}{\lambda_1} \right) + \left(c_3 - \frac{\delta}{2} \right) \lambda_1 \right]. \quad (6.16)$$

The general pattern for the parameter fitting in order to obtain discrete data sets, correlating structural features to phenomenological parameters, is summarized in Fig. 6.2.

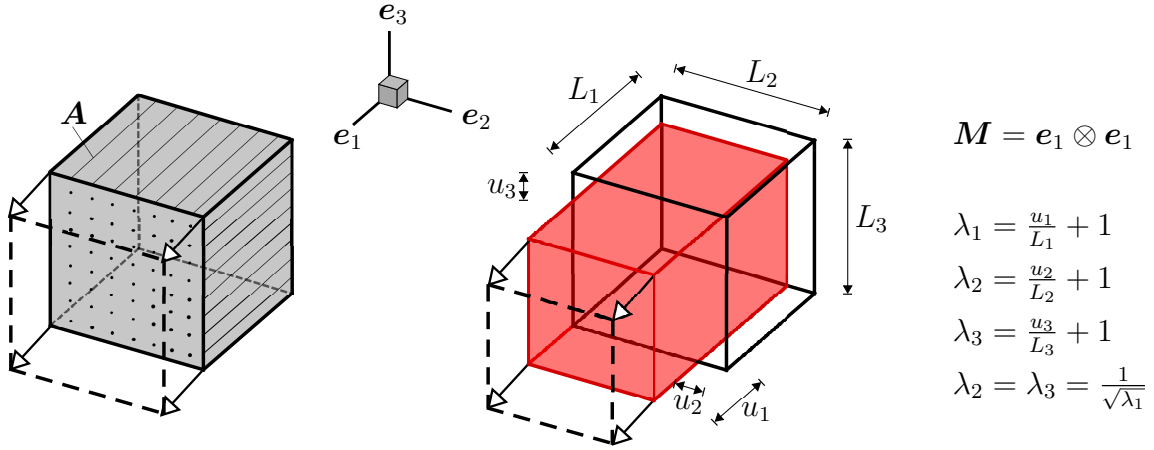


Figure 6.1: Uniaxial tension test used to create the benchmark data. The collagen fibers and the loading direction are aligned with the axis \mathbf{e}_1 . The body is assumed to be incompressible.

The creation of benchmark data based on W_u^{multi} is to be explained in Sec. 6.1.1. Subsequently, the generated stress-strain curves are then fitted to W_u^{exp} . The optimization strategy for the parameter identification is presented in Sec. 6.1.2. The main focus lies on expressing the phenomenological material parameters of set \mathcal{K} associated to W_{exp} in terms of the structural parameter set \mathcal{F} associated to W_{multi} . Explicit definitions are given in the course of this chapter.

6.1.1 Benchmark Data

The multiscale homogenization model W_{multi} incorporates several structural parameters. The reader is referred to MARINO AND VAIRO [111] for detailed information. Among these parameters are the amplitude of initially crimped collagen fibers $H_{F,o}$, the collagen fiber cross-section radius r_F , the intermolecular cross-link stiffness Λ_K between adjacent collagen molecules and the persistence length ℓ_p . These parameters are to be varied within the multiscale approach in order to generate a discrete set of numerical uniaxial tension experiments. The basic reference values of the four mentioned parameters are defined according to Tab. 6.3 and are numbered consecutively from \bar{f}_1 to \bar{f}_4 .

Table 6.3: Reference values of the considered multiscale parameters to be varied.

$\bar{f}_1 = \bar{H}_{F,o}$	$\bar{f}_2 = \bar{r}_F$	$\bar{f}_3 = \bar{\Lambda}_K$	$\bar{f}_4 = \bar{\ell}_p$
13.04 μm	1.63 μm	7.0 nN/ μm	14.5 nm

The discrete values to be studied for the variation are collected in the four sets

$$\tilde{f}_i = \{0.5\bar{f}_i, 0.75\bar{f}_i, 1.0\bar{f}_i, 1.25\bar{f}_i, 1.5\bar{f}_i, 1.75\bar{f}_i, 2.0\bar{f}_i\}_{i=1,2,3,4} \quad (6.17)$$

of cardinality seven. Each set is associated to one specific material parameter. The range of variation lies between 50% and 200% from the reference values. Then, the set of all ordered 4-tuple elements is defined through

$$\mathcal{F} = \tilde{f}_1 \times \tilde{f}_2 \times \tilde{f}_3 \times \tilde{f}_4, \quad (6.18)$$

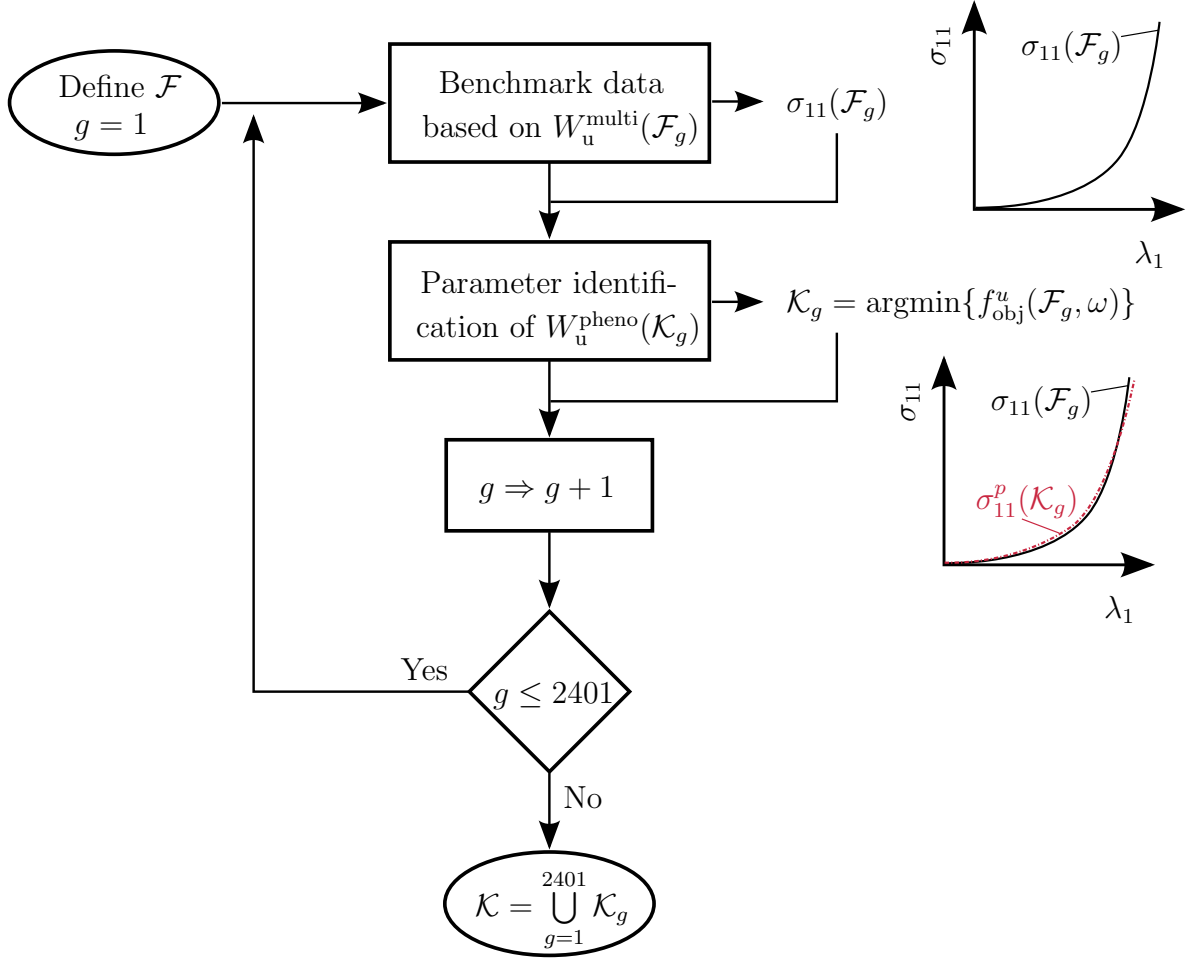


Figure 6.2: Flow chart describing the computation of set $\mathcal{K}(\mathcal{F})$.

which is of cardinality $7^4 = 2401$. This set in turn may be split into a number of 2401 different subsets

$$\mathcal{F} = \bigcup_{g=1}^{2401} \mathcal{F}_g \quad \text{with} \quad \mathcal{F}_g = \{f_1^g, f_2^g, f_3^g, f_4^g\}, \quad (6.19)$$

where $\mathcal{F}_g \subset \mathcal{F}$ is a 4-tuple element of cardinality one and $f_i^g \in \tilde{f}_i|_{i=1,2,3,4}$. The subset exclusively consisting of the reference values, for example, is given by

$$\bar{\mathcal{F}} = \{\bar{f}_1, \bar{f}_2, \bar{f}_3, \bar{f}_4\} \in \mathcal{F}. \quad (6.20)$$

Benchmark data based on the multiscale approach is computed for uniaxial, displacement driven tension tests for each set \mathcal{F}_g . All other parameters remain unaltered with regard to Tab. 6.2.

The stress-stretch curve for the reference set $\bar{\mathcal{F}}_g$ is shown in Fig. 6.3. Here, it is distinguished between the large strain regime shown in a) and the small strain regime shown in b). In each of these two regions 100 equi-distant measuring points are indicated with help of the dots. The boundaries of the small strain and large strain regime are defined with help of the estimates

$$\lambda_{100}^s = 0.005 + \lambda_{\text{str}}(H_{F,o}) \quad \text{and} \quad \lambda_{100}^\ell = 0.1 + \lambda_{\text{str}}(H_{F,o}), \quad (6.21)$$

respectively. These are based on the theoretical stretch

$$\lambda_{\text{str}} = \sqrt{1 + \frac{4H_{F,o}}{L_{F,o}}} \quad (6.22)$$

in fiber direction at which the initially crimped fiber with an amplitude $H_{F,o}$ and period $L_{F,o}$ straightens out. The small and large strain regime are then identified by

$$\mathcal{R}_s = [1, \lambda_{100}^s] \quad \text{and} \quad \mathcal{R}_\ell = [\lambda_{100}^s, \lambda_{100}^\ell]. \quad (6.23)$$

Accordingly, this kind of stress-strain data is generated 2401 times for any ordered 4-tuple \mathcal{F}_g in set \mathcal{F} .

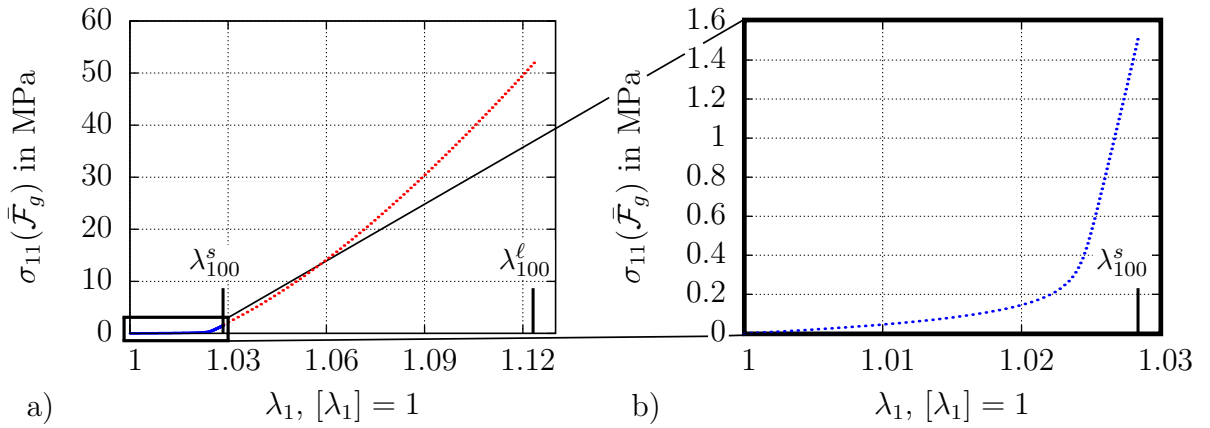


Figure 6.3: Stress-stretch curves computed for a uniaxial tension test based on the multi-scale approach W_u^{multi} and using parameter set $\bar{\mathcal{F}}_g$. In a) the large strain regime \mathcal{R}_ℓ is shown and in b) the small strain regime \mathcal{R}_s .

6.1.2 Parameter Identification

In a second step, each of the resulting stress-strain curves is fitted to the parameters of the exponential macroscopic, hyperelastic strain-energy function W_{exp} defined in Eq. (6.10) which is used in Eq. (6.13). Each of the generated stress-strain curves is fitted to this function such that we obtain sets of optimized parameters

$$\mathcal{K}_g = \{k_1, k_2, k_3\} := \mathcal{K}_g(\mathcal{F}_g), \quad (6.24)$$

associated to the structural parameters \mathcal{F}_g . Please note that each set \mathcal{K}_g is a 3-tuple element of cardinality one. Again, the complete parameter set is given by the union of all sets

$$\mathcal{K} = \bigcup_{g=1}^{2401} \mathcal{K}_g, \quad (6.25)$$

which is of cardinality 2401 and also made up of 3-tuple elements. In order to find the optimal parameters in \mathcal{K}_g within a numerical scheme, we define the objective function

$$f_{\text{obj}}^u = (1 - \omega)\mathcal{E}_s + \omega\mathcal{E}_\ell, \quad (6.26)$$

which is to be minimized. Here, $\omega \in [0, 1]$ denotes a weighting factor between the error measures \mathcal{E}_s and \mathcal{E}_ℓ of the benchmark data and the hyperelastic function in the small strain and large strain regimes defined in Eq. (6.23). The value of ω is set to 0.5 in the following in order to equally weight the small strain and large strain regime error. The parameter fitting is performed in least squares sense using the specific error functionals

$$\begin{aligned} \mathcal{E}_s &= \sqrt{\frac{1}{100} \sum_{n=1}^{100} \frac{\|\sigma_{11}(\mathcal{F}_g, \lambda_n^s) - \sigma_{11}^p(\mathcal{K}_g, \lambda_n^s)\|^2}{[\sigma_{11}(\mathcal{F}_g, \lambda_{100}^s)]^2}} & \text{with } \lambda_n^s &\in [1, \lambda_{100}^s], \\ \mathcal{E}_\ell &= \sqrt{\frac{1}{100} \sum_{n=1}^{100} \frac{\|\sigma_{11}(\mathcal{F}_g, \lambda_n^\ell) - \sigma_{11}^p(\mathcal{K}_g, \lambda_n^\ell)\|^2}{[\sigma_{11}(\mathcal{F}_g, \lambda_{100}^\ell)]^2}} & \text{with } \lambda_n^\ell &\in [\lambda_{100}^s, \lambda_{100}^\ell]. \end{aligned} \quad (6.27)$$

As mentioned before, for both functionals 100 evaluation/measuring points are used. The *Cauchy*-stress components obtained employing the phenomenological description W_u^{pheno} are labeled with σ_{11}^p . Finally, the set of optimal phenomenological parameters associated to the structural parameters in one specific set \mathcal{F}_g is formally described by the expression

$$\mathcal{K}_g(\mathcal{F}_g) = \operatorname{argmin}\{f_{\text{obj}}^u(\mathcal{F}_g, \omega)\}. \quad (6.28)$$

To solve the equation above, the *MATLAB* built-in function *fmincon* is used. This tool allows for a constrained optimization based on numerical tangents computed from perturbations ([180]). Due to the fact that the function f_{obj}^u is not convex, a multi-start algorithm is implemented. The optimization procedure is repeated several times with random starting values of k_1 , k_2 and k_3 in order to more or less ensure that the optimal parameters are found.

6.1.3 Regression Analysis of Discrete Data Sets

The procedure presented in Sec. 6.1 only allows for a discrete relationship. Therefore, it seems reasonable to introduce an interpolation function, providing a continuous relationship. The quadratic polynomial function

$$k_h^r = b_0^h + \sum_{j=1}^4 b_j^h \left(\frac{f_j}{f_j} - 1\right) + \sum_{q=1}^4 \sum_{r=q}^4 b_{qr}^h \left(\frac{f_q}{f_q} - 1\right) \left(\frac{f_r}{f_r} - 1\right) \Big|_{h=1,2,3} \quad (6.29)$$

depends on the variables f_1, f_2, f_3 and f_4 , which represent the four investigated structural features. The polynomial is made up of the set of interpolation parameters

$$\mathcal{P}_h = \{b_0^h, b_1^h, b_2^h, b_3^h, b_4^h, b_{11}^h, b_{12}^h, b_{13}^h, b_{14}^h, b_{22}^h, b_{23}^h, b_{24}^h, b_{33}^h, b_{34}^h, b_{44}^h\} \Big|_{h=1,2,3} \quad (6.30)$$

incorporating 15 elements. Here, the index $h = 1, 2, 3$ specifies the phenomenological parameter k_1, k_2 or k_3 to be interpolated. Thus, there are three optimizations problems

$$\mathcal{P}_h = \operatorname{argmin}\{f_{\text{obj}}^{r,h}\} \Big|_{h=1,2,3} \quad (6.31)$$

to determine the interpolation parameters in Eq (6.30). The associated objective function of the optimization problem is defined through

$$f_{\text{obj}}^{r,h} = \sqrt{\frac{1}{G_r} \sum_{\mathcal{F}_g \in \mathcal{F}^r} \frac{\|k_h^r(\mathcal{P}_h, \mathcal{F}_g) - k_h(\mathcal{F}_g)\|^2}{\max_{\mathcal{F}_g \in \mathcal{F}^r}(k_h)}} \Big|_{h=1,2,3}, \quad (6.32)$$

where the discrete values $k_h(\mathcal{F}_g)$ computed in the previous section are used as the set of known data points. Since it is not possible to have a quadratic regression for the whole data, regression is preformed on a subset

$$\mathcal{F}^r = \tilde{f}_1^r \times \tilde{f}_2^r \times \tilde{f}_3^r \times \tilde{f}_4^r \quad \text{with} \quad \mathcal{F}^r \subset \mathcal{F}, \quad (6.33)$$

where the range of the multiscale parameters varies between 75% and 150% percent of the reference values and

$$\tilde{f}_i^r = \{0.75\bar{f}_i, 1.0\bar{f}_i, 1.25\bar{f}_i, 1.5\bar{f}_i\}_{|i=1,2,3,4}. \quad (6.34)$$

Then the cardinality of set \mathcal{F}^r is given by $G_r = 4^4 = 256$ and the regression triplets form the sets

$$\mathcal{K}_g^r = \{k_1^r, k_2^r, k_3^r\} \quad \text{and} \quad \mathcal{K}^r = \bigcup_{g=1}^{256} \mathcal{K}_g^r. \quad (6.35)$$

6.1.4 Linear Interpolation of Discrete Data Sets

Let us define the sets

$$\tilde{f}_i^{\text{Int}} = \{0.625\bar{f}_i, 0.875\bar{f}_i, 1.125\bar{f}_i, 1.375\bar{f}_i, 1.625\bar{f}_i, 1.875\bar{f}_i\}_{|i=1,2,3,4}, \quad (6.36)$$

where parameter values above were chosen such that they lie exactly in between the values of the sets \tilde{f}_1 , \tilde{f}_2 , \tilde{f}_3 and \tilde{f}_4 , respectively.

Then the parameters are linearly interpolated for all members of the *Cartesian* product

$$\mathcal{F}^{\text{Int}} = \tilde{f}_1^{\text{Int}} \times \tilde{f}_2^{\text{Int}} \times \tilde{f}_3^{\text{Int}} \times \tilde{f}_4^{\text{Int}} \quad \text{with} \quad \mathcal{F}^{\text{Int}} \cap \mathcal{F} = \emptyset,$$

which is of cardinality $6^4 = 1296$. Again, this set in turn may be split into a number of 1296 different subsets

$$\mathcal{F}^{\text{Int}} = \bigcup_{g=1}^{1296} \mathcal{F}_g^{\text{Int}}, \quad (6.37)$$

where $\mathcal{F}_g^{\text{Int}} \subset \mathcal{F}^{\text{Int}}$ is a 4-tuple element of cardinality one and $f_i^g \in \tilde{f}_i|_{i=1,2,3,4}$. Interpolated values

$$\mathcal{K}_g^{\text{Int}}(\mathcal{F}_g^{\text{Int}}) = \{k_1^{\text{Int}}, k_2^{\text{Int}}, k_3^{\text{Int}}\} \quad \text{with} \quad \mathcal{K}^{\text{Int}} = \bigcup_{g=1}^{1296} \mathcal{K}_g^{\text{Int}} \quad (6.38)$$

are compared with the optimized values according to

$$\mathcal{K}_g^* = \text{argmin}\{f_{\text{obj}}^u(\mathcal{F}_g^{\text{Int}}, \omega)\}, \quad \mathcal{K}_g^* = \{k_1, k_2, k_3\}, \quad \text{and} \quad \mathcal{K}^* = \bigcup_{g=1}^{1296} \mathcal{K}_g^* \quad (6.39)$$

with $\omega = 0.5$, cf. Eq. (6.28). The quality of the interpolation can then be estimated with help of the deviation of $\mathcal{K}_g^{\text{Int}}$ and \mathcal{K}_g^* . In a best case scenario, the interpolated set $\mathcal{K}_g^{\text{Int}}$ and the optimal set \mathcal{K}_g^* are identical.

6.1.5 Results: Parameter Identification

The results of the parameter optimizations according to the flowchart in Fig. 6.2 are briefly presented in the following. In Fig. 6.4 the entire set \mathcal{K} of optimized parameters is depicted. Each point represents a subset \mathcal{K}_g of \mathcal{K} according to Eq. (6.25). The identical triplets \mathcal{K}_g are plotted four times. However, in each of these plots the contour color is associated to a different multiscale parameter f_i which is normed with respect to reference value \bar{f}_i . It becomes apparent that there exists a strong correlation between k_3 and $H_{F,o}$, while Λ_K and ℓ_p in particular vary in the k_1 - k_2 plane. In contrast the fiber radius r_F appears to be weakly correlated to the phenomenological parameters at first glance.

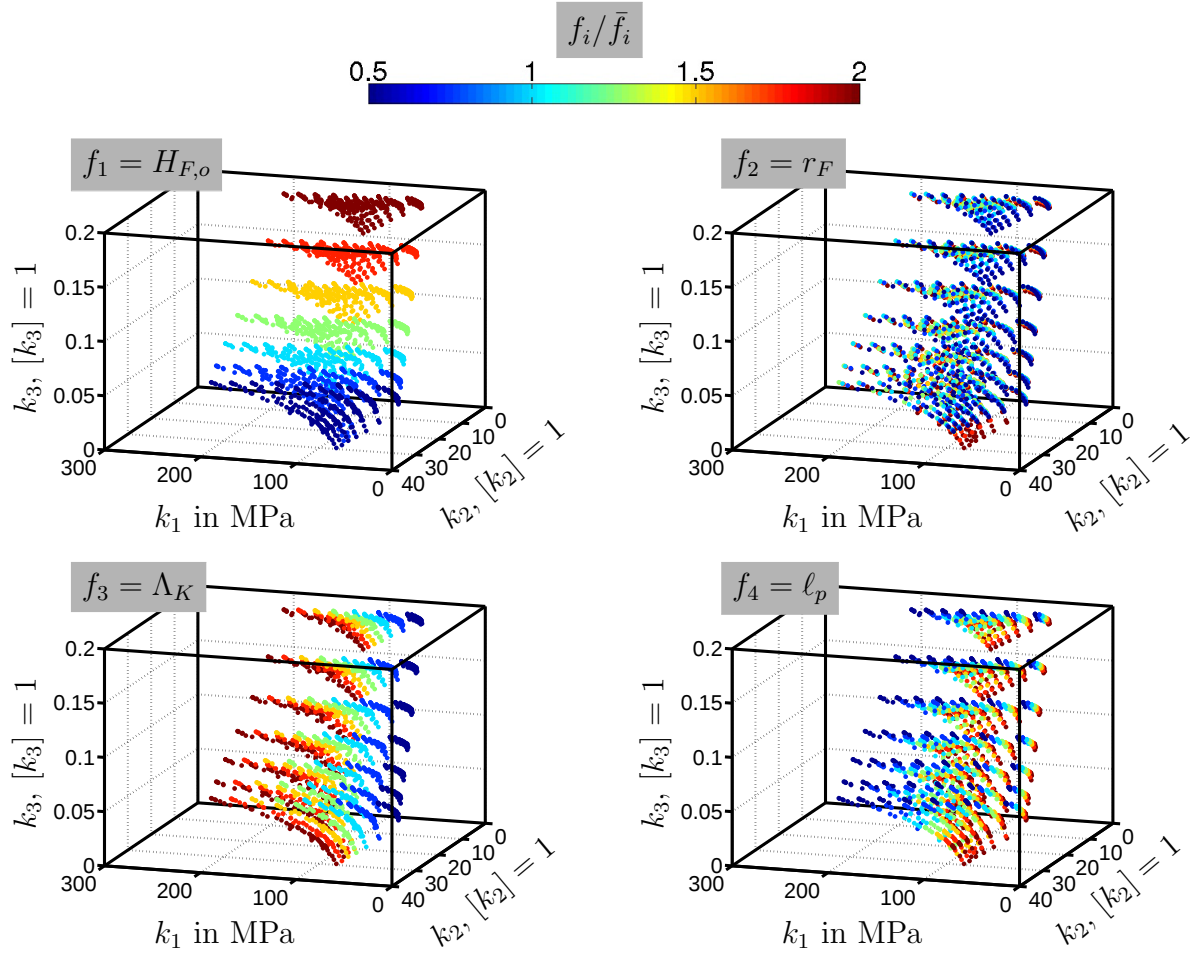


Figure 6.4: Different contour plots of all 2401 optimized triplets $\mathcal{K}_g(\mathcal{F}_g)$. The four varied structural features f_i are normed with respect to the reference values \bar{f}_i , see Tab. 6.3.

Additional plots in selected planes of the generated data set are included in Appendix D. These indicate that the discrete data sets appear smooth and could be in principle well approximated by continuous functions. Moreover, in Fig. 6.5 all generated benchmark stress-strain plots $\sigma_{11}(\mathcal{F}_g)$ and fitted curves $\sigma_{11}^p(\mathcal{K}_g)$ of the sets

$$\begin{aligned} \mathcal{F}^{(1)} &= \tilde{f}_1 \times \tilde{f}_2 \times \tilde{f}_3 \times \tilde{f}_4, & \mathcal{F}^{(2)} &= \bar{f}_1 \times \tilde{f}_2 \times \bar{f}_3 \times \bar{f}_4, \\ \mathcal{F}^{(3)} &= \bar{f}_1 \times \bar{f}_2 \times \tilde{f}_3 \times \bar{f}_4, & \mathcal{F}^{(4)} &= \bar{f}_1 \times \bar{f}_2 \times \bar{f}_3 \times \tilde{f}_4 \end{aligned}$$

of cardinality seven are shown. All four defined sets are subsets of the complete set \mathcal{F} and

share the set $\bar{\mathcal{F}}$ of reference values as the only common member, i.e.

$$\mathcal{F}^{(i)}|_{i=1,2,3,4} \subset \mathcal{F} \quad \text{and} \quad \mathcal{F}^{(i)} \bigcap_{i \neq j} \mathcal{F}^{(j)} = \bar{\mathcal{F}}. \quad (6.40)$$

Generally, the considered strain-energy W_u^{pheno} provides good fitting results. In Fig. 6.5a) it becomes visible that the theoretical choice of the large strain regime in Eq. (6.21) leads to comparable maximum stresses. For the other plots in Fig. 6.5b)–d) the value of $\bar{H}_{F,o}$ was applied. This is why the maximum stretch λ_{100}^l is identical for all cases. In Fig. 6.5b) the differences in the large strain regime are negligibly small. Therefore, the stress-strain curves for $\mathcal{F}^{(2)}$ (varying r_F) and $\mathcal{F}^{(4)}$ (varying ℓ_p) are shown in Fig. 6.6.

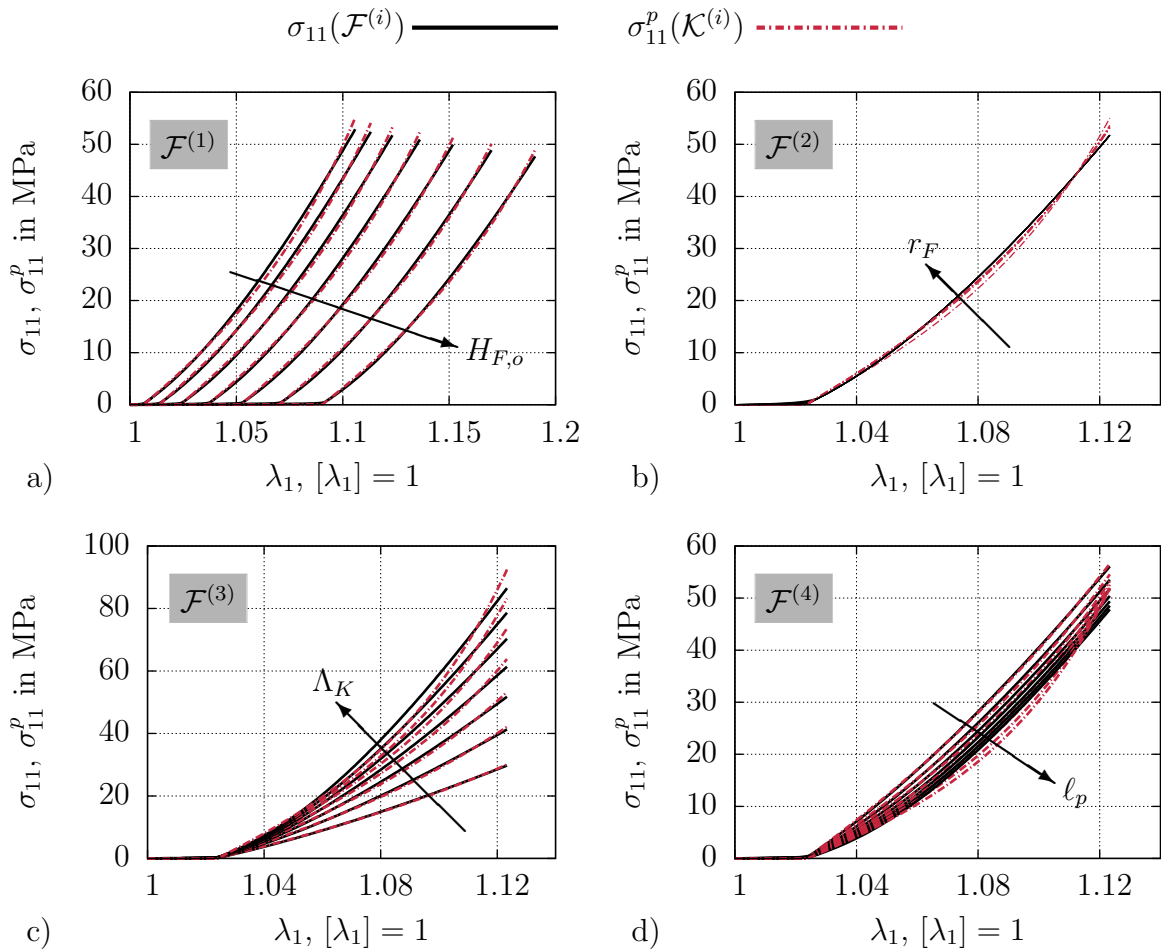


Figure 6.5: Stress strain curves $\sigma_{11}(\mathcal{F}^{(i)})$ of the benchmark data and fitted uniaxial stress-strain curves $\sigma_{11}^p(\mathcal{K}^{(i)})$. In a) only structural feature $H_{F,o}$, in b) fiber radius r_F , in c) cross-link stiffness Λ_K and in d) persistence length ℓ_p is varied. The structural feature values increase in direction of the indicated arrow.

The radius is an important factor during the uncrimping process of collagen fibers in the small strain regime since it determines the moment of inertia within the beam model. The persistence length influences the entropic deformation mechanism on the nanoscale which dominates the small-strain response. Unfortunately, the strain-energy function W_u^{pheno} yielding $\sigma_{11}^p(\mathcal{K}_g)$ struggles to reproduce the multiscale response $\sigma_{11}(\mathcal{F}_g)$ adequately. This was also observed in MARINO ET AL. [113]. Different strain-energies may be tested which

might be more appropriate. In view of patient-specific modeling, it could also be meaningful to chose different strain-energy functions for different patients in order to obtain better fits. However, we will continue to demonstrate the features of the proposed scheme based on W_u^{pheno} exclusively.

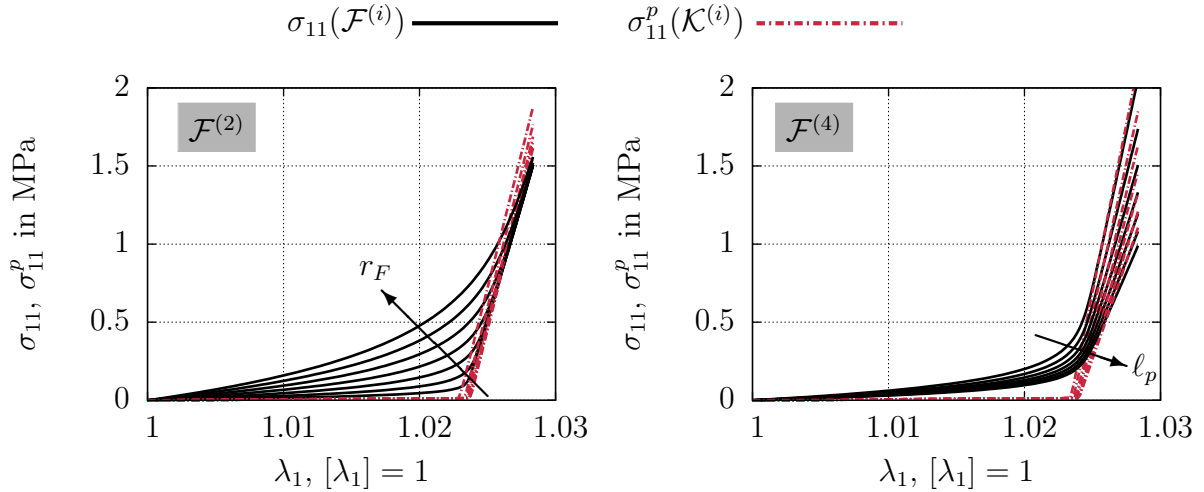


Figure 6.6: Stress strain curves $\sigma_{11}(\mathcal{F}^{(i)})$ of the benchmark data and fitted uniaxial stress-strain curves $\sigma_{11}^p(\mathcal{K}^{(i)})$ in the small strain regime \mathcal{R}_s . In a) only fiber radius r_F and in b) only persistence length ℓ_p is varied. The structural feature values increase in direction of the indicated arrow.

6.1.6 Results: Regression Analysis

The results of the regression analysis in subset \mathcal{F}^r are plotted in Fig. 6.7. That means that only subsets $\mathcal{F}_g \in \mathcal{F}^r$ are evaluated. In Figs. 6.7a)–c) the regression values $k_h^r | h = 1, 2, 3$ are compared with the optimal values $k_h | h = 1, 2, 3$ obtained from the parameter optimization. The regression values are computed based on the scheme described in Sec. 6.1.3 and specifically according to Eq. (6.29). The associated 15 optimal regression coefficients \mathcal{P}_h , cf. Eq. (6.30), are listed in Tab. D.1 in the Appendix. It can be seen that the estimated regression values are very close to the optimal values along the ideal line in each case. In case of k_3 in Fig. 6.7c), the data pairs appear to be very densely concentrated on four spots. This is due to the very strong correlation of k_3 and $H_{F,o}$, compare also Fig. 6.4a), and the cardinality of $\tilde{f}_1^r = 4$. Using the parameter set \mathcal{K}_g^r and computing the stress-strain curve $\sigma_{11}^p(\mathcal{K}_g^r)$ will result in an objective function value $f_{\text{obj}}^u(\mathcal{K}_g^r)$ when replacing \mathcal{K}_g with \mathcal{K}_g^r in Eqs. (6.26) and (6.27). These are plotted in d) in comparison to the optimal objective function values. It can be seen that the regression values can be used without any harm to the predictive quality. In conclusion, the generated data set can be part wise well approximated by continuous quadratic regression functions. This can also be used to find suitable starting values for a parameter optimization of non-convex problems in order to efficiently determine the optimal values.

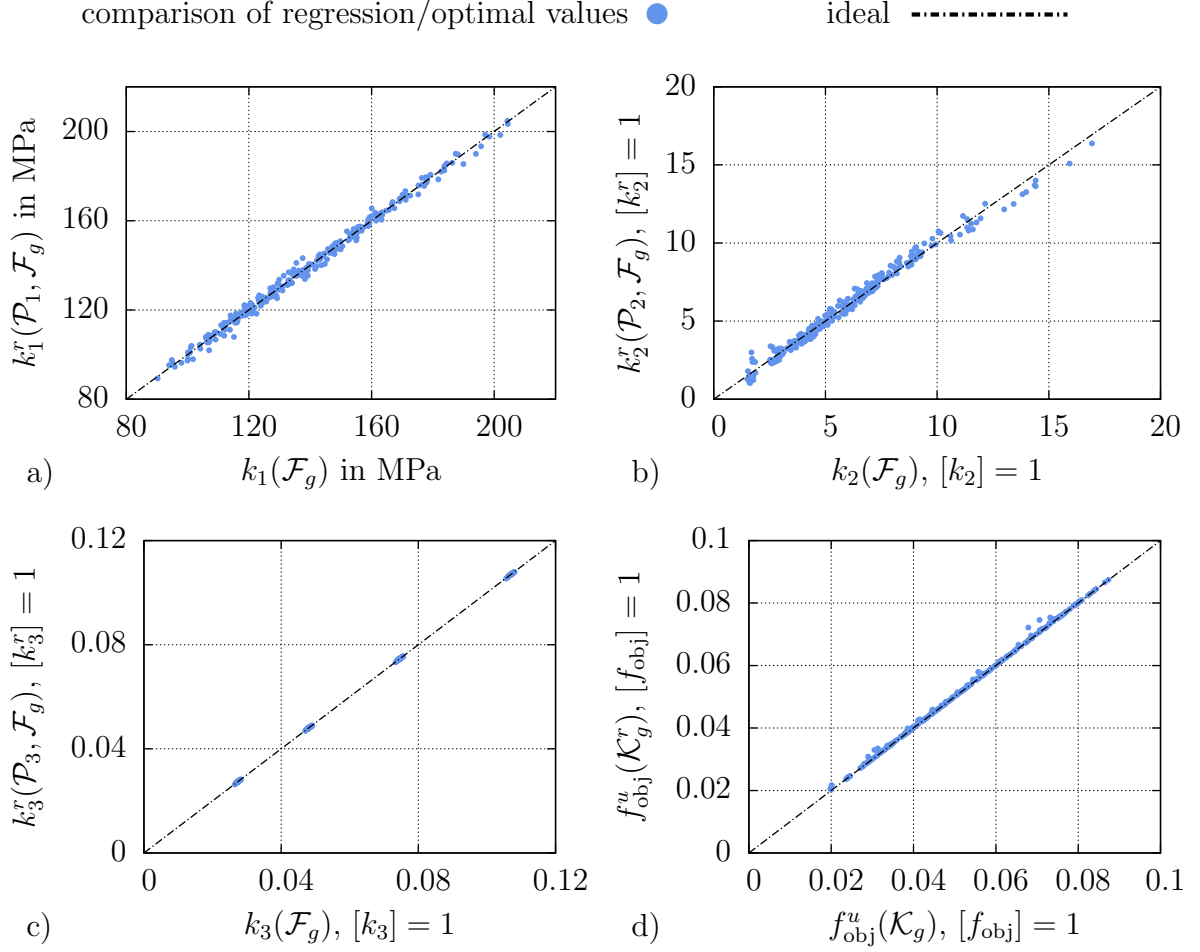


Figure 6.7: a)–c) Comparison of the 256 regression values k_h^r and the optimal values k_h .
 d) Comparison of the error estimates of the stress-strain curves computed based on the regression values ($f_{\text{obj}}^u(\mathcal{K}_g^r)$) and based on the optimal values ($f_{\text{obj}}^u(\mathcal{K}_g)$). In each figure the plotted ideal straight line corresponds to the best possible matches.

6.1.7 Results: Interpolation

All of the previous results strongly suggest the continuous distribution of the data set \mathcal{K} . Having a more or less continuous function is of utmost interest when trying to relate phenomenological to physical parameters. In order to confirm the assumption, let us compare the linearly interpolated parameters $k_h^{\text{Int}}(\mathcal{F}_g^{\text{Int}})$ and optimized parameter triplets $k_h(\mathcal{F}_g^{\text{Int}})$.

In a first step, the phenomenological parameters $k_1^{\text{Int}}, k_2^{\text{Int}}$ and k_3^{Int} are linearly interpolated from the data obtained from the optimization of \mathcal{F} in the previous section for all 1296 members $\mathcal{F}_g^{\text{Int}}$ of \mathcal{F}^{Int} . In a second step, the parameters k_1, k_2 and k_3 were numerically optimized according to Eq. (6.28), again for all 1296 members $\mathcal{F}_g^{\text{Int}}$ of \mathcal{F}^{Int} . The comparison of the interpolated and the optimized data can be found in Figs. 6.8a)–c). As can be seen, only very few points considerably deviate from the ideal line of matching parameters as it was expected. This strongly supports the impression that the phenomenological parameters correlate well with the multiscale parameters. Lastly, in Fig. 6.8d) the objective function values are compared. Using the interpolated triplets $\mathcal{K}_g^{\text{Int}}$ and computing the stress-strain curve $\sigma_{11}^p(\mathcal{K}_g^{\text{Int}})$ will result in an objective function value $f_{\text{obj}}^u(\mathcal{K}_g^{\text{Int}})$. This is to

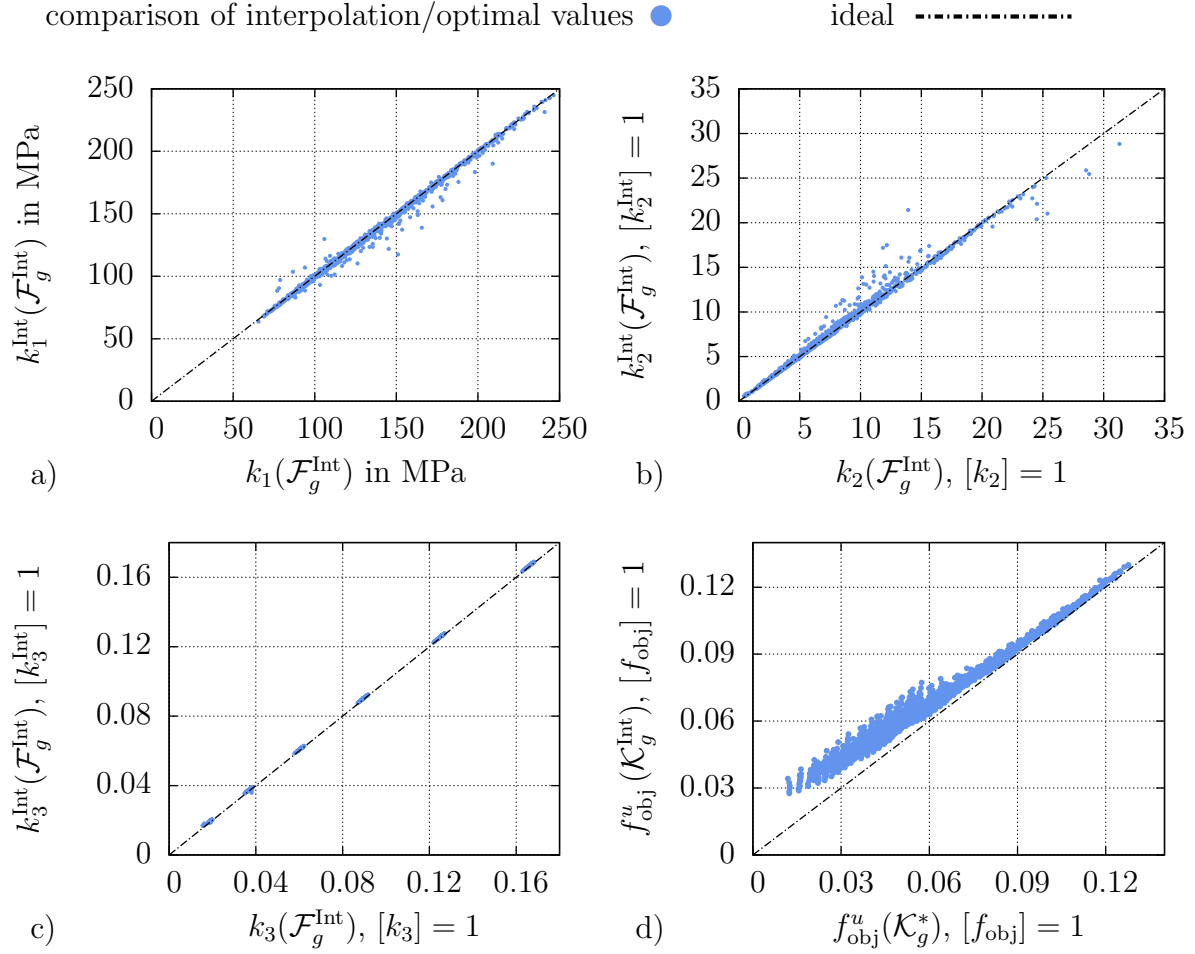


Figure 6.8: a)–c) Comparison of the 1296 interpolated values k_h^{Int} and the optimal values k_h . d) Comparison of the error estimates of the stress-strain curves computed based on the interpolated values ($f_{\text{obj}}^u(\mathcal{K}_g^{\text{Int}})$) and based on the optimal values ($f_{\text{obj}}^u(\mathcal{K}_g^*)$). In each figure the plotted ideal straight line corresponds to the best possible matches.

be compared with the objective function values $f_{\text{obj}}^u(\mathcal{K}_g^*)$ of the associated optimal values \mathcal{K}_g^* and stresses $\sigma_{11}^p(\mathcal{K}_g^*)$. No considerable outliers are visible once again and linear interpolation seems to be a highly appropriate method for the estimation over the complete range of the parameter set $\mathcal{K}(\mathcal{F})$.

6.2 Correlations of Planar Collagen Arrangements Under Biaxial Tension

The following biaxial testing setup and optimization strategies were developed in VON HOEGEN ET AL. [186]. In contrast to the uniaxial setup, a number of n_F fibers is assumed. Here, the modified strain-energies for the biaxial setup are given by

$$W_b^{\text{multi}}(\mathbf{C}, \mathbf{M}) = (1 - V_C)W_{\text{MR}}(\mathbf{C}) + \sum_{a=1}^{n_F=180} V_C^{(a)}W_{\text{multi}}^{(a)}(\mathbf{C}, \mathbf{M}_{(a)}), \quad (6.41)$$

$$W_b^{\text{pheno}} = \begin{cases} W_{b,\text{exp}}^{\text{pheno}}(\mathbf{C}, \mathbf{M}) = (1 - V_C)W_{\text{MR}}(\mathbf{C}) + \sum_{a=1}^{n_F=2} V_C^{(a)}W_{\text{exp}}(\mathbf{C}, \mathbf{M}_{(a)}) & \text{or} \\ W_{b,\text{GST}}^{\text{pheno}}(\mathbf{C}, \mathbf{H}) = (1 - V_C)W_{\text{MR}}(\mathbf{C}) + \sum_{a=1}^{n_F=2} V_C^{(a)}W_{\text{exp}}(\mathbf{C}, \mathbf{H}_{(a)}), & \end{cases} \quad (6.42)$$

where $V_C^{(a)}$ denotes the discrete volume fraction of a specific fiber orientation associated to a structural tensor

$$\mathbf{M}_{(a)} = \mathbf{A}_{(a)} \otimes \mathbf{A}_{(a)} \quad \text{with} \quad \mathbf{A}_{(a)} = (\cos \beta_o^{(a)} \mathbf{e}_1 + \sin \beta_o^{(a)} \mathbf{e}_2) \quad (6.43)$$

and the two-dimensional generalized structural tensor

$$\mathbf{H}_{(a)} = \varsigma \mathbf{1}^* + (1 - 2\varsigma) \mathbf{A}_{(a)} \otimes \mathbf{A}_{(a)} \quad \text{with} \quad \mathbf{1}^* = \mathbf{e}_1 \otimes \mathbf{e}_1 + \mathbf{e}_2 \otimes \mathbf{e}_2 \quad \text{and} \quad \varsigma \in [0, 0.5]. \quad (6.44)$$

The reader is referred to Sec. 5.4 and Appendix C for further information on the concept of generalized structural tensors and the dispersion associated parameter ς . Here, $\beta_o^{(a)}$ denotes the specific fiber angle in the \mathbf{e}_1 - \mathbf{e}_2 plane. In Eq. (6.42) two different cases are distinguished for the phenomenological model. While $W_{b,\text{GST}}$ takes into account the classical structural tensors $\mathbf{M}_{(a)}$, in $W_{b,\text{GST}}$ they are replaced by the generalized tensors $\mathbf{H}_{(a)}$. The concept of generalized tensors has already been explained in Sec. 5.4 and the reader is referred to Appendix C for the derivation of Eq. (6.44). Considering an orthogonal *Cartesian* coordinate system $(\mathbf{e}_1, \mathbf{e}_2, \mathbf{e}_3)$ in tissue reference configuration, collagen fibers are assumed to lie in the fibrous plane spanned by unit vectors \mathbf{e}_1 and \mathbf{e}_2 . The fibrous tissue will be tested under tensile biaxial loading conditions, where the tissue is stretched in the fibrous plane. Testing conditions are displayed in Fig. 6.9. The principal stretches $\lambda_i = 1 + u_i/L_i$ with $i = 1, 2, 3$ directly follow from the deformations u_i and the initial lengths L_i in the corresponding directions. As shown in Eq. (6.45), for the assumed testing conditions the third principal stretch can be directly computed from the incompressibility condition. Then the deformation gradient and the right *Cauchy-Green* tensor follow to

$$\mathbf{F} = \begin{pmatrix} \lambda_1 & 0 & 0 \\ 0 & \lambda_2 & 0 \\ 0 & 0 & \frac{1}{\lambda_1 \lambda_2} \end{pmatrix} \quad \text{and} \quad \mathbf{C} = \begin{pmatrix} \lambda_1^2 & 0 & 0 \\ 0 & \lambda_2^2 & 0 \\ 0 & 0 & \frac{1}{\lambda_1^2 \lambda_2^2} \end{pmatrix}. \quad (6.45)$$

Within the biaxial tension test framework, different stretch ratios are addressed. Depending on the stretches in the two deformation driven directions, the loading angle

$$\alpha = \tan^{-1} \left(\frac{\lambda_2 - 1}{\lambda_1 - 1} \right) \quad (6.46)$$

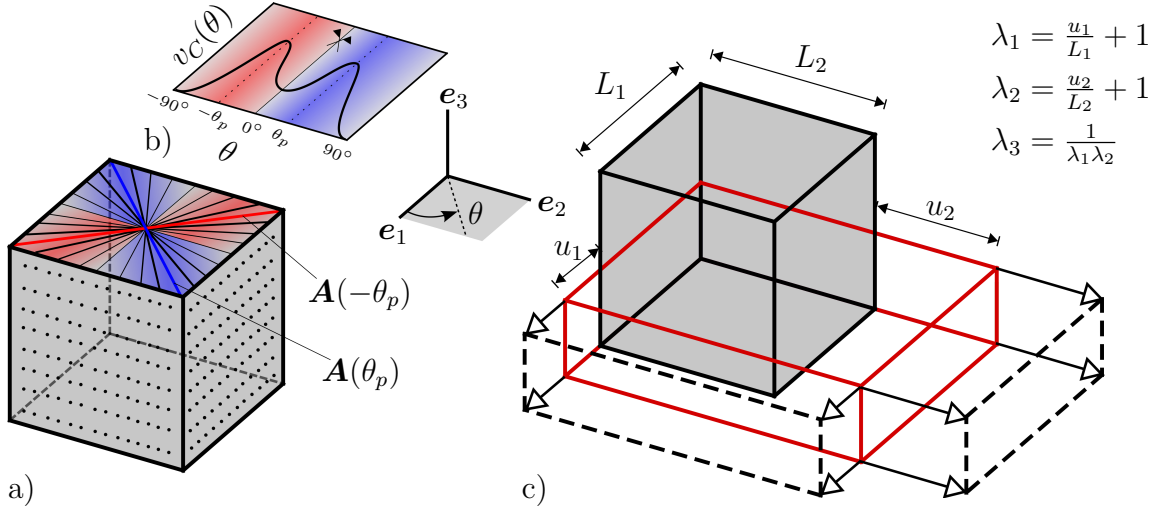


Figure 6.9: a) Planar dispersive fiber arrangement of a tissue sample and b) associated fiber density distribution function. The dispersed fibers are symmetric regarding the axis e_1 . The volume fraction $v_C := v_C(\theta)$ is indicated by the line thickness of $A(\theta)$. c) Biaxial testing conditions.

is conveniently introduced for describing the ratio of the principal stretches λ_1 and λ_2 . The load angle is held constant during each load step in each numerical experiment. Discrete fiber directions $\mathbf{A}_{(a)}$ and volume fractions $V_C^{(a)}$ are invariably arranged symmetrically regarding the e_1 axis. Tissues are often characterized by fibers arranged in a planar dispersive angular pattern, cf. Sec. 2. The dispersive fiber distribution in W_b^{multi} is obtained by introducing a discrete number of $n_F = 180$ fibers, approximating the symmetric and continuous collagen fiber density function $v_C(\theta)$, where θ represents the azimuth angle with respect to e_1 . Addressing $a = 1, \dots, n_F$ discrete fibers it results

$$\beta_o^{(a)} = -\pi/2 + (a-1)\pi/180, \quad (6.47)$$

which defines the orientation of each fiber with a volume fraction equal to

$$V_C^{(a)} = v_C(\beta_o^{(a)})/c_\beta, \quad (6.48)$$

where c_β is a constant identified by enforcing that the discrete distribution, accounting for n_F families, respects the partition of unity, namely $\sum_{a=1}^{n_F} V_C^{(a)}/V_C = 1$. Accordingly, the total collagen volume fraction is given by

$$V_C = \int_{-\pi/2}^{\pi/2} v_C(\theta) d\theta. \quad (6.49)$$

The fiber volume fraction $v_C(\theta)$ is assumed to be distributed symmetrically with regard to the e_1 axis with $\theta = 0^\circ$ and two predominant, dispersed fiber families are considered, cf. Fig. 6.9a) and b). This is indicated by different line thickness in a) and the two peaks in b).

For the considered biaxial loading conditions the benchmark stress tensor reduces to the principal stresses $\sigma_{11}(\lambda_1, \lambda_2)$ and $\sigma_{22}(\lambda_1, \lambda_2)$ in direction of e_1 and e_2 , respectively. However, it needs to be ensured that $\sigma_{33} = 0$. Therefore, from Eq. (6.14) we obtain

$$p = \frac{2(1-V_C)}{\lambda_1^2 \lambda_2^2} \left[c_1 + c_2 (\lambda_1^2 + \lambda_2^2) + \left(c_3 - \frac{\delta}{2} \right) \lambda_1^2 \lambda_2^2 \right] \quad (6.50)$$

for the hydrostatic pressure. The general pattern for the parameter fitting in order to obtain discrete data sets correlating histological dispersion features to phenomenological parameters is summarized in Fig. 6.10.

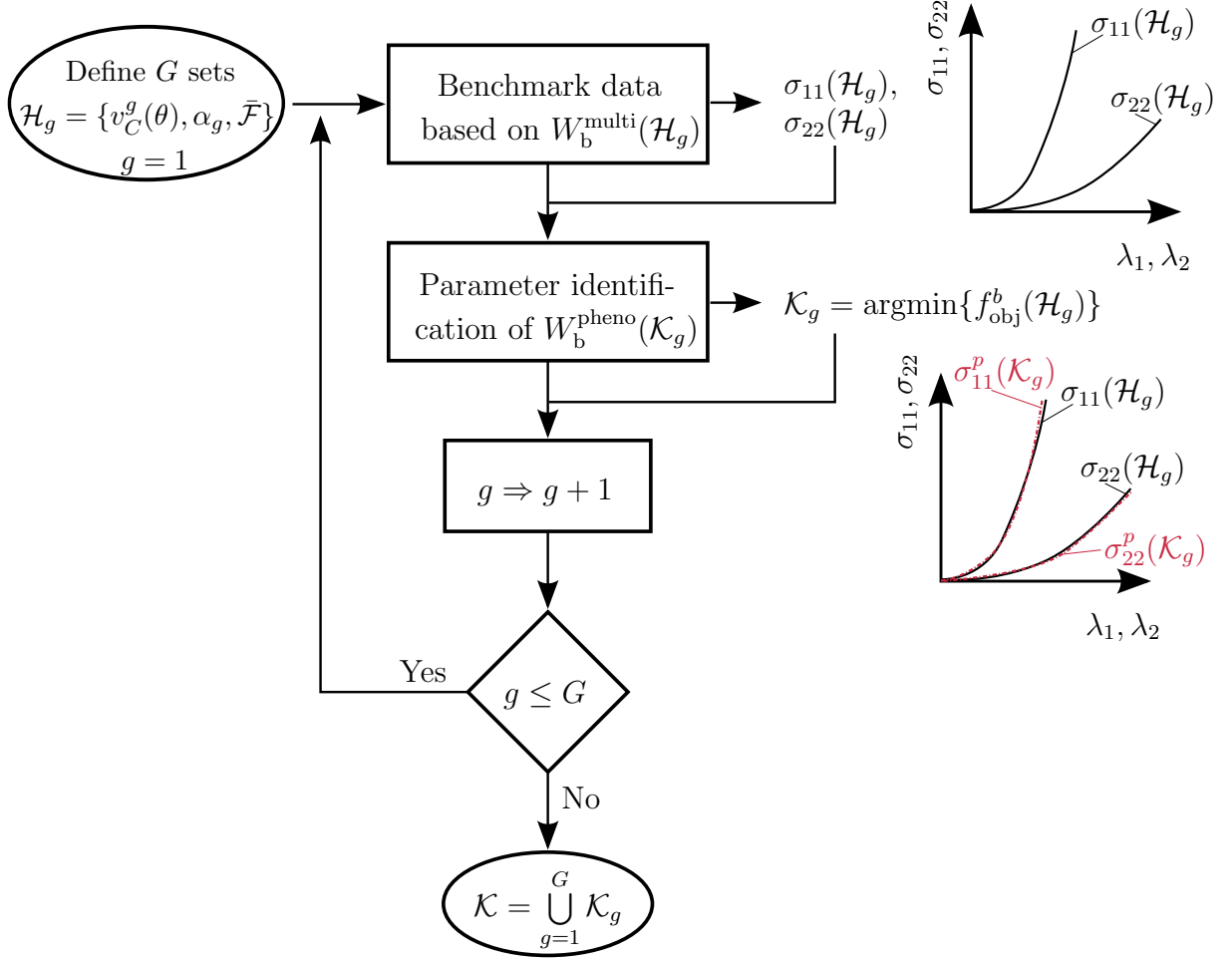


Figure 6.10: Flow chart describing the computation of set $\mathcal{K}(\mathcal{F})$.

6.2.1 Benchmark Data

Benchmark data sets $\boldsymbol{\sigma}(\mathcal{H}_g)$ are computed based on the introduced multiscale approach W_b^{multi} . A set $\mathcal{H}_g = \{v_C^g(\theta), \alpha_g, \bar{\mathcal{F}}\}$ consists of a specific fiber density distribution $v_C^g(\theta)$ and a load angle α_g . Furthermore, only the structural reference parameters $\mathcal{F}_g = \bar{\mathcal{F}}$ of the multiscale model according to Tab. 6.3 are considered for each fiber in each example in the following. In order to study the influence of the dispersive fiber arrangement on estimated parameters k_1 , k_2 and k_3 , it is meaningful to vary the underlying distribution $v_C^g(\theta)$. The analysis is restricted to a symmetric von Mises distribution, where

$$v_C^g(\theta) = \frac{V_C}{2} \left(\frac{\exp\{b \cos[2(\theta - \varpi)]\}}{2\pi I_0(b)} + \frac{\exp\{b \cos[2(\theta + \varpi)]\}}{2\pi I_0(b)} \right). \quad (6.51)$$

The parameter b is called concentration parameter while ϖ roughly defines the peak location and $I_0(b)$ denotes the modified *Bessel* function of order zero. A concentration parameter $b = 0$ would result in a uniform distribution, referring to the case of maximal

dispersion. With increasing values of b , the level of dispersion will decrease. In the spirit of the uniaxial tests, the experimental data reported in SCHRIEFL ET AL. [149] is chosen for defining a reference orientation distribution $\bar{v}_C(\theta)$. Therefore, the values \bar{b} and $\bar{\varpi}$ in Eq. (6.51) have been identified in order to obtain the best fitting (in a least-square sense) of the reference function $\bar{v}_C(\theta)$ to the experimental measurements. It is meaningful to characterize the distribution function for later comparison in terms of the following scalar quantities:

1. the peak angles $\pm\theta_p$, such that

$$\theta_p(v_C(\theta)) = \operatorname{argmax}(v_C(\theta)), \quad (6.52)$$

2. the mean angle θ_m , defined as

$$\theta_m(v_C(\theta)) = \frac{2}{V_C} \int_0^{\pi/2} v_C(\theta) \theta \, d\theta, \quad (6.53)$$

3. the variance Var with respect to the mean angle, defined as

$$\operatorname{Var}(v_C(\theta)) = \frac{2}{V_C} \int_0^{\pi/2} v_C(\theta) (\theta_m - \theta)^2 \, d\theta. \quad (6.54)$$

The obtained function $\bar{v}_C(\theta)$, characterized by peak and mean angles $\bar{\theta}_p$ and $\bar{\theta}_m$, respectively, as well as variance $\overline{\operatorname{Var}}$ is shown in Fig. 6.11. The associated parameters and characteristic values are given in Tab. 6.4.

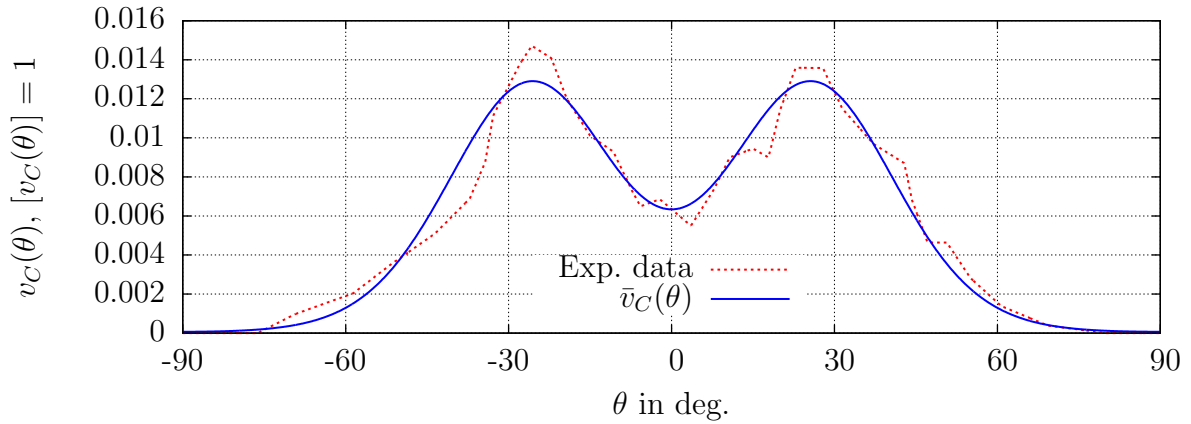


Figure 6.11: Experimentally measured fiber distribution from SCHRIEFL ET AL. [149] and the adjusted, symmetric distribution $\bar{v}_C(\theta)$ obtained with help of Eq. (6.51).

Table 6.4: Parameters of the fiber distribution $\bar{v}_C(\theta)$ depicted in Fig. 6.11.

$\bar{\varpi}$ in deg.	\bar{b} [\bar{b}] = 1	$\bar{\theta}_p$ in deg.	$\bar{\theta}_m$ in deg.	$\sqrt{\overline{\operatorname{Var}}}$ in deg.
25.90	3.65	25.78	26.83	14.94

Only the loading angle α , defining the ratio of λ_1 and λ_2 (see Eq. (6.46)) and the assumed underlying fiber orientation $v_C^g(\theta)$ will be varied. In case of the latter, it seems plausible to use the already introduced variance \mathbf{Var} and the mean angle θ_m as comparative criteria. Modification of the fiber distribution function is then effectively managed within the following scenario:

- **Assign a Mean Angle $\hat{\theta}_m$ and Variance $\widehat{\mathbf{Var}}$ to $v_C^g(\theta)$**

A modified volume fraction distributions $v_C^g(\theta)$ is built, such that user defined values $\hat{\theta}_m$ and $\widehat{\mathbf{Var}}$ for the mean angle $\theta_m(v_C^g(\theta))$ and variance $\mathbf{Var}(v_C^g(\theta))$ are present. The realization of the described scenario is presented in Tab. 6.5. In a first step, the auxiliary distribution $v_{\text{aux}}(\theta)$ is introduced, where the concentration parameter b and angle ϖ are regarded as free parameters, which are to be optimized. Both b and ϖ in $v_{\text{aux}}(\theta)$ will be iterated to fit the specifically chosen values for $\hat{\theta}_m$ and $\widehat{\mathbf{Var}}$. This is facilitated in an optimization problem $\min[(\theta_m(b, \varpi) - \hat{\theta}_m)^2 + (\mathbf{Var}(b, \varpi) - \widehat{\mathbf{Var}})^2]$ which is solved for $b = b_{\min}$ and $\varpi = \varpi_{\min}$. In order to guarantee a fair comparison, the total volume fraction associated with the new distribution $v_C^g(\theta)$ shall remain constant to the original value V_C , namely

$$V_C(v_C^g) = \int_{-\pi/2}^{\pi/2} v_C^g(\theta) d\theta = V_C(\bar{v}_C). \quad (6.55)$$

Therefore, $v_{\text{aux}}(\theta)$ needs to be scaled by the factor V_{aux}/V_C . Here, V_{aux} denotes the total volume fraction of $v_{\text{aux}}(\theta)$.

<ul style="list-style-type: none"> • Goal: $\theta_m(v_C^g(\theta)) = \hat{\theta}_m \quad \text{and} \quad \mathbf{Var}(v_C^g(\theta)) = \widehat{\mathbf{Var}}$ <ul style="list-style-type: none"> • Define: $v_{\text{aux}}(\theta, b, \varpi) = \frac{V_C}{2} \left(\frac{\exp\{b \cos[2(\theta - \varpi)]\}}{2\pi I_0(b)} + \frac{\exp\{b \cos[2(\theta + \varpi)]\}}{2\pi I_0(b)} \right)$ <ul style="list-style-type: none"> • Compute: $[b_{\min}, \varpi_{\min}] = \operatorname{argmin} \left\{ [\theta_m(b, \varpi) - \hat{\theta}_m]^2 + [\mathbf{Var}(b, \varpi) - \widehat{\mathbf{Var}}]^2 \right\}$ $V_{\text{aux}} = \int_{-\pi/2}^{\pi/2} v_{\text{aux}}(\theta, b_{\min}, \varpi_{\min}) d\theta$ $v_C^g(\theta) = v_{\text{aux}}(\theta, b_{\min}, \varpi_{\min}) \frac{V_{\text{aux}}}{V_C}$

Table 6.5: Algorithmic box describing the computation of $v_C^g(\theta)$.

6.2.2 Parameter Identification

In the following, we aim to fit the described phenomenological strain-energy function W_b^{pheno} to the results of the benchmark data under biaxial, deformation driven loading.

Two fiber families (i.e., $n_F = 2$) with mechanically identical properties

$$\mathcal{K}_g = \mathcal{K}_g^{(1)} = \mathcal{K}_g^{(2)} = \begin{cases} \{k_1, k_2, k_3, \beta_f\} & \text{if } W_b^{\text{pheno}} = W_{b,\text{exp}}^{\text{pheno}} \\ \{k_1, k_2, k_3, \varsigma, \beta_f\} & \text{if } W_b^{\text{pheno}} = W_{b,\text{GST}}^{\text{pheno}} \end{cases} \quad (6.56)$$

and symmetrical fiber arrangement (i.e., $\beta_f = \beta_f^{(1)} = -\beta_f^{(2)}$) are considered with

$$\mathbf{A}_{(1)} = \begin{pmatrix} \cos \beta_f \\ \sin \beta_f \\ 0 \end{pmatrix} \quad \text{and} \quad \mathbf{A}_{(2)} = \begin{pmatrix} \cos(-\beta_f) \\ \sin(-\beta_f) \\ 0 \end{pmatrix}. \quad (6.57)$$

In order to find the optimal parameters of \mathcal{K}_g within a numerical optimization scheme, we define the objective function

$$f_{\text{obj}}^b = \mathcal{E}^{(11)} + \mathcal{E}^{(22)}, \quad (6.58)$$

where $\mathcal{E}^{(11)}$ denotes the error regarding σ_{11} and $\mathcal{E}^{(22)}$ the error regarding σ_{22} . The two error functions

$$\begin{aligned} \mathcal{E}^{(11)}(\mathcal{K}_g, \mathcal{H}_g) &= \sqrt{\frac{1}{N} \sum_{n=1}^N \frac{\|\sigma_{11}(\mathcal{H}_g, \lambda_1^n) - \sigma_{11}^p(\mathcal{K}_g, \lambda_1^n, \alpha_g)\|^2}{[\sigma_{11}(\mathcal{H}_g, \lambda_1^{\max})]^2}} \\ \mathcal{E}^{(22)}(\mathcal{K}_g, \mathcal{H}_g) &= \sqrt{\frac{1}{N} \sum_{n=1}^N \frac{\|\sigma_{22}(\mathcal{H}_g, \lambda_1^n) - \sigma_{22}^p(\mathcal{K}_g, \lambda_1^n, \alpha_g)\|^2}{[\sigma_{22}(\mathcal{H}_g, \lambda_1^{\max})]^2}}, \end{aligned} \quad (6.59)$$

are used for one specific load angle α and one specific density function $v_C^g(\theta)$. The *Cauchy*-stress components obtained employing the phenomenological description W_b^{pheno} are labeled with σ_{11}^p and σ_{22}^p . Moreover, recall from the previous subsection that σ_{11} and σ_{22} denote the *Cauchy*-stresses of the benchmark data. The relation of the stretches λ_1^n and λ_2^n is directly obtained with help of the load angle α , see Eq. (6.46). Here, a total number of $N = 100$ measuring points is taken, for which the stresses are evaluated. To this aim, referring to N values of stretch we have $\lambda_1^n \in [1, \lambda_1^{\max}]$ with $n = 1 \dots N$ and $\lambda_1^N = \lambda_1^{\max}$. The value λ_1^{\max} refers to the maximum stretch which is applied. Throughout this study, the maximum stretch is defined through

$$\lambda_1^{\max} = \begin{cases} 1.2 & \text{if } \alpha \leq 45^\circ \\ \frac{1.2-1}{\tan \alpha} + 1 & \text{if } \alpha > 45^\circ. \end{cases} \quad (6.60)$$

Measuring points are defined in terms of evenly spaced stretches λ_1^n . The identification of constitutive parameters \mathcal{K}_g from structural features $v_C^g(\theta)$ in a numerical way is conducted, introducing the optimization problem

$$\mathcal{K}_g(\mathcal{H}_g) = \operatorname{argmin}\{f_{\text{obj}}^b(\mathcal{H}_g)\}. \quad (6.61)$$

The optimization problem allows to find a relationship between the phenomenological parameters and the considered loading angle as well as the underlying fiber orientation $v_C^g(\theta)$ for the computation of the benchmark data stresses σ_{11} and σ_{22} . Since it is impossible to find an analytical solution for this relationship the minimization problem is only solved for a discrete number of experimental tests. Again, the parameter fitting is performed with help of a Sequential Quadratic Programming (SQP) algorithm for nonlinear numerical constrained optimization problems implemented in *MATLAB*. The gradient needed for the optimization procedure is calculated based on a finite difference scheme.

6.2.3 Regression Function for the Variance

The optimization scheme described in Eqs. (6.58) and (6.61) leads to discrete data sets involving the variance and the mean angle of the fiber distribution on the one hand and the optimized material parameters \mathcal{K}_g on the other hand. In the course of this section, it will be shown that based on the presented numerical results it is meaningful to apply a regression function

$$\sqrt{\text{Var}_r} = b_0 + b_1\theta_m + b_2\varsigma + b_{12}\theta_m\varsigma + b_{11}\theta_m^2 + b_{22}\varsigma^2 \quad (6.62)$$

for the standard deviation. The regression function specifically addresses pairs $\{\theta_m, \varsigma\}$ with $\varsigma \in \mathcal{K}_g$ of function $W_{\text{b,GST}}^{\text{pheno}}$. Considering the set of regression parameters

$$\mathcal{P} = \{b_0, b_1, b_2, b_{12}, b_{11}, b_{22}\}, \quad (6.63)$$

incorporating six elements leads to the optimization problem

$$\mathcal{P} = \text{argmin}\{f_{\text{obj}}^r\}. \quad (6.64)$$

The associated objective function of the optimization problem is defined through

$$f_{\text{obj}}^r(\mathcal{P}) = \sqrt{\frac{1}{G} \sum_{g=1}^G \frac{\|\sqrt{\text{Var}}(\mathcal{H}_g) - \sqrt{\text{Var}_r}(\mathcal{P}, \theta_m, \varsigma)\|^2}{\max_{g=1\dots G} \sqrt{\text{Var}}(\mathcal{H}_g)}}, \quad (6.65)$$

where the known discrete values Var and θ_m of v_C^g are used. In line with linear least-square regression fitting, the problem is a convex optimization problem and is solved by means of a QR decomposition algorithm in *MATLAB* [180]. A total number of $G = 63$ discrete values is considered in the following.

6.2.4 Results: Inverse Identification of the Fiber Mean Angle

In the following, a strategy to estimate the characteristic value θ_m from biaxial material tests in the absence of histological data is demonstrated. In that regard, parameters of $W_{\text{b}}^{\text{pheno}}$ are fitted to the biaxial stress-strain curves of the multiscale model $W_{\text{b}}^{\text{multi}}$. In doing so, different load angles α and fiber orientation distributions v_C^g are considered. Fig. 6.12a)–c) shows the optimized parameters of $W_{\text{b,exp}}^{\text{pheno}}$ for three different load angles in case that the fiber distribution is varied. Specifically, the variance is varied while $\theta_m = \bar{\theta}_m = 26.83^\circ$ is the same for each distribution. The corresponding parameters of the von Mises distributions are listed Appendix D in Tab. D.2. While the load angle has a significant influence on the optimized parameters k_1 , the influence on k_2 and k_3 is less distinct. In case that $\alpha = 45^\circ$ the parameters k_1 , k_2 and k_3 are independent of the variance Var and only the fiber angle β_f is affected. However, the optimized fiber angle β_f of a non-dispersed distribution remains completely independent of the load angle α . As can also be seen in Fig. 6.12d), only in case that the mean angle coincides with the load angle, i.e. $\alpha = \bar{\theta}_m = \theta_m$, the optimized angle β_f deviates less than 1° from the mean angle, independently from the level of dispersion. As an inverse relation between the mean angle θ_m and the optimized fiber angle β_f , it is suspected that $\theta_m \approx \alpha$ if $\beta_f = \alpha$. In order to verify this statement, we choose additional underlying fiber distributions which are presented in Fig. 6.13a). The parameters ϖ and b in Eq. (6.51) were optimized such that we obtain a

specified mean angle θ_m and variance Var , displayed in Fig. 6.13b). The specific parameter values are listed in Appendix D in Tab. D.3. The results in Fig. 6.14 confirm that β_f and α coincide, if $\theta_m = \alpha$, independently of the amount of Var . This can be considered as the desired inverse relationship between one specific structural parameter and the mean angle of the fiber distribution.

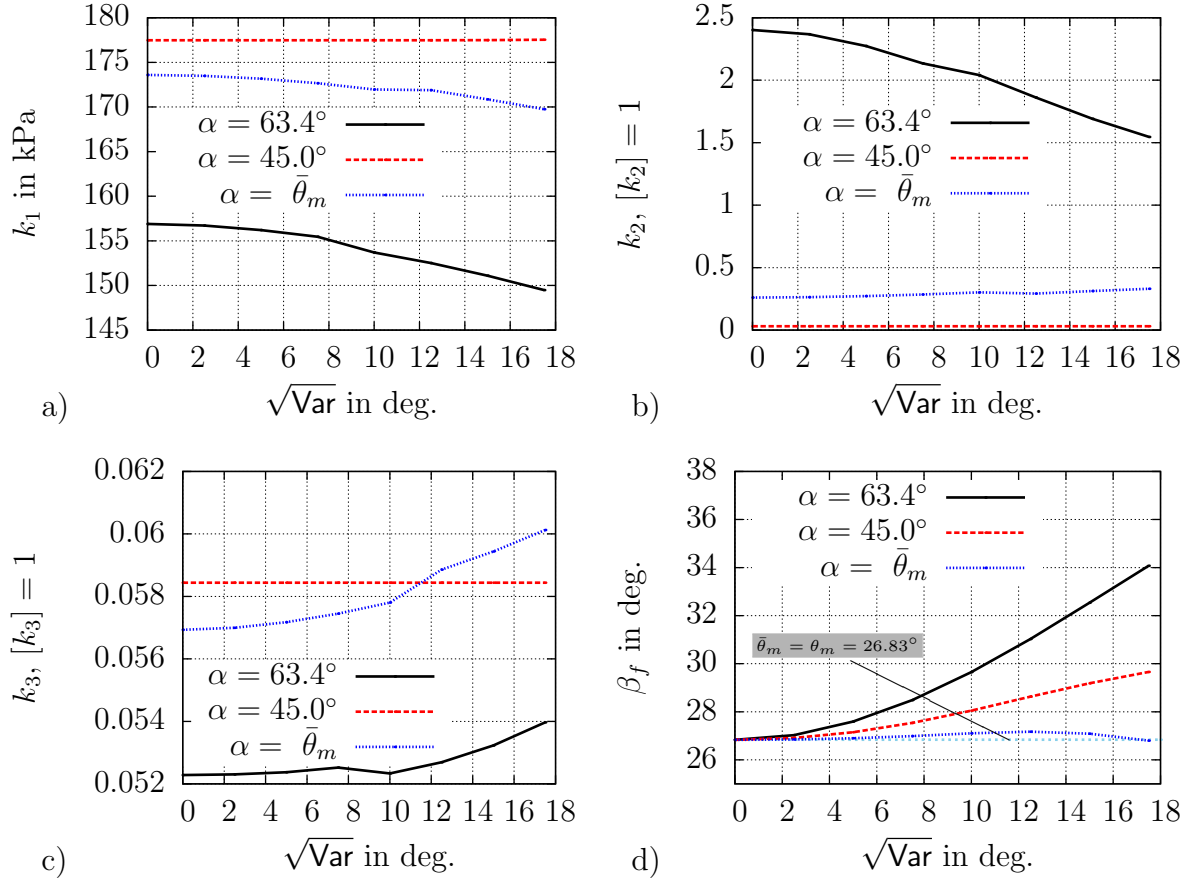


Figure 6.12: Evolution of k_1 , k_2 , k_3 and β_f over the standard deviation $\sqrt{\text{Var}}$. The mean angle of each underlying fiber distribution is equal to $\theta_m = \bar{\theta}_m = 26.83^\circ$ and three different load angles are applied. The energy density $W_b^{\text{pheno}} = W_{b,\text{exp}}^{\text{pheno}}$ is chosen.

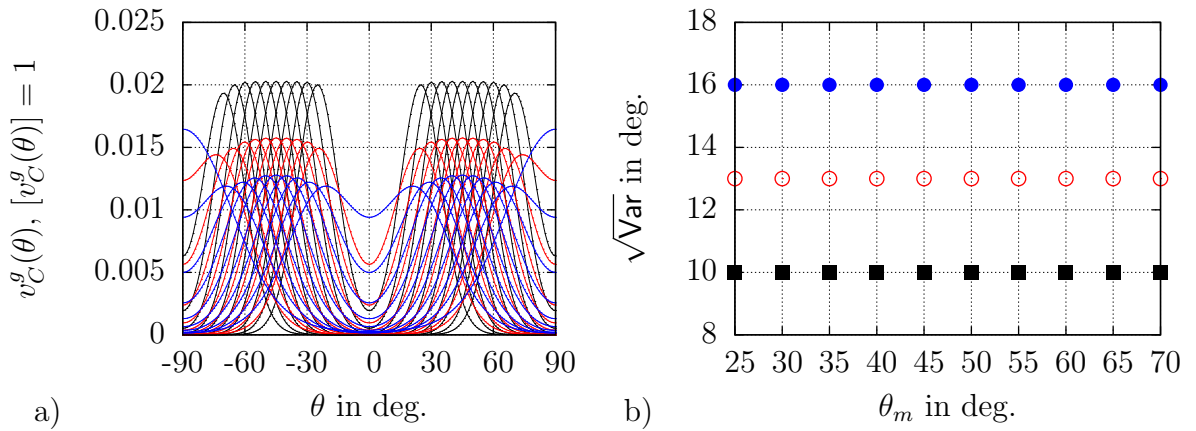


Figure 6.13: a) Different generated fiber volume fraction distributions v_C^g and b) corresponding $\sqrt{\text{Var}}$ and θ_m values.

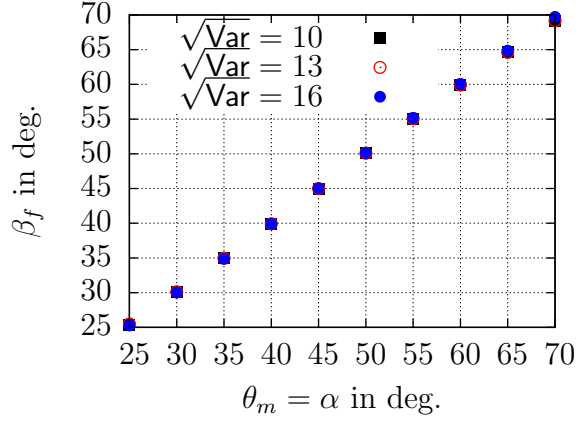


Figure 6.14: Evolution of $\beta_f^{(1)}$ over the mean angle. The fiber volume fraction distributions were chosen according to Fig. 6.13. The load angle α is chosen to coincide with θ_m in each case.

6.2.5 Results: Inverse Identification of the Variance as a Measure of Fiber Dispersion

In the next step, we want to show how to quantify the level of dispersion, i.e. $\sqrt{\text{Var}}$, from biaxial material testing. In order to do so, the concept of generalized structural tensors and the strain energy $W_b^{\text{pheno}} = W_{b,\text{GST}}^{\text{pheno}}$ is applied. From a theoretical point of view, the parameter ζ should be directly associated to the level of fiber dispersion. However, in the considered biaxial setup some limitations in view of the parameter optimization need to be clarified. Let the two-dimensional generalized structural tensor

$$\mathbf{H} = (1 - \zeta)\mathbf{I}^* + \zeta\mathbf{A} \otimes \mathbf{A} = \begin{pmatrix} a & c & 0 \\ c & 1 - a & 0 \\ 0 & 0 & 0 \end{pmatrix} \quad \text{with} \quad \text{tr } \mathbf{H} = 1 \quad (6.66)$$

be given, where $a \geq 0$ and c are arbitrary values. Recalling from Eq. (6.43) that $\mathbf{A} = \cos \beta_f \mathbf{e}_1 + \sin \beta_f \mathbf{e}_2$, one may find the relations

$$\begin{aligned} a &= \zeta + (1 - 2\zeta) \cos^2 \beta_f, \\ 1 - a &= \zeta + (1 - 2\zeta) \sin^2 \beta_f, \\ c &= (1 - 2\zeta) \sin \beta_o \cos \beta_f. \end{aligned} \quad (6.67)$$

The first and the second line are linear dependent. In the framework of a shear free biaxial test, the transversely isotropic invariant results in $\mathbf{C} : \mathbf{H} = a\lambda_1^2 + (1 - a)\lambda_2^2$ with \mathbf{C} according to Eq. (6.45). Due to the discovered linear dependency there exists an infinite number of pairs of $\{\zeta, \beta_f\}$ that result in identical invariant values $\mathbf{C} : \mathbf{H}$. In the special case that $\beta_f = 45^\circ$, it immediately follows that $a = 1 - a = 0.5$. The latter is completely independent of ζ . Thus, in a parameter optimization scheme random values of ζ yield identical results. In any other case, rather the relationship of ζ and β_f is fitted than actually meaningful values.

The fitting to shear tests would overcome this problem, since also the non-diagonal terms of \mathbf{C} and \mathbf{H} would be of importance. However, due to the technical difficulties in performing shear tests of soft-biological tissues this case is more or less irrelevant in practice. Having developed an estimate of the mean angle previously, it is reasonable to consider

θ_m to be known and to predefine $\beta_f = \theta_m$. In that way, it is ensured that ς takes a unique value and the set of parameters to be optimized reduces to

$$\mathcal{K}_g(W_{b,\text{GST}}^{\text{pheno}}) = \{k_1, k_2, k_3, \varsigma\}. \quad (6.68)$$

To find an inverse relationship for the variance, a number of 63 fiber distributions, generated according to Tab. 6.5, are considered. Pairs of (θ_m, Var) are chosen in the range of

$$\theta_m \in [25^\circ, 70^\circ] \quad \text{and} \quad \sqrt{\text{Var}} \in [2.5, 17.5]. \quad (6.69)$$

Specific values of b and ϖ are listed for all 63 distributions in Tab. D.4 and D.5 in Appendix D. Please note that the structure of the assumed fiber density distribution in Eq. (6.51) does not allow for very high variances for a mean angle close to 0° or 90° . The load angle α is equal to 45° in each numerical experiment. The optimized values of ς for all distributions are plotted in Fig. 6.15 over $\sqrt{\text{Var}}$. For small values of $\sqrt{\text{Var}}$ there is a clear correlation to ς . However, as can be seen for an increasing level of dispersion, the value of ς also depends on the mean angle θ_m . This is due to the construction of the fiber distributions involving two superimposed von Mises distributions, see Eq. (6.51) and it justifies the form of the regression function in Eq. (6.65) which involves both ς and θ_m . The obtained regression parameters \mathcal{P} of the optimization problem in Eq. (6.64) are reported in Tab. 6.6. As can be seen, the magnitudes of b_2 and b_{22} which are multiplied with ς and ς^2 , respectively, are much larger. This indicates a strong dependency of the variance on ς and a low dependency on θ_m . The estimates of the regression values $\sqrt{\text{Var}}_r$ are compared with the (optimal) values $\sqrt{\text{Var}}$ in Fig. 6.15b) showing a good matching in general. Thus, the conceived regression function in Eq. (6.62) serves as an inverse tool to define the level of dispersion.

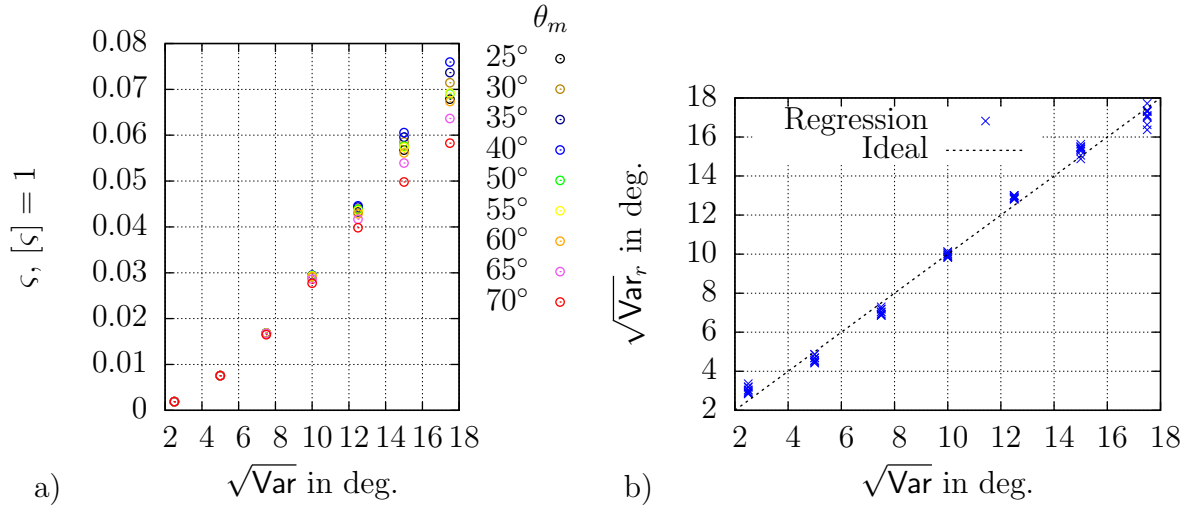


Figure 6.15: Inverse analysis of the variance in biaxial tests. a) Optimal values of ς over the standard deviation $\sqrt{\text{Var}}$ for 63 generated fiber distributions $v_C^g(\theta)$. Mean angles θ_m are assigned according to the legend. A loading angle $\alpha = 45^\circ$ is applied and the fiber angle is excluded from the optimization with $\beta_f = \theta_m$ in $W_{b,\text{GST}}^{\text{pheno}}$. b) Verification of the linear regression fitting. Regression function values $\sqrt{\text{Var}}_r$ are plotted over the ideal values $\sqrt{\text{Var}}$ of $v_C^g(\theta)$.

Table 6.6: Optimal regression parameters \mathcal{P} in Eq. (6.62) from the optimization problem in Eq. (6.64). The parameters are optimized based on the data presented in Fig. 6.15a) and serve to compute the regression function values $\sqrt{\text{Var}_r}$ in Fig. 6.15b).

b_0 in deg.	b_1 [b_1] = 1	b_2 in deg.	b_{12} [b_{12}] = 1	b_{11} in 1/deg.	b_{22} in deg.
4.5072	-0.0884	264.4547	0.5057	$8.8515 \cdot 10^{-4}$	-1089.95

7 Incorporation of Residual Stress/Strain

As explained in Sec. 2.3, residual stresses are present in (almost) all biological tissues. Here, the focus is on arterial walls. Mechanical testing of excised tissue stripes as considered in the previous chapter cannot account for this material characteristic since cutting of the samples releases the residual stresses. The discussed approaches in the following are based on modifications of the general numerical framework introduced in SCHRÖDER AND BRINKHUES [150]. Therefore, the residual stresses or strains are estimated from the current loading state and incorporated subsequently. This concept allows to use material parameters from experiments, which were carried out ex-vivo.

7.1 Material Models for Arterial Walls

For the numerical analysis two different transversely isotropic strain-energy functions are used. The first one is polyconvex and based on the right *Cauchy-Green* tensor:

$$W_{\mathbf{C}}(\mathbf{C}, \mathbf{M}_{(1)}, \mathbf{M}_{(2)}) = W_{\text{MR}}(\mathbf{C}) + W_{\text{Pen}}(\mathbf{C}) + \sum_{a=1}^2 W_{\text{HGO}}(\mathbf{C}, \mathbf{M}_{(a)}). \quad (7.1)$$

It comprises of the isotropic *Mooney-Rivlin* type model

$$W_{\text{MR}} = c_1 I_1^{\mathbf{C}} + c_2 I_2^{\mathbf{C}} + c_3 I_3^{\mathbf{C}} - \delta \log \sqrt{I_3^{\mathbf{C}}}, \quad (7.2)$$

the penalty function

$$W_{\text{Pen}} = \frac{\kappa_{\text{Pen}}}{2} (I_3^{\mathbf{C}} - 1)^2 \quad (7.3)$$

and two superimposed transversely isotropic energy-densities

$$W_{\text{HGO}} = \begin{cases} \frac{\mu_1}{2k_1} \left\{ \exp \left[k_1 \underbrace{(\mathbf{C} : \mathbf{M}_{(a)})}_{I_4^{\mathbf{C}^1}} - 1 \right] - 1 \right\} & \text{if } \mathbf{C} : \mathbf{M}_{(a)} = \|\mathbf{F}\mathbf{A}_{(a)}\|^2 \geq 1 \\ 0 & \text{if } \mathbf{C} : \mathbf{M}_{(a)} = \|\mathbf{F}\mathbf{A}_{(a)}\|^2 < 1, \end{cases} \quad (7.4)$$

according to HOLZAPFEL ET AL. [77], which display exponential strain hardening. For $\delta = 2c_1 + 4c_2 + 2c_3$ the material response becomes stress-free in the reference configuration with $\mathbf{C} = \mathbf{1}$, where c_1, c_2, c_3 as well as κ_{Pen} denote additional stress-like material parameters. A large penalty parameter κ_{Pen} effects quasi-incompressible material behavior. The definitions of the principal invariants $I_1^{\mathbf{C}}, I_2^{\mathbf{C}}$ and $I_3^{\mathbf{C}}$ have already been introduced in Eq. (3.78). Further, μ_1 is a stress-like and k_1 a dimensionless material parameter associated to W_{HGO} . The anisotropic part of the strain-energy incorporates a tension compression switch based on the squared stretch in fiber direction $\mathbf{C} : \mathbf{M}_{(a)}$. That means compressed or shortened fibers are excluded from the constitutive material response. The function is not continuous because in the absence of a switching criterion the analytical tangent $\partial^2 W_{\text{HGO}} / \partial \mathbf{C} \partial \mathbf{C} \neq \mathbf{0}$ for $\mathbf{C} : \mathbf{M}_{(a)} = 1$.

As a second choice, the strain-energy

$$W_{\mathbb{H}}(\log \mathbf{U}, \mathbf{M}_{(1)}, \mathbf{M}_{(2)}) = W_{\text{eH}}(\log \mathbf{U}) + \sum_{a=1}^2 W_{\text{SHN}}(\log \mathbf{U}, \mathbf{M}_{(a)}) \quad (7.5)$$

is employed. It is solely based on the *Hencky* strain measure and similarly to $W_{\mathbb{C}}$ it is split into an isotropic and an anisotropic part. It consists of the isotropic exponentiated *Hencky*-energy

$$W_{\text{eH}}(\log \mathbf{U}) = \frac{\mu}{k} \exp [k \|\text{dev} \log \mathbf{U}\|^2] + \frac{\kappa}{2\hat{k}} \exp \left\{ \hat{k} [\text{tr}(\log \mathbf{U})]^2 \right\} \quad (7.6)$$

introduced in NEFF ET AL. [124], where μ and κ are the infinitesimal shear and compression moduli and k and \hat{k} are dimensionless strain stiffening parameters. Regarding the anisotropic part, again two superimposed transversely isotropic functions

$$W_{\text{SHN}} = \begin{cases} \frac{\mu_1}{2k_1} \left\{ \exp \left[k_1 \underbrace{(\log \mathbf{U} : \mathbf{M}_{(a)})^\varepsilon}_{I_4^{\text{H}^1}} \left[\underbrace{(\log \mathbf{U})^2 : \mathbf{M}_{(a)}}_{I_4^{\text{H}^2}} \right]^2 \right] - 1 \right\} & \text{if } \log \mathbf{U} : \mathbf{M}_{(a)} \geq 0 \\ 0 & \text{if } \log \mathbf{U} : \mathbf{M}_{(a)} < 0 \end{cases} \quad (7.7)$$

are considered as recently proposed in SCHRÖDER ET AL. [157]. The switching criterion is based on the logarithmic invariant $I_4^{\text{H}^1} = \log \mathbf{U} : \mathbf{M}$ and therefore different from the one in W_{HGO} in Eq. (7.4). However, recalling the fundamental inequality

$$\mathbf{C} : \mathbf{M}_{(a)} - 1 \geq \log \mathbf{U} : \mathbf{M}_{(a)} \quad \text{for } \mathbf{C} : \mathbf{M}_{(a)} \geq 1 \quad (7.8)$$

derived earlier in Eq. (3.89), it is ensured that physically compressed/shortened fibers are excluded from the constitutive response. The transition zone of both switching criteria marked in Fig. 3.4 can be somehow regarded as an initial fiber crimp, delaying the distortion dependent capability of fibers to carry loads. The part $(\log \mathbf{U} : \mathbf{M}_{(a)})^\varepsilon$, which is multiplied to the governing invariant $I_4^{\text{H}^2} = (\log \mathbf{U})^2 : \mathbf{M}_{(a)}$ in order to guarantee a continuous function, precludes jumps at switch over points $\log \mathbf{U} : \mathbf{M}_{(a)} = 0$. For all numerical examples in the further course ε is set to 10^{-8} . In contrast to W_{HGO} , the function W_{SHN} is continuously differentiable because at the switching points the tangent results in $\partial^2 W_{\text{SHN}} / \partial \mathbf{C} \partial \mathbf{C} = \mathbf{0}$ if $\log \mathbf{U} : \mathbf{M}_{(a)} = 0$.

7.2 Adjustment to Experiments of Excised Tissue Samples

The above defined strain-energies $W_{\mathbb{C}}$ and $W_{\mathbb{H}}$ are fitted to uniaxial tension tests on human abdominal aorta performed in HOLZAPFEL [72]. Due to the fact that the female donate was 80 years old, the material response can be expected to be relatively stiff. Excised tissue samples of the media and the adventitia were loaded in longitudinal (\mathbf{e}_z) and circumferential (\mathbf{e}_Φ) direction. The testing procedure and material directions are depicted in Fig. 7.1. The third axis of the local cylindrical coordinate system is determined by the radial direction \mathbf{e}_r . The two considered fiber families $\mathbf{A}_{(1)}$ and $\mathbf{A}_{(2)}$ are assumed to be arranged crosswise helically along the axial direction in the \mathbf{e}_Φ - \mathbf{e}_z plane. Thus, for the tested samples the preferred directions are given by

$$\mathbf{A}_{(1)} = 0 \mathbf{e}_r + \cos \beta_f \mathbf{e}_\Phi - \sin \beta_f \mathbf{e}_z \quad \text{and} \quad \mathbf{A}_{(2)} = 0 \mathbf{e}_r + \cos \beta_f \mathbf{e}_\Phi + \sin \beta_f \mathbf{e}_z, \quad (7.9)$$

where β_f is the angle between a fiber and the circumferential direction. Then the angle of inclination between two crosswise orientated fibers results in $2\beta_f = \arccos(\mathbf{A}_{(1)} \cdot \mathbf{A}_{(2)})$. The fiber directions form the structural tensors

$$\mathbf{M}_{(1)} = \mathbf{A}_{(1)} \otimes \mathbf{A}_{(1)} \quad \text{and} \quad \mathbf{M}_{(2)} = \mathbf{A}_{(2)} \otimes \mathbf{A}_{(2)}. \quad (7.10)$$

Under the described circumstances, for an incompressible, homogenous, uniaxial tension test the constitutive response is driven by the deformation measures

$$\mathbf{F} = \mathbf{U} = \begin{pmatrix} \frac{1}{\lambda_\Phi \lambda_z} & 0 & 0 \\ 0 & \lambda_\Phi & 0 \\ 0 & 0 & \lambda_z \end{pmatrix}, \quad \mathbf{C} = \begin{pmatrix} \frac{1}{\lambda_\Phi^2 \lambda_z^2} & 0 & 0 \\ 0 & \lambda_\Phi^2 & 0 \\ 0 & 0 & \lambda_z^2 \end{pmatrix} \quad \text{and}$$

$$\log \mathbf{U} = \begin{pmatrix} \log\left(\frac{1}{\lambda_\Phi \lambda_z}\right) & 0 & 0 \\ 0 & \log(\lambda_\Phi) & 0 \\ 0 & 0 & \log(\lambda_z) \end{pmatrix},$$

with the radial, circumferential and longitudinal stretches $\lambda_r = 1/(\lambda_\Phi \lambda_z)$, λ_Φ and λ_z .

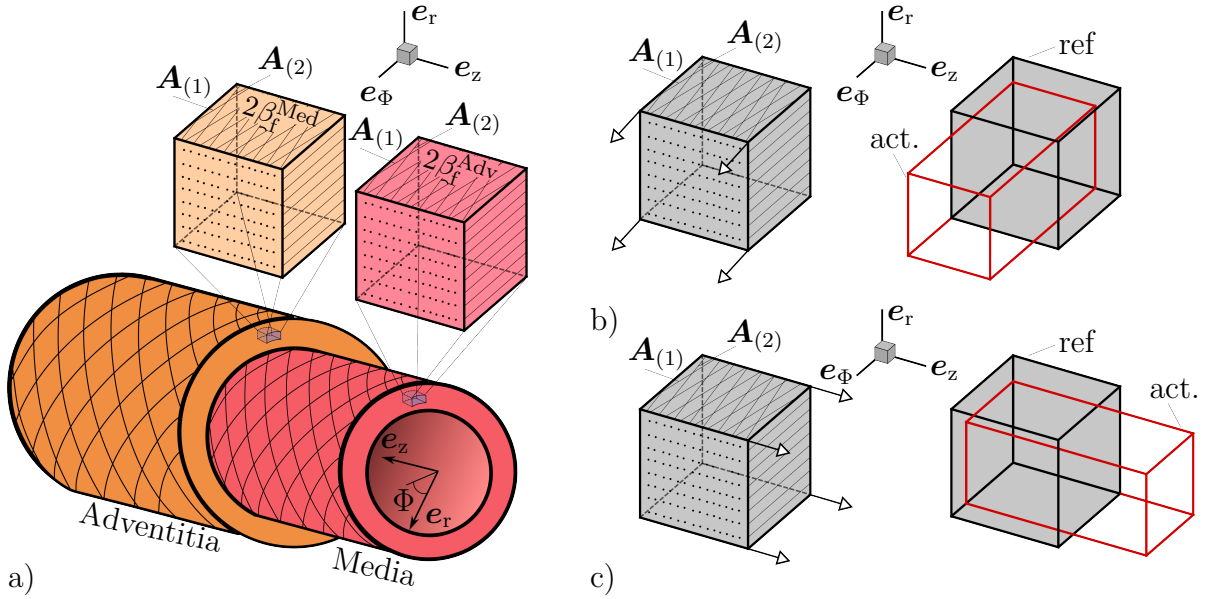


Figure 7.1: a) Excised tissue samples and uniaxial tension tests in b) circumferential and c) axial direction. Taken from SCHRÖDER ET AL. [157].

In order to enforce the incompressibility condition, again the hydrostatic pressure p is added to the *Cauchy* stress, cf. Eq. (6.14). Applying a push-backward operation and considering the derivatives of a generic strain-energy density W with respect to the eigenvalues, the 2nd *Piola-Kirchhoff* stress $\mathbf{S} = \text{diag}[S_{rr}; S_{\Phi\Phi}; S_{zz}]$ may be rewritten as

$$S_{rr} = 2 \frac{\partial W}{\partial \frac{1}{\lambda_\Phi^2 \lambda_z^2}} - \frac{p}{\frac{1}{\lambda_\Phi^2 \lambda_z^2}}, \quad S_{\Phi\Phi} = 2 \frac{\partial W}{\partial \lambda_\Phi^2} - \frac{p}{\lambda_\Phi^2}, \quad S_{zz} = 2 \frac{\partial W}{\partial \lambda_z^2} - \frac{p}{\lambda_z^2}. \quad (7.11)$$

If the tissue is stretched in the circumferential direction, it immediately follows that $S_{\Phi\Phi}$ is the only stress component which is different from zero, while the hydrostatic pressure p and the lateral stretch λ_z remain as unknowns for a given value of λ_Φ . In a numerical scheme, the hydrostatic pressure is computed from the constraint

$$S_{zz}(\lambda_z^i) \stackrel{!}{=} 0 \quad \Rightarrow \quad p = 2 \frac{\partial W}{\partial (\lambda_z^i)^2} (\lambda_z^i)^2 \quad (7.12)$$

and λ_z^{i+1} is updated according to a *Newton*-iteration scheme with

$$S_{rr}(\lambda_z^i) \stackrel{!}{=} 0 \quad \Rightarrow \quad \lambda_z^{n+1} = \sqrt{(\lambda_z^i)^2 - \frac{S_{rr}(\lambda_z^i)}{\text{Lin } S_{rr}(\lambda_z^i)}}, \quad \text{with} \quad \text{Lin } S_{rr}(\lambda_z^i) = \frac{\partial S_{rr}(\lambda_z^i)}{\partial (\lambda_z^i)^2} \quad (7.13)$$

until the solution λ_z^{i+1} meets the second constraint $S_{rr} = 0$ within a certain tolerance. Here, superscript i denotes the iteration index. For the tension test in longitudinal direction, λ_Φ and p are iterated in analogy for a given value of λ_z , making use of the constraint $S_{\Phi\Phi}(\lambda_\Phi) \stackrel{!}{=} 0$.

In accordance with Sec. 6, let us define an objective function based on the error functions

$$\mathcal{E}_\Phi(\mathcal{K}_W) := \sqrt{\frac{1}{N_\Phi} \sum_{n=1}^{N_\Phi} \left(\frac{\sigma_{\Phi\Phi}^{\text{exp}}(\lambda_\Phi^n) - \sigma_{\Phi\Phi}^p(\lambda_\Phi^n, \mathcal{K}_W)}{\max(\sigma_{\Phi\Phi}^{\text{exp}})} \right)^2}, \quad (7.14)$$

$$\mathcal{E}_z(\mathcal{K}_W) := \sqrt{\frac{1}{N_z} \sum_{n=1}^{N_z} \left(\frac{\sigma_{zz}^{\text{exp}}(\lambda_z^n) - \sigma_{zz}^p(\lambda_z^n, \mathcal{K}_W)}{\max(\sigma_{zz}^{\text{exp}})} \right)^2} \quad (7.15)$$

for the circumferential and axial uniaxial tension test, respectively. Here, N_Φ and N_z denote the numbers of experimental measuring points and $\sigma_{\Phi\Phi}^{\text{exp}}$ and σ_{zz}^{exp} the measured stresses at the corresponding measuring point with associated stretches $\lambda_{\Phi\Phi}^n$ or λ_{zz}^n . Then the objective function

$$f^{\text{obj}}(\mathcal{K}_W) = \frac{1}{2}(\mathcal{E}_\Phi + \mathcal{E}_z) \quad (7.16)$$

is minimized within the *fmincon* function in *MATLAB* [180], solving the problem

$$\mathcal{K}_W = \text{argmin}(f^{\text{obj}}). \quad (7.17)$$

Depending on the energy function, optimized parameter sets

$$\mathcal{K}_W = \begin{cases} \mathcal{K}_W(W_{\mathbb{C}}) = \{c_1, c_2, c_3, \mu_1, k_1, \beta_f\} & \text{if } W = W_{\mathbb{C}} \\ \mathcal{K}_W(W_{\mathbb{H}}) = \{k, \mu_1, k_1, \beta_f\} & \text{if } W = W_{\mathbb{H}} \end{cases} \quad (7.18)$$

are returned. Please note that the parameters κ_{Pen} , κ and \hat{k} are excluded from the optimization since fitting is impossible when assuming incompressibility due to the fact that $\det \mathbf{C} = 1$ and $\text{tr}(\log \mathbf{U}) = 0$. Further, due to the special property of $W_{\mathbb{H}}$ that $\mathbb{C}|_{\log \mathbf{U}=\mathbf{0}}$ is only a function of the infinitesimal shear modulus μ (and the compression modulus κ in the compressive case) it is directly estimated from the experiments. Considering the linearized initial stress increment

$$\Delta \mathbf{S} = \mathbb{C}|_{\log \mathbf{U}=\mathbf{0}} : \frac{1}{2} \Delta \mathbf{C}, \quad (7.19)$$

where $\mathbb{C}|_{\log \mathbf{U}=\mathbf{0}}$ only depends on μ , its value can be directly computed for the first measuring points. In that regard, the values for the circumferential and longitudinal experimental stresses are averaged for the estimation of μ .

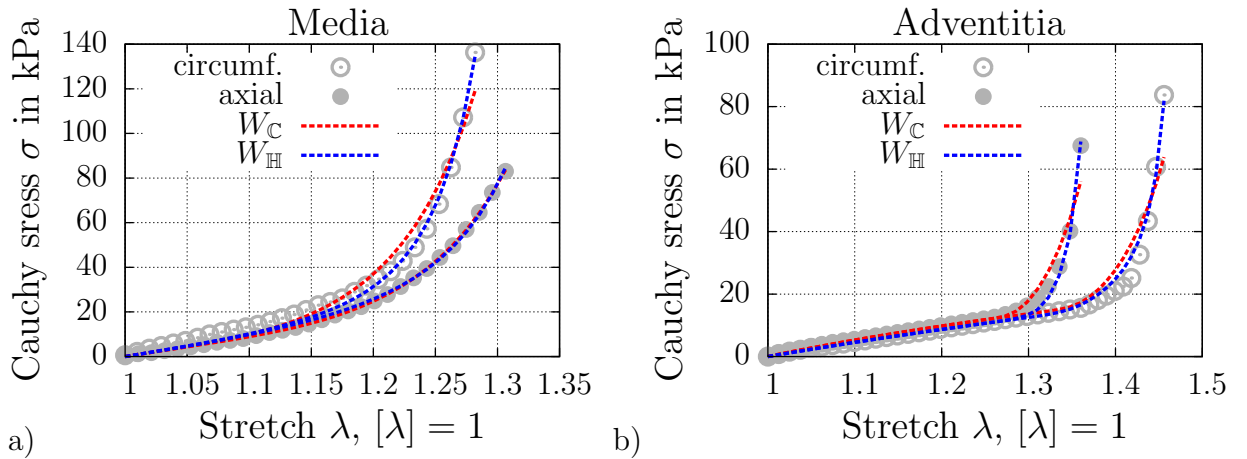
The resulting optimized parameter sets $\mathcal{K}_W(W_{\mathbb{C}})$ and $\mathcal{K}_W(W_{\mathbb{H}})$ are given in Tabs. 7.1 and 7.2, respectively. The optimized fiber angles β_f are similar for both models and lie in the range of the experimentally measured mean fiber angles of 37.8° for the media and 58.9° for the adventitia which were also determined in HOLZAPFEL [72]. Corresponding stress-strain curves in comparison to the experimental data are shown in Fig. 7.2. As can be seen, the fitting capabilities of both functions are good, whereby $W_{\mathbb{H}}$ performs slightly better for both material layers which is reflected by lower objective function values in the aforementioned tables.

Table 7.1: Optimized parameter sets $\mathcal{K}_W(W_C)$ of the media and adventitia and corresponding objective function values.

	W_{MR}			W_{HGO}			
	c_1 in kPa	c_2 in kPa	c_3 in kPa	μ_1 in kPa	k_1 [k_1] = 1	β_f in deg.	f^{obj} [f^{obj}] = 1
Media	3.38	11.17	60.81	5.55	417.35	43.67	2.99e-02
Adventitia	1.00e-08	9.66	72.29	4.50e-08	297.43	47.16	4.69e-02

Table 7.2: Optimized parameter sets $\mathcal{K}_W(W_H)$ of the media and adventitia and corresponding objective function values. Please note that the shear modulus values are marked with a * since they were not part of the fitting procedure, as explained above.

	W_{eH}		W_{SHN}			
	μ in kPa	k [k] = 1	μ_1 in kPa	k_1 [k_1] = 1	β_f in deg.	f^{obj} [f^{obj}] = 1
Media	31.16*	3.16	527.59	1612.51	40.56	2.21e-02
Adventitia	15.90*	1.00e-08	5.79e-03	3708.75	50.44	2.38e-02


Figure 7.2: Comparison of the fitted stress-strain curves of models W_C and W_H with the experimental data. In a) the results of the media and in b) the results of the adventitia are shown.

The parameters κ_{Pen} , κ and \hat{k} which cannot be fitted within the described optimization procedure are set according to Tab. 7.3. They are appropriate to limit the change in volume to become less than 1% in the following examples. In view of the numerical robustness, mixed finite element formulations are favorable for quasi-incompressible applications. Further, for the application of high penalty parameters it is beneficial to use an augmented *Lagrange* approach ([54, 55],[18]). These ideas were successfully implemented in SCHRÖDER AND BRINKHUES [150] and SCHRÖDER AND VON HOEGEN [153] for residual stress estimations.

Here, we restrict ourselves to standard elements and classical penalty approaches for simplicity and in order to allow for a fair comparison of the considered strain-energies.

Table 7.3: Chosen parameters associated to the volume expansion of the material. These cannot be fitted in the presented optimization strategy.

$W_{\mathbb{C}}$	$W_{\mathbb{H}}$	
κ_{Pen} in kPa	κ in kPa	\hat{k} [\hat{k}] = 1
500	100	2

7.3 Fiber Stress Invariants

In the large strain regime the material response of arterial tissues is primarily determined by the stiffening of collagen fibers. Consequently, the material behavior displays strong anisotropic effects. In phenomenological material modeling this is taken into account by the incorporation of transversely isotropic invariants in the underlying strain-energy function W . The fundamental assumption that the state of stress in radial direction becomes more uniform due to the existence of residual stresses motivates the consideration of stress invariants that meet the demand to display the anisotropy and trigger the evolution of residual stress.

In order to do so, in a first step the *Cauchy*-stresses

$$\boldsymbol{\sigma} = \boldsymbol{\sigma}^* + \boldsymbol{\sigma}^{\text{reac}}, \quad (7.20)$$

may be additively split into a ground stress $\boldsymbol{\sigma}^*$ and a reaction stress $\boldsymbol{\sigma}^{\text{reac}}$. The latter represents a reaction due to an assumed inextensible behavior in direction of the preferred direction. Considering two present major fiber directions, the reaction stress is defined through

$$\boldsymbol{\sigma}^{\text{reac}} = \sum_{a=1}^2 T_{(a)} \widetilde{\mathbf{m}}_{(a)}, \quad (7.21)$$

where $T_{(1)}$ and $T_{(2)}$ denote fiber invariants to be determined in the following and

$$\widetilde{\mathbf{m}}_{(a)} = \widetilde{\mathbf{a}}_{(a)} \otimes \widetilde{\mathbf{a}}_{(a)} \quad (7.22)$$

are the corresponding structural tensors in the actual configuration. These are constructed based on the unit vectors

$$\widetilde{\mathbf{a}}_{(a)} = \frac{\mathbf{a}_{(a)}}{\|\mathbf{a}_{(a)}\|} \quad \text{with} \quad \mathbf{a}_{(a)} = \mathbf{F} \mathbf{A}_{(a)}. \quad (7.23)$$

The transformation in Eq. (7.23) yields a vector pointing in the actual fiber direction which is then divided by its norm and removes the elongation/contraction initiated by the transformation of the unit vector $\mathbf{A}_{(a)}$. To solve for the fiber invariants, additional

constraints are required. These are given by the assumption that the projection of the ground stresses in the actual fiber direction vanishes, i.e.

$$\boldsymbol{\sigma}^* : \widetilde{\mathbf{m}}_{(a)} = \mathbf{0}. \quad (7.24)$$

Similar ideas, especially for the construction of convenient sets of invariants, have been proposed by MULHERN ET AL. [120] and SPENCER [171]. Then the projection of the complete *Cauchy*-stress results in the two equations

$$\boldsymbol{\sigma} : \widetilde{\mathbf{m}}_{(1)} = T_{(1)} + T_{(2)} \widetilde{\mathbf{m}}_{(1)} : \widetilde{\mathbf{m}}_{(2)} \quad \text{and} \quad \boldsymbol{\sigma} : \widetilde{\mathbf{m}}_{(2)} = T_{(1)} \widetilde{\mathbf{m}}_{(2)} : \widetilde{\mathbf{m}}_{(1)} + T_{(2)} \quad (7.25)$$

with only two unknowns $T_{(1)}$ and $T_{(2)}$. Solving the above system of equations finally yields

$$T_{(1)} = \frac{\boldsymbol{\sigma} : \widetilde{\mathbf{m}}_{(1)} - \boldsymbol{\sigma} : \widetilde{\mathbf{m}}_{(2)} \xi}{1 - \xi^2} \quad \text{and} \quad T_{(2)} = \frac{\boldsymbol{\sigma} : \widetilde{\mathbf{m}}_{(2)} - \boldsymbol{\sigma} : \widetilde{\mathbf{m}}_{(1)} \xi}{1 - \xi^2}, \quad (7.26)$$

where $\xi = (\widetilde{\mathbf{a}}_{(1)} \cdot \widetilde{\mathbf{a}}_{(2)})^2$ and $\widetilde{\mathbf{a}}_{(1)} \neq \widetilde{\mathbf{a}}_{(2)}$. Please note that $\widetilde{\mathbf{m}}_{(a)} : \widetilde{\mathbf{m}}_{(a)} = 1$.

7.4 Residual Stress Approach

Based on the precedent discussion on the origins and characteristics of residual stresses in Sec. 2.3, the approach is based on the following hypothesis:

The superposition of eigenstresses in arterial walls should decrease the gradient of suitable stress-measures of the in-vivo stress state in radial direction.

More specifically, the discussed method aims to smooth the derived fiber invariants in Eq. (7.26) across the wall thickness. It is implemented within an algorithmic procedure, where the fiber invariants in certain parts of the arteries are gradually adapted. After each step of adaption a new equilibrium state needs to be iterated. Local target values for the adaption are based on a domain decomposition into segments or sectors. In the following the domain \mathcal{B}^\angle is called a segment and the domain $\mathcal{B}^{\angle, \text{mat}}|_{\text{mat}=\{\text{adv}, \text{med}\}}$ a sector. Thereby, a segment is defined as the entirety of all finite elements whose center is lying inside a specific range of the polar angle Φ with regard to the center of the lumen. Regarding the sectors an additional distinction is made in view of the material associated to an element, i.e. media or adventitia, such that

$$\mathcal{B}^\angle = \mathcal{B}^{\angle, \text{med}} \cup \mathcal{B}^{\angle, \text{adv}} \quad \text{and} \quad \mathcal{B}^{\angle, \text{med}} \cap \mathcal{B}^{\angle, \text{adv}} = \emptyset. \quad (7.27)$$

The decomposition of an ideal tube with a circular cross-section is shown in Fig. 7.3, where Γ denotes the interface of the two material layers. The number of segments n_{SG} and the number of sectors $n_{\text{SC}}^{2\text{D}}$ and $n_{\text{SC}}^{3\text{D}}$ in two- or three-dimensional problems, respectively, are connected through the simple relationships

$$n_{\text{SC}}^{2\text{D}} = n_{\text{SG}} \cdot n_{\text{MAT}} \quad \text{and} \quad n_{\text{SC}}^{3\text{D}} = n_{\text{SC}}^{2\text{D}} \cdot n_L. \quad (7.28)$$

Here, n_L represents the number of additional subdivisions in longitudinal direction and n_{mat} is the total number of material layers. In the depicted examples the domain is composed of $n_{\text{SG}} = 8$ segments and $n_{\text{mat}} = 2$ materials and therefore $n_{\text{SC}}^{2\text{D}} = 8 \cdot 2 = 16$. Then

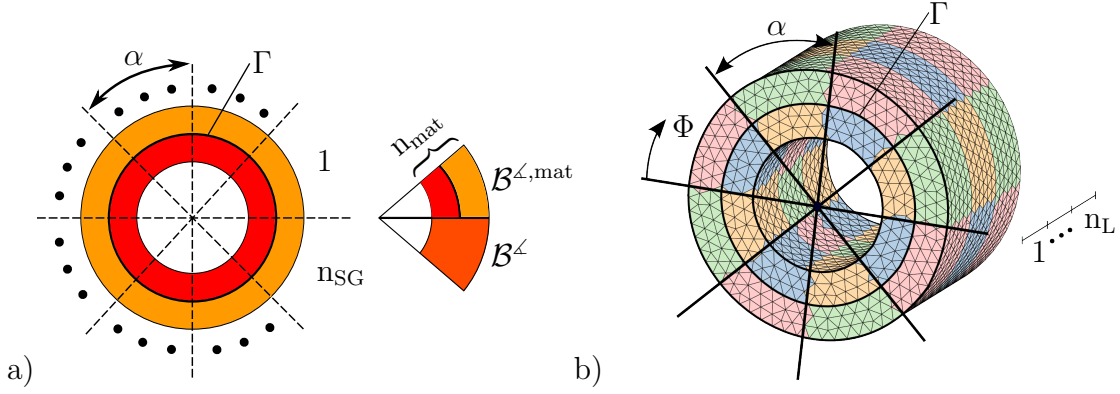


Figure 7.3: Exemplary definition of segments and sectors of an ideal tube in a) 2-D and b) 3-D. Two material layers with an interface Γ are considered. In a) the media is colored in red and the adventitia in orange. Taken from SCHRÖDER AND VON HOEGEN [153].

each segment is associated with a polar angle range of $\alpha = 360^\circ/8 = 45^\circ$. The tube in b) is additionally subdivided into $n_L = 3$ parts and therefore $n_{SG}^{3D} = 16 \cdot 3 = 48$.

In each segment or sector domain, one may compute the volume averaged spatial mean values

$$\overline{(\bullet)}^\Delta = \frac{1}{v^\Delta} \int_{\mathcal{B}^\Delta} (\bullet)(\mathbf{x}) dv \quad \text{and} \quad \overline{(\bullet)}^{\Delta, \text{mat}} = \frac{1}{v^{\Delta, \text{mat}}} \int_{\mathcal{B}^{\Delta, \text{mat}}} (\bullet)(\mathbf{x}) dv \quad (7.29)$$

of a scalar quantity (\bullet) depending on the local position vector \mathbf{x} . Here, v^Δ and $v^{\Delta, \text{mat}}$ denote the spatial volumes of the segment and sector domains \mathcal{B}^Δ and $\mathcal{B}^{\Delta, \text{mat}}$, respectively. According to the latter equation, we obtain the averaged fiber stress invariants $\overline{T}_{(a)}^\Delta$, $\overline{T}_{(a)}^{\Delta, \text{med}}$ and $\overline{T}_{(a)}^{\Delta, \text{adv}}$ with $a = 1, 2$, which will serve as possible target values

$$\overline{T}_{(a)} = \begin{cases} \overline{T}_{(a)}^\Delta = \frac{1}{v^\Delta} \int_{\mathcal{B}^\Delta} T_{(a)}(\mathbf{x}) dv & \text{for segments} \\ \overline{T}_{(a)}^{\Delta, \text{mat}} = \frac{1}{v^{\Delta, \text{mat}}} \int_{\mathcal{B}^{\Delta, \text{mat}}} T_{(a)}(\mathbf{x}) dv & \text{for sectors} \end{cases} \quad (7.30)$$

in each iteration step of the presented numerical scheme. This provides the opportunity for the user to decide either to choose segment-specific or sector-specific target values. The local deviations from the target values on each integration point of the associated subdomain follow to

$$\Delta T_{(a)} = T_{(a)} - \overline{T}_{(a)}. \quad (7.31)$$

All introduced quantities are illustrated in Fig. 7.4. Based on an exemplary fiber-stress distribution of a two-layered artery, in a) the sector mean stresses and in b) the segment mean stress and the corresponding deviations $\Delta T_{(a)}$ are shown. Here, r_i and r_a denote the inner and outer radius and $\tilde{r} \in [r_i, r_a]$. The sudden fall in stress at the layer interface with a radius r_Γ is due to the distinct difference in stiffness of the media and adventitia. It is crucial to note that only the radial stresses need to be continuous in a tube because of the equilibrium requirement.

Within this framework, we aim to iterate local residual stress tensors \mathbf{S}^{res} which facilitate to smooth the stress gradient of the fiber stress invariants and accomplishes the

fundamental hypothesis. Subtraction from the strain-energy driven stresses yields

$$\mathbf{S} = \mathbf{S}^* - \mathbf{S}^{\text{res}} \quad \text{with} \quad \mathbf{S}^* = 2 \frac{\partial W}{\partial \mathbf{C}}. \quad (7.32)$$

The local increment of the residual stress tensor is estimated according to

$$\Delta \boldsymbol{\sigma}^{\text{res}} = \sum_{a=1}^2 \Delta T_{(a)} \widetilde{\mathbf{m}}_{(a)} \quad (7.33)$$

in compliance with Eq. (7.21). In each iteration step the residual stress tensor initialized with $\mathbf{0}$ will be added up according to

$$\boldsymbol{\sigma}^{\text{res}} \leftarrow \boldsymbol{\sigma}^{\text{res}} + \frac{\gamma}{n_{\text{inc}}} \Delta \boldsymbol{\sigma}^{\text{res}}, \quad \text{where } \gamma \in [0, 1]. \quad (7.34)$$

This is facilitated within a number of $n_{\text{inc}} \in \mathbb{N}$ sub-incrementation loops in which a total proportion γ of the residual stress increment $\Delta \boldsymbol{\sigma}^{\text{res}}$ is applied. Finally the residual stress tensor

$$\mathbf{S}^{\text{res}} = J \mathbf{F}^{-1} \boldsymbol{\sigma}^{\text{res}} \mathbf{F}^{-T} \quad (7.35)$$

is pushed back to the reference configuration. After subtraction in Eq. (7.32), the equilibrium condition will be violated, making it necessary to iterate a new equilibrium state. The residual stresses are held constant during this iteration, i.e. \mathbf{S}^{res} is independent of the deformation \mathbf{u} . After convergence new average stresses $\bar{T}_{(a)}$ and local deviations $\Delta T_{(a)}$ may be calculated and a new equilibrium state based on the updated residual stress tensors $\boldsymbol{\sigma}^{\text{res}}$ and \mathbf{S}^{res} needs to be found.

The sequence of computations is summarized in Tab. 7.4. After initially dividing the arterial segment into subdomains it is loaded with the internal blood pressure, neglecting residual stresses. That means $\mathbf{S}^{\text{res}} = \mathbf{0}$. The resulting stress field is then used to subsequently estimate the residual stresses with help of so-called smoothing loops. In each loop the estimate $\Delta \boldsymbol{\sigma}^{\text{res}}$ is overwritten and the residual stress tensor is in turn updated in sub-incrementation loops. In each of these, the calculation of a new deformation state is necessary due to the modified local stresses.

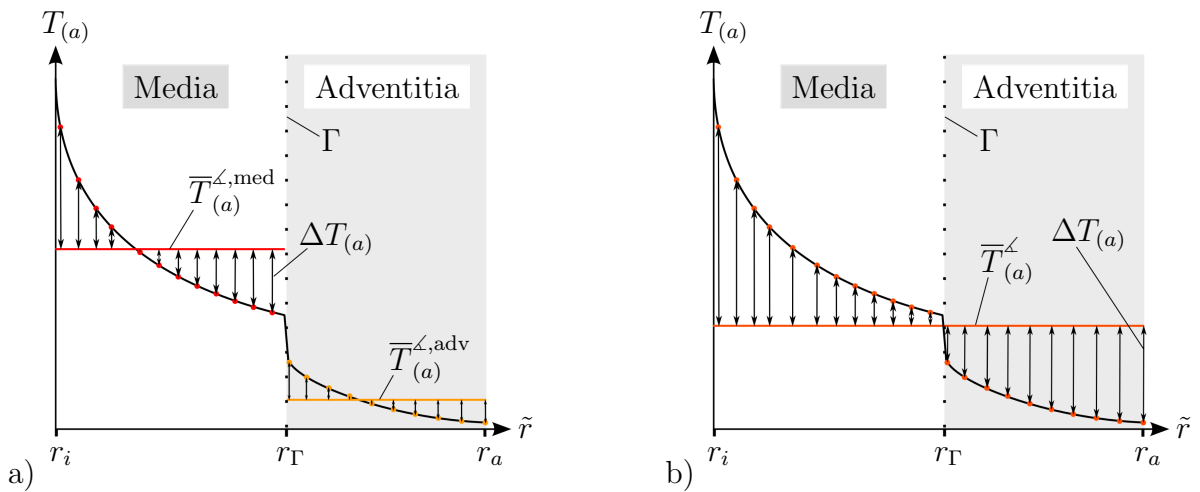


Figure 7.4: Exemplary fiber stress distribution over the wall thickness \tilde{r} and corresponding deviations $\Delta T_{(a)}$ with respect to a) the sector mean stresses $\bar{T}_{(a)}^{\angle, \text{mat}}$ and b) the segment mean stress $\bar{T}_{(a)}^{\angle}$.

<ul style="list-style-type: none"> • Divide domain \mathcal{B} into $n_{\text{SG}}^{3\text{D}}$ sectors with subdomains $\mathcal{B}^{\angle, \text{mat}}$ or n_{SG} segments with subdomains \mathcal{B}^{\angle}; initialize $\boldsymbol{\sigma}^{\text{res}} = \mathbf{0}$ • Apply internal pressure p_i (incrementally) and solve the nonlinear boundary value problem: compute \mathbf{F}, \mathbf{S} • DO number of smoothing loops (n_{SL}) <ul style="list-style-type: none"> a) Given: $\boldsymbol{\sigma} = \mathbf{F} \mathbf{S} \mathbf{F}^T / J$ and $T_{(a)}$ b) Compute: local volume averages of fiber-stresses $\bar{T}_{(a)}$, Eq. (7.30) c) Compute: deviations $\Delta T_{(a)}$, Eq. (7.31) d) Compute: residual stresses $\Delta \boldsymbol{\sigma}^{\text{res}}$, Eq. (7.33) e) DO number of sub-incrementation loops (n_{inc}) <ul style="list-style-type: none"> $\boldsymbol{\sigma}^{\text{res}} \leftarrow \boldsymbol{\sigma}^{\text{res}} + \frac{\gamma}{n_{\text{inc}}} \Delta \boldsymbol{\sigma}^{\text{res}}, \gamma \in [0, 1]$ $\mathbf{S}^{\text{res}} = J \mathbf{F}^{-1} \boldsymbol{\sigma}^{\text{res}} \mathbf{F}^{-T}$ $\mathbf{S} = \mathbf{S}^* - \mathbf{S}^{\text{res}}$, with $\mathbf{S}^* = 2 \partial_{\mathbf{C}} W$ Solve balance of linear momentum: compute $\mathbf{F}, \mathbf{S}, T_{(a)}$ <p style="text-align: right; margin-right: 20px;"> } sub-incrementation } smoothing-loop </p> <p style="margin-left: 20px;">END DO</p> <p>END DO</p>
--

Table 7.4: Algorithmic box describing the numerical implementation of the residual stress approach. Adapted from SCHRÖDER AND VON HOEGEN [153].

7.5 Results of the Residual Stress Approach

7.5.1 Numerical Simulation of an Ideal Tube

In a first step, the described algorithm is tested for an ideal tube. Due to rotational symmetry, only one half of the tube is considered in order to decrease the computation time. The bisected, two-layered tube is shown in Fig. 7.5a). It is discretized with 5000 quadratic brick elements and the dimensions of the radii $r_i = 5.25$ mm, $r_{\Gamma} = 6.5$ mm and $r_a = 7.5$ mm are in the range of an abdominal aorta, see HOLZAPFEL ET AL. [80]. Furthermore, in this particular case the fiber stress invariants $T_{(1)} = T_{(2)}$ are identical on each *Gauss*-point due to the symmetric fiber arrangement and it is sufficient to decompose the tube in only one segment $n_{\text{SG}} = 1$ because $T_{(a)}$ is a pure function of the radius \tilde{r} . The tube is loaded with an internal pressure p_i of 13.33 kPa which corresponds to a blood pressure of 100 mmHg. The boundary conditions of an intact closed artery are shown in Fig. 7.5b), while the boundary conditions for the simulation of the opening angle are depicted in Fig. 7.5c).

In Figs. 7.6 and 7.7 different stress distributions over the radius \tilde{r} are plotted for both considered energy functions after 0,1 and 3 smoothing loops with a proportionate factor γ of 100%. Boundary conditions according to Fig. 7.5b) are applied. Only *Gauss*-points were evaluated for the plots. In Fig. 7.6 the stress averaging was performed on sector domains $\mathcal{B}^{\angle, \text{mat}}$, i.e separately on each material layer, while in Fig. 7.7 the stress averaging was performed on segment domains \mathcal{B}^{\angle} . The plotted curves before smoothing, i.e.

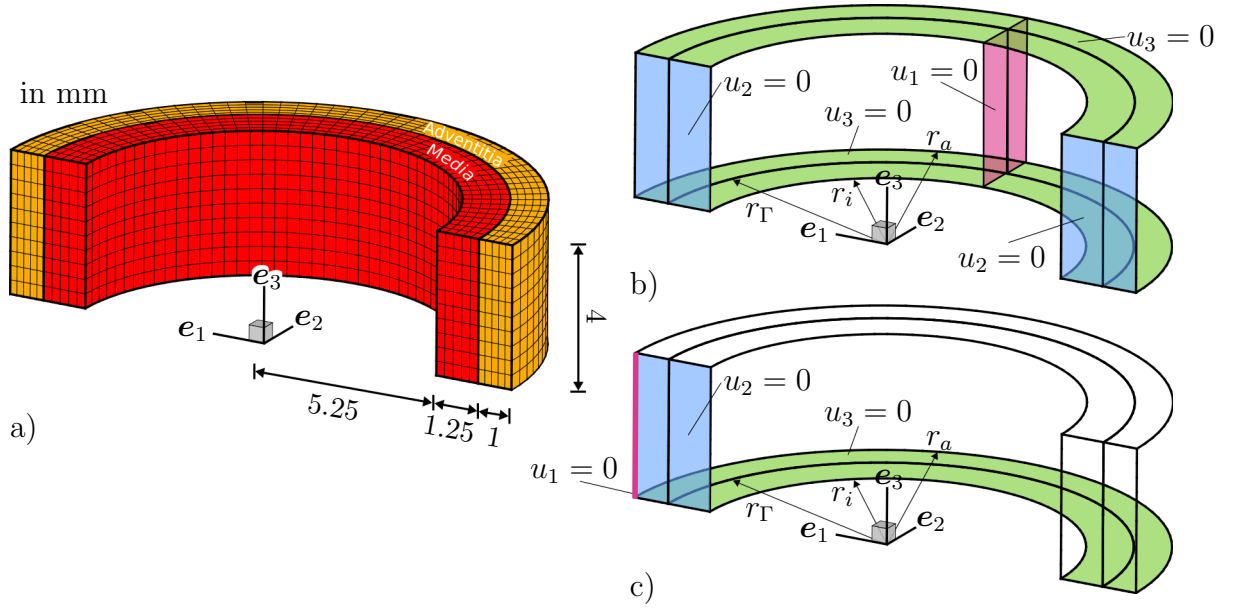


Figure 7.5: a) Dissected tube, discretized with 5000 quadratic bricks. b) Boundary conditions to simulate the artery loaded with an internal blood pressure $p_i = 13.33$ kPa. c) Boundary conditions to simulate the opening of the residually stressed artery in the absence of external loads.

for 0 SL (smoothing loops), are therefore identical in both figures. Apparently, there are considerable differences for the two chosen material models which were fitted to the same experiments. The stress invariant $T_{(1)}$ at the inner surface of the tube with $\tilde{r} = r_i$ is about twice the magnitude for W_C compared to W_H . The differences of the computed stresses become even more apparent in the axial stresses $\sigma_{zz} = \boldsymbol{\sigma} : \mathbf{e}_z \otimes \mathbf{e}_z$, while the circumferential *Cauchy*-stresses $\sigma_{\Phi\Phi} = \boldsymbol{\sigma} : \mathbf{e}_\Phi \otimes \mathbf{e}_\Phi$ are relatively similar. The radial stresses $\sigma_{rr} = \boldsymbol{\sigma} : \mathbf{e}_r \otimes \mathbf{e}_r$ have to be similar on grounds of the equilibrium condition. Values on the inner surface are constrained by the internal pressure and need to be zero on the outer surface.

After application of the algorithm summarized in Tab. 7.4, the distribution of the target figure $T_{(1)}$ is noticeably smoothed with increasing number of smoothing loops as it was intended. After 3 SL in each case a constant distribution over the radius \tilde{r} is maintained with regard to the associated averaging domain $\mathcal{B}^{\Delta, \text{mat}}$ or \mathcal{B}^Δ . In the event of sector based smoothing, the distinct jump at the layer interface Γ is striking. The smoothing of $T_{(1)}$ and $T_{(2)}$ goes along with the smoothing of circumferential stresses $\sigma_{\Phi\Phi}$ for both material laws. In case of W_C , this also applies for the axial stresses σ_{zz} . In contrast to that, the radial gradient of σ_{zz} becomes significantly larger for W_H . The radial stresses σ_{rr} remain relatively unaffected for both strain-energy functions with the tendency to become more linear over the radius.

In addition, the fiber stretch invariants $I_4^{C1} = \mathbf{C} : \mathbf{M}_{(1)} = \mathbf{C} : \mathbf{M}_{(2)}$ and $I_4^{H2} = (\log \mathbf{U})^2 : \mathbf{M}_{(1)} = (\log \mathbf{U})^2 : \mathbf{M}_{(2)}$ are plotted in Fig. 7.8. It is conspicuous that the application of the residual stress has a relatively low influence on the invariants which only become slightly larger. Since the elastic material behavior is primarily driven by the strain-stiffening of the fibers and the associated evolution of the invariants one

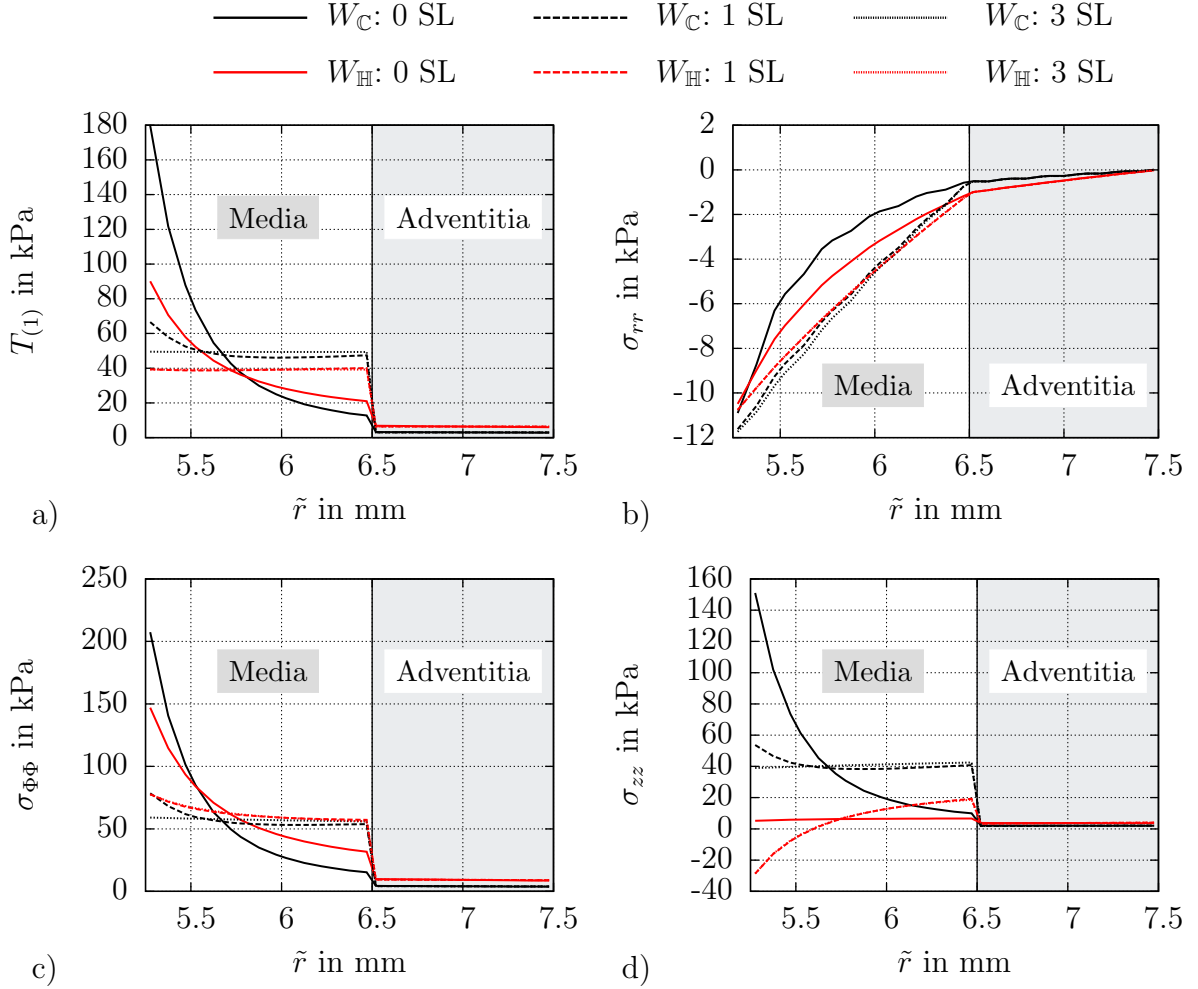


Figure 7.6: Transmural distribution of a) the fiber stress $T_{(1)} = T_{(2)}$, b) the radial stress σ_{rr} , c) the circumferential stress $\sigma_{\Phi\Phi}$ and d) the axial stress σ_{zz} after different amounts of smoothing loops (SL) with $\gamma = 100\%$ for W_C and W_H . Averaging is performed sector wise, i.e. over domains $\mathcal{B}^{\angle, \text{mat}}$.

may conclude that also the constitutive function W remains comparable. It is evident that the smoothing of the stresses does not go along with the smoothing of stretches.

In a second step, the unloaded and residual stress free configuration is loaded incrementally with the estimated local stress tensor \mathbf{S}^{res} . Then a new balance state with

$$\mathbf{S} = \mathbf{S}^* - \mathbf{S}^{\text{res}} \quad \text{and} \quad \mathbf{S}^* = 2 \frac{\partial W}{\partial \mathbf{C}}$$

needs to be iterated. If a radial slice is additionally considered, this refers to the simulation of the opened configuration from which the opening angle according to Fig. 2.5 is frequently measured in experiments. This applies for the depicted boundary conditions in Fig. 7.5c). Results for the estimated residual stresses \mathbf{S}^{res} after 1 SL with $\gamma = 100\%$ are depicted in Fig. 7.9 for W_C and in Fig. 7.10 for W_H . Only one half of the tube was simulated, however for the plots this half is mirrored to produce the more intuitive full artery images. Again, it is distinguished between averaging over sector domains $\mathcal{B}^{\angle, \text{mat}}$ on the top row and segment domains \mathcal{B}^{\angle} on the bottom row in both figures.

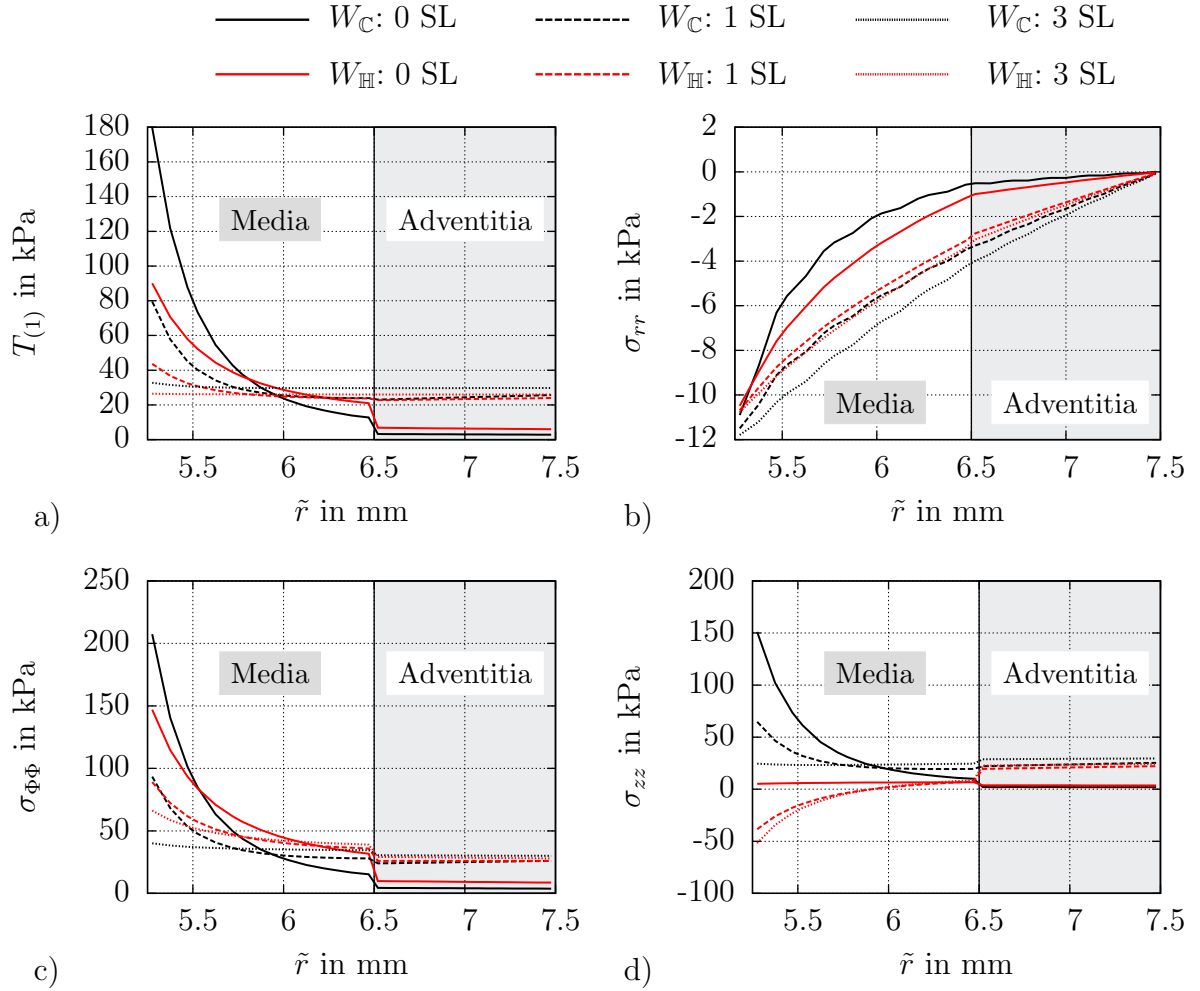


Figure 7.7: Transmural distribution of a) the fiber stress $T_{(1)} = T_{(2)}$, b) the radial stress σ_{rr} , c) the circumferential stress $\sigma_{\Phi\Phi}$ and d) the axial stress σ_{zz} after different amounts of smoothing loops (SL) with $\gamma = 100\%$ for W_C and W_H . Averaging is performed sector wise, i.e. over domains \mathcal{B}^\angle .

Further, the opened configurations are simulated separately for the whole artery and the individual material layers media and adventitia. Layer specific experiments were conducted in HOLZAPFEL ET AL. [80]. Essential to determine the magnitude of the residual stresses are the fiber stress deviations from the mean values, see Eq. (7.31). On the adventitia the deviations will obviously be considerable higher and purely tensile, when averaging is performed over the segment domains \mathcal{B}^\angle . This leads to a larger and more realistic opening angle compared to averaging over $\mathcal{B}^{\angle, \text{mat}}$.

On the media the tensile deviations near by the lumen are smaller while the compressive deviations near by the media adventitia interface become higher, when averaging is performed over the sector domains $\mathcal{B}^{\angle, \text{mat}}$. This leads to a more bending dominated problem, resulting in the larger opening angle of the media for $\mathcal{B}^{\angle, \text{mat}}$.

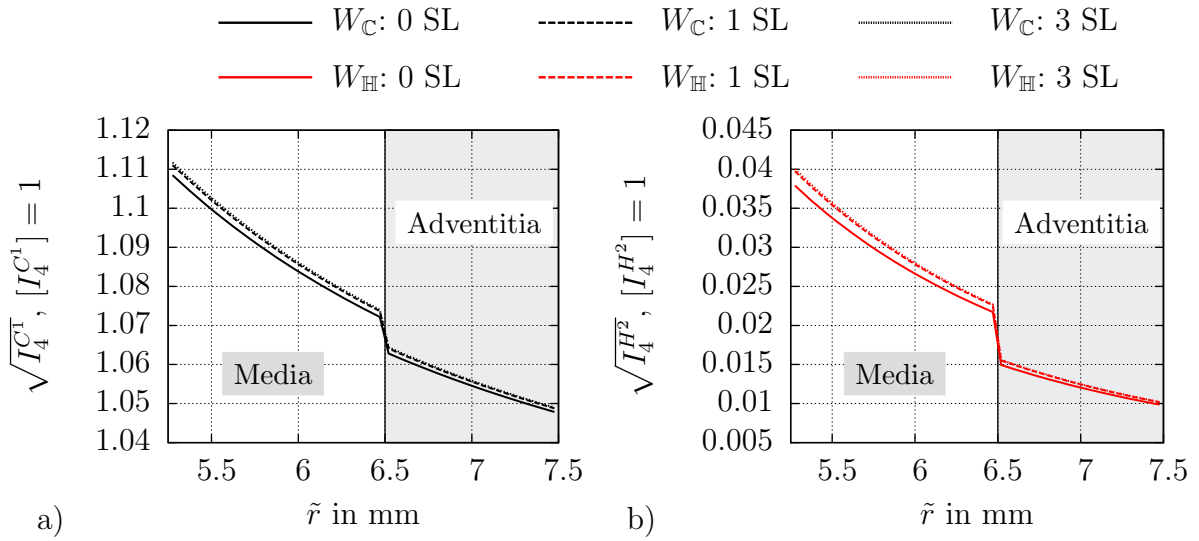


Figure 7.8: Transmural distribution of the invariants $I_4^{C^1} = \mathbf{C} : \mathbf{M}_{(1)} = \mathbf{C} : \mathbf{M}_{(2)}$ and $I_4^{H^2} = (\log \mathbf{U})^2 : \mathbf{M}_{(1)} = (\log \mathbf{U})^2 : \mathbf{M}_{(2)}$ after different amounts of smoothing loops. Averaging is performed sector wise, i.e. over domains \mathcal{B}^\angle .

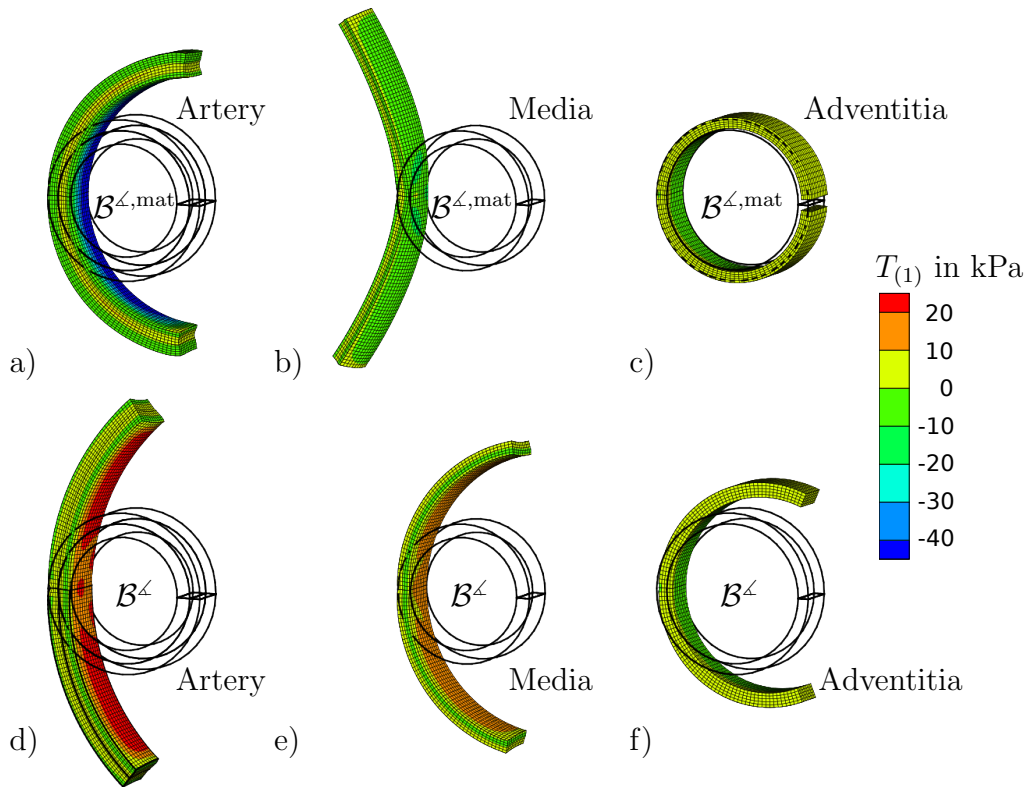


Figure 7.9: Simulations of the opened configuration. Depicted configurations of a) the complete artery , b) the single media and c) the single adventitia in the top line are based on averaging over sector domains $\mathcal{B}^{\angle, \text{mat}}$. Depicted configurations of d) the complete artery , e) the single media and f) the single adventitia in the bottom line are based on averaging over segment domains \mathcal{B}^\angle . One smoothing-loop with $\gamma = 100\%$ is applied in each case. The contour plots depict the fiber stress $T_{(1)}$. Strain-energy W_C is used.

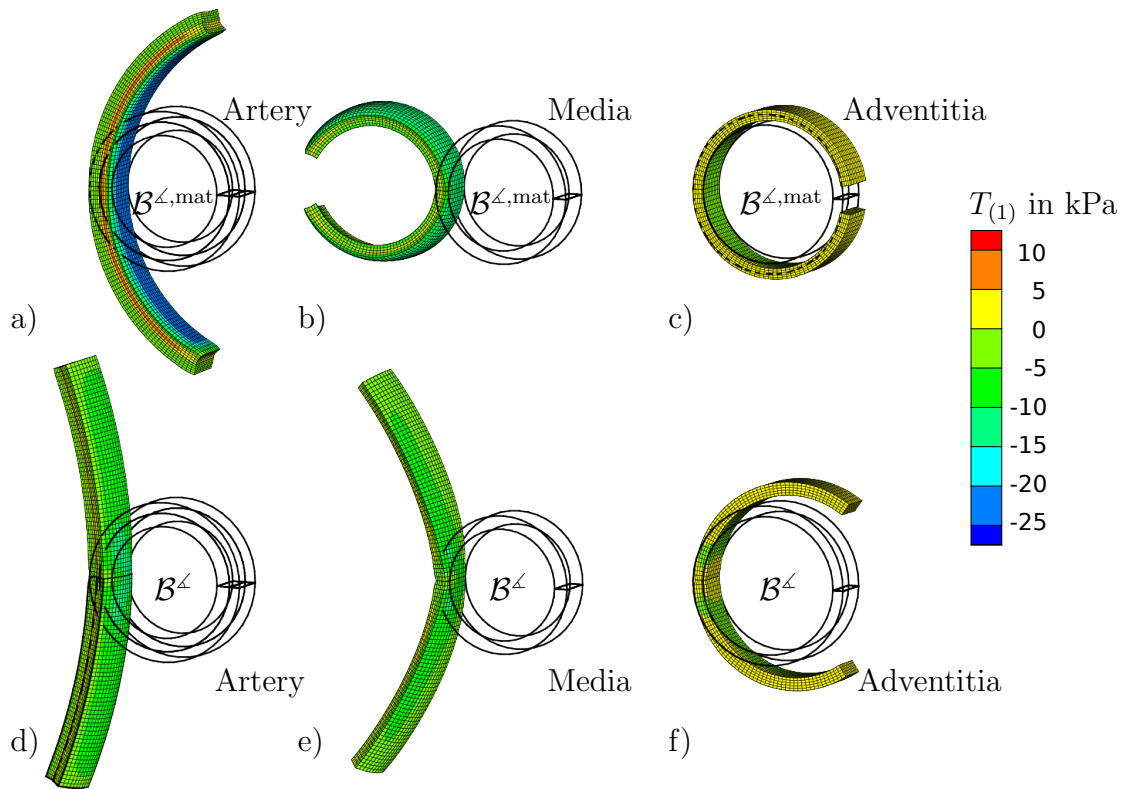


Figure 7.10: Simulations of the opened configuration. Depicted configurations of a) the complete artery , b) the single media and c) the single adventitia in the top line are based on averaging over sector domains $\mathcal{B}^{\angle,mat}$. Depicted configurations of d) the complete artery , e) the single media and f) the single adventitia in the bottom line are based on averaging over segment domains \mathcal{B}^{\angle} . One smoothing-loop with $\gamma = 100\%$ is applied in each case. The contour plots depict the fiber stress $T_{(1)}$. Strain-energy W_{H} is used.

Overall, the opening appears to be more pronounced in Fig. 7.10. An accurate assessment how realistic the estimated/predicted opened configurations are is difficult in view of the range of data in literature and the measured differences depending on age, gender or location of the artery along the vascular tree. Anyhow, the basic characteristics of the opening angle experiment are well approximated in the simulations. The observation that the opened configuration of the media deforms stronger than the one of the adventitia is confirmed in the experimental findings by HOLZAPFEL ET AL. [80]. Moreover, as can be seen all of the opened configurations are not completely free of stresses such that the application of additional cuts would lead to additional deformations as it is also observed in experiments.

7.5.2 Numerical Simulation of a Patient-Specific Arterial Segment

In the following, the performance of the discussed approach is tested for a reconstructed patient-specific coronary arterial segment. The arterial geometry is reconstructed based on two sequenced two-dimensional *virtual histology (VH) intravascular ultrasound (IVUS)* images. This is a catheter based method which provides a series of grey-scale images. These in turn facilitate to identify the lumen and the media-adventitia interface Γ . However, IVUS images struggle to identify the interface of the adventitia and the surrounding connective tissue. Therefore, the thickness of the adventitia can only be estimated. This is facilitated by computing the centroid of the media-adventitia interface and scaling the radius of each interface point by a factor of 1.15. The resulting line is defined as the interface between the adventitia and the surrounding connective tissue. Due to the fact that the adventitia is relatively soft compared to the media, it can be assumed to be of minor importance in case of physiological loading conditions.

The reconstruction strategy is described extensively in BALZANI ET AL. [11] and is used to generate the segment depicted in Fig. 7.11. The shown cross-section A-A is used for presenting the results.

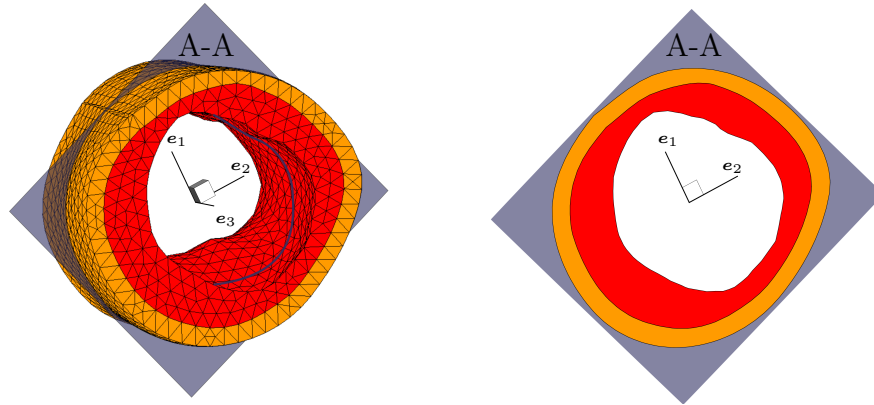


Figure 7.11: Reconstructed, healthy aortic segment meshed with 10-noded quadratic tetrahedron elements and definition of cross-section A-A.

Applying the same simulation scheme as before, the stress distributions $T_{(1)}$ over the complete artery, as well as $T_{(2)}$ in cross-section A-A, without consideration of residual stresses (0 SL) and after several amounts of smoothing loops are depicted in Fig. 7.12 and Fig. 7.13. As it was already done in case of the ideal tube, the evaluation of the results is carried out separately for W_C and W_H . Averaging is performed on $n_{SG} \times n_L = 12 \times 3$ segment domains \mathcal{B}^k . The significant stress peaks without consideration of residual stresses (0 SL) vanish with increasing application of smoothing loops. A proportionate factor γ of 50% is chosen here. Further, the progressive alignment of the fiber stresses within segment domains \mathcal{B}^k becomes apparent. In principle, the contour plots for W_C and W_H seem to be very similar. However, the disproportionately greater increase in volume of the lumen in case of W_H is immediately evident. This effect has already been observed in SCHRÖDER ET AL. [157] and also in Sec. 5.2.2 if the constitutive response is driven by the invariants $\mathbf{E}^2 : \mathbf{M}$ or $I_4^{H^2}$. Additional consideration of inflation experiments within the calibration of the material parameters, in conjunction with the discussed residual stress algorithm, could serve to ensure the right overall conditions.

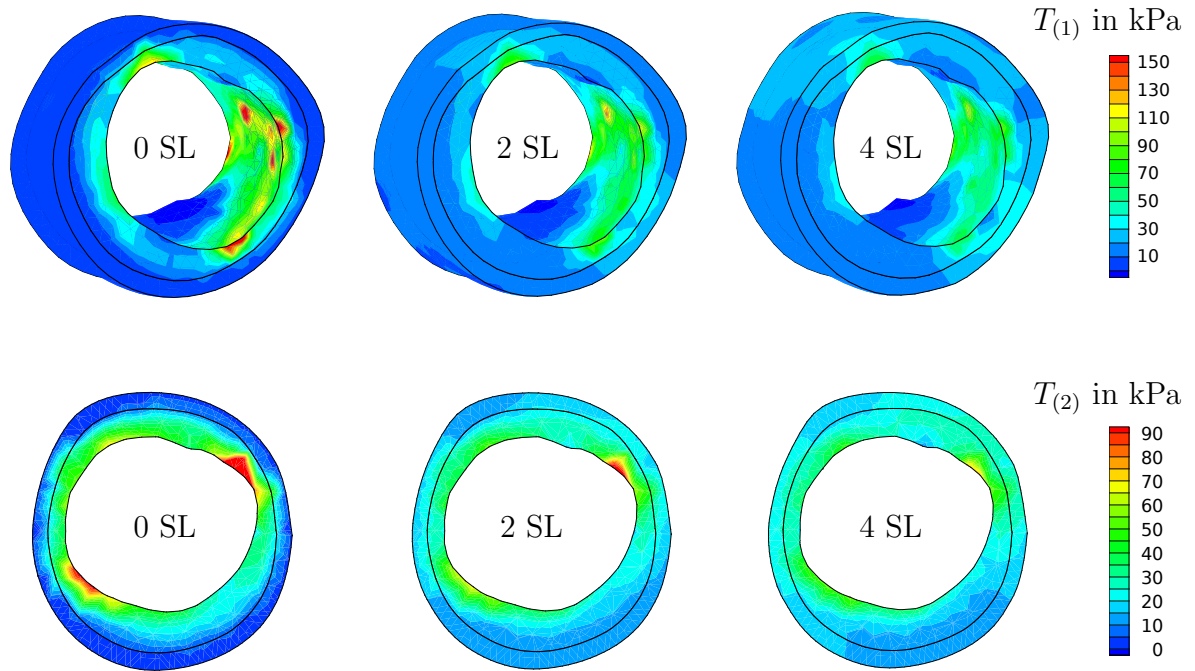


Figure 7.12: Deformed configurations after different amounts of smoothing loops (SL). In the top row the arterial segment and fiber stress $T_{(1)}$ are plotted. In the bottom row section A-A and fiber stress $T_{(2)}$ are plotted. Strain-energy W_C is used.

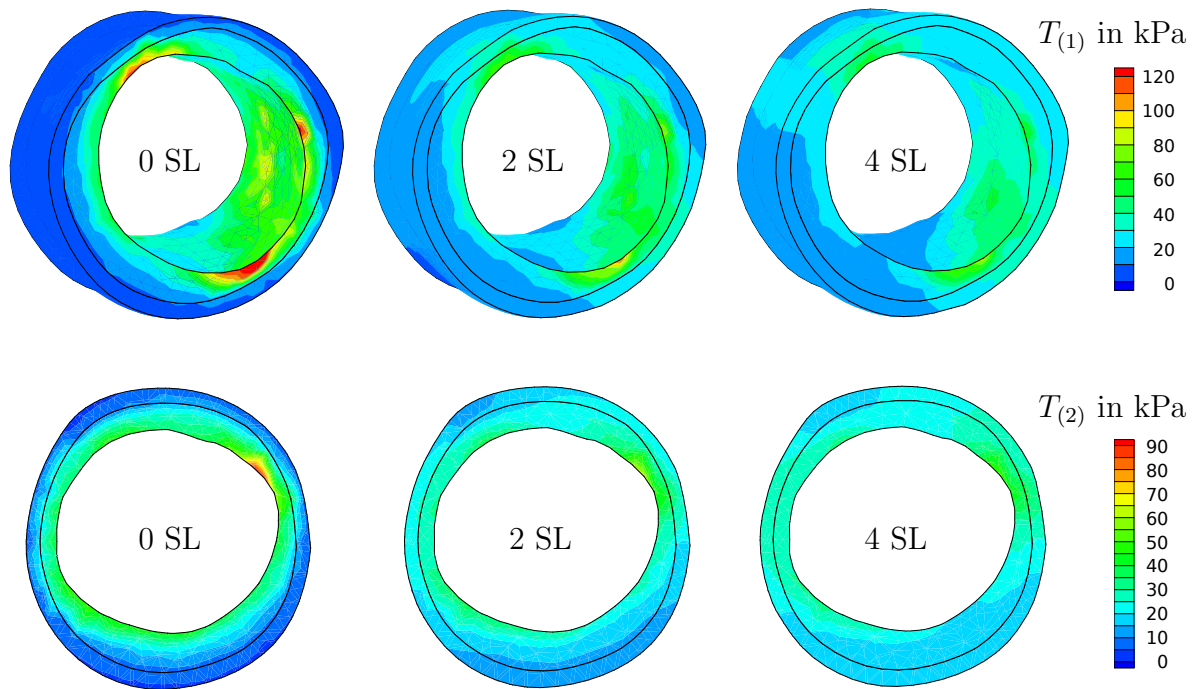


Figure 7.13: Deformed configurations after different amounts of smoothing loops (SL). In the top row the arterial segment and fiber stress $T_{(1)}$ are plotted. In the bottom row section A-A and fiber stress $T_{(2)}$ are plotted. Strain-energy W_H is used.

Irrespective of that, the stress smoothing algorithm is robust and suitable to implement the fundamental hypothesis in view of patient-specific problems. Moreover, the numerical prediction of the opening angle still remains possible. In Fig. 7.14 the simulated opened configurations of the separated media after application of one, two and four smoothing loops with $\gamma = 50\%$ are shown. With increasing amount of smoothing loops, the general stress level increases on the one hand. On the other hand, also the extent of deformation increases. Therefore, both the stress distribution and the opening angle can be controlled with the applied amount of smoothing loops and can possibly be fitted to experiments.

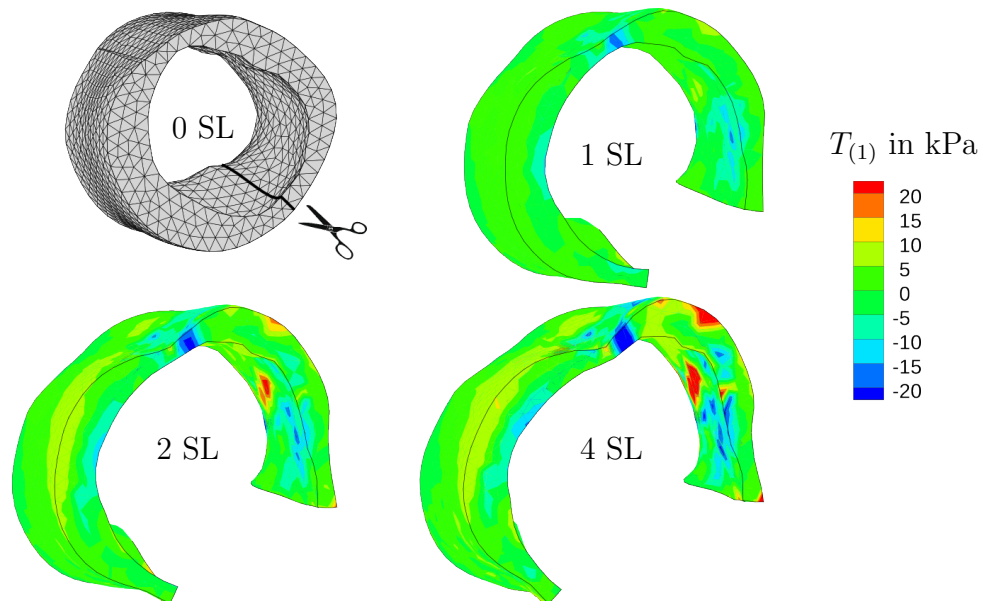


Figure 7.14: Opened configurations after various amounts of smoothing loops (SL) with $\gamma = 50\%$. Stresses, as well as deformations, are increasing with the applied number of SL.

7.5.3 Application of an Inverse Form Finding Algorithm

The IVUS VH images, which are used for the reconstruction of the artery, are captured in-vivo. Therefore, only the loaded actual geometries are known. In the so-far presented examples this fact has been neglected since the non-loaded and not residually stressed configuration was assumed to be known. Nevertheless, the discussed scheme can easily be adapted to an inverse modeling finite element formulation such as introduced by GOVINDJEE AND MIHALIC [57], where the deformed configuration and current loads are known and the unknown reference configuration is computed. In their formulation the weak form of the balance of momentum is parametrized in terms of the inverse motion φ^{-1} and its consistent linearization is derived. Here, the algorithm can easily be adjusted to estimate a residual stress tensor in the described way. The inverse concept was also extended to three-field functionals for quasi incompressible problems, see GOVINDJEE AND MIHALIC [58] and LIU ET AL. [102]. Likewise, the method developed in GEE ET AL. [52], which is based on a modified updated Lagrangian formulation, can be adapted to account for residual stresses. It is rather based on an incremental update of the deformation gradient instead of the displacement field. However, in this case the stress-free configuration is not explicitly computed. The adaption is feasible because both mentioned approaches are based on weak forms which include conventional stress tensors.

In the following, we will restrict ourselves to the algorithm developed by SELIER [160]. This provides a relatively simple and robust method in order to determine the stress-free configuration in terms of an inverse form finding problem. In a first step, the actual configuration is initialized such that the assumed reference configuration coincides with the known configuration from medical imaging, i.e. $\mathbf{X} = \mathbf{x}$. The goal is now to iteratively find a reference configuration \mathbf{X} , corresponding to an actual configuration $\mathbf{x}^* = \mathbf{X} + \mathbf{u}$, which nearly coincides with the known vector field \mathbf{x} derived from medical imaging. After application of the described smoothing algorithm in Tab. 7.4, the reference configuration is updated according to the formula

$$\mathbf{X} \Leftarrow \mathbf{X} - (\mathbf{x}^* - \mathbf{x}). \quad (7.36)$$

Thereafter, a new simulation is initiated, starting from the updated reference configuration with placement vectors \mathbf{X} . The procedure can be repeated until the deviation $\mathbf{x}^* - \mathbf{x}$ becomes sufficiently small. The algorithmic treatment is summarized in Tab. 7.5.

The computed final solution for \mathbf{X} represents the unloaded, residually stressed placement. Thus, if an artery based on the iterated placement \mathbf{X} is loaded with the computed residual stresses we are able to perform the opening angle simulation in the framework of the correct configuration. Note that once an appropriate reference placement for a certain number of smoothing loops has been found, this placement should be used as the initial guess if the number of smoothing loops is changed. Nevertheless, this method dramatically increases the computational cost. In that respect, the above mentioned alternative approaches would be more effective.

The results are shown in Fig. 7.15. In 7.15a) the reconstructed artery from medical imaging is depicted which was already shown earlier in Fig. 7.11. From a theoretical point of view, this configuration is already the loaded one with an internal pressure p_i and residually stressed. The corresponding iterated stress-free configuration according to Tab. 7.5, where 4 SL with $\gamma = 50\%$ are applied, is shown in b). Loading this configuration in turn

- Initialize: $\mathbf{X} = \mathbf{x}$
- Iteration loop
 - a) Application of the proposed algorithm in Tab. 7.4, for a fixed number of smoothing loops SL and using \mathbf{X} as the reference placement: Compute \mathbf{u}
 - b) Compute the corresponding actual placement $\mathbf{x}^* = \mathbf{X} + \mathbf{u}$
 - c) Update the reference placement $\mathbf{X} \leftarrow \mathbf{X} - (\mathbf{x}^* - \mathbf{x})$
If $|\mathbf{x}^* - \mathbf{x}| < \text{tol}$: exit
- end

Table 7.5: Algorithmic box for the computation of the unknown, stress-free reference placement \mathbf{X} .

with an internal pressure p_i and applying the mentioned number of smoothing-loops results in the configuration depicted in c) which is more or less identical with a), i.e. $\mathbf{x}^* \approx \mathbf{x}$. Lastly, the stress-free configuration in Fig. 7.15b) can be exclusively loaded with the estimated residual stresses in c). This yields the non-loaded, residually stressed configuration depicted in d). This computation is in line with the performed opening simulations except of the fact that the artery was not radially sliced. The artery shows considerable fiber stresses in this case which are compressive on the inside near by the lumen and tensile on the outside.

7.6 Residual Strain Approach

It is well known that biology and mechanics can mutually influence each other. Bones, for example, are believed to strongly adapt to the mechanical environment. This leads to the remodeling of the material properties or for instance of the mass. These processes play a key role in the understanding of growing biological tissues. Mechanical forces or stresses can possibly be interpreted as a stimulus of growth. The tissue is then optimized with respect to the stimulus. In case of arterial walls, this is supposed to lead to smoothed stress gradients. In the following, the algorithmic treatment of the residual stress approach is adapted to be capable to smooth the stress gradient by means of elastic stretches instead. For this purpose, a multiplicative split of the deformation gradient

$$\mathbf{F} = \mathbf{F}_e \mathbf{F}_g \quad (7.37)$$

into an elastic part \mathbf{F}_e and a growth part \mathbf{F}_g is introduced as proposed by RODRIGUEZ ET AL. [142]. It is analogous to the split of the deformation gradient in finite strain plasticity. The mapping is summarized in Fig. 7.16, where the intermediate configuration \mathcal{B}_g has a density $\rho_g(\mathbf{X})$ and is in general incompatible as indicated. After multiplication with \mathbf{F}_e we end up with the compatible actual deformation state and configuration \mathcal{B} .

Two different approaches according to Sec. 7.6.2 and 7.6.3 to construct growth tensors \mathbf{F}_g are to be compared. While the first growth tensor refers to isotropic-volumetric growth, the

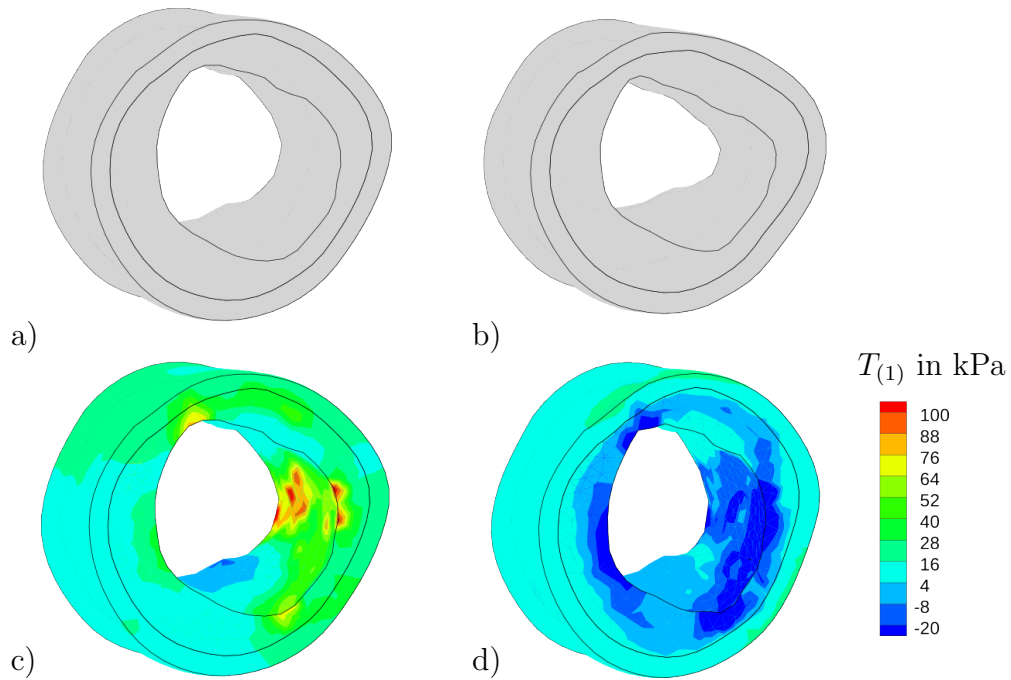


Figure 7.15: Results of the inverse approach: a) Loaded and residually stressed configuration obtained from medical imaging and reconstruction. b) Iterated stress-free configuration. c) Loaded and residually stressed configuration, considering b) as the reference configuration. d) Unloaded and residually stressed configuration, considering b) as the reference configuration.

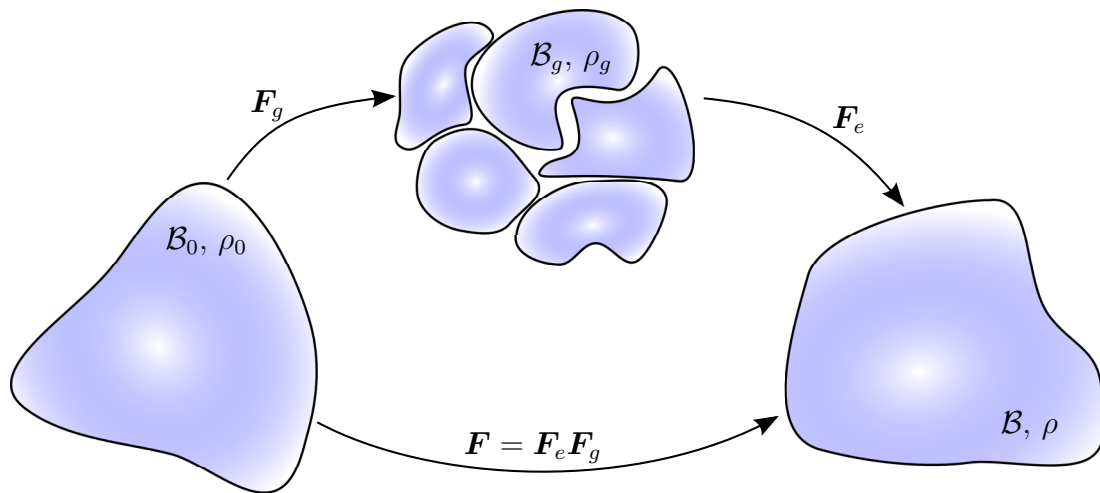


Figure 7.16: Representation of the multiplicative split of the deformation gradient into an elastic part \mathbf{F}_e and a growth part \mathbf{F}_g .

second one represents a novel, incompressible, anisotropic alternative. The general concept of evolution equations for growth tensors presented in HIMPEL ET AL. [69] is applied and coupled with an algorithmic treatment for subsequent consideration of residual strains. The basic strategy is very similar to the already presented residual stress approach. Target values are again defined on arterial sub-domains and the residual strains are incorporated in an iterative scheme based on smoothing-loops.

7.6.1 Incorporation of Residual Strains in the Framework of Open System Thermodynamics

The growth of living tissues demands an energetic mass supply in consideration of the balance equations summarized in Sec. 3.3. The concept of so-called open system thermodynamics is explained in detail in EPSTEIN AND MAUGIN [36]. More information is also provided in HIMPEL ET AL. [69], KUHL ET AL. [93] or MENZEL AND KUHL [115]. In view of the balance of mass one may add a mass source term R_0 with

$$\dot{\rho}_0 = R_0 \quad \text{and} \quad \rho_0 = \det \mathbf{F}_g \rho_g, \quad (7.38)$$

cf. also Eq. (3.32). Only in case that the density of the intermediate configuration is assumed to be constant, it results

$$R_0 = \dot{\rho}_0 = \rho_0 \operatorname{tr} \mathbf{l}_g \quad \text{if} \quad \rho_g = \text{const.} \quad (7.39)$$

with $\mathbf{l}_g = \dot{\mathbf{F}}_g \mathbf{F}_g^{-1}$, cf. Eq. (3.8). It would also be meaningful to consider a mass flux. If this is neglected, the balance of momentum remains unaltered. However, source and flux terms need to be added to the entropy inequality

$$\mathbf{S} : \frac{1}{2} \dot{\mathbf{C}} - \dot{W} - \Theta(\operatorname{Div} \mathbf{T} - T_0) \geq 0, \quad (7.40)$$

where \mathbf{T} denotes the entropy flux, T_0 the entropy source term and the temperature Θ is constant. Further, the time derivative of a free-energy density function $W := W(\mathbf{C}_e) := W(\mathbf{C}, \mathbf{F}_g)$ with the elastic right *Cauchy-Green* tensor $\mathbf{C}_e = \mathbf{F}_e^T \mathbf{F}_e$ is given by

$$\begin{aligned} \dot{W} &= \frac{\partial W}{\partial \mathbf{C}} : \dot{\mathbf{C}} + \frac{\partial W}{\partial \mathbf{F}_g} : \dot{\mathbf{F}}_g \\ &= \left(\frac{\partial W}{\partial \mathbf{C}_e} : \frac{\partial \mathbf{C}_e}{\partial \mathbf{C}} \right) : \dot{\mathbf{C}} + \frac{\partial W}{\partial \mathbf{F}_g} \mathbf{F}_g^T : (\dot{\mathbf{F}}_g \mathbf{F}_g^{-1}) \\ &= \left[\frac{\partial W}{\partial \mathbf{C}_e} : (\mathbf{F}_g^{-T} \boxtimes \mathbf{F}_g^{-T}) \right] : \dot{\mathbf{C}} + \left(\frac{\partial W}{\partial \mathbf{F}_e} : \frac{\partial \mathbf{F}_e}{\partial \mathbf{F}} : \frac{\partial \mathbf{F}}{\partial \mathbf{F}_g} \mathbf{F}_g^T \right) : \mathbf{l}_g \\ &= \left(\mathbf{F}_g^{-1} \frac{\partial W}{\partial \mathbf{C}_e} \mathbf{F}_g^{-T} \right) : \dot{\mathbf{C}} + \left[\frac{\partial W}{\partial \mathbf{F}_e} : (\mathbf{1} \boxtimes \mathbf{F}_g^{-T}) : (\mathbf{F}_e \boxtimes \mathbf{1}) \mathbf{F}_g^T \right] : \mathbf{l}_g \\ &= \left(\mathbf{F}_g^{-1} \frac{\partial W}{\partial \mathbf{C}_e} \mathbf{F}_g^{-T} \right) : \dot{\mathbf{C}} + \left(\mathbf{F}_e^T \frac{\partial W}{\partial \mathbf{F}_e} \right) : \mathbf{l}_g. \end{aligned} \quad (7.41)$$

Inserting the latter equation in Eq. (7.40) results in

$$\left(\mathbf{S} - 2 \mathbf{F}_g^{-1} \frac{\partial W}{\partial \mathbf{C}_e} \mathbf{F}_g^{-T} \right) : \frac{1}{2} \dot{\mathbf{C}} - \left(\mathbf{F}_e^T \frac{\partial W}{\partial \mathbf{F}_e} \right) : \mathbf{l}_g - \Theta(\operatorname{Div} \mathbf{T} - T_0) \geq 0. \quad (7.42)$$

The first part vanishes, if we introduce the constitutive equation

$$\mathbf{S} = 2 \mathbf{F}_g^{-1} \frac{\partial W}{\partial \mathbf{C}_e} \mathbf{F}_g^{-T}. \quad (7.43)$$

The flux and source term need to obey the restriction

$$-\mathbf{M}_e : \mathbf{l}_g \geq \Theta(\operatorname{Div} \mathbf{T} - T_0). \quad (7.44)$$

The tensor \mathbf{M}_e denotes the so-called *Mandel* stresses, see MANDEL [108], which is given by

$$\mathbf{M}_e = \mathbf{F}_e^T \mathbf{P}_e = \mathbf{C}_e \mathbf{S}_e \quad \text{with} \quad \mathbf{P}_e = \frac{\partial W}{\partial \mathbf{F}_e} = \mathbf{F}_e \mathbf{S}_e \quad \text{and} \quad \mathbf{S}_e = 2 \frac{\partial W}{\partial \mathbf{C}_e}. \quad (7.45)$$

In the following, the growth associated deformation gradient is formulated in terms of only one scalar valued variable ϑ and

$$\mathbf{F}_g := \mathbf{F}_g(\vartheta). \quad (7.46)$$

The evolution equation

$$\dot{\vartheta} := \dot{\vartheta}(\vartheta, \mathbf{M}_e) := f_1(\vartheta, \mathbf{M}_e)[f_2(\mathbf{M}_e) - f_2^*] \quad (7.47)$$

is motivated by the entropy inequality and therefore considers the *Mandel* stress as the driving force. Specifically, it is based on two separate scalar valued functions f_1 depending on ϑ and \mathbf{M}_e and f_2 depending only on the *Mandel* stress \mathbf{M}_e . Eq. (7.47) is constructed as a quadratic dissipation potential which is convex like in standard plasticity, the interested reader is referred to HALPHEN AND NGUYEN [63]. Inspired by LUBARDA AND HOGER [104] and HIMPEL ET AL. [69], the evolution criterion f_1 is defined through

$$f_1(\vartheta, \mathbf{M}_e) = \begin{cases} k^+ \left(\frac{\vartheta^+ - \vartheta}{\vartheta^+ - 1} \right)^{m^+} & \text{if } f_2(\mathbf{M}_e) > f_2^* \\ k^- \left(\frac{\vartheta - \vartheta^-}{1 - \vartheta^-} \right)^{m^-} & \text{if } f_2(\mathbf{M}_e) < f_2^* \end{cases}. \quad (7.48)$$

Herein, m^+ , m^- , k^+ , k^- are material parameters controlling the speed of adaption while ϑ^+ and ϑ^- denote growth limit values ensuring that $\vartheta \in [\vartheta^-, \vartheta^+]$. The applied case distinction based on f_2 is decisive to distinguish growth (upper case, label with superscripts +) with $\vartheta^+ > 1$ and atrophy (lower case, labeled with superscripts -) with $\vartheta^- < 1$.

The variable f_2^* represents a target value which is held constant during a single time step. From a theoretical point of view, time dependent growth/atrophy evolves until $f_2 = f_2^*$. As proposed in the residual stress approach, the target values are based on the sector/segment specific averaged target value

$$\bar{f}_2 = \begin{cases} \bar{f}_2^\triangleleft = \frac{1}{v^\triangleleft} \int_{\mathcal{B}^\triangleleft} f_2(\mathbf{x}) dv & \text{for segments} \\ \bar{f}_2^{\triangleleft, \text{mat}} = \frac{1}{v^{\triangleleft, \text{mat}}} \int_{\mathcal{B}^{\triangleleft, \text{mat}}} f_2(\mathbf{x}) dv & \text{for sectors.} \end{cases} \quad (7.49)$$

To increase the robustness of the developed finite element based algorithm the target value f_2^* is not immediately set to the mean value \bar{f}_2 . Instead, the local deviation

$$\Delta f_2 = f_2 - \bar{f}_2 \quad (7.50)$$

is used to compute

$$f_2^* \Leftarrow f_2^* - \frac{\gamma}{n_{\text{inc}}} \Delta f_2, \quad \text{where } \gamma \in [0, 1]. \quad (7.51)$$

in analogy to Eq. (7.34). This is facilitated within a number of n_{inc} sub-incrementation loops in which a total proportion γ of the deviation is applied. The local value of f_2^* is

initialized with $f_2^* = f_2$ after computing the average value in Eq. (7.49). The complete smoothing algorithm is summarized in Tab. 7.6. The first two steps will yield identical results as in Tab. 7.4. After initially dividing the arterial segment into subdomains, it is loaded with the internal blood pressure, neglecting residual stresses. That means the evolution of ϑ is switched off and $\mathbf{F}_g = \mathbf{1}$ while the artery is loaded with the internal pressure p_i . The resulting stress field is then used to subsequently estimate the residual strain with help of smoothing loops. In each loop the estimate Δf_2 is recomputed. This, in turn, is used to update the target value f_2^* in n_{inc} sub-incrementation loops. In each of these, the calculation of a new deformation state is necessary.

<ul style="list-style-type: none"> • Divide domain \mathcal{B} into $n_{\text{SC}}^{2\text{D}}$ or $n_{\text{SC}}^{3\text{D}}$ sectors with subdomains $\mathcal{B}^{\angle, \text{mat}}$ or n_{SG} segments with \mathcal{B}^{\angle}, initialize $\mathbf{F}_g = \mathbf{1}$ • Apply internal pressure p_i (incrementally) and solve the nonlinear boundary value problem: compute \mathbf{F}, \mathbf{S} with $\dot{\vartheta} = 0$ • DO number of smoothing loops (n_{SL}) <ul style="list-style-type: none"> a) Given: $\boldsymbol{\sigma} = \mathbf{F} \mathbf{S} \mathbf{F}^T / J$ and ϑ b) Compute: local volume averages of fiber-stresses \bar{f}_2, Eq. (7.49) Initialize $f_2^* = f_2$ on each <i>Gauss</i>-point and choose Δt c) Compute: deviation Δf_2, Eq. (7.50) e) DO number of sub-incrementation loops (n_{inc}) <ul style="list-style-type: none"> $f_2^* = f_2 - \frac{\gamma}{n_{\text{inc}}} \Delta f_2$, where $\gamma \in [0, 1]$ Switch on growth evolution, i.e. $\dot{\vartheta} \neq 0$ and solve balance of linear momentum: compute $\mathbf{F}, \mathbf{S}, \vartheta$ <p style="text-align: right; margin-right: 20px;">END DO END DO</p>	<div style="display: flex; align-items: center; justify-content: center;"> <div style="font-size: 3em; margin-right: 10px;">}</div> <div style="writing-mode: vertical-rl; transform: rotate(180deg); font-size: 1.2em; margin-right: 10px;">sub-incrementation</div> <div style="font-size: 3em; margin-right: 10px;">}</div> <div style="writing-mode: vertical-rl; transform: rotate(180deg); font-size: 1.2em;">smoothing-loop</div> </div>
--	---

Table 7.6: Algorithmic box describing the numerical implementation of the residual strain approach.

For the numerical treatment of the internal variable ϑ an implicit backward Euler algorithm can be used according to HIMPEL ET AL. [69] in order to determine

$$\vartheta = \vartheta_n + \dot{\vartheta} \Delta t \quad (7.52)$$

in the current time step. Here, ϑ_n denotes the growth associated variable of the previous time-step and Δt the current time increment. Due to the general non-linearity of the equation, the *Newton*-method is used to approximate the root

$$f(\vartheta) = -\vartheta + \vartheta_n + \dot{\vartheta} \Delta t \stackrel{!}{\approx} 0. \quad (7.53)$$

Introducing the *Newton*-iteration index i results in the update

$$\begin{aligned} \vartheta_{i+1} &= \vartheta_i - \frac{f(\vartheta_i)}{\partial_{\vartheta} f(\vartheta_i)} \quad \text{with} \quad \vartheta_{i=0} = \vartheta_n \quad \text{and} \\ \frac{\partial f(\vartheta)}{\partial \vartheta} &= -1 + \frac{\partial \dot{\vartheta}}{\partial \vartheta} \Delta t = -1 + \left[\frac{\partial f_1}{\partial \vartheta} (f_2 - f_2^*) + f_1 \frac{\partial f_2}{\partial \vartheta} \right] \Delta t. \end{aligned} \quad (7.54)$$

In view of Eq. (7.48) we may find that

$$\frac{\partial f_1}{\partial \vartheta} = \begin{cases} \frac{m^+}{\vartheta - \vartheta^+} f_1 & \text{if } f_2(\mathbf{M}_e) > f_2^* \\ \frac{m^-}{\vartheta - \vartheta^-} f_1 & \text{if } f_2(\mathbf{M}_e) < f_2^* \end{cases}. \quad (7.55)$$

Finally, the required material tangent for the finite element implementation is given by

$$\mathbb{C} = 2 \frac{d\mathbf{S}}{d\mathbf{C}} = 2 \frac{\partial \mathbf{S}}{\partial \mathbf{C}_e} : \frac{\partial \mathbf{C}_e}{\partial \mathbf{C}} + 2 \frac{\partial \mathbf{S}}{\partial \vartheta} \otimes \frac{\partial \vartheta}{\partial \mathbf{C}_e} : \frac{\partial \mathbf{C}_e}{\partial \mathbf{C}} = 2 \frac{d\mathbf{S}}{d\mathbf{C}_e} : \frac{\partial \mathbf{C}_e}{\partial \mathbf{C}}. \quad (7.56)$$

7.6.2 Volumetric Growth Tensor

The isotropic, volumetric growth tensor, its time derivative and its inverse are given by

$$\mathbf{F}_g = \vartheta \mathbf{1}, \quad \dot{\mathbf{F}}_g = \dot{\vartheta} \mathbf{1} \quad \text{and} \quad \mathbf{F}_g^{-1} = \frac{1}{\vartheta} \mathbf{1}. \quad (7.57)$$

Thus, the elastic right *Cauchy-Green* tensor follows to

$$\mathbf{C}_e = \mathbf{F}_e^T \mathbf{F}_e = \frac{1}{\vartheta^2} \mathbf{C}. \quad (7.58)$$

In view of the entropy inequality in Eq. (7.44), we identify

$$\mathbf{l}_g = \dot{\mathbf{F}}_g \mathbf{F}_g^{-1} = \frac{\dot{\vartheta}}{\vartheta} \mathbf{1} \quad \text{and} \quad \mathbf{M}_e : \mathbf{l}_g = \frac{\dot{\vartheta}}{\vartheta} \text{tr } \mathbf{M}_e. \quad (7.59)$$

Motivated by the latter, the function f_2 is constructed according to

$$f_2(\mathbf{M}_e) = \text{tr } \mathbf{M}_e. \quad (7.60)$$

In doing so, the necessary entropy source and flux terms to obey the entropy inequality can be directly calculated from Eq. (7.44) and the second *Piola-Kirchhoff* stress is given by

$$\mathbf{S} = 2 \frac{\partial W}{\partial \mathbf{C}_e} : \frac{\partial \mathbf{C}_e}{\partial \mathbf{C}} = \frac{1}{\vartheta^2} \frac{\partial W}{\partial \mathbf{C}_e} = \frac{1}{\vartheta^2} \mathbf{S}_e \quad \text{with} \quad \frac{\partial \mathbf{C}_e}{\partial \mathbf{C}} = \frac{\partial \frac{1}{\vartheta^2} \mathbf{C}}{\partial \mathbf{C}} = \frac{1}{\vartheta^2} \mathbf{1} \boxtimes \mathbf{1}. \quad (7.61)$$

The required derivatives for the non-symmetric material tangent \mathbb{C} are specified in Appendix E.1 for the sake of completeness.

7.6.3 Novel Anisotropic Growth Tensor

Let us introduce the ansatz

$$\mathbf{F}_g = \hat{\alpha} \mathbf{1} + \hat{\beta} \mathbf{M}_\Phi \quad \text{and} \quad \dot{\mathbf{F}}_g = \dot{\hat{\alpha}} \mathbf{1} + \dot{\hat{\beta}} \mathbf{M}_\Phi \quad (7.62)$$

for a symmetric growth tensor. Here, \mathbf{N}_Φ denotes the circumferential direction of the artery with the associated structural tensor $\mathbf{M}_\Phi = \mathbf{N}_\Phi \otimes \mathbf{N}_\Phi$. Then the analytical inverse of \mathbf{F}_g is given by

$$\mathbf{F}_g^{-1} = \hat{\alpha}^{-1} (\mathbf{1} - \mathbf{M}_\Phi) + (\hat{\alpha} + \hat{\beta})^{-1} \mathbf{M}_\Phi. \quad (7.63)$$

If $\det \mathbf{F}_g = 1$ is assumed, one can express both

$$\hat{\alpha} = \vartheta^{-1/2} \quad \text{and} \quad \hat{\beta} = \vartheta - \vartheta^{-1/2} \quad (7.64)$$

in terms of only one internal variable ϑ and it follows that

$$\dot{\hat{\alpha}} = (\vartheta^{-1/2})^\cdot = -\frac{1}{2}\vartheta^{-3/2}\dot{\vartheta} \quad \text{and} \quad \dot{\hat{\beta}} = (\vartheta - \vartheta^{-1/2})^\cdot = \dot{\vartheta} + \frac{1}{2}\vartheta^{-3/2}\dot{\vartheta}. \quad (7.65)$$

In this specific case the growth tensor is actually incompressible and no additional mass supply is required. Moreover, the elastic right *Cauchy-Green* tensor is given by

$$\mathbf{C}_e = \vartheta \mathbf{C} + \left(\frac{1}{\sqrt{\vartheta}} - \vartheta \right) (\mathbf{M}_\Phi \mathbf{C} + \mathbf{C} \mathbf{M}_\Phi) + \left(\frac{1}{\vartheta} - \frac{1}{\sqrt{\vartheta}} \right)^2 \mathbf{M}_\Phi \mathbf{C} \mathbf{M}_\Phi. \quad (7.66)$$

Please note the remarkable property that the stretch of \mathbf{F}_g in direction of \mathbf{N}_Φ , i.e. $\|\mathbf{F}_g \mathbf{N}_\Phi\|$, is equal to ϑ . In that regard, the proposed novel ansatz is very effective in controlling the strain of a specific predefined direction. Furthermore, we obtain the growth related spatial velocity gradient

$$\mathbf{l}_g = \dot{\mathbf{F}}_g \mathbf{F}_g^{-1} = \frac{\dot{\hat{\alpha}}}{\hat{\alpha}} \mathbf{1} + \left(\frac{\dot{\hat{\alpha}} + \dot{\hat{\beta}}}{\hat{\alpha} + \hat{\beta}} - \frac{\dot{\hat{\alpha}}}{\hat{\alpha}} \right) \mathbf{M}_\Phi \quad (7.67)$$

and in the dissipation inequality we identify the term

$$\mathbf{M}_e : \mathbf{l}_g = \frac{\dot{\hat{\alpha}}}{\hat{\alpha}} \text{tr} \mathbf{M}_e + \left(\frac{\dot{\hat{\alpha}} + \dot{\hat{\beta}}}{\hat{\alpha} + \hat{\beta}} - \frac{\dot{\hat{\alpha}}}{\hat{\alpha}} \right) \mathbf{M}_e : \mathbf{M}_\Phi = \frac{\dot{\vartheta}}{\vartheta} \left(\frac{3}{2} \mathbf{M}_e : \mathbf{M}_\Phi - \frac{1}{2} \text{tr} \mathbf{M}_e \right). \quad (7.68)$$

In analogy to the ideas of the volumetric growth model, motivated by the entropy inequality in Eq. (7.44) it appears attractive to construct the function

$$f_2 = \left(\frac{3}{2} \mathbf{M}_e : \mathbf{M}_\Phi - \frac{1}{2} \mathbf{M}_e : \mathbf{1} \right). \quad (7.69)$$

The second *Piola-Kirchhoff* stress is given by

$$\mathbf{S} = 2 \frac{\partial W}{\partial \mathbf{C}_e} : \frac{\partial \mathbf{C}_e}{\partial \mathbf{C}} = \vartheta \mathbf{S}_e + \left(\frac{1}{\sqrt{\vartheta}} - \vartheta \right) (\mathbf{M}_\Phi \mathbf{S}_e + \mathbf{S}_e \mathbf{M}_\Phi) + \left(\frac{1}{\vartheta} - \sqrt{\vartheta} \right)^2 \mathbf{M}_\Phi \mathbf{S}_e \mathbf{M}_\Phi. \quad (7.70)$$

The required derivatives for the non-symmetric material tangent \mathbb{C} as well as $\partial_{\mathbf{C}} \mathbf{C}_e$ are given in Appendix E.2 for the sake of completeness.

7.7 Results of the Residual Strain Approach

7.7.1 Numerical Simulation of an Ideal Tube

To establish comparability of the residual stress and residual strain approach, the same boundary value problem as in Sec. 7.5.1 is discussed. The dimensions and boundary conditions of the ideal tube have already been specified in Fig. 7.5. The averaging of the growth criterion value is evaluated on segment domains $\mathcal{B}^\mathcal{L}$ and thus $\bar{f}_2 = \bar{f}_2^\mathcal{L}$, see Eq. (7.49). Furthermore, only the strain-energy density $W_{\mathbb{C}}$ is considered and the additional parameters determining the growth evolution are set according to Tab. 7.7.

In view of the two introduced growth tensors, it is distinguished between

- ❶: volumetric growth with $\mathbf{F}_g = \vartheta \mathbf{1}$ and $f_2 = \mathbf{M}_e : \mathbf{1}$ according to Sec. 7.6.2 and
- ❷: anisotropic growth with $\mathbf{F}_g = \vartheta^{-1/2} \mathbf{1} + (\vartheta - \vartheta^{-1/2}) \mathbf{M}_\Phi$ and $f_2 = \frac{3}{2} \mathbf{M}_e : \mathbf{M}_\Phi - \frac{1}{2} \mathbf{M}_e : \mathbf{1}$ according to Sec. 7.6.3.

In the presented results, the labels ❶ and ❷ indicate which growth tensor is used. The transmural distributions of the stresses f_2 , σ_{rr} , $\sigma_{\Phi\Phi}$ and σ_{zz} as well as of the internal growth variable ϑ are shown in Fig. 7.17. Under the selected conditions, these are directly comparable to the stress plots associated to W_C in Fig. 7.7.

Table 7.7: Additional parameters for the evolution of growth, cf Eq. (7.48).

k^+ in 1/(kPa s)	m^+ [m^+] = 1	ϑ^+ [ϑ^+] = 1	k^- in 1/(kPa s)	m^- [m^-] = 1	ϑ^- [ϑ^-] = 1	Δt in s
1	5	1.3	2	3	0.5	10

Since the residual stresses and strains are both applied subsequently, the stress plots before smoothing, i.e. after 0 SL, are identical for W_C in Fig. 7.7 and for ❶ and ❷ in Fig. 7.17. In the last mentioned figure, the solid black line and solid red line overlap because the same strain-energy density W_C is used. This is also the reason why the red solid line is not visible. Only for f_2 in Fig. 7.17a) arises a difference due to the different definitions in Eqs. (7.60) and (7.69). As can be seen, the distribution is considerably smoothed in both cases with application of a smoothing loop. The minimization of the radial gradient proceeds with an increasing proportionate factor γ . This becomes apparent when comparing the distributions with $\gamma = 50\%$ and $\gamma = 100\%$. Although not shown in the results, it is worth mentioning that in case of the continued application of further smoothing loops (SL) the gradient would completely vanish, resulting in a constant distribution. The adjustment of f_2 is driven by the internal growth variable ϑ which is plotted over the radius \tilde{r} in e). In the range of the media it generally appears that $\vartheta > 1$ while in the range of the adventitia it appears that $\vartheta < 1$. This seems to be coherent in consideration of the case distinction in Eq. 7.48. As a rough guideline one can state that $f_2 > \bar{f}_2^<$ in the range of the media and therefore ϑ is stimulated to increase. On the other hand, in general one may find that $f_2 < \bar{f}_2^<$ in the range of the adventitia and therefore ϑ is stimulated to decrease. The jump of ϑ at the material interface is a result of the jump of f_2 at 0 SL. Further, it is important to mention that $\det \mathbf{F} \approx \vartheta^3$ in case of the volumetric growth concept ❶ since the penalty part W_{Pen} ensures that $\det \mathbf{F}_e \approx 1$. It follows that $\det \mathbf{F} = \det \mathbf{F}_e \det \mathbf{F}_g \approx \det \mathbf{F}_g = \vartheta^3$. As a consequence, in contrast to ❷ the simulation is far away from being quasi-incompressible. This could only be dealt with within an inverse scheme as presented in Sec. 7.5.3, where a pre-grown reference configuration could be calculated.

It is evident that smoothing of the function f_2 in Fig. 7.17a) goes along with a significant smoothing of $\sigma_{\Phi\Phi}$ in c) and σ_{zz} in d). This is very similar to the residual stress approach and completely in line with the fundamental hypothesis of reduced in-vivo stress gradients. As mentioned several times before, the radial stress distribution depicted in b) is less

flexible due to the equilibrium conditions. However, the distribution becomes more linear with application of the residual strain algorithm as it was also observed for the residual stress algorithm.

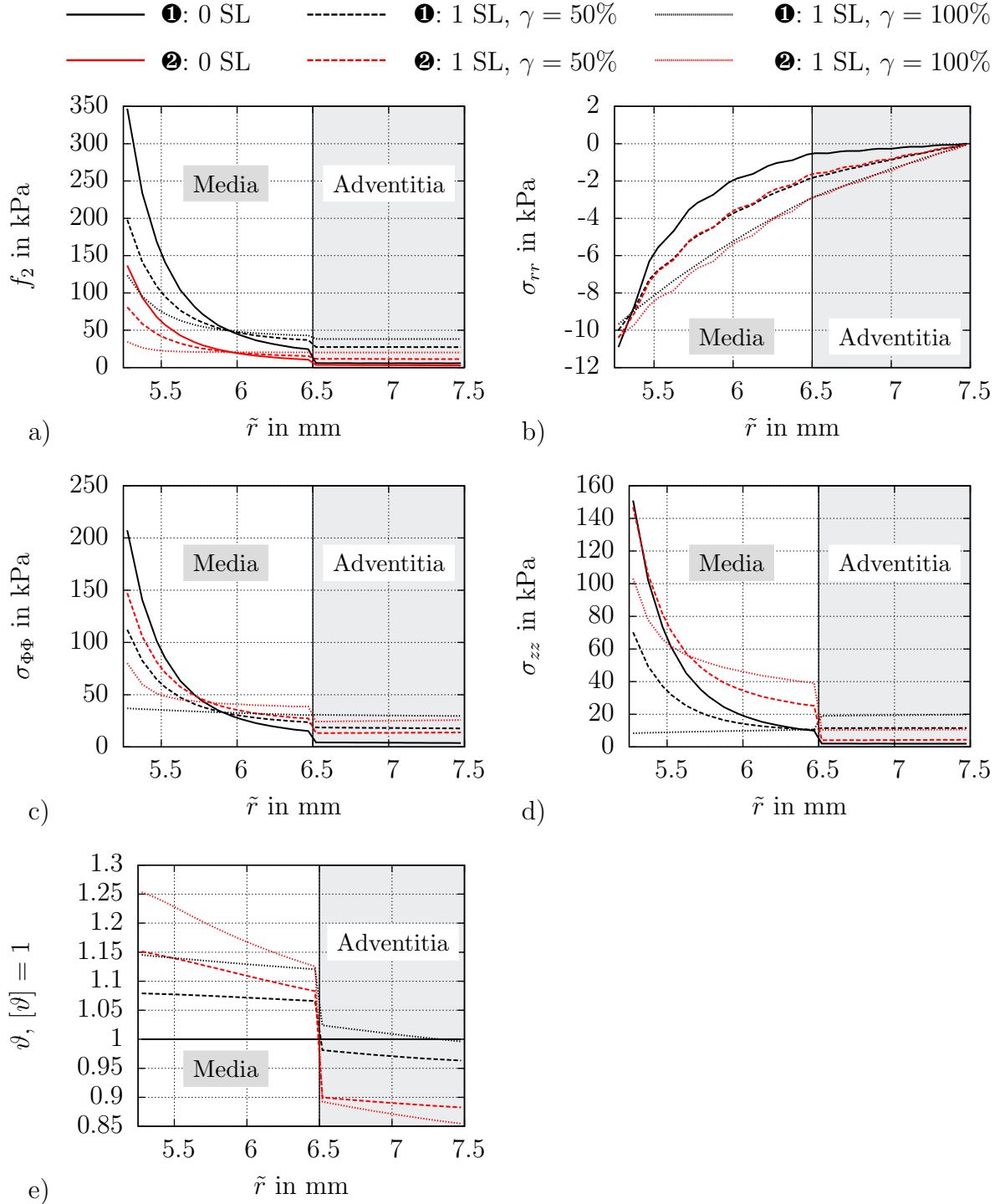


Figure 7.17: Transmural distribution of a) the growth criterion value f_2 which is to be smoothed, b) the radial stress σ_{rr} , c) the circumferential stress $\sigma_{\Phi\Phi}$, d) the axial stress σ_{zz} and e) the growth associated internal variable ϑ after one smoothing loop (SL) with $\gamma = 50\%$ and $\gamma = 100\%$. The strain-energy density W_C is considered. Averaging is performed sector wise, i.e. over domains $B^{\mathcal{L}}$.

In addition, the elastic fiber stretch invariants $I_4^{C^1} = \mathbf{C}_e : \mathbf{M}_{(1)} = \mathbf{C}_e : \mathbf{M}_{(2)}$ are plotted in Fig. 7.18. In contrast to the residual stress approach, compare Fig. 7.8, these are heavily altered after application of the smoothing algorithm. As can be seen, on both material layers the transmural distribution becomes nearly constant although the growth criterion is triggered by a stress function. In conclusion, the superposition of residual stresses to obtain a constant specific stress measure over the radius as presented in Sec. 7.5 predicts very similar distributions like constant elastic fiber stretches over the radius.

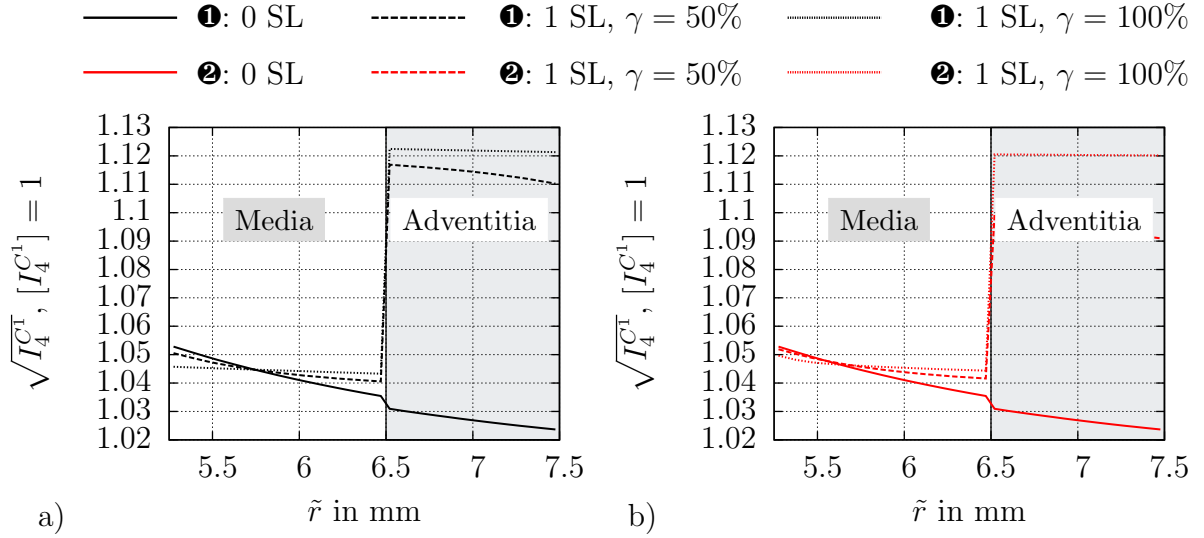


Figure 7.18: Transmural distribution of the invariant $I_4^{C^1} = \mathbf{C} : \mathbf{M}_{(1)} = \mathbf{C} : \mathbf{M}_{(2)}$ after one smoothing loops with $\gamma = 50\%$ and $\gamma = 100\%$. The strain-energy density W_C is considered. Averaging is performed sector wise, i.e. over domains \mathcal{B}^A .

Overall, the results of the residual stress and strain approach are very comparable so far. In order to complete this comparative study, it is reasonable to take also the opened configurations into account. Therefore, the computed local values of ϑ in Fig. 7.17 can be stepwise applied to the unloaded ($p_i = 0$) artery and solved for equilibrium. During each iteration step ϑ is held constant such that the computation of the stress and the material tangent simplifies to

$$\mathbf{S} = 2 \frac{\partial W(\mathbf{C}_e)}{\partial \mathbf{C}_e} : \frac{\partial \mathbf{C}_e}{\partial \mathbf{C}} \quad \text{and} \quad \mathbf{C} = 4 \frac{\partial \mathbf{C}_e}{\partial \mathbf{C}} : \frac{\partial^2 W(\mathbf{C}_e)}{\partial \mathbf{C}_e \partial \mathbf{C}_e} : \frac{\partial \mathbf{C}_e}{\partial \mathbf{C}}. \quad (7.71)$$

Please note that it was considered here that \mathbf{C}_e is linear in \mathbf{C} and thus $\partial^2 \mathbf{C}_e / (\partial \mathbf{C} \partial \mathbf{C}) = \mathbf{0}$. In Fig. 7.19 the computed opened configurations of the artery and the single material layers are shown after consideration of 1 SL with a proportionate factor $\gamma = 100\%$. In the top line the configurations for growth concept **1** are shown and in the bottom line for concept **2**. In both cases the deformation is largest for the artery, while it is quite similar for the media and the adventitia. In a direct comparison, the opening is significantly larger in case of the anisotropic growth scheme **2**. For the final comparison to the residual stress approach the readers attention is drawn to the bottom line of Fig. 7.9. The general characteristic and the ratio of the opening of the artery, the media and the adventitia is again very similar. Especially in view of growth criterion **2** the similarity of the deformed shapes is remarkable. Distinct differences are however revealed when looking

at the occurring stress magnitudes displayed in the contour plots. These are a lot smaller for the residual strain approaches.

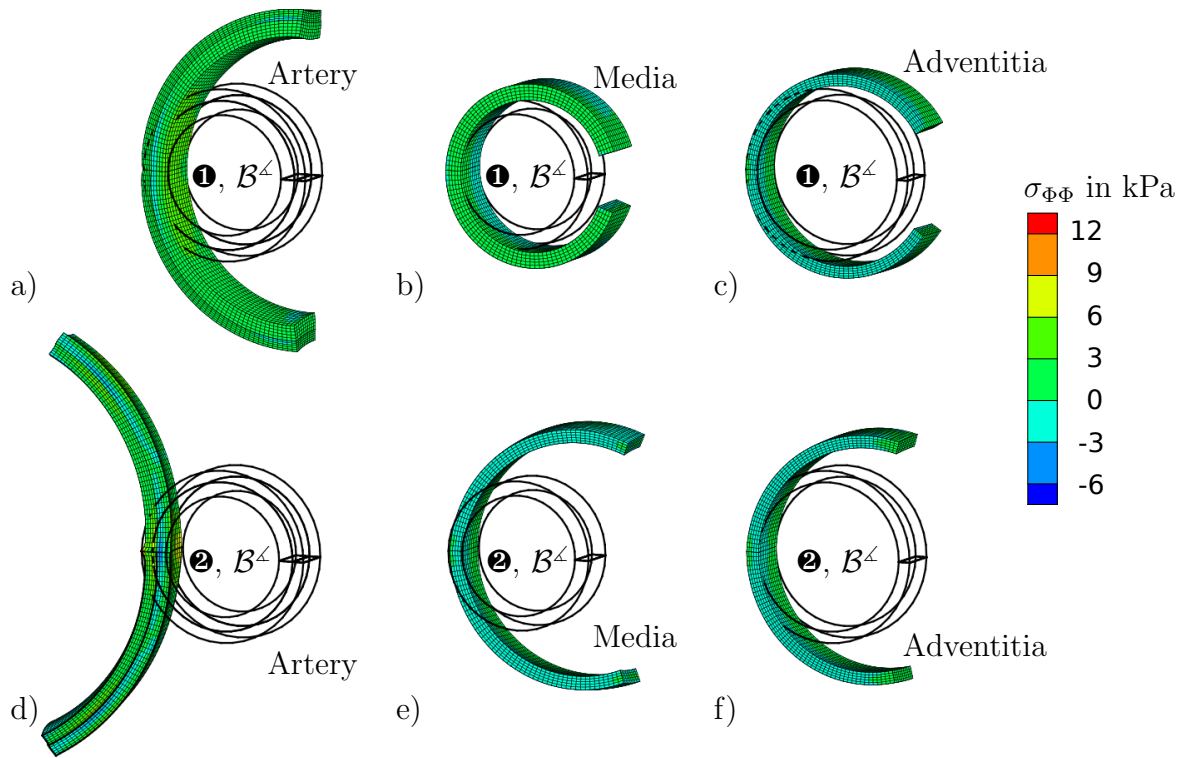


Figure 7.19: Simulations of the opened configuration of the complete artery, the single media and the single adventitia after one smoothing-loop with $\gamma = 100\%$ and averaging over segment domains \mathcal{B}^l . In the top line results of the volumetric growth model ① are shown, while the results of the anisotropic growth model ② are shown in the bottom line. The contour plots depict the circumferential stress $\sigma_{\phi\phi}$. Strain-energy $W_{\mathbb{C}}$ is used.

8 Conclusion & Outlook

Conclusion The present thesis deals with various aspects of constitutive modeling of soft biological tissues from defining strain-energy functions over parameter estimation to the incorporation of residual stresses.

In the first part, a brief overview of the continuum mechanical framework is given. Isotropic and anisotropic large strain invariants are introduced. Based on the right *Cauchy-Green* tensor \mathbf{C} and the *Hencky* strain tensor $\log \mathbf{U}$ different anisotropic invariants are compared and the possibility to distinguish between fiber compression and extension is discussed. It is particularly derived that:

- A switching criterion based on the sign of the invariant $\log \mathbf{U} : \mathbf{M}$ ensures the exclusion of compressed fibers from the constitutive response. However, there may be slightly elongated fibers that are also excluded.

Moreover, an anisotropic micromorphic continuum approach enhanced with additional degrees of freedom is described. This formulation enables a fiber bundle to experience deformations independent from the macroscopic motion. The potential of strain-energies based on \mathbf{C} , $\log \mathbf{U}$ and a micromorphic energy principle are studied on a number of academical examples in view of biomechanical applications. These allow to draw the following generalizing conclusions:

- The micromorphic continuum of order one shows distinct anisotropic properties. Clearly, the effects of independent, elastic fiber reorientation can be detected which can effectively be controlled with help of a penalty formulation. The latter favors affine fiber kinematics. Fiber dispersion can be incorporated directly by considering a director function $\mathbf{A}(\zeta)$ on the micro-space \mathcal{S}_0 which is straightforward to integrate on the 1-D continuum.
- The infinitesimal elasticity tensors at $\mathbf{C} = \mathbf{U} = \mathbf{1}$ of the basic energies formulated in terms of \mathbf{C} and $\log \mathbf{U}$ are identical and also the impact of the preferred direction orientation under tension is quite similar.
- The *Hencky* tensor formulation shows preferable properties for anisotropic problems under compression.

The exploitation of advanced multiscale approaches in biomechanics is attractive in many respects. In this thesis a method is proposed that aims to transfer the high information content included in a multiscale model to considerably simpler and more user-friendly constitutive material laws. The usage of the chosen multiscale approach thereby allows to make relevant data (stress-strain curves) accessible that most probably will never be empirically (experimentally) available to a sufficient extent. This includes the possibility to study the influence of single structural or physical quantities independently from other factors. Additionally, the influence of fiber dispersion in terms of a fiber-density distribution function is evaluated.

The main outcomes of the analysis can be summarized as follows:

- The exponential phenomenological constitutive model shows satisfying fitting properties except of for high values of the collagen fiber radius.
- The plots of the discrete data sets indicate a clear continuous correlation between physical/structural features and phenomenological parameters.
- A closed form-relationship and interpolation of the obtained discrete data set to unveil the correlation of structural and phenomenological parameters appear appropriate and attractive for a wide range of variation of structural properties.
- An inverse relationship to estimate the mean angle of two-dimensional fiber-distributions from biaxial tension tests was developed. If the optimal fiber angle β_f of the phenomenological approach approximately coincides with the loading angle α one may conclude that $\theta_m \approx \alpha \approx \beta_f$.
- An inverse relationship to estimate the variance of two-dimensional fiber-distributions from biaxial tension tests was developed. In particular, a regression function involving the mean angle and the optimized, dispersion related material parameter ζ of the generalized structural tensor was found. In that regard, the fiber direction of the generalized structural tensor has to be informed with the fiber orientation a-priori in shear-free tests.

The constitutive modeling of soft biological tissues based on insights that are solely derived on ex-vivo mechanical tests, however, is not sufficient. As an example, residual stresses occurring in arteries are discussed. Two methods to subsequently incorporate residual stresses or strains in simulations while maintaining the calibration of parameters by means of ex-vivo experiments is described in detail. The presented algorithm is based on the assumption that the stress gradient of suitable invariants in radial direction is smaller than what can be expected from pure mechanical considerations. The invariants take into account the distinct anisotropy of the material. Numerical simulations of ideal tubes and patient-specific segments derived from medical imaging are used to demonstrate the operation of the algorithm. In summary, results show that:

- An extended exponentiated *Hencky* model is able to predict uniaxial tension tests of human arterial samples.
- For both evaluated strain energies based on \mathbf{C} and $\log \mathbf{U}$ the radial stress gradient is significantly smoothed. The opening angle of a sliced artery can be reproduced. The magnitude of the opening can be controlled with help of the applied number of smoothing loops n_{SL} .
- It is simple to adapt the algorithm to an inverse problem in order to distinguish between the stress-free configuration, the unloaded and residually stressed configuration and the blood pressure loaded and residually stressed configuration derived from medical imaging.

- The predictions of the residual stress approach are very comparable to a novel residual strain based approach with an adapted algorithmic concept. The residual strain algorithm is based on a multiplicative tensor split of the deformation gradient and volumetric or anisotropic growth tensors.

Outlook Follow-up studies are conceivable in many respects due to the complexity of the structure of biological tissues. The reliable prediction of stresses and strains is governed by many different factors. In that regard, the active material response due to muscle contraction and viscoelastic effects, which are neglected throughout this thesis, play a key role.

For the micromorphic model only the potential of the formulation in view of biomechanical applications was outlined. A constitutive function that is able to fit experimental data still needs to be developed and validated.

Further, it appears essential to validate the obtained results of the parameter correlations in Sec. 6 based on more experimental tests. Full-field measurements may be considered in order to estimate the difference from the homogenous testing conditions in the presented simulations. The missing availability of shear-experiments constitutes a general limitation. However, the replacement of invasive experiments by simulations remains an inevitable demand. When considering more structural features also the application of artificial intelligence strategies may help to recognize correlations and to continuously update the latest information. In this context, instead of deriving correlations to phenomenological parameters it could be a promising alternative to use purely data-driven models, see KIRCHDOERFER AND ORTIZ [90], which are free of parameters.

Likewise, the consideration of additional experiments to validate residual stress algorithms appears attractive. Apart from solely focusing on the measurements of opening angles and related features, the stress-deformation curves of inflation tests and excised samples under uniaxial or biaxial tension could be taken into account additionally. From a theoretical point of view, the magnitude of the residual stresses should become apparent since the intact artery in an inflation test is residually stressed while the tissue samples are approximately free of those. This discrepancy could be used as an alternative calibration opportunity. From the numerical point of view it would be interesting to test C^1 -continuous discretization schemes such as mesh-free approximations. In that case, the continuity of the stress would allow to replace the expensive computation of the averaged spatial mean values based on a domain decomposition by simpler local conditions which reduce the stress-gradient in radial direction.

In the context of biological growth, the presented anisotropic framework for the *Hencky* strain tensor $\log \mathbf{U}$ could gain special attention. Possibly, usage of the *Hencky* tensor in the constitutive material law allows for an additive split of the deformation gradient instead of the multiplicative split as it is the case in finite plasticity. This would potentially simplify the implementation details.

A Notes on the Notation

Arbitrary base system:

The same tensor may be written in different coordinate system. Considering three arbitrary base vectors $\mathbf{g}_1, \mathbf{g}_2, \mathbf{g}_3$, exemplary tensors of different order can be expressed according to:

$$\begin{aligned} \text{Vector:} \quad \mathbf{A} &:= A^i \mathbf{g}_i = A_i \mathbf{g}^i \\ \text{2nd-order tensor:} \quad \mathbf{E} &:= E^{ij} \mathbf{g}_i \otimes \mathbf{g}_j = E_{ij} \mathbf{g}^i \otimes \mathbf{g}^j = E_i^j \mathbf{g}^i \otimes \mathbf{g}_j = E^i_j \mathbf{g}_i \otimes \mathbf{g}^j \\ \text{4th-order tensor:} \quad \mathbf{C} &:= C^{ijkl} \mathbf{g}_i \otimes \mathbf{g}_j \otimes \mathbf{g}_k \otimes \mathbf{g}_l = C_{ijkl} \mathbf{g}^i \otimes \mathbf{g}^j \otimes \mathbf{g}^k \otimes \mathbf{g}^l \\ &= C^i_{jkl} \mathbf{g}_i \otimes \mathbf{g}^j \otimes \mathbf{g}^k \otimes \mathbf{g}^l = C^{ij}_{kl} \mathbf{g}_i \otimes \mathbf{g}_j \otimes \mathbf{g}^k \otimes \mathbf{g}^l = \dots, \end{aligned}$$

where the *Einstein* summation convention is used. The quantities $A^i, A_i, E^{ij}, E_{ij}, C^{ijkl}, C_{ijkl}, \dots$ denote tensor coefficients. Thereby, it is distinguished between covariant, contravariant and mixed quantities:

$$\begin{aligned} \text{Covariant:} \quad & A_i, E_{ij}, C_{ijkl}, \mathbf{g}_i \\ \text{Contravariant:} \quad & A^i, E^{ij}, C^{ijkl}, \mathbf{g}^i \\ \text{Mixed:} \quad & E_i^j, E^i_j, C^i_{jkl}, C^{ij}_{kl}, \dots \end{aligned}$$

A superscript generally represents a contravariant and a subscript a covariant quantity. Co- and contravariant base vectors are uniquely defined in terms of the scalar products

$$\delta_i^j = \mathbf{g}_i \cdot \mathbf{g}^j = \begin{cases} 1 & \text{if } i = j \\ 0 & \text{if } i \neq j \end{cases} \quad \text{and} \quad \delta^i_j = \mathbf{g}^i \cdot \mathbf{g}_j = \begin{cases} 1 & \text{if } i = j \\ 0 & \text{if } i \neq j \end{cases}. \quad (\text{A.1})$$

The representation of the coefficients can be transformed according to

$$A_i = A^j \mathbf{g}_i \cdot \mathbf{g}_j \quad \text{and} \quad A^i = A_j \mathbf{g}^i \cdot \mathbf{g}^j.$$

and further it holds that

$$A_i = A_j \delta_i^j \quad \text{and} \quad A^i = A^j \delta_j^i.$$

Orthonormal base system:

Provided that the coordinate base vectors are orthogonal unit vectors it is easy to show that the co- and contravariant representations are identical and a distinction can therefore be omitted. Choosing the *Cartesian* axes vectors $\mathbf{e}_1, \mathbf{e}_2$ and \mathbf{e}_3 , exemplary tensors of first, second and fourth order are expressed through:

$$\begin{aligned} \text{Vector:} \quad \mathbf{A} &:= A_i \mathbf{e}_i \\ \text{2nd-order tensor:} \quad \mathbf{E} &:= E_{ij} \mathbf{e}_i \otimes \mathbf{e}_j \\ \text{4th-order tensor:} \quad \mathbf{C} &:= C_{ijkl} \mathbf{e}_i \otimes \mathbf{e}_j \otimes \mathbf{e}_k \otimes \mathbf{e}_l. \end{aligned}$$

The scalar product of the base vectors results in the *Kronecker*-delta

$$\delta_{ij} = \mathbf{e}_i \cdot \mathbf{e}_j = \begin{cases} 1 & \text{if } i = j \\ 0 & \text{if } i \neq j \end{cases}. \quad (\text{A.2})$$

Computation specifications:

Considering an orthonormal base system the basic computation rules are shown in Tab. A.1 for some examples. The order of the resulting tensor of a single contraction is equal two the sum of orders of the two involved tensors minus two. Please note that a single contraction of two vectors $\mathbf{A} \cdot \mathbf{B}$ results in a scalar (tensor of order zero) which is independent of any base system. Similarly, a double contraction of two tensors results in a tensor whose order is equal to the sum of the orders of the involved tensors minus four. The resulting tensor of a dyadic product operation has the order of the sum of orders of the two involved tensors. The superscript $(\bullet)^T$ in Tab. A.1 denotes a transpose operation of a 2nd-order tensor which will exchange the base vectors. If the transposed tensor is of higher order than two of the base vectors need to be specified according to $(\bullet)^{ijT}$, exchanging vectors at position i and j . The \boxtimes operator denotes the *Kronecker* product of second-order tensors. Let \mathbf{C} and \mathbf{D} denote two second-order tensors and \mathbf{A} and \mathbf{B} two first-order tensors, then the operator is defined by $(\mathbf{C} \boxtimes \mathbf{D}) : (\mathbf{A} \otimes \mathbf{B}) = (\mathbf{C}\mathbf{A}) \otimes (\mathbf{D}\mathbf{B})$.

Single contractions	$\mathbf{A} \cdot \mathbf{B}$ $\mathbf{C}\mathbf{D}$	$= A_i e_i \cdot B_j e_j = A_i B_j \delta_{ij} = A_i B_i$ $= C_{ij} e_i \otimes e_j \cdot D_{kl} e_k \otimes e_l = C_{ij} D_{kl} \delta_{jk} \delta_{il} = C_{ij} D_{jl} e_i \otimes e_l$
Double contractions	$\mathbf{C} : \mathbf{D}$ $\mathbb{C} : \mathbf{D}$	$= C_{ij} e_i \otimes e_j : D_{kl} e_k \otimes e_l = C_{ij} D_{kl} \delta_{ik} \delta_{jl} = C_{ij} D_{ij}$ $= \mathbb{C}_{ijkl} e_i \otimes e_j \otimes e_k \otimes e_l : D_{op} e_o \otimes e_p$ $= \mathbb{C}_{ijkl} D_{op} \delta_{ko} \delta_{lp} e_i \otimes e_j = \mathbb{C}_{ijkl} D_{kl} e_i \otimes e_j$
Dyadic Products	$\mathbf{A} \otimes \mathbf{B}$ $(\mathbf{A} \otimes \mathbf{B})^T$ $\mathbf{C} \otimes \mathbf{D}$ $\mathbf{C} \boxtimes \mathbf{D}$ $(\mathbf{C} \otimes \mathbf{D} \otimes \mathbf{E})^{35T}$	$= A_i e_i \otimes B_j e_j = A_i B_j e_i \otimes e_j$ $= (A_i B_j e_i \otimes e_j)^T = (A_i B_j e_j \otimes e_i) = \mathbf{B} \otimes \mathbf{A}$ $= C_{ij} e_i \otimes e_j \otimes D_{kl} e_k \otimes e_l = C_{ij} D_{kl} e_i \otimes e_j \otimes e_k \otimes e_l$ $= C_{ij} e_i \otimes e_j \boxtimes D_{kl} e_k \otimes e_l = C_{ij} D_{kl} e_i \otimes e_k \otimes e_j \otimes e_l$ $= (C_{ij} e_i \otimes e_j \otimes D_{kl} e_k \otimes e_l \otimes E_{op} e_o \otimes e_p)^{35T}$ $= C_{ij} D_{kl} E_{op} e_i \otimes e_j \otimes e_o \otimes e_l \otimes e_k \otimes e_p$

Table A.1: Tensor calculus rules in index notation. While \mathbf{A} and \mathbf{B} are vectors, \mathbf{C} , \mathbf{D} and \mathbf{E} denote 2nd-order tensors and \mathbb{C} is a 4th-order tensor.

Voigt-notation:

The *Voigt*-notation provides a condensed representation of 2nd- and 4th-order tensors. The implementation is numerically efficient and promoted by the symmetry properties of specific tensors. Thereby, symmetric 2nd-order tensors are stored as vectors and the 4th-order material tangent \mathbb{C} as a 6×6 matrix. Thus the increment of the 2nd *Piola-Kirchhoff* stresses

$$\Delta \mathbf{S}^V = \mathbb{C}^V : \Delta \mathbf{E}^V \quad (\text{A.3})$$

may be written in the compact form

$$\begin{pmatrix} \Delta S_{11} \\ \Delta S_{22} \\ \Delta S_{33} \\ \Delta S_{12} \\ \Delta S_{23} \\ \Delta S_{13} \end{pmatrix} = \begin{pmatrix} \mathbf{C}_{1111} & \mathbf{C}_{1122} & \mathbf{C}_{1133} & \mathbf{C}_{11(12)} & \mathbf{C}_{11(23)} & \mathbf{C}_{11(13)} \\ & \mathbf{C}_{2222} & \mathbf{C}_{2233} & \mathbf{C}_{22(12)} & \mathbf{C}_{22(23)} & \mathbf{C}_{22(13)} \\ & & \mathbf{C}_{3333} & \mathbf{C}_{33(12)} & \mathbf{C}_{33(23)} & \mathbf{C}_{33(13)} \\ & & & \mathbf{C}_{(12)(12)} & \mathbf{C}_{(12)(23)} & \mathbf{C}_{(12)(13)} \\ & \text{symm.} & & & \mathbf{C}_{(23)(23)} & \mathbf{C}_{(23)(13)} \\ & & & & & \mathbf{C}_{(13)(13)} \end{pmatrix} \begin{pmatrix} \Delta E_{11} \\ \Delta E_{22} \\ \Delta E_{33} \\ 2\Delta E_{12} \\ 2\Delta E_{23} \\ 2\Delta E_{13} \end{pmatrix}, \quad (\text{A.4})$$

where the abbreviations

$$\mathbf{C}_{ij(kl)} = \frac{1}{2}(\mathbf{C}_{ijkl} + \mathbf{C}_{ijlk}) \quad (\text{A.5})$$

$$\mathbf{C}_{(ij)(kl)} = \frac{1}{4}(\mathbf{C}_{ijkl} + \mathbf{C}_{ijlk} + \mathbf{C}_{jikl} + \mathbf{C}_{jilk}) \quad (\text{A.6})$$

are used.

B Notes on Elasticity Models in Terms of the *Hencky* Strain

The choice of the finite *Hencky* strain $\log \mathbf{U}$ requires some additional derivations and projection tensors to formulate the stress and tangent moduli. Let $\partial_{\log \mathbf{U}} \widehat{W}(\log \mathbf{U})$ be the stress measure work conjugate to $\log \mathbf{U} = \frac{1}{2} \log \mathbf{C}$, then the transformation rule for the second *Piola-Kirchhoff* stress tensor \mathbf{S} is given by

$$\mathbf{S} = 2 \frac{\partial \widehat{W}(\log \mathbf{U})}{\partial \mathbf{C}} = 2 \frac{\partial \widehat{W}(\log \mathbf{U})}{\partial \log \mathbf{U}} : \frac{\partial \log \mathbf{U}}{\partial \mathbf{C}} = \frac{\partial \widehat{W}(\log \mathbf{U})}{\partial \log \mathbf{U}} : \mathbb{P}_H. \quad (\text{B.1})$$

Let us recall the spectral decomposition of the right *Cauchy-Green* tensor \mathbf{C} and the *Hencky* strain:

$$\mathbf{C} = \sum_{k=1}^3 \lambda_k^2 \mathbf{P}_k, \quad \log \mathbf{U} = \sum_{k=1}^3 \log(\lambda_k) \mathbf{P}_k \quad \text{with} \quad \mathbf{P}_k = \mathbf{N}_k \otimes \mathbf{N}_k,$$

where λ_k and \mathbf{N}_k denote the eigenvalues and eigenvectors, respectively. The fourth-order projection tensor \mathbb{P}_H can only be derived with help of the spectral decomposition and yields

$$\begin{aligned} \mathbb{P}_H &= \sum_{k=1}^3 \sum_{j=1}^3 P_{kkjj} \mathbf{N}_k \otimes \mathbf{N}_k \otimes \mathbf{N}_j \otimes \mathbf{N}_j \\ &\quad + 2 \sum_{k=1}^3 \sum_{k \neq j}^3 P_{kjkj} (\mathbf{N}_k \otimes \mathbf{N}_j) \otimes (\mathbf{N}_k \otimes \mathbf{N}_j + \mathbf{N}_j \otimes \mathbf{N}_k) \\ P_{kkjj} &= \delta_{kj} \lambda_k^{-2} \\ P_{kjkj} &= \begin{cases} \frac{\log \lambda_k - \log \lambda_j}{\lambda_k^2 - \lambda_j^2} & \text{for } \lambda_k \neq \lambda_j \\ \lim_{\lambda_k \rightarrow \lambda_j} \frac{\log \lambda_k - \log \lambda_j}{\lambda_k^2 - \lambda_j^2} =: \partial_{\lambda_k}(\log \lambda_k) = (\lambda_k)^{-1} & \text{for } \lambda_k = \lambda_j, \end{cases} \end{aligned} \quad (\text{B.2})$$

see also OGDEN [129] and SIMO [164]. Please note that generally

$$\mathbb{P}_H \neq 2 \frac{\partial \log \mathbf{U}}{\partial \mathbf{C}} \quad (\text{B.3})$$

and Eq. (B.2) is only valid due to the symmetry of $\partial_{\log \mathbf{U}} \widehat{W}(\log \mathbf{U})$. The explicit derivative is given by

$$\begin{aligned} \frac{\partial \log \mathbf{U}}{\partial \mathbf{C}} &= \sum_{k=1}^3 \mathbf{P}_k \otimes \frac{\partial \log \lambda_k}{\partial \mathbf{C}} + \log \lambda_k \frac{\partial \mathbf{P}_k}{\partial \mathbf{C}} \\ &= \sum_{k=1}^3 \mathbf{P}_k \otimes \frac{\partial \log \lambda_k}{\partial \lambda_k^2} \frac{\partial \lambda_k^2}{\partial \mathbf{C}} + \log \lambda_k \frac{\partial \mathbf{P}_k}{\partial \mathbf{C}} \\ &= \sum_{k=1}^3 \frac{1}{2} \lambda_k^{-2} \mathbf{P}_k \otimes \frac{\partial \lambda_k^2}{\partial \mathbf{C}} + \log \lambda_k \frac{\partial \mathbf{P}_k}{\partial \mathbf{C}} \end{aligned} \quad (\text{B.4})$$

and further considering the fundamental derivatives

$$\frac{\partial \lambda_k^2}{\partial \mathbf{C}} = \mathbf{P}_k \quad \text{and} \quad \frac{\partial \mathbf{P}_k}{\partial \mathbf{C}} = \sum_{j=1, j \neq k}^3 \frac{\mathbf{P}_k \boxtimes \mathbf{P}_j^T + \mathbf{P}_j \boxtimes \mathbf{P}_k^T}{\lambda_k^2 - \lambda_j^2}, \quad (\text{B.5})$$

see for instance JOG [88]. Inserting the latter derivatives will result in

$$\frac{\partial \log \mathbf{U}}{\partial \mathbf{C}} = \sum_{k=1}^3 \frac{1}{2} \lambda_k^{-2} \mathbf{P}_k \otimes \mathbf{P}_k + \sum_{k=1}^3 \sum_{\substack{j=1 \\ k \neq j}}^3 \frac{(\log \lambda_k) - (\log \lambda_j)}{\lambda_k^2 - \lambda_j^2} (\mathbf{P}_k \boxtimes \mathbf{P}_j + \mathbf{P}_j \boxtimes \mathbf{P}_k). \quad (\text{B.6})$$

As explained in Sec. 4, the tangent moduli

$$\mathbb{C} = 4 \frac{\partial^2 \widehat{W}(\log \mathbf{U})}{\partial \mathbf{C} \partial \mathbf{C}} = \mathbb{P}_H : \mathbb{C}^H : \mathbb{P}_H + \frac{\partial \widehat{W}(\log \mathbf{U})}{\partial \log \mathbf{U}} : \mathbb{K} \quad (\text{B.7})$$

is required to apply the finite element method to non-linear problems. In the latter equation the chain rule is used again with

$$\mathbb{C}^H = \frac{\partial^2 \widehat{W}(\log \mathbf{U})}{\partial \log \mathbf{U} \partial \log \mathbf{U}} \quad \text{and} \quad \mathbb{K} = 4 \frac{\partial^2 \log \mathbf{U}}{\partial \mathbf{C} \partial \mathbf{C}}. \quad (\text{B.8})$$

The second derivative of $\log \mathbf{U}$ with respect to \mathbf{C} is then necessary to define the 6th order projection tensor \mathbb{K} . It is given by

$$\begin{aligned} \frac{\partial^2 \log \mathbf{U}}{\partial \mathbf{C} \partial \mathbf{C}} &= \sum_{k=1}^3 \mathbf{P}_k \otimes \mathbf{P}_k \otimes \frac{\partial^2 \lambda_k^{-2}}{\partial \mathbf{C}} + \frac{1}{2} \lambda_k^{-2} \left[\left(\frac{\partial \mathbf{P}_k}{\partial \mathbf{C}} \otimes \mathbf{P}_k \right)^{\boxtimes 3} + \mathbf{P}_k \otimes \frac{\partial \mathbf{P}_k}{\partial \mathbf{C}} \right] \\ &\quad + (\log \lambda_k) \frac{\partial^2 \mathbf{P}_k}{\partial \mathbf{C} \partial \mathbf{C}} + \frac{\partial \mathbf{P}_k}{\partial \mathbf{C}} \otimes \frac{\partial \lambda_k^{-2}}{\partial \mathbf{C}} \\ &= \sum_{k=1}^3 -\frac{1}{2} \lambda_k^{-4} \mathbf{P}_k \otimes \mathbf{P}_k \otimes \mathbf{P}_k + \frac{1}{2} \lambda_k^{-2} \left[\left(\frac{\partial \mathbf{P}_k}{\partial \mathbf{C}} \otimes \mathbf{P}_k \right)^{\boxtimes 3} + \mathbf{P}_k \otimes \frac{\partial \mathbf{P}_k}{\partial \mathbf{C}} \right] \\ &\quad + (\log \lambda_k) \frac{\partial^2 \mathbf{P}_k}{\partial \mathbf{C} \partial \mathbf{C}} + \frac{1}{2} \lambda_k^{-2} \frac{\partial \mathbf{P}_k}{\partial \mathbf{C}} \otimes \mathbf{P}_k, \end{aligned} \quad (\text{B.9})$$

considering the abbreviation

$$\begin{aligned} \frac{\partial^2 \mathbf{P}_k}{\partial \mathbf{C} \partial \mathbf{C}} &= \sum_{\substack{j=1 \\ k \neq j}}^3 \frac{1}{\lambda_k^2 - \lambda_j^2} \left[\left(\mathbf{P}_j^T \otimes \left(\frac{\partial \mathbf{P}_k}{\partial \mathbf{C}} \right)^{12}_T \right)^{23}_T + \left(\mathbf{P}_k \otimes \frac{\partial \mathbf{P}_j}{\partial \mathbf{C}} \right)^{23}_T \right. \\ &\quad \left. + \left(\mathbf{P}_k^T \otimes \left(\frac{\partial \mathbf{P}_j}{\partial \mathbf{C}} \right)^{12}_T \right)^{23}_T + \left(\mathbf{P}_j \otimes \frac{\partial \mathbf{P}_k}{\partial \mathbf{C}} \right)^{23}_T \right] \\ &\quad + \frac{1}{(\lambda_k^2 - \lambda_j^2)^2} (\mathbf{P}_k \boxtimes \mathbf{P}_j + \mathbf{P}_j \boxtimes \mathbf{P}_k) \otimes (\mathbf{P}_j - \mathbf{P}_k). \end{aligned} \quad (\text{B.10})$$

C The Concept of Generalized Structural Tensors (GST)

In the following, the dispersion model proposed in GASSER ET AL. [50] is described for the special case of planar fiber dispersion. This case was also addressed in LI ET AL. [100]. Any fiber direction

$$\begin{aligned} \mathbf{A} &= \sin\left(\frac{\pi}{2}\right) \cos\theta \mathbf{e}_1 + \sin\left(\frac{\pi}{2}\right) \sin\theta \mathbf{e}_2 + \cos\left(\frac{\pi}{2}\right) \mathbf{e}_3 \\ &= \cos\theta \mathbf{e}_1 + \sin\theta \mathbf{e}_2 \end{aligned} \quad (\text{C.1})$$

in the fibrous plane spanned by \mathbf{e}_1 and \mathbf{e}_2 may be described by the *Eulerian* angle $\theta \in [-\pi, \pi]$. The fiber density function $\rho_f(\mathbf{A}(\theta)) := \rho_f(\theta)$ is normalized, such that the condition

$$\frac{1}{2\pi} \int_{-\pi}^{\pi} \rho_f(\theta) \, d\theta = 1 \quad (\text{C.2})$$

holds. Then the ansatz of the generalized structural reads as follows:

$$\mathbf{H} = \frac{1}{2\pi} \int_{-\pi}^{\pi} \rho_f(\theta) \mathbf{A}(\theta) \otimes \mathbf{A}(\theta) \, d\theta. \quad (\text{C.3})$$

In index notation it may be written as

$$\mathbf{H} = \alpha_{ij} \mathbf{e}_i \otimes \mathbf{e}_j, \quad (\text{C.4})$$

with

$$\begin{aligned} \alpha_{11} &= \frac{1}{2\pi} \int_{-\pi}^{\pi} \rho_f(\theta) \cos^2\theta \, d\theta, \\ \alpha_{22} &= \frac{1}{2\pi} \int_{-\pi}^{\pi} \rho_f(\theta) \sin^2\theta \, d\theta, \\ \alpha_{33} &= \alpha_{13} = \alpha_{23} = 0, \\ \alpha_{12} &= \frac{1}{2\pi} \int_{-\pi}^{\pi} \rho_f(\theta) \sin\theta \cos\theta \, d\theta. \end{aligned} \quad (\text{C.5})$$

Without loss of generality, let us assume the preferred direction $\mathbf{A}(\theta_{\max})$ for which ρ_f is maximal to coincide with \mathbf{e}_2 , i.e. $\theta_{\max} = \pi/2$. Then the density function is symmetric regarding this specific orientation $\mathbf{A}(\pi/2)$, i.e. $\rho_f(\theta + \pi/2) = \rho_f(-\theta + \pi/2)$ and the

function $(\sin \theta \cos \theta)$ is antisymmetric regarding $\mathbf{A}(\pi/2)$. Therefore, it follows that also $(\rho_f(\theta) \sin \theta \cos \theta)$ is an antisymmetric function on the interval $[-\pi, \pi]$ and thus integration yields

$$\alpha_{12} = 0. \quad (\text{C.6})$$

Further, the relations

$$\alpha_{11} = \varsigma \quad \text{and} \quad \alpha_{22} = \varsigma - 1 \quad \text{with} \quad \varsigma = \frac{1}{2\pi} \int_{-\pi}^{\pi} \rho_f(\theta) \cos^2 \theta \, d\theta \quad (\text{C.7})$$

hold true. Through simple rotation of the coordinate system the general, alternative representation

$$\mathbf{H} = \varsigma \mathbf{I}^* + (1 - 2\varsigma) \mathbf{A}(\theta_{\max}) \otimes \mathbf{A}(\theta_{\max}) \quad (\text{C.8})$$

can be achieved with $\mathbf{I}^* = \mathbf{e}_1 \otimes \mathbf{e}_1 + \mathbf{e}_2 \otimes \mathbf{e}_2$ and an arbitrary angle θ_{\max} . Please note that the ansatz in Eq. C.3 represents a simplification which allows for analytical integration. However, a strain energy formulated with help of a generalized structural tensor is in general not equivalent to the analytical consideration of a fiber distribution function:

$$W(\mathbf{C}, \mathbf{H}) \neq \frac{1}{2\pi} \int_{-\pi}^{\pi} W(\mathbf{C}, \rho_f \mathbf{A}(\theta) \otimes \mathbf{A}(\theta)) \, d\theta. \quad (\text{C.9})$$

D Micromechanical Correlations

D.1 Selected Plots of the Parameter Identification Results and Set $\mathcal{K}(\mathcal{F})$

The following depictions of the results are carried out on the planes

$$\begin{aligned} \mathcal{F}^{(12)} &= \tilde{f}_1 \times \tilde{f}_2 \times \bar{f}_3 \times \bar{f}_4, & \mathcal{F}^{(23)} &= \bar{f}_1 \times \tilde{f}_2 \times \tilde{f}_3 \times \bar{f}_4, \\ \mathcal{F}^{(13)} &= \tilde{f}_1 \times \bar{f}_2 \times \tilde{f}_3 \times \bar{f}_4, & \mathcal{F}^{(24)} &= \bar{f}_1 \times \tilde{f}_2 \times \bar{f}_3 \times \tilde{f}_4, \\ \mathcal{F}^{(14)} &= \tilde{f}_1 \times \bar{f}_2 \times \bar{f}_3 \times \tilde{f}_4, & \mathcal{F}^{(34)} &= \bar{f}_1 \times \bar{f}_2 \times \tilde{f}_3 \times \tilde{f}_4, \end{aligned} \quad (\text{D.1})$$

which are all of cardinality $7 \cdot 7 \cdot 1 \cdot 1 = 49$. The parameters k_1 , k_2 and k_3 are plotted in Figs. D.1–D.3, whereby discrete data points are marked with a black circle. The fitting quality in terms of the objective function value is addressed in Fig. D.4. In summary, all figures together indicate that

- the discrete data sets appear smooth and could be in principle well approximated by continuous functions
- there is no one-by-one structure-mechanics, i.e. especially the parameters k_1 , k_2 , but also k_3 are affected by all structural parameters
- the parameters are subject to significant variation with alteration of structural features at both micro- and nanoscale
- the relationship between structural features and phenomenological parameters appears non-linear in general
- the objective function error is in general sufficiently small but however increases with the fiber radius r_F

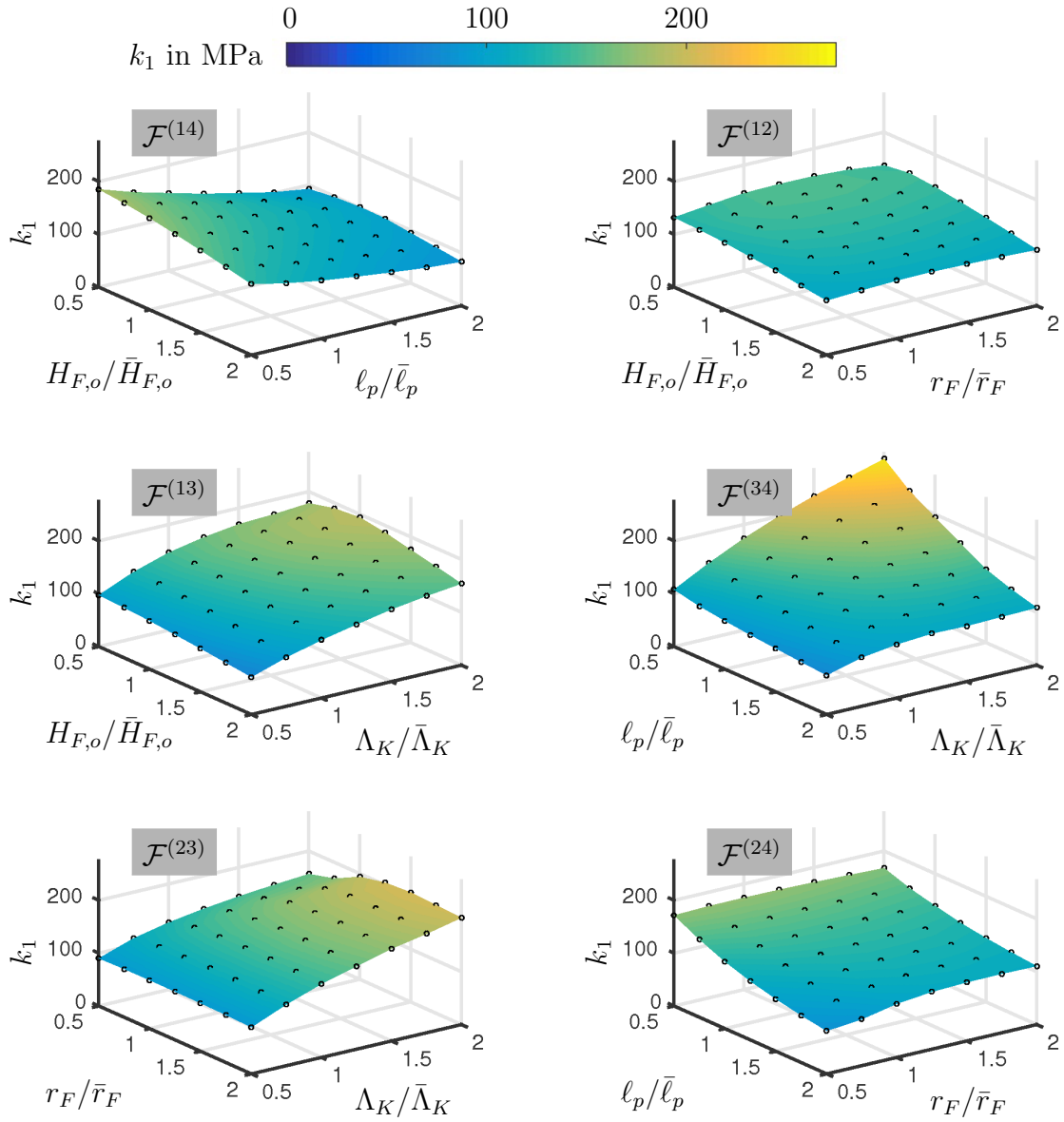


Figure D.1: Dependency of the parameter k_1 plotted on the planes defined in Eq. (D.1). The 49 discrete data points used to generate the surface plots are marked with black circles.

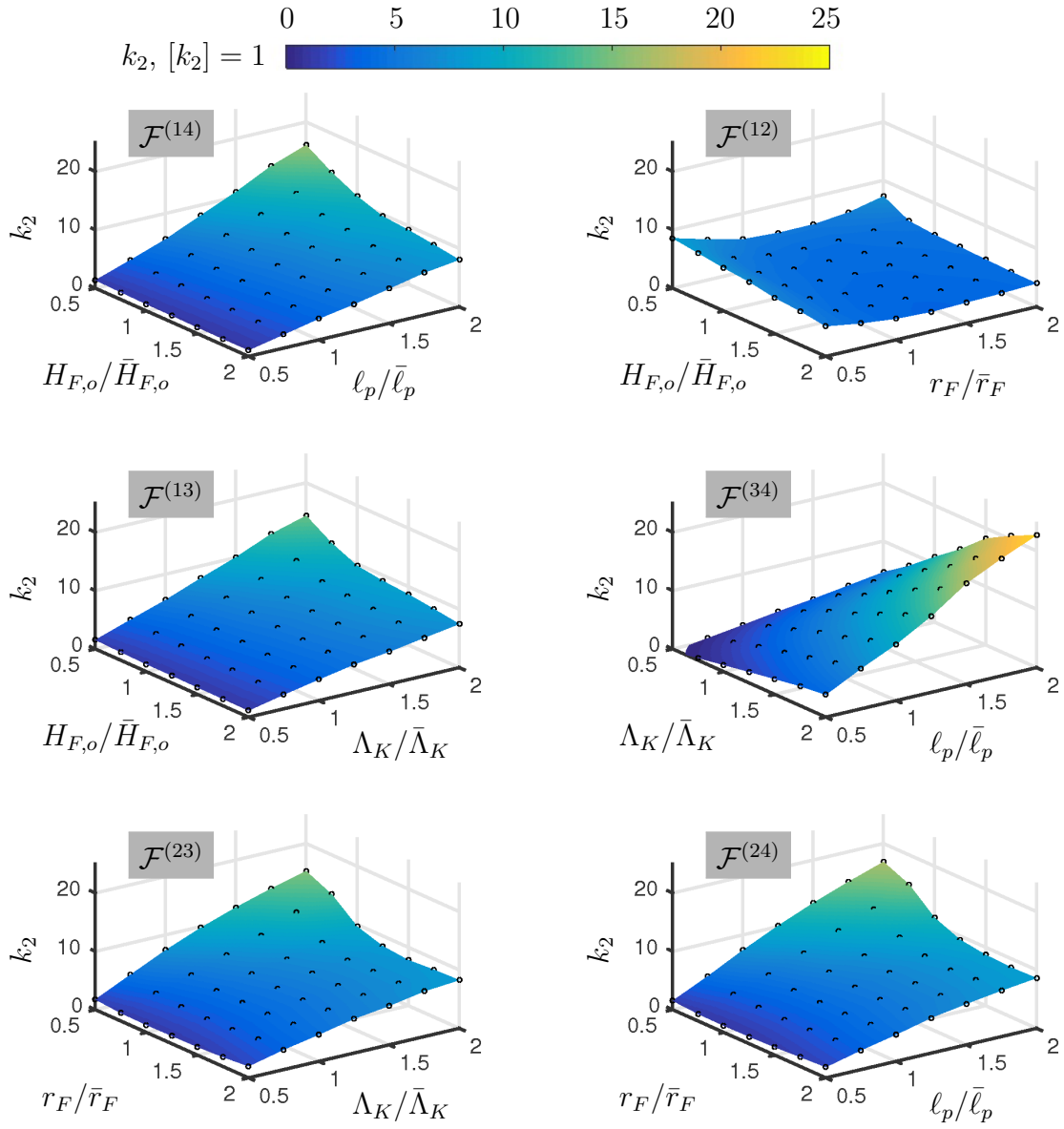


Figure D.2: Dependency of the parameter k_2 plotted on the planes defined in Eq. (D.1). The 49 discrete data points used to generate the surface plots are marked with black circles.

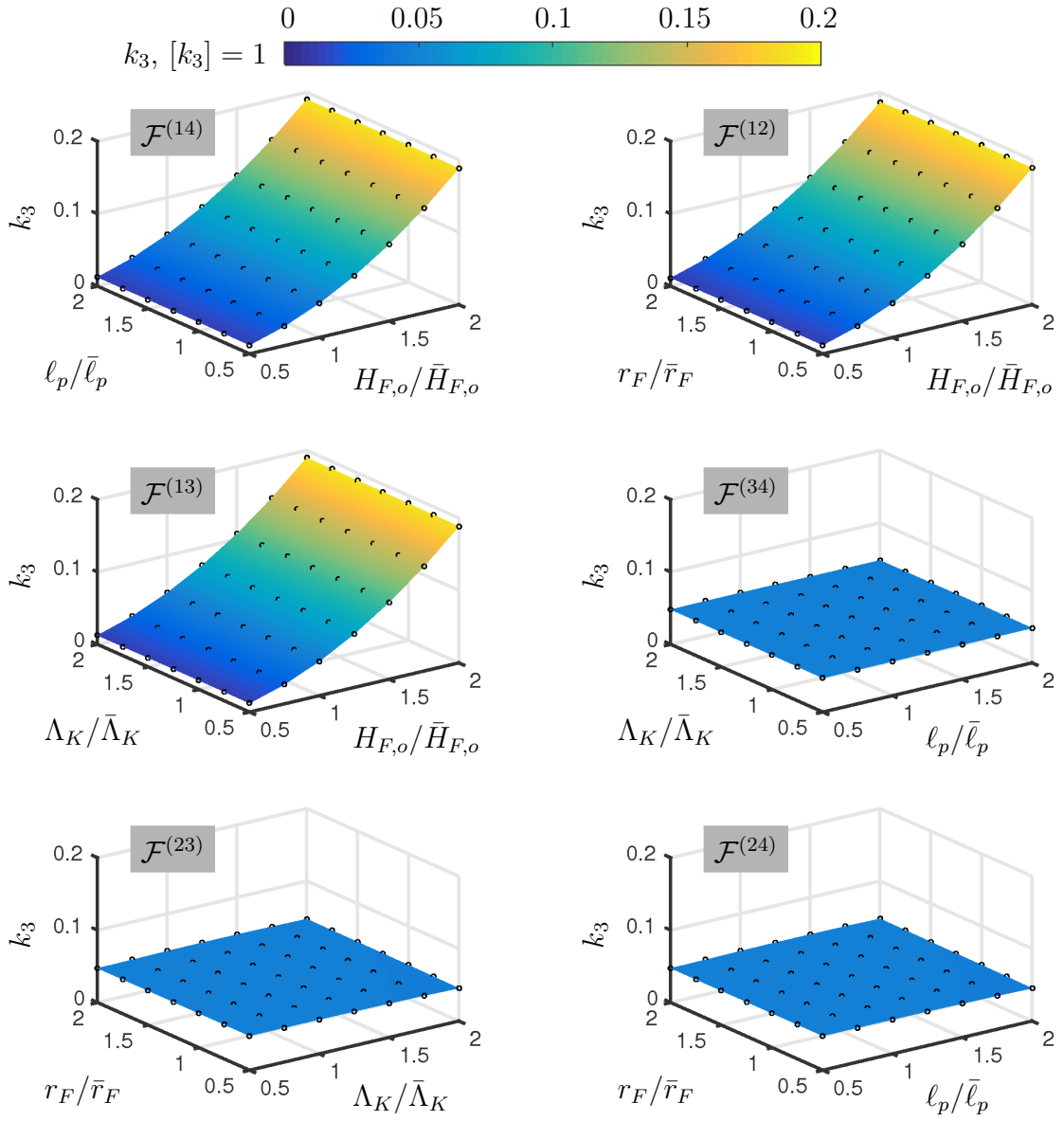


Figure D.3: Dependency of the parameter k_3 plotted on the planes defined in Eq. (D.1). The 49 discrete data points used to generate the surface plots are marked with black circles.

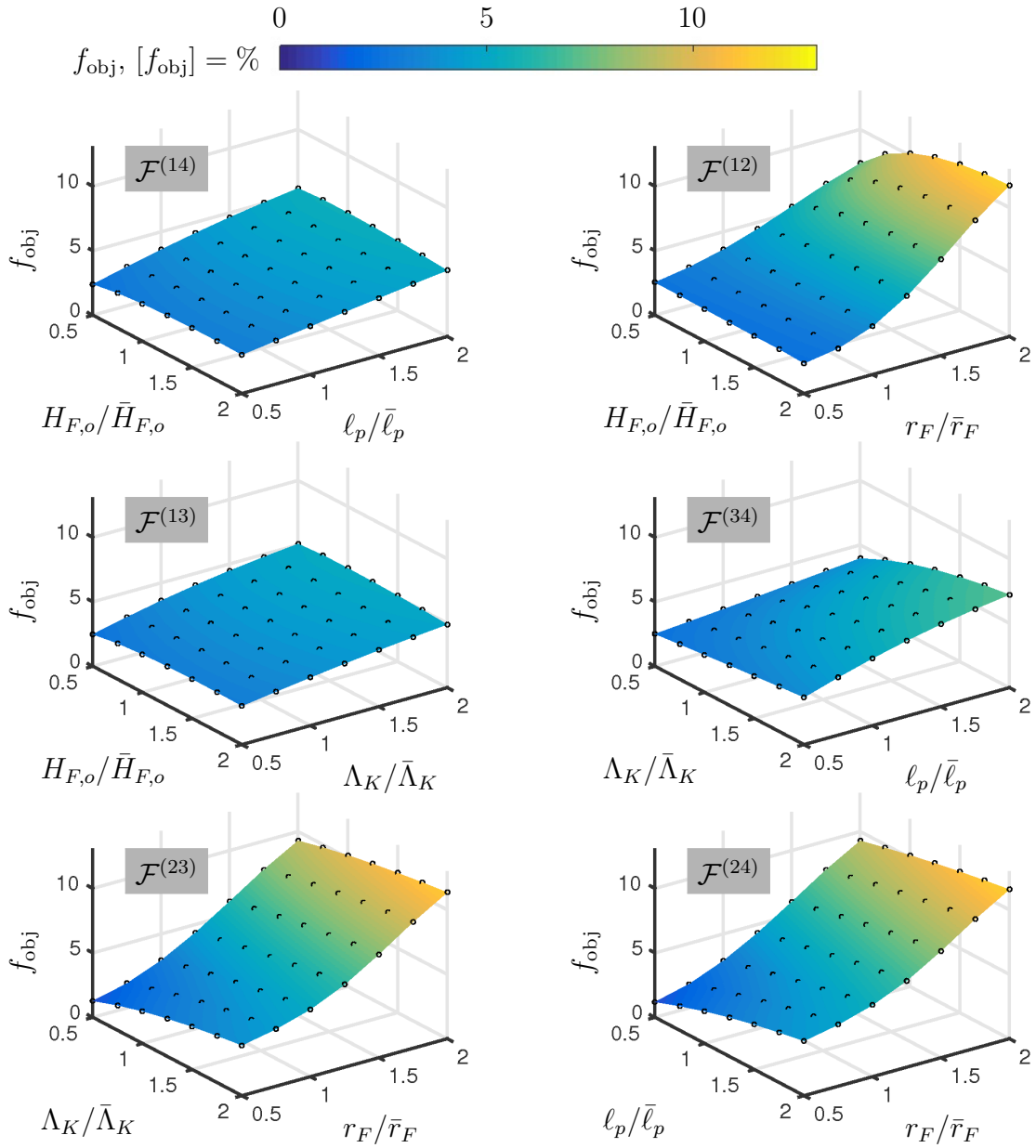


Figure D.4: Dependency of the objective function value f_{obj} plotted on the planes defined in Eq. (D.1). The 49 discrete data points used to generate the surface plots are marked with black circles.

D.2 Regression Coefficients

The regression coefficients in Eq. (6.29), determined by evaluating the minimization problems in Eq. (6.31), are given in Tab. D.1. These are in turn used to compute the regression values k_1^r , k_2^r and k_3^r in Fig. 6.7.

Table D.1: Optimal coefficients $\mathcal{P}_h|_{h=1,2,3}$ of the regression function in Eq. (6.29) to approximate the values of k_1 , k_2 and k_3 .

	$\mathcal{P}_1(h=1)$ [\mathcal{P}_1] = MPa	$\mathcal{P}_2(h=2)$ [\mathcal{P}_2] = 1	$\mathcal{P}_3(h=3)$ [\mathcal{P}_3] = %		$\mathcal{P}_1(h=1)$ [\mathcal{P}_1] = MPa	$\mathcal{P}_2(h=2)$ [\mathcal{P}_2] = 1	$\mathcal{P}_3(h=3)$ [\mathcal{P}_3] = %
b_0^h	142.0687	4.2573	4.8082	b_{22}^h	28.5742	-6.3481	0.1670
b_1^h	-19.0880	-1.6889	9.4264	b_{23}^h	-50.9435	5.5159	-0.0312
b_2^h	15.3174	-3.0489	0.0384	b_{24}^h	-18.6631	1.6737	4.6648
b_3^h	74.1688	6.7804	0.0758	b_{33}^h	-28.7542	5.5906	-0.2038
b_4^h	-56.0694	7.3334	0.0907	b_{34}^h	-29.2143	-0.8305	-0.0525
b_{11}^h	-8.7954	1.5006	-0.0402	b_{44}^h	17.4180	0.0934	-0.0640
b_{12}^h	-2.6776	-2.5041	0.0475				
b_{13}^h	18.5607	-2.7567	0.0548				
b_{14}^h	33.3198	-5.5369	0.1444				

D.3 Collection of Coefficients Used to Generate the Fiber-Density Distributions $v_C^g(\theta)$ for the Biaxial Tension Tests

The optimization scheme according to Tab. 6.5 was used to create the results displayed in Fig. 6.12. The corresponding parameters b and ϖ for the 7 different underlying fiber orientation distributions are shown in Tab. D.2. As can be seen the mean angle θ_m is the same for each case while the variance is different. Since three different load angles $\alpha = \{\bar{\theta}_m, 45^\circ, 63.4^\circ\}$ are applied, this results in $G = 3 \times 7 = 21$ optimization problems according to Eq. (6.61).

Table D.2: Parameters of the fiber distributions v_C^g considered for the optimization problems in Fig. 6.12. All parameters are stated in [\bullet] = deg. except of [b] = 1.

b	ϖ	θ_m	$\sqrt{\text{Var}}$
131.8146	26.8315	26.83	2.5
33.3372	26.8315	26.83	5.0
15.0965	26.8303	26.83	7.5
8.6019	26.7973	26.83	10.0
5.4339	26.5900	26.83	12.5
3.6184	25.8726	26.83	15.0
2.4593	23.9034	26.83	17.5

The 30 different von Mises distributions displayed in Fig. 6.13a) were created based on the optimization scheme in Tab. 6.5. The corresponding determined parameters are shown in Tab. D.3. Variance and mean angle which are included in the table are also plotted in Fig. 6.13b). Since each time only one load angle $\alpha = \theta_m$ was applied, this results in $G = 1 \times 30 = 30$ optimization problems according to Eq. (6.61).

Table D.3: Parameters of the fiber distributions generated in Fig. 6.13a). All parameters are stated in $[\bullet] = \text{deg.}$ except of $[b] = 1$.

b	ϖ	θ_m	$\sqrt{\text{Var}}$	b	ϖ	θ_m	$\sqrt{\text{Var}}$
8.5152	24.9410	25	10	4.8330	24.4981	25	13
8.6842	29.9867	30	10	5.1754	29.8360	30	13
8.7318	34.9971	35	10	5.3203	34.9426	35	13
8.7442	39.9994	40	10	5.3780	39.9814	40	13
8.7466	45.0000	45	10	5.3932	45.0000	45	13
8.7442	50.0006	50	10	5.3780	50.0186	50	13
8.7318	55.0029	55	10	5.3203	55.0574	55	13
8.6842	60.0133	60	10	5.1754	60.0845	60	13
8.5152	65.0590	65	10	4.8330	65.5019	65	13
7.9534	70.2722	70	10	4.0437	71.8853	70	13

b	ϖ	θ_m	$\sqrt{\text{Var}}$
2.9252	22.7387	25	16
3.3237	29.1729	30	16
3.5301	34.6612	35	16
3.6269	39.8736	40	16
3.6551	45.0000	45	16
3.6269	50.1264	50	16
3.5301	55.3388	55	16
3.3237	60.8272	60	16
2.9252	67.2613	65	16
2.2124	79.3473	70	16

Lastly, the optimization scheme in Tab. 6.5 was used once more to generate the fiber orientation distributions which are used to create the results shown in Fig. 6.15. For a specific mean angle $\hat{\theta}_m$ the parameters b and ϖ were adjusted to result in seven different values of $\sqrt{\text{Var}}$. The mean angle ranges between 25° and 70° with a step size of 5° . $\sqrt{\text{Var}}$ ranges between 2.5° and 17.5° with a step size of 2.5° . In total 63 distributions were evaluated for a loading angle of 45° , resulting in $G = 63 \times 1 = 63$ optimization problems according to Eq. (6.61). The parameters are shown in Tab. D.4 and D.5.

Table D.4: Parameters b and ϖ for the fiber distributions of the benchmark data used in Fig. 6.15. Resulting values of characteristic features θ_m and $\sqrt{\text{Var}}$ in Eqs. (6.53) and (6.54) are also specified. All parameters are stated in $[\bullet] = \text{deg.}$ except of $[b] = 1$.

b	ϖ	θ_m	$\sqrt{\text{Var}}$
131.8137	25.0000	25	2.5
33.3372	25.0000	25	5.0
15.0787	24.9974	25	7.5
8.5152	24.9410	25	10.0
5.2823	24.6269	25	12.5
3.4428	23.5752	25	15.0
2.2869	20.6260	25	17.5

b	ϖ	θ_m	$\sqrt{\text{Var}}$
131.8145	30.0000	30	2.5
33.3373	30.0000	30	5.0
15.1081	29.9998	30	7.5
8.6842	29.9867	30	10.0
5.6030	29.8825	30	12.5
3.8346	29.4892	30	15.0
2.6859	28.4059	30	17.5

b	ϖ	θ_m	$\sqrt{\text{Var}}$
131.8145	35.0000	35	2.5
33.3373	35.0000	35	5.0
15.1116	35.0000	35	7.5
8.7318	34.9970	35	10.0
5.7326	34.9608	35	12.5
4.0266	34.7979	35	15.0
2.9062	34.3284	35	17.5

b	ϖ	θ_m	$\sqrt{\text{Var}}$
131.8145	40.0000	40	2.5
33.3373	40.0000	40	5.0
15.1119	40.0000	40	7.5
8.7442	39.9994	40	10.0
5.7819	39.9878	40	12.5
4.1128	39.9268	40	15.0
3.0147	39.7425	40	17.5

b	ϖ	θ_m	$\sqrt{\text{Var}}$
131.8139	50.0000	50	2.5
33.3373	50.0000	50	5.0
15.1119	50.0000	50	7.5
8.7442	50.0006	50	10.0
5.7819	50.0122	50	12.5
4.1128	50.0732	50	15.0
3.0147	50.2574	50	17.5

b	ϖ	θ_m	$\sqrt{\text{Var}}$
131.8148	55.0000	55	2.5
33.3373	55.0000	55	5.0
15.1116	55.0000	55	7.5
8.7318	55.0030	55	10.0
5.7326	55.0392	55	12.5
4.0266	55.2022	55	15.0
2.9062	55.6716	55	17.5

b	ϖ	θ_m	$\sqrt{\text{Var}}$
131.8154	60.0000	60	2.5
33.3373	60.0000	60	5.0
15.1081	60.0003	60	7.5
8.6842	60.0133	60	10.0
5.6030	60.1175	60	12.5
3.8346	60.5107	60	15.0
2.6859	61.5940	60	17.5

b	ϖ	θ_m	$\sqrt{\text{Var}}$
131.8152	65.0000	65	2.5
33.3372	65.0000	65	5.0
15.0787	65.0026	65	7.5
8.5152	65.0590	65	10.0
5.2823	65.3731	65	12.5
3.4428	66.4248	65	15.0
2.2869	69.3738	65	17.5

Table D.5: Remaining parameters b and ϖ for the fiber distributions of the benchmark data used in Fig. 6.15. Resulting values of characteristic features θ_m and $\sqrt{\text{Var}}$ in Eqs. (6.53) and (6.54) are also specified. All parameters are stated in $[\bullet] = \text{deg.}$ except of $[b] = 1$.

b	ϖ	θ_m	$\sqrt{\text{Var}}$
131.8141	70.0000	70	2.5
33.3319	70.0001	70	5.0
14.8780	70.0229	70	7.5
7.9534	70.2722	70	10.0
4.5048	71.4186	70	12.5
2.6921	75.4242	70	15.0
1.7562	90.0647	70	17.5

E Consistent Material Tangents of Growth Algorithms

E.1 Volumetric Growth Tangent

The tangent modulus of the intermediate configuration is given by

$$\mathbb{C}_{eg} = \frac{d\mathbf{S}_e}{d\mathbf{C}_e} = \frac{\partial\mathbf{S}_e}{\partial\mathbf{C}_e} + \frac{\partial\mathbf{S}_e}{\partial\vartheta} \otimes \frac{\partial\vartheta}{\partial\mathbf{C}_e}, \quad (\text{E.1})$$

where the explicit derivatives are defined according to

$$\begin{aligned} \frac{\partial\mathbf{S}_e}{\partial\vartheta} &= \frac{\partial\mathbf{S}_e}{\partial\mathbf{C}_e} : \frac{\partial\mathbf{C}_e}{\partial\vartheta}, \\ \frac{\partial\mathbf{C}_e}{\partial\vartheta} &= -\frac{2}{\vartheta}\mathbf{C}_e, \\ \frac{\partial\mathbf{S}}{\partial\vartheta} &= \frac{\partial\frac{1}{\vartheta^2}\mathbf{S}_e}{\partial\vartheta} = -\frac{2}{\vartheta^3}\mathbf{S}_e + \frac{1}{\vartheta^2}\frac{\partial\mathbf{S}_e}{\partial\vartheta}, \\ \frac{\partial\vartheta}{\partial\mathbf{C}_e} &= \left\{ 1 - \left[\frac{\partial f_1}{\partial\vartheta}(f_2 - f_2^*) + f_1 \frac{\partial f_2}{\partial\vartheta} \right] \Delta t \right\}^{-1} f_1 \frac{\partial f_2}{\partial\mathbf{C}_e} \Delta t, \\ \frac{\partial f_2}{\partial\vartheta} &= \frac{\partial \text{tr} \mathbf{M}_e}{\partial\vartheta} = -\frac{1}{\vartheta} \left(2 \text{tr} \mathbf{M}_e + 2\mathbf{C}_e : \frac{\partial\mathbf{S}_e}{\partial\mathbf{C}_e} : \mathbf{C}_e \right), \\ \frac{\partial f_2}{\partial\mathbf{C}_e} &= \frac{\partial \text{tr} \mathbf{M}_e}{\partial\mathbf{C}_e} = \mathbf{S}_e + \mathbf{C}_e : \frac{\partial\mathbf{S}_e}{\partial\mathbf{C}_e}. \end{aligned} \quad (\text{E.2})$$

In view of Eq. (7.70), we may then determine the derivative

$$\frac{d\mathbf{S}}{d\mathbf{C}_e} = \frac{d\frac{1}{\vartheta^2}\mathbf{S}_e}{d\mathbf{C}_e} = \frac{1}{\vartheta^2}\mathbb{C}_{eg} - \frac{2}{\vartheta^3}\mathbf{S}_e \otimes \frac{\partial\vartheta}{\partial\mathbf{C}_e}. \quad (\text{E.3})$$

Lastly, recalling the final consistent material tangent

$$\mathbb{C} = 2 \frac{d\mathbf{S}}{d\mathbf{C}_e} : \frac{\partial\mathbf{C}_e}{\partial\mathbf{C}}$$

from Eq. (7.56), the projection tensor

$$\frac{\partial \mathbf{C}_e}{\partial \mathbf{C}} = \frac{\partial \frac{1}{\vartheta^2} \mathbf{C}}{\partial \mathbf{C}} = \frac{1}{\vartheta^2} \mathbf{1} \boxtimes \mathbf{1} \quad (\text{E.4})$$

is required.

E.2 Anisotropic Growth Tangent

Again, the tangent modulus of the intermediate configuration is given by

$$\mathbf{C}_{eg} = \frac{d\mathbf{S}_e}{d\mathbf{C}_e} = \frac{\partial \mathbf{S}_e}{\partial \mathbf{C}_e} + \frac{\partial \mathbf{S}_e}{\partial \vartheta} \otimes \frac{\partial \vartheta}{\partial \mathbf{C}_e}, \quad (\text{E.5})$$

where the explicit derivatives are defined according to

$$\begin{aligned} \frac{\partial \mathbf{S}_e}{\partial \vartheta} &= \frac{\partial \mathbf{S}_e}{\partial \mathbf{C}_e} : \frac{\partial \mathbf{C}_e}{\partial \vartheta}, \\ \frac{\partial \mathbf{C}_e}{\partial \vartheta} &= \mathbf{C} + \left(\frac{-1}{2\vartheta^{3/2}} - 1 \right) (\mathbf{M}_\Phi \mathbf{C} + \mathbf{C} \mathbf{M}_\Phi) + 2 \left(\frac{1}{\vartheta} - \sqrt{\vartheta} \right) \left(\frac{-1}{\vartheta^2} - \frac{1}{2\sqrt{\vartheta}} \right) \mathbf{M}_\Phi \mathbf{C} \mathbf{M}_\Phi, \\ \frac{\partial \vartheta}{\partial \mathbf{C}_e} &= \left\{ 1 - \left[\frac{\partial f_1}{\partial \vartheta} (f_2 - f_2^*) + f_1 \frac{\partial f_2}{\partial \vartheta} \right] \Delta t \right\}^{-1} f_1 \frac{\partial f_2}{\partial \mathbf{C}_e} \Delta t, \\ \frac{\partial f_2}{\partial \vartheta} &= \frac{3}{2} \left[\left(\frac{\partial \mathbf{C}_e}{\partial \vartheta} \mathbf{S}_e \right) : \mathbf{M}_\Phi + \left(\mathbf{C}_e \frac{\partial \mathbf{S}_e}{\partial \vartheta} \right) : \mathbf{M}_\Phi \right] - \frac{1}{2} \left(\frac{\partial \mathbf{C}_e}{\partial \vartheta} : \mathbf{S}_e + \mathbf{C}_e : \frac{\partial \mathbf{S}_e}{\partial \vartheta} \right), \\ \frac{\partial f_2}{\partial \mathbf{C}_e} &= \frac{3}{2} \left(\mathbf{M}_\Phi \mathbf{S}_e + \frac{1}{2} [\mathbf{C}_e \mathbf{M}_\Phi] : \frac{\partial \mathbf{S}_e}{\partial \mathbf{C}_e} \right) - \frac{1}{2} \left(\mathbf{S}_e + \frac{1}{2} \mathbf{C}_e : \frac{\partial \mathbf{S}_e}{\partial \mathbf{C}_e} \right). \end{aligned} \quad (\text{E.6})$$

In view of Eq. (7.70) the tangent $d\mathbf{S}/d\mathbf{C}_e$ requires the summation of the four derivatives

$$\begin{aligned} \frac{d\vartheta \mathbf{S}_e}{d\mathbf{C}_e} &= \frac{1}{2} \vartheta \mathbf{C}_{eg} + \mathbf{S}_e \otimes \frac{\partial \vartheta}{\partial \mathbf{C}_e}, \\ \frac{d \left(\frac{1}{\sqrt{\vartheta}} - \vartheta \right) \mathbf{M}_\Phi \mathbf{S}_e}{d\mathbf{C}_e} &= \left(\frac{1}{\sqrt{\vartheta}} - \vartheta \right) \mathbf{M}_\Phi \cdot \mathbf{C}_{eg} + \left(-\frac{1}{2} \vartheta^{-1.5} - 1 \right) \mathbf{M}_\Phi \mathbf{S}_e \otimes \frac{\partial \vartheta}{\partial \mathbf{C}_e}, \\ \frac{d \left(\frac{1}{\sqrt{\vartheta}} - \vartheta \right) \mathbf{S}_e \mathbf{M}_\Phi}{d\mathbf{C}_e} &= \left(\frac{1}{\sqrt{\vartheta}} - \vartheta \right) (\mathbf{M}_\Phi \cdot \mathbf{C}_{eg}^T)^{12} + \left(-\frac{1}{2} \vartheta^{-1.5} - 1 \right) \mathbf{S}_e \mathbf{M}_\Phi \otimes \frac{\partial \vartheta}{\partial \mathbf{C}_e}, \\ \frac{d \left(\frac{1}{\vartheta} - \sqrt{\vartheta} \right)^2 \mathbf{M}_\Phi \mathbf{S}_e \mathbf{M}_\Phi}{d\mathbf{C}_e} &= \left(\frac{1}{\vartheta} - \sqrt{\vartheta} \right)^2 (\mathbf{M}_\Phi \cdot \mathbf{C}_{eg}^T \cdot \mathbf{M}_\Phi)^{24} \\ &\quad + 2 \left(\frac{1}{\vartheta} - \sqrt{\vartheta} \right) \left(\frac{-1}{\vartheta^2} - \frac{1}{2\sqrt{\vartheta}} \right) \mathbf{M}_\Phi \mathbf{S}_e \mathbf{M}_\Phi \otimes \frac{\partial \vartheta}{\partial \mathbf{C}_e}. \end{aligned} \quad (\text{E.7})$$

Lastly, once more recalling the final material tangent

$$\mathbf{C} = 2 \frac{d\mathbf{S}}{d\mathbf{C}_e} : \frac{\partial \mathbf{C}_e}{\partial \mathbf{C}}$$

from Eq. (7.56), the projection tensor

$$\frac{\partial \mathbf{C}_e}{\partial \mathbf{C}} = \vartheta \mathbf{1} \boxtimes \mathbf{1} + \left(\frac{1}{\sqrt{\vartheta}} - \vartheta \right) (\mathbf{M}_\Phi \boxtimes \mathbf{1} + \mathbf{1} \boxtimes \mathbf{M}_\Phi) + \left(\frac{1}{\vartheta} - \frac{1}{\sqrt{\vartheta}} \right)^2 \mathbf{M}_\Phi \boxtimes \mathbf{M}_\Phi \quad (\text{E.8})$$

is required.

List of Figures

2.1	Hierarchical structure of a tendon across different scales. Taken from FRATZL [41] with permission.	10
2.2	Schematic stress-strain relationship of a fiber reinforced uniaxial tension test and associated microscopic images of the collagen network (taken from KRASNY ET AL. [91] with permission). The fibers are initially crimped (left) and straighten with increasing load (right). The fiber distribution is dispersed which means that not all fibers are aligned.	11
2.3	Theoretical comparison of affine and non-affine scale dependent deformations of a (microscopic) plane.	12
2.4	Schematic hierarchical structure of the myocardium allowing for relative slippage of adjacent sheets. The fiber fiber direction is labeled with \mathbf{V}_f , sheet direction with \mathbf{V}_s and the sheet normal direction with \mathbf{V}_n	13
2.5	Different experiments to release residual stresses. The top row shows excised tissue stripes while rings are tested in the bottom row. The images indicate the different opening angles of the artery, the media and the adventitia, respectively. The intima is neglected in this case.	14
3.1	Arbitrary body in the undeformed and deformed configuration \mathcal{B}_0 and \mathcal{B} , respectively. Corresponding base vectors as well as infinitesimal volume-, surface- and line-elements are indicated.	18
3.2	Contour plots of transversely isotropic invariants (left column) based on $\mathbf{C} = \text{diag}[1.35; 0.9; 0.7]$, see Eq. (3.88), and corresponding plots of the signum function (right column). Each point on the spheres is associated with a specific preferred direction $\mathbf{A}(x_1, x_2, x_3)$	31
3.3	Contour plot of transversely isotropic invariants (left column) based on $\log \mathbf{U} = 1/2 \log \mathbf{C}$ with $\mathbf{C} = \text{diag}[1.35; 0.9; 0.7]$, see Eq. (3.88), and corresponding plots of the signum function (right column). Each point on the spheres is associated with a specific preferred direction $\mathbf{A}(x_1, x_2, x_3)$	32
3.4	Comparison of the signum function of $\mathbf{C} : \mathbf{M} - 1$ and $(\log \mathbf{U}) : \mathbf{M}$. Only three different cases are to be distinguished, the transition zone with different sign is colored in light gray. Again, the right <i>Cauchy-Green</i> tensor is set to $\mathbf{C} = \text{diag}[1.35; 0.9; 0.7]$, see Eq. (3.88).	33
3.5	Micromorphic continuum spaces. Taken from VON HOEGEN ET AL. [185].	35
3.6	Micromorphic continuum with a micro-continuum of first order.	35
4.1	Boundary conditions of a continuum in the reference and actual configuration.	42
4.2	Exemplary mesh of a body in the deformed and undeformed configuration discretized with four quadrilateral elements. The nodes of the elements are shown as white dots. The element \mathcal{B}_0^4 is highlighted in orange for further consideration in the following figure.	44

4.3	Exemplary deformation maps of element \mathcal{B}^4 to a reference unit element $\mathcal{B}_{\text{unit}}$. The nodes are numbered counter clockwise with the specific numbers $I = 1, 2, 3, 4$ are circled. Additionally, the placement and deformation vectors \mathbf{X}_I , \mathbf{x}_I and \mathbf{u}_I for node three with $I = 3$ are shown.	45
4.4	Shape functions N_I , Gauss-points \mathbf{GP}_K and corresponding integration weights ω_K of a linear four-noded quadrilateral element.	48
5.1	a) Boundary value problem with varying fiber orientation β_f . b)–d) Displacement plots over β_f for three different constitutive laws and parameter set 1.	58
5.2	a) Boundary value problem with varying fiber orientation β_f . b)–d) Displacement plots over β_f for two different constitutive laws and parameter set 2.	59
5.3	a) Displacement driven equi-biaxial test of a double-symmetric perforated plate. b) Deformed shapes after different applied deformations \bar{u} . c)–d) Deformed geometry and orientation of the director deformations \mathbf{w} for $\bar{u} = 8 \text{ mm}$ and $\bar{u} = 20 \text{ mm}$, respectively. All computations were carried out using the parameters of \widetilde{W}_M according to Tab. 5.3.	61
5.4	Deformed shapes of the perforated plates for different material parameters and deformations \bar{u} on the boundary. Strain-energies formulated in term of the <i>Hencky</i> strain are displayed on the top row and strain-energies formulated in terms of the <i>Green</i> strain on the bottom row. Computations were carried out using the parameters according to Tab. 5.4.	61
5.5	a) Considered boundary value problem and b)–d) deformed shapes after different applied deformations \bar{u} for W_H , W_C and \widetilde{W}_M and material parameters according to Tab. 5.5.	63
5.6	a) Considered boundary value problem and b)–d) deformed shapes after different applied deformations \bar{u} for the micromorphic model \widetilde{W}_M and penalty parameters according to the legend. The remaining parameters are listed in Tab. 5.5.	63
5.7	Deformed shapes after applied deformations $\bar{u} = 0.3 \text{ mm}$ and $\bar{u} = 1.5 \text{ mm}$ for W_H and W_C and material parameters according to Tab. 5.6.	64
5.8	Uniaxial compression and tension test, where the preferred direction and the loading direction are aligned. Taken from SCHRÖDER ET AL. [157].	65
5.9	a) Normalized stress-stretch relationships under uniaxial loading and b) associated lateral stretches. Material parameters according to Tab. 5.7 were used.	66
5.10	Equi-biaxial tension test with a) non-uniform director orientation over the micro-space \mathcal{S}_0 and c) generalized strain tensors. Corresponding results are shown in b), d) and e), where the stress-ratio of horizontal (σ_{11}) and vertical stresses (σ_{22}) is plotted over the displacement \bar{u} of the boundary condition. The example is adapted from VON HOEGEN ET AL. [185].	68

6.1	Uniaxial tension test used to create the benchmark data. The collagen fibers and the loading direction are aligned with the axis \mathbf{e}_1 . The body is assumed to be incompressible.	73
6.2	Flow chart describing the computation of set $\mathcal{K}(\mathcal{F})$	74
6.3	Stress-stretch curves computed for a uniaxial tension test based on the multiscale approach W_u^{multi} and using parameter set $\bar{\mathcal{F}}_g$. In a) the large strain regime \mathcal{R}_ℓ is shown and in b) the small strain regime \mathcal{R}_s	75
6.4	Different contour plots of all 2401 optimized triplets $\mathcal{K}_g(\mathcal{F}_g)$. The four varied structural features f_i are normed with respect to the reference values \bar{f}_i , see Tab. 6.3.	78
6.5	Stress strain curves $\sigma_{11}(\mathcal{F}^{(i)})$ of the benchmark data and fitted uniaxial stress-strain curves $\sigma_{11}^p(\mathcal{K}^{(i)})$. In a) only structural feature $H_{F,o}$, in b) fiber radius r_F , in c) cross-link stiffness Λ_K and in d) persistence length ℓ_p is varied. The structural feature values increase in direction of the indicated arrow.	79
6.6	Stress strain curves $\sigma_{11}(\mathcal{F}^{(i)})$ of the benchmark data and fitted uniaxial stress-strain curves $\sigma_{11}^p(\mathcal{K}^{(i)})$ in the small strain regime \mathcal{R}_s . In a) only fiber radius r_F and in b) only persistence length ℓ_p is varied. The structural feature values increase in direction of the indicated arrow.	80
6.7	a)–c) Comparison of the 256 regression values k_h^r and the optimal values k_h . d) Comparison of the error estimates of the stress-strain curves computed based on the regression values ($f_{\text{obj}}^u(\mathcal{K}_g^r)$) and based on the optimal values ($f_{\text{obj}}^u(\mathcal{K}_g)$). In each figure the plotted ideal straight line corresponds to the best possible matches.	81
6.8	a)–c) Comparison of the 1296 interpolated values k_h^{Int} and the optimal values k_h . d) Comparison of the error estimates of the stress-strain curves computed based on the interpolated values ($f_{\text{obj}}^u(\mathcal{K}_g^{\text{Int}})$) and based on the optimal values ($f_{\text{obj}}^u(\mathcal{K}_g^*)$). In each figure the plotted ideal straight line corresponds to the best possible matches.	82
6.9	a) Planar dispersive fiber arrangement of a tissue sample and b) associated fiber density distribution function. The dispersed fibers are symmetric regarding the axis \mathbf{e}_1 . The volume fraction $v_C := v_C(\theta)$ is indicated by the line thickness of $\mathbf{A}(\theta)$. c) Biaxial testing conditions.	84
6.10	Flow chart describing the computation of set $\mathcal{K}(\mathcal{F})$	85
6.11	Experimentally measured fiber distribution from SCHRIEFL ET AL. [149] and the adjusted, symmetric distribution $\bar{v}_C(\theta)$ obtained with help of Eq. (6.51).	86
6.12	Evolution of k_1 , k_2 , k_3 and β_f over the standard deviation $\sqrt{\text{Var}}$. The mean angle of each underlying fiber distribution is equal to $\theta_m = \bar{\theta}_m = 26.83^\circ$ and three different load angles are applied. The energy density $W_b^{\text{pheno}} = W_{b,\text{exp}}^{\text{pheno}}$ is chosen.	90
6.13	a) Different generated fiber volume fraction distributions v_C^g and b) corresponding $\sqrt{\text{Var}}$ and θ_m values.	90

- 6.14 Evolution of $\beta_f^{(1)}$ over the mean angle. The fiber volume fraction distributions were chosen according to Fig. 6.13. The load angle α is chosen to coincide with θ_m in each case. 91
- 6.15 Inverse analysis of the variance in biaxial tests. a) Optimal values of ς over the standard deviation $\sqrt{\text{Var}}$ for 63 generated fiber distributions $v_C^g(\theta)$. Mean angles θ_m are assigned according to the legend. A loading angle $\alpha = 45^\circ$ is applied and the fiber angle is excluded from the optimization with $\beta_f = \theta_m$ in $W_{b,\text{GST}}^{\text{pheno}}$. b) Verification of the linear regression fitting. Regression function values $\sqrt{\text{Var}_r}$ are plotted over the ideal values $\sqrt{\text{Var}}$ of $v_C^g(\theta)$ 92
- 7.1 a) Excised tissue samples and uniaxial tension tests in b) circumferential and c) axial direction. Taken from SCHRÖDER ET AL. [157]. 97
- 7.2 Comparison of the fitted stress-strain curves of models W_C and W_H with the experimental data. In a) the results of the media and in b) the results of the adventitia are shown. 99
- 7.3 Exemplary definition of segments and sectors of an ideal tube in a) 2-D and b) 3-D. Two material layers with an interface Γ are considered. In a) the media is colored in red and the adventitia in orange. Taken from SCHRÖDER AND VON HOEGEN [153]. 102
- 7.4 Exemplary fiber stress distribution over the wall thickness \tilde{r} and corresponding deviations $\Delta T_{(a)}$ with respect to a) the sector mean stresses $\overline{T}_{(a)}^{\angle,\text{mat}}$ and b) the segment mean stress $\overline{T}_{(a)}^{\angle}$ 103
- 7.5 a) Dissected tube, discretized with 5000 quadratic bricks. b) Boundary conditions to simulate the artery loaded with an internal blood pressure $p_i = 13.33$ kPa. c) Boundary conditions to simulate the opening of the residually stressed artery in the absence of external loads. 105
- 7.6 Transmural distribution of a) the fiber stress $T_{(1)} = T_{(2)}$, b) the radial stress σ_{rr} , c) the circumferential stress $\sigma_{\Phi\Phi}$ and d) the axial stress σ_{zz} after different amounts of smoothing loops (SL) with $\gamma = 100\%$ for W_C and W_H . Averaging is performed sector wise, i.e. over domains $\mathcal{B}^{\angle,\text{mat}}$ 106
- 7.7 Transmural distribution of a) the fiber stress $T_{(1)} = T_{(2)}$, b) the radial stress σ_{rr} , c) the circumferential stress $\sigma_{\Phi\Phi}$ and d) the axial stress σ_{zz} after different amounts of smoothing loops (SL) with $\gamma = 100\%$ for W_C and W_H . Averaging is performed sector wise, i.e. over domains \mathcal{B}^{\angle} 107
- 7.8 Transmural distribution of the invariants $I_4^{C^1} = \mathbf{C} : \mathbf{M}_{(1)} = \mathbf{C} : \mathbf{M}_{(2)}$ and $I_4^{H^2} = (\log \mathbf{U})^2 : \mathbf{M}_{(1)} = (\log \mathbf{U})^2 : \mathbf{M}_{(2)}$ after different amounts of smoothing loops. Averaging is performed sector wise, i.e. over domains \mathcal{B}^{\angle} 108

- 7.9 Simulations of the opened configuration. Depicted configurations of a) the complete artery , b) the single media and c) the single adventitia in the top line are based on averaging over sector domains $\mathcal{B}^{\angle, \text{mat}}$. Depicted configurations of d) the complete artery , e) the single media and f) the single adventitia in the bottom line are based on averaging over segment domains \mathcal{B}^{\angle} . One smoothing-loop with $\gamma = 100\%$ is applied in each case. The contour plots depict the fiber stress $T_{(1)}$. Strain-energy $W_{\mathbb{C}}$ is used. 108
- 7.10 Simulations of the opened configuration. Depicted configurations of a) the complete artery , b) the single media and c) the single adventitia in the top line are based on averaging over sector domains $\mathcal{B}^{\angle, \text{mat}}$. Depicted configurations of d) the complete artery , e) the single media and f) the single adventitia in the bottom line are based on averaging over segment domains \mathcal{B}^{\angle} . One smoothing-loop with $\gamma = 100\%$ is applied in each case. The contour plots depict the fiber stress $T_{(1)}$. Strain-energy $W_{\mathbb{H}}$ is used. 109
- 7.11 Reconstructed, healthy aortic segment meshed with 10-noded quadratic tetrahedron elements and definition of cross-section A-A. 110
- 7.12 Deformed configurations after different amounts of smoothing loops (SL). In the top row the arterial segment and fiber stress $T_{(1)}$ are plotted. In the bottom row section A-A and fiber stress $T_{(2)}$ are plotted. Strain-energy $W_{\mathbb{C}}$ is used. 111
- 7.13 Deformed configurations after different amounts of smoothing loops (SL). In the top row the arterial segment and fiber stress $T_{(1)}$ are plotted. In the bottom row section A-A and fiber stress $T_{(2)}$ are plotted. Strain-energy $W_{\mathbb{H}}$ is used. 111
- 7.14 Opened configurations after various amounts of smoothing loops (SL) with $\gamma = 50\%$. Stresses, as well as deformations, are increasing with the applied number of SL. 112
- 7.15 Results of the inverse approach: a) Loaded and residually stressed configuration obtained from medical imaging and reconstruction. b) Iterated stress-free configuration. c) Loaded and residually stressed configuration, considering b) as the reference configuration. d) Unloaded and residually stressed configuration, considering b) as the reference configuration. 115
- 7.16 Representation of the multiplicative split of the deformation gradient into an elastic part \mathbf{F}_e and a growth part \mathbf{F}_g 115
- 7.17 Transmural distribution of a) the growth criterion value f_2 which is to be smoothed, b) the radial stress σ_{rr} , c) the circumferential stress $\sigma_{\Phi\Phi}$, d) the axial stress σ_{zz} and e) the growth associated internal variable ϑ after one smoothing loop (SL) with $\gamma = 50\%$ and $\gamma = 100\%$. The strain-energy density $W_{\mathbb{C}}$ is considered. Averaging is performed sector wise, i.e. over domains \mathcal{B}^{\angle} 122
- 7.18 Transmural distribution of the invariant $I_4^{C^1} = \mathbf{C} : \mathbf{M}_{(1)} = \mathbf{C} : \mathbf{M}_{(2)}$ after one smoothing loops with $\gamma = 50\%$ and $\gamma = 100\%$. The strain-energy density $W_{\mathbb{C}}$ is considered. Averaging is performed sector wise, i.e. over domains \mathcal{B}^{\angle} 123

7.19	Simulations of the opened configuration of the complete artery, the single media and the single adventitia after one smoothing-loop with $\gamma = 100\%$ and averaging over segment domains \mathcal{B}^λ . In the top line results of the volumetric growth model ❶ are shown, while the results of the anisotropic growth model ❷ are shown in the bottom line. The contour plots depict the circumferential stress $\sigma_{\Phi\Phi}$. Strain-energy W_C is used.	124
D.1	Dependency of the parameter k_1 plotted on the planes defined in Eq. (D.1). The 49 discrete data points used to generate the surface plots are marked with black circles.	135
D.2	Dependency of the parameter k_2 plotted on the planes defined in Eq. (D.1). The 49 discrete data points used to generate the surface plots are marked with black circles.	136
D.3	Dependency of the parameter k_3 plotted on the planes defined in Eq. (D.1). The 49 discrete data points used to generate the surface plots are marked with black circles.	137
D.4	Dependency of the objective function value f_{obj} plotted on the planes defined in Eq. (D.1). The 49 discrete data points used to generate the surface plots are marked with black circles.	138

List of Tables

2.1	Summary of available mechanical experiments on arterial tissue in the literature.	16
3.1	Definition of the degrees of freedom of the micromorphic continuum of order n . Taken from VON HOEGEN ET AL. [185].	36
3.2	Split of the generalized right <i>Cauchy-Green</i> tensor, neglecting higher-order terms in ζ	36
5.1	Parameter set 1 for the uniaxial tension test in Fig. 5.1. All parameters are stated in $[\bullet] = \text{MPa}$ except of $[L_a] = \text{mm}$	57
5.2	Parameter set 2 for the uniaxial tension test in Fig. 5.2. All parameters are stated in $[\bullet] = \text{MPa}$	58
5.3	Parameter set for the equi-biaxial tension test in Fig. 5.3. All parameters are stated in $[\bullet] = \text{MPa}$ except of $[L_a] = \text{mm}$	60
5.4	Parameter sets for the equi-biaxial tension tests carried out in Fig. 5.4. All parameters are stated in $[\bullet] = \text{MPa}$	60
5.5	Parameter sets for the tension tests performed in Fig. 5.5. All parameters are stated in $[\bullet] = \text{MPa}$ except of $[L_a] = \text{mm}$	62
5.6	Parameter sets for the tension tests performed in Fig. 5.7. All parameters are stated in $[\bullet] = \text{MPa}$	64
5.7	Material parameters used to generate the uniaxial stress-strain responses shown in Fig. 5.9. All parameters are stated in $[\bullet] = \text{MPa}$ except of $[L_a] = \text{mm}$	65

5.8	Material parameters used to generate the plots depicted in Fig. 5.10. All parameters are stated in $[\bullet] = \text{MPa}$ except of $[L_a] = \text{mm}$	67
6.1	Computation of the along-the-chord collagen fiber stiffness E_C	70
6.2	Parameters of W_{multi} and considered basic values to compute the numerical experiments. Adapted from MARINO ET AL. [113].	71
6.3	Reference values of the considered multiscale parameters to be varied.	73
6.4	Parameters of the fiber distribution $\bar{v}_C(\theta)$ depicted in Fig. 6.11.	86
6.5	Algorithmic box describing the computation of $v_C^g(\theta)$	87
6.6	Optimal regression parameters \mathcal{P} in Eq. (6.62) from the optimization problem in Eq. (6.64). The parameters are optimized based on the data presented in Fig. 6.15a) and serve to compute the regression function values $\sqrt{\text{Var}_r}$ in Fig. 6.15b).	93
7.1	Optimized parameter sets $\mathcal{K}_W(W_{\mathbb{C}})$ of the media and adventitia and corresponding objective function values.	99
7.2	Optimized parameter sets $\mathcal{K}_W(W_{\mathbb{H}})$ of the media and adventitia and corresponding objective function values. Please note that the shear modulus values are marked with a * since they were not part of the fitting procedure, as explained above.	99
7.3	Chosen parameters associated to the volume expansion of the material. These cannot be fitted in the presented optimization strategy.	100
7.4	Algorithmic box describing the numerical implementation of the residual stress approach. Adapted from SCHRÖDER AND VON HOEGEN [153].	104
7.5	Algorithmic box for the computation of the unknown, stress-free reference placement \mathbf{X}	114
7.6	Algorithmic box describing the numerical implementation of the residual strain approach.	118
7.7	Additional parameters for the evolution of growth, cf Eq. (7.48).	121
A.1	Tensor calculus rules in index notation. While \mathbf{A} and \mathbf{B} are vectors, \mathbf{C} , \mathbf{D} and \mathbf{E} denote 2nd-order tensors and \mathbf{C} is a 4th-order tensor.	130
D.1	Optimal coefficients $\mathcal{P}_h _{h=1,2,3}$ of the regression function in Eq. (6.29) to approximate the values of k_1 , k_2 and k_3	139
D.2	Parameters of the fiber distributions v_C^g considered for the optimization problems in Fig. 6.12. All parameters are stated in $[\bullet] = \text{deg}$. except of $[b] = 1$	139
D.3	Parameters of the fiber distributions generated in Fig. 6.13a). All parameters are stated in $[\bullet] = \text{deg}$. except of $[b] = 1$	140
D.4	Parameters b and ϖ for the fiber distributions of the benchmark data used in Fig. 6.15. Resulting values of characteristic features θ_m and $\sqrt{\text{Var}}$ in Eqs. (6.53) and (6.54) are also specified. All parameters are stated in $[\bullet] = \text{deg}$. except of $[b] = 1$	141

- D.5 Remaining parameters b and ϖ for the fiber distributions of the benchmark data used in Fig. 6.15. Resulting values of characteristic features θ_m and $\sqrt{\text{Var}}$ in Eqs. (6.53) and (6.54) are also specified. All parameters are stated in $[\bullet] = \text{deg.}$ except of $[b] = 1$ 142

References

- [1] M. Abrahams. Mechanical behavior of tendon in vitro. *Medical and Biological Engineering*, 5:433–443, 1967.
- [2] V. Alastrué, E. Peña, M. A. Martínez, and M. Doblaré. Assessing the use of the “opening angle method” to enforce residual stresses in patient-specific arteries. *Annals of Biomedical Engineering*, 35:1821–1837, 2007.
- [3] V. Alastrué, M. A. Martínez, and M. Doblaré. Modelling adaptive volumetric finite growth in patient-specific residually stressed arteries. *Journal of Biomechanics*, 41:1773–1781, 2008.
- [4] G. Angel and V. Gheorghe. Interferometric evaluation of collagen concentration in tendon fibers. *Connective Tissue Research*, 13:323–337, 1985.
- [5] H. Åstrand, J. Stålhånd, J. Karlsson, M. Karlsson, B. Sonesson, and T. Länne. In vivo estimation of the contribution of elastin and collagen to the mechanical properties in the human abdominal aorta: effect of age and sex. 110:176–187, 2011.
- [6] E. U. Azeloglu, M. B. Albro, V. A. Thimmappa, G. A. Ateshian, and K. D. Costa. Heterogeneous transmural proteoglycan distribution provides a mechanism for regulating residual stresses in the aorta. *American Journal of Physiology - Heart and Circulatory Physiology*, 294:H1197–H1205, 2008.
- [7] P. Badel, K. Genovese, and S. Avril. 3D residual stress field in arteries: novel inverse method based on optical full-field measurements. *Strain*, 48:528–538, 2012.
- [8] J. M. Ball. Constitutive inequalities and existence theorems in nonlinear elastostatics. In *Nonlinear Analysis and Mechanics: Symposium held at Heriot-Watt University*, 1977.
- [9] D. Balzani, P. Neff, J. Schröder, and G. A. Holzapfel. A polyconvex framework for soft biological tissues. Adjustment to experimental data. *International Journal of Solids and Structures*, 43:6052–6070, 2006.
- [10] D. Balzani, J. Schröder, and D. Gross. Numerical simulation of residual stresses in arterial walls. *Computational Materials Science*, 39:117–123, 2007.
- [11] D. Balzani, D. Böse, D. Brands, R. Erbel, A. Klawonn, O. Rheinbach, and J. Schröder. Parallel simulation of patient-specific atherosclerotic arteries for the enhancement of intravascular ultrasound diagnostics. *Engineering Computations*, 29:888–906, 2012.
- [12] D. H. Bergel. *The visco-elastic properties of the arterial wall*. PhD thesis, University of London, London, 1960.
- [13] J. Black and G. Hastings, editors. *Handbook of biomaterial properties*. Springer Science & Business Media, 2013.
- [14] J. P. Boehler. Lois de comportement anisotrope des milieux continus. *Journal de Mécanique*, 17:153–190, 1978.

-
- [15] J. P. Boehler. A simple derivation of representations for non-polynomial constitutive equations in some cases of anisotropy. *Zeitschrift für angewandte Mathematik und Mechanik*, 59:157–167, 1979.
- [16] J. P. Boehler. Introduction to the invariant formulation of anisotropic constitutive equations. In J. P. Boehler, editor, *Applications of Tensor Functions in Solid Mechanics*, volume 292 of *CISM Courses and Lectures*, pages 13–30. Springer, 1987.
- [17] L. Bozec and M. Horton. Topography and mechanical properties of single molecules of type I collagen using atomic force microscopy. *Biophysical Journal*, 88:4223–4231, 2005.
- [18] S. Brinkhues, A. Klawonn, O. Rheinbach, and J. Schröder. Augmented Lagrange methods for quasi-incompressible materials-applications to soft biological tissue. *International Journal for Numerical Methods in Biomedical Engineering*, 29:332–350, 2013.
- [19] M. J. Buehler and S. Y. Wong. Entropic elasticity controls nanomechanics of single tropocollagen molecules. *Biophysical Journal*, 93:37–43, 2007.
- [20] R. Bustamante and G. A. Holzapfel. Methods to compute 3D residual stress distributions in hyperelastic tubes with application to arterial walls. *International Journal of Engineering Science*, 48:1066–1082, 2010.
- [21] L. Cardamone, A. Valentin, J. F. Eberth, and J. D. Humphrey. Origin of axial pre-stretch and residual stress in arteries. *Biomechanics and Modeling in Mechanobiology*, 8:431–446, 2009.
- [22] Y.-C. Chen and J. F. Eberth. Constitutive function, residual stress, and state of uniform stress in arteries. *Journal of the Mechanics and Physics of Solids*, 60:1145–1157, 2012.
- [23] C. J. Chuong and Y. C. Fung. Three-dimensional stress distribution in arteries. *Journal of Biomechanical Engineering*, 105:268–274, 1983.
- [24] C. J. Chuong and Y. C. Fung. On residual stress in arteries. *Journal of Biomechanical Engineering*, 108:189–193, 1986.
- [25] P. Ciarletta, M. Destrade, and A. L. Gower. On residual stresses and homeostasis: an elastic theory of functional adaptation in living matter. *Scientific Reports*, 6:24390, 2016.
- [26] D. H. Cortes and D. M. Elliott. Accurate prediction of stress in fibers with distributed orientations using generalized high-order structure tensors. *Mechanics of Materials*, 75:73–83, 2014.
- [27] E. Cosserat and F. Cosserat. Théorie des corps déformables. *Herman et fils*, 1909.
- [28] K. D. Costa, J. W. Holmes, and A. D. McCulloch. Modelling cardiac mechanical properties in three dimensions. *Philosophical Transactions of the Royal Society of London A: Mathematical, Physical and Engineering Sciences*, 359:1233–1250, 2001.

-
- [29] R. H. Cox. Anisotropic properties of the canine carotid artery in vitro. *Journal of Biomechanics*, 8:293–300, 1975.
- [30] A. M. Cribb and J. E. Scott. Tendon response to tensile stress: an ultrastructural investigation of collagen: proteoglycan interactions in stressed tendon. 187:423–428, 1995.
- [31] A. Delfino, N. Stergiopoulos, J. E. Moore, and J.-J. Meister. Residual strain effects on the stress field in a thick wall finite element model of the human carotid bifurcation. *Journal of Biomechanics*, 30:777–786, 1997.
- [32] J. Diamant, A. Keller, E. Baer, M. Litt, and R. G. C. Arridge. Collagen: ultrastructure and its relation to mechanical properties as a function of ageing. *Proceedings of the Royal Society London B*, 180:293–315, 1972.
- [33] P. B. Dobrin, T. Canfield, and S. Sinha. Development of longitudinal retraction of carotid arteries in neonatal dogs. *Experientia*, 31:1295–1296, 1975.
- [34] P. B. Dobrin, T. H. Schwarcz, and R. Mrkvicka. Longitudinal retractive force in pressurized dog and human arteries. 48:116–120, 1990.
- [35] V. Ebbing, J. Schröder, and P. Neff. Approximation of anisotropic elasticity tensors at the reference state with polyconvex energies. *Archive of Applied Mechanics*, 79: 651–657, 2009.
- [36] M. Epstein and G. A. Maugin. Thermomechanics of volumetric growth in uniform bodies. *International Journal of Plasticity*, 16:951–978, 2000.
- [37] A. Eringen and E. Suhubi. Nonlinear theory of simple micro-elastic solids - I. *International Journal of Engineering Science*, 2:189–203, 1964.
- [38] A. C. Eringen. *Microcontinuum Field Theories I. Foundations and Solids*. Springer-Verlag New York, 1999.
- [39] S. Fausten, D. Balzani, and J. Schröder. An algorithmic scheme for the automated calculation of fiber orientations in arterial walls. *Computational Mechanics*, 58: 861–878, 2016.
- [40] M. Ferretti, A. Madeo, F. dell’Isola, and P. Boisse. Modeling the onset of shear boundary layers in fibrous composite reinforcements by second-gradient theory. *Zeitschrift für angewandte Mathematik und Physik*, 65:587–612, 2014.
- [41] P. Fratzl. Cellulose and collagen: from fibres to tissues. *Current Opinion in Colloid and Interface Science*, 8:32–39, 2003.
- [42] P. Fratzl, editor. *Collagen - Structure and Mechanics*. Springer, 2008.
- [43] P. Fratzl and R. Weinkamer. Nature’s hierarchical materials. *Progress in Materials Science*, 52:1263–1334, 2007.
- [44] P. Fratzl, K. Misof, I. Zizak, G. Rapp, H. Amenitsch, and S. Bernstorff. Fibrillar structure and mechanical properties of collagen. *Journal of Structural Biology*, 122: 119–122, 1998.

-
- [45] Y. C. Fung. What principle governs the stress distribution in living organism? In Y. Fung, E. Fukada, and J. Wang, editors, *Biomechanics in China, Japan and USA*, pages 1–13. Science Press, Beijing, 1984.
- [46] Y. C. Fung. *Biomechanics: mechanical properties of living tissues*. Springer Science & Business Media, 2nd edition, 2013.
- [47] Y. C. Fung and S. Q. Liu. Change of residual strains in arteries due to hypertrophy caused by aortic constriction. 65:1340–1349, 1989.
- [48] A. García, E. Pēna, A. Laborda, F. Lostalé, M. A. De Gregorio, M. Doblare, and M. A. Martínez. Experimental study and constitutive modelling of the passive mechanical properties of the porcine carotid artery and its relation to histological analysis: Implications in animal cardiovascular device trials. 33:665–676, 2011.
- [49] T. C. Gasser. Biomechanical rupture risk assessment. A consistent and objective decision-making tool for abdominal aortic aneurysm patients. *Aorta*, 4:42–60, 2016.
- [50] T. C. Gasser, R. W. Ogden, and G. A. Holzapfel. Hyperelastic modelling of arterial layers with distributed collagen fibre orientations. *Journal of the Royal Society Interface*, 3:15–35, 2006.
- [51] T. C. Gasser, S. Gallinetti, X. Xing, C. Forsell, J. Swedenborg, and J. Roy. Spatial orientation of collagen fibers in the abdominal aortic aneurysm’s wall and its relation to wall mechanics. *Acta Biomaterialia*, 8:3091–3103, 2012.
- [52] M. W. Gee, C. Förster, and W. A. Wall. A computational strategy for prestressing patient-specific biomechanical problems under finite deformation. *International Journal for Numerical Methods in Biomedical Engineering*, 26:52–72, 2010.
- [53] K. Genovese. A video-optical system for time-resolved whole-body measurement on vascular segments. *Optics and Lasers in Engineering*, 47:995–1008, 2009.
- [54] R. Glowinski and P. Le Tallec. Numerical solution of problems in incompressible finite elasticity by augmented Lagrangian methods I. Two-dimensional and axisymmetric problems. *SIAM Journal on Applied Mathematics*, 42:400–429, 1982.
- [55] R. Glowinski and P. Le Tallec. Numerical solution of problems in incompressible finite elasticity by augmented Lagrangian methods II. three-dimensional problems. *SIAM Journal on Applied Mathematics*, 44:710–733, 1984.
- [56] S. Göktepe, S. N. S. Acharya, J. Wong, and E. Kuhl. Computational modeling of passive myocardium. *International Journal for Numerical Methods in Biomedical Engineering*, 27:1–12, 2011.
- [57] S. Govindjee and P. A. Mihalic. Computational methods for inverse finite elastostatics. *Computer Methods in Applied Mechanics and Engineering*, 136:47–57, 1996.
- [58] S. Govindjee and P. A. Mihalic. Computational methods for inverse deformations in quasi-incompressible finite elasticity. *International Journal for Numerical Methods in Engineering*, 43:821–838, 1998.

-
- [59] S. E. Greenwald, J. E. Moore, A. Rachev, T. P. C. Kane, and J.-J. Meister. Experimental investigation of the distribution of residual strains in the artery wall. *Journal of Biomechanical Engineering*, 119:438–444, 1997.
- [60] G. V. Guinea, J. M. Atienza, M. Elices, P. Aragoncillo, and K. Hayashi. Thermomechanical behavior of human carotid arteries in the passive state. *American Journal of Physiology - Heart and Circulatory Physiology*, 288:H2940–H2945, 2005.
- [61] X. Guo, Y. Lanir, and G. S. Kassab. Effect of osmolarity on the zero-stress state and mechanical properties of aorta. *American Journal of Physiology - Heart and Circulatory Physiology*, 293:H2328–H2334, 2007.
- [62] M. E. Gurtin. *An introduction to continuum mechanics*, volume 158 of *Mathematics in science and engineering*. New York: Academic Press, 1981.
- [63] B. Halphen and Q. S. Nguyen. Sur les matériaux standard généralisés. *Journal de Mécanique*, 14:39–63, 1975.
- [64] H. C. Han and Y. C. Fung. Species dependence of the zero-stress state of aorta: pig versus rat. *Journal of Biomechanical Engineering*, 113:446–451, 1991.
- [65] K. A. Hansen, J. A. Weiss, and J. K. Barton. Recruitment of tendon crimp with applied tensile strain. *Journal of Biomechanical Engineering*, 124:72–77, 2002.
- [66] I. Hariton, G. deBotton, T. C. Gasser, and G. A. Holzapfel. Stress-driven collagen fiber remodeling in arterial walls. *Biomechanics and Modeling in Mechanobiology*, 6:163–175, 2007.
- [67] H. Hencky. Über die Form des Elastizitätsgesetzes bei ideal elastischen Stoffen. *Zeitschrift für technische Physik*, 9:215–220, 1928.
- [68] R. Hill. On constitutive inequalities for simple materials - I. *Journal of the Mechanics and Physics of Solids*, 16:229–242, 1968.
- [69] G. Himpel, E. Kuhl, A. Menzel, and P. Steinmann. Computational modeling of isotropic multiplicative growth. *Computer Modeling in Engineering and Sciences*, 8:119–134, 2005.
- [70] G. Himpel, A. Menzel, E. Kuhl, and P. Steinmann. Time-dependent fibre reorientation of transversely isotropic continua - Finite element formulation and consistent linearization. *International Journal for Numerical Methods in Engineering*, 73:1413–1433, 2008.
- [71] G. A. Holzapfel. *Nonlinear Solid Mechanics: A Continuum Approach for Engineering*. John Wiley and Sons, 2000.
- [72] G. A. Holzapfel. Determination of material models for arterial walls from uniaxial extension tests and histological structure. *Journal of Theoretical Biology*, 238:290–302, 2006.

-
- [73] G. A. Holzapfel and R. W. Ogden. Constitutive modelling of passive myocardium: a structurally based framework for material characterization. *Philosophical Transactions of the Royal Society of London A: Mathematical, Physical and Engineering Sciences*, 367:3445–3475, 2009.
- [74] G. A. Holzapfel and R. W. Ogden. Constitutive modelling of arteries. *Philosophical Transactions of the Royal Society of London A: Mathematical, Physical and Engineering Sciences*, 466:1551–1597, 2010.
- [75] G. A. Holzapfel and R. W. Ogden. Modelling the layer-specific three-dimensional residual stresses in arteries, with an application to the human aorta. *Journal of the Royal Society Interface*, 7:787–799, 2010.
- [76] G. A. Holzapfel and R. W. Ogden. On the tension-compression switch in soft fibrous solids. *European Journal of Mechanics - A/Solids*, 49:561–569, 2015.
- [77] G. A. Holzapfel, T. C. Gasser, and R. W. Ogden. A new constitutive framework for arterial wall mechanics and a comparative study of material models. *Journal of Elasticity*, 61:1–48, 2000.
- [78] G. A. Holzapfel, G. Sommer, and P. Regitnig. Anisotropic mechanical properties of tissue components in human atherosclerotic plaques. *Journal of Biomechanical Engineering*, 126:657–665, 2004.
- [79] G. A. Holzapfel, G. Sommer, C. T. Gasser, and P. Regitnig. Determination of layer-specific mechanical properties of human coronary arteries with nonatherosclerotic intimal thickening and related constitutive modeling. *American Journal of Physiology - Heart and Circulatory Physiology*, 289:H2048–H2058, 2005.
- [80] G. A. Holzapfel, G. Sommer, M. Auer, P. Regitnig, and R. W. Ogden. Layer-specific 3D residual deformations of human aortas with non-atherosclerotic intimal thickening. *Annals of Biomedical Engineering*, 35:530–545, 2007.
- [81] G. A. Holzapfel, J. A. Niestrawska, R. W. Ogden, A. J. Reinisch, and A. J. Schriefl. Modelling non-symmetric collagen fibre dispersion in arterial walls. *Journal of the Royal Society Interface*, 12:20150188, 2015.
- [82] D. J. S. Hulmes. Collagen diversity, synthesis and assembly. In P. Fratzl, editor, *Collagen - Structure and Mechanics*, pages 15–47. Springer, 2008.
- [83] J. D. Humphrey. *Cardiovascular solid mechanics: cells, tissues, and organs*. Springer-Verlag, New York, 2002.
- [84] J. D. Humphrey and K. R. Rajagopal. A constrained mixture model for growth and remodeling of soft tissues. *Mathematical Models and Methods in Applied Sciences*, 12:407–430, 2002.
- [85] S. K. Hyun and H. Nakajima. Anisotropic compressive properties of porous copper produced by unidirectional solidification. *Material Science and Engineering*, A340:258–264, 2003.

-
- [86] M. Itskov and N. Aksel. A class of orthotropic and transversely isotropic hyperelastic constitutive models based on a polyconvex strain energy function. *International Journal of Solids and Structures*, 41:3833–3848, 2004.
- [87] M. Itskov, A. E. Ehret, and D. Mavrilas. A polyconvex anisotropic strain-energy function for soft collagenous tissues. *Biomechanics and Modeling in Mechanobiology*, 5:17–26, 2006.
- [88] C. S. Jog. Derivatives of the stretch, rotation and exponential tensors in n-dimensional vector spaces. *Journal of Elasticity*, 82:175–192, 2006.
- [89] J. Kim and S. Baek. Circumferential variations of mechanical behavior of the porcine thoracic aorta during the inflation test. *Journal of Biomechanics*, 44:1941–1947, 2011.
- [90] T. Kirchdoerfer and M. Ortiz. Data-driven computational mechanics. *Computer Methods in Applied Mechanics and Engineering*, 304:81–101, 2016.
- [91] W. Krasny, C. Morin, H. Magoariec, and S. Avril. A comprehensive study of layer-specific morphological changes in the microstructure of carotid arteries under uniaxial load. *Acta Biomaterialia*, 57:342–351, 2017.
- [92] W. Krasny, H. Magoariec, C. Morin, and S. Avril. Kinematics of collagen fibers in carotid arteries under tension-inflation loading. *Journal of the Mechanical Behavior of Biomedical Materials*, 77:718–726, 2018.
- [93] E. Kuhl, R. Maas, G. Himpel, and A. Menzel. Computational modeling of arterial wall growth. *Biomechanics and Modeling in Mechanobiology*, 6:321–331, 2007.
- [94] C. Lally, A. J. Reid, and P. J. Prendergast. Elastic behavior of porcine coronary artery tissue under uniaxial and equibiaxial tension. *Annals of Biomedical Engineering*, 32:1355–1364, 2004.
- [95] Y. Lanir. Constitutive equations for fibrous connective tissues. *Journal of Biomechanics*, 16:1–12, 1983.
- [96] Y. Lanir, G. Hayam, M. Abovsky, A. Y. Zlotnick, G. Uretzky, E. Nevo, and S. A. Ben-Haim. Effect of myocardial swelling on residual strain in the left ventricle of the rat. *American Journal of Physiology - Heart and Circulatory Physiology*, 270:H1736–H1743, 1996.
- [97] B. M. Learoyd and M. G. Taylor. Alterations with age in the viscoelastic properties of human arterial walls. *Circulation Research*, 18:278–292, 1966.
- [98] I. J. LeGrice, B. H. Smaill, L. Z. Chai, S. G. Edgar, J. B. Gavin, and P. J. Hunter. Lamellar structure of the heart: ventricular myocyte arrangement and connective tissue architecture in the dog. *American Journal of Physiology - Heart and Circulatory Physiology*, 269:H571–H582, 1995.
- [99] I. J. LeGrice, Y. Takayama, and J. W. Covell. Transverse shear along myocardial cleavage planes provides a mechanism for normal systolic wall thickening. *Circulation Research*, 77:182–193, 1995.

-
- [100] K. Li, R. W. Ogden, and G. A. Holzapfel. Computational method for excluding fibers under compression in modeling soft fibrous solids. *European Journal of Mechanics - A/Solids*, 57:178–193, 2016.
- [101] M. A. Lillie, R. E. Shadwick, and J. M. Gosline. Mechanical anisotropy of inflated elastic tissue from the pig aorta. *Journal of Biomechanics*, 43:2070–2078, 2010.
- [102] J. Liu, X. Zhou, and M. L. Raghavan. Computational method of inverse elastostatics for anisotropic hyperelastic solids. *International Journal for Numerical Methods in Engineering*, 69:1239–1261, 2007.
- [103] S. Q. Liu and Y. C. Fung. Relationship between hypertension, hypertrophy, and opening angle of zero-stress state of arteries following aortic constriction. *Journal of Biomechanical Engineering*, 111:325–335, 1989.
- [104] V. A. Lubarda and A. Hoger. On the mechanics of solids with a growing mass. *International Journal of Solids and Structures*, 39:4627–4664, 2002.
- [105] B. Lynch, S. Bancelin, C. Bonod-Bidaud, J.-B. Gueusquin, F. Ruggiero, M.-C. Schanne-Klein, and J.-M. Allain. A novel microstructural interpretation for the biomechanics of mouse skin derived from multiscale characterization. *Acta Biomaterialia*, 50:302–311, 2017.
- [106] F. Maceri, M. Marino, and G. Vairo. A unified multiscale mechanical model for soft collagenous tissues with regular fiber arrangement. *Journal of Biomechanics*, 43:355–363, 2010.
- [107] D. A. MacKenna, J. H. Omens, and J. W. Covell. Left ventricular perimysial collagen fibers uncoil rather than stretch during diastolic filling. *Basic Research in Cardiology*, 91:111–122, 1996.
- [108] J. Mandel. *Plasticité Classique et Viscoplasticité*. Number 97 in CISM lecture notes. Springer, 1972.
- [109] M. Marino. Molecular and intermolecular effects in collagen fibril mechanics: a multiscale analytical model compared with atomistic and experimental studies. *Biomechanics and Modeling in Mechanobiology*, 15:133–154, 2016.
- [110] M. Marino and G. Vairo. Multiscale elastic models of collagen bio-structures: from cross-linked molecules to soft tissues. In A. Gefen, editor, *Multiscale Computer Modeling in Biomechanics and Biomedical Engineering*, volume 14 of *Studies in Mechanobiology, Tissue Engineering and Biomaterials*, pages 73–102. Springer, 2013.
- [111] M. Marino and G. Vairo. Computational modelling of soft tissues and ligaments. In Z. Jin, editor, *Computational Modelling of Biomechanics and Biotribology in the Musculoskeletal System*, volume 81 of *Woodhead Publishing Series in Biomaterials*, pages 141–172. Woodhead Publishing, 2014.
- [112] M. Marino and P. Wriggers. Finite strain response of crimped fibers under uniaxial traction: an analytical approach applied to collagen. *Journal of the Mechanics and Physics of Solids*, 98:429–453, 2017.

-
- [113] M. Marino, M. von Hoegen, J. Schröder, and P. Wriggers. Direct and inverse identification of constitutive parameters from the structure of soft tissues. Part 1: micro- and nano-structure of collagen fibers. *Biomechanics and Modeling in Mechanobiology*, 17:1011–1036, 2018.
- [114] G. Martufi and T. C. Gasser. A constitutive model for vascular tissue that integrates fibril, fiber and continuum levels with application to the isotropic and passive properties of the infrarenal aorta. *Journal of Biomechanics*, 44:2544–2550, 2011.
- [115] A. Menzel and E. Kuhl. Frontiers in growth and remodeling. *Mechanics Research Communications*, 42:1–14, 2012.
- [116] C. Miehe, N. Apel, and M. Lamprecht. Anisotropic additive plasticity in the logarithmic strain space: modular kinematic formulation and implementation based on incremental minimization principles for standard materials. *Computer Methods in Applied Mechanics and Engineering*, 191:5383–5425, 2002.
- [117] R. D. Mindlin. Micro-structure in linear elasticity. *Archive for Rational Mechanics and Analysis*, 16:51–78, 1964.
- [118] D. Mohan and J. W. Melvin. Failure properties of passive human aortic tissue. II-Biaxial tension tests. *Journal of Biomechanics*, 16:31–44, 1983.
- [119] K. L. Monson, N. M. Barbaro, and G. T. Manley. Biaxial response of passive human cerebral arteries. *Annals of Biomedical Engineering*, 36:2028–2041, 2008.
- [120] J. F. Mulhern, T. G. Rogers, and A. J. M. Spencer. A continuum model for fibre-reinforced plastic materials. *Proceedings of the Royal Society London A*, 301:473–492, 1967.
- [121] M. P. Nash and P. J. Hunter. Computational mechanics of the heart. *Journal of Elasticity*, 61:113–141, 2000.
- [122] P. Neff and I. D. Ghiba. The exponentiated Hencky-logarithmic strain energy. Part III: Coupling with idealized multiplicative isotropic finite strain plasticity. *Continuum Mechanics and Thermodynamics*, 28:477–487, 2016.
- [123] P. Neff, I. D. Ghiba, A. Madeo, L. Placidi, and G. Rosi. A unifying perspective: the relaxed linear micromorphic continuum. *Continuum Mechanics and Thermodynamics*, 26:639–681, 2014.
- [124] P. Neff, I. D. Ghiba, and J. Lankeit. The exponentiated Hencky-logarithmic strain energy. Part I: constitutive issues and rank-one convexity. *Journal of Elasticity*, 121:143–234, 2015.
- [125] P. Neff, J. Lankeit, I. D. Ghiba, R. J. Martin, and D. J. Steigmann. The exponentiated Hencky-logarithmic strain energy. Part II: coercivity, planar polyconvexity and existence of minimizers. *Zeitschrift für angewandte Mathematik und Physik*, 66:1671–1693, 2015.
- [126] P. Neff, B. Eidel, and R. J. Martin. Geometry of logarithmic strain measures in solid mechanics. *Archive for Rational Mechanics and Analysis*, 222:507–572, 2016.

- [127] J. A. Niestrawska, C. Viertler, P. Regitnig, T. U. Cohnert, G. Sommer, and G. A. Holzapfel. Microstructure and mechanics of healthy and aneurysmatic abdominal aortas: experimental analysis and modelling. *Journal of the Royal Society Interface*, 13:20160620, 2016.
- [128] M. K. O’Connell, S. Murthy, S. Phan, C. Xu, J. Buchanan, R. Spilker, R. L. Dalman, C. K. Zarins, W. Denk, and C. A. Taylor. The three-dimensional micro- and nanostructure of the aortic medial lamellar unit measured using 3D confocal and electron microscopy imaging. *Matrix Biology*, 27:171–181, 2008.
- [129] R. W. Ogden. *Non-linear elastic deformations*. Dover Publications, 1984.
- [130] R. J. Okamoto, J. E. Wagenseil, W. R. DeLong, S. J. Peterson, N. T. Kouchoukos, and T. M. Sundt. Mechanical properties of dilated human ascending aorta. *Annals of Biomedical Engineering*, 30:624–635, 2002.
- [131] T. Olsson and A. Klarbring. Residual stresses in soft tissue as a consequence of growth and remodeling: application to an arterial geometry. *European Journal of Mechanics - A/Solids*, 27:959–974, 2008.
- [132] J. H. Omens and Y. C. Fung. Residual strain in rat left-ventricle. *Circulation Research*, 60:37–45, 1990.
- [133] A. Pandolfi and M. Vasta. Fiber distributed hyperelastic modeling of biological tissues. *Mechanics of Materials*, 44:151–162, 2012.
- [134] E. Peña, M. A. Martínez, B. Calvo, and M. Doblaré. On the numerical treatment of initial strains in biological soft tissues. *International Journal for Numerical Methods in Engineering*, 68:836–860, 2006.
- [135] J. A. Peña, M. A. Martínez, and E. Peña. Layer-specific residual deformations and uniaxial and biaxial mechanical properties of thoracic porcine aorta. *Journal of the Mechanical Behavior of Biomedical Materials*, 50:55–69, 2015.
- [136] S. Polzer, J. Bursa, T. C. Gasser, R. Staffa, and R. Vlachovsky. A numerical implementation to predict residual strains from the homogeneous stress hypothesis with application to abdominal aortic aneurysms. *Annals of Biomedical Engineering*, 41:1516–1527, 2013.
- [137] M. L. Raghavan, M. W. Webster, and D. A. Vorp. Ex vivo biomechanical behavior of abdominal aortic aneurysm: assessment using a new mathematical model. *Annals of Biomedical Engineering*, 24:573–582, 1996.
- [138] J. S. Ren. Growth and residual stresses of arterial walls. *Journal of Theoretical Biology*, 337:80–88, 2013.
- [139] R. Rezakhaniha, A. Agianniotis, J. T. C. Schrauwen, A. Griffa, D. Sage, C. V. C. Bouten, F. N. van de Vosse, M. Unser, and N. Stergiopoulos. Experimental investigation of collagen waviness and orientation in the arterial adventitia using confocal laser scanning microscopy. *Biomechanics and Modeling in Mechanobiology*, 11:461–473, 2012.

-
- [140] H. Richter. Das isotrope Elastizitätsgesetz. *Zeitschrift für angewandte Mathematik und Mechanik*, 28:205–209, 1948.
- [141] T. F. Robinson, M. A. Geraci, E. H. Sonnenblick, and S. M. Factor. Coiled perimysial fibers of papillary muscle in rat heart: morphology, distribution, and changes in configuration. *Circulation Research*, 63:577–592, 1988.
- [142] E. K. Rodriguez, A. Hoger, and A. D. McCulloch. Stress-dependent finite growth in soft elastic tissues. *Journal of Biomechanics*, 27:455–467, 1994.
- [143] A. Saini, C. Berry, and S. E. Greenwald. Effect of age and sex on residual stress in the aorta. *Journal of Vascular Research*, 32:398–405, 1995.
- [144] M. Saito, K. Marumo, K. Fujii, and N. Ishioka. Single-column high-performance liquid chromatographic-fluorescence detection of immature, mature, and senescent cross-links of collagen. *Analytical Biochemistry*, 253:26–32, 1997.
- [145] C. Sansour, S. Skatulla, and H. Zbib. A formulation for the micromorphic continuum at finite inelastic strains. *International Journal of Solids and Structures*, 47:1546–1554, 2010.
- [146] U. Saravanan, S. Baek, K. R. Rajagopal, and J. D. Humphrey. On the deformation of the circumflex coronary artery during inflation tests at constant length. *Experimental Mechanics*, 46:647–656, 2006.
- [147] F. Schmid, G. Sommer, M. Rappolt, C. A. J. Schulze-Bauer, P. Regitnig, G. A. Holzapfel, P. Laggner, and H. Amenitsch. In situ tensile testing of human aortas by time-resolved small-angle X-ray scattering. *Journal of Synchrotron Radiation*, 12:727–733, 2005.
- [148] H. Schmid, M. P. Nash, A. A. Young, and P. J. Hunter. Myocardial material parameter estimation - A comparative study for simple shear. *Journal of Biomechanics*, 128:742–750, 2006.
- [149] A. J. Schriefl, G. Zeindlinger, D. M. Pierce, P. Regitnig, and G. A. Holzapfel. Determination of the layer-specific distributed collagen fibre orientations in human thoracic and abdominal aortas and common iliac arteries. *Journal of the Royal Society Interface*, 9:1275–1286, 2012.
- [150] J. Schröder and S. Brinkhues. A novel scheme for the approximation of residual stresses in arterial walls. *Archive of Applied Mechanics*, 84:881–898, 2014.
- [151] J. Schröder and D. Gross. Invariant formulation of the electromechanical enthalpy function of transversely isotropic piezoelectric materials. *Archive of Applied Mechanics*, 73:533–552, 2004.
- [152] J. Schröder and P. Neff. Invariant formulation of hyperelastic transverse isotropy based on polyconvex free energy functions. *International Journal of Solids and Structures*, 40:401–445, 2003.
- [153] J. Schröder and M. von Hoegen. An engineering tool to estimate eigenstresses in three-dimensional patient-specific arteries. *Computer Methods in Applied Mechanics and Engineering*, 306:364–381, 2016.

-
- [154] J. Schröder, P. Neff, and D. Balzani. A variational approach for materially stable anisotropic hyperelasticity. *International Journal of Solids and Structures*, 42:4352–4371, 2005.
- [155] J. Schröder, P. Neff, and V. Ebbing. Anisotropic polyconvex energies on the basis of crystallographic motivated structural tensors. *Journal of the Mechanics and Physics of Solids*, 56:3486–3506, 2008.
- [156] J. Schröder, N. Viebahn, D. Balzani, and P. Wriggers. A novel mixed finite element for finite anisotropic elasticity; the SKA-element Simplified Kinematics for Anisotropy. *Computer Methods in Applied Mechanics and Engineering*, 310:475–494, 2016.
- [157] J. Schröder, M. von Hoegen, and P. Neff. The exponentiated Hencky energy: anisotropic extension and case studies. *Computational Mechanics*, 61:657–685, 2018.
- [158] C. A. J. Schulze-Bauer, C. Mörth, and G. A. Holzapfel. Passive biaxial mechanical response of aged human iliac arteries. *Journal of Biomechanical Engineering*, 125:395–406, 2003.
- [159] H. R. C. Screen, D. L. Bader, D. A. Lee, and J. C. Shelton. Local strain measurement within tendon. *Strain*, 40:157–163, 2004.
- [160] M. Sellier. An iterative method for the inverse elasto-static problem. *Journal of Fluids and Structures*, 27:1461–1470, 2011.
- [161] B. R. Seth. Generalized strain measure with applications to physical problems. In M. Reiner and D. Abir, editors, *Second-Order Effects in Elasticity, Plasticity and Fluid Dynamics*. Pergamon Press: Oxford, 1964.
- [162] M. Shams, M. Destrade, and R. W. Ogden. Initial stresses in elastic solids: constitutive laws and acoustoelasticity. *Wave Motion*, 48:552–567, 2011.
- [163] V. R. Sherman, W. Yeng, and M. A. Meyers. The materials science of collagen. *Journal of the Mechanical Behavior of Biomedical Materials*, 52:22–50, 2015.
- [164] J. C. Simo. Numerical analysis and simulation of plasticity. In P. G. Ciarlet and J. L. Lions, editors, *Handbook of Numerical Analysis*, volume 6, pages 183–499. Elsevier, 1998.
- [165] J. C. Simo and F. Armero. Geometrically non-linear enhanced strain mixed methods and the method of incompatible modes. *International Journal for Numerical Methods in Engineering*, 33:1413–1449, 1992.
- [166] R. Skalak, S. Zargaryan, R. K. Jain, P. A. Netti, and A. Hoger. Compatibility and the genesis of residual stress by volumetric growth. *Journal of Mathematical Biology*, 34:889–914, 1996.
- [167] D. P. Sokolis. Passive mechanical properties and structure of the aorta: segmental analysis. *Acta Physiologica*, 190:277–289, 2007.

-
- [168] D. P. Sokolis, G. D. Savva, S. A. Papadodima, and S. K. Kourkoulis. Regional distribution of circumferential residual strains in the human aorta according to age and gender. *Journal of the Mechanical Behavior of Biomedical Materials*, 67:87–100, 2017.
- [169] G. Sommer, P. Regitnig, L. Költringer, and G. A. Holzapfel. Biaxial mechanical properties of intact and layer-dissected human carotid arteries at physiological and suprphysiological loadings. *American Journal of Physiology - Heart and Circulatory Physiology*, 298:H898–H912, 2010.
- [170] G. Sommer, S. Sherifova, P. J. Oberwalder, O. E. Dapunt, P. A. Ursomanno, A. De-Anda, B. E. Griffith, and G. A. Holzapfel. Mechanical strength of aneurysmatic and dissected human thoracic aortas at different shear loading modes. *Journal of Biomechanics*, 49:2374–2382, 2016.
- [171] A. J. M. Spencer. *Deformations of fibre-reinforced materials*. Clarendon Press, 1972.
- [172] A. J. M. Spencer. *Continuum mechanics*. Longman, 1980.
- [173] H. M. Spotnitz, W. D. Spotnitz, T. S. Cottrell, D. Spiro, and E. H. Sonnenblick. Cellular basis for volume related wall thickness changes in the rat left ventricle. *Journal of Molecular and Cellular Cardiology*, 6:317–331, 1974.
- [174] D. J. Steigmann. Frame-invariant polyconvex strain-energy functions for some anisotropic solids. *Mathematics and Mechanics of Solids*, 8:497–506, 2003.
- [175] S. Sugita and T. Matsumoto. Multiphoton microscopy observations of 3D elastin and collagen fiber microstructure changes during pressurization in aortic media. *Biomechanics and Modeling in Mechanobiology*, 16:763–773, 2017.
- [176] L. A. Taber and J. D. Humphrey. Stress-modulated growth, residual stress, and vascular heterogeneity. *Journal of Biomechanical Engineering*, 123:528–535, 2001.
- [177] K. Takamizawa and K. Hayashi. Strain energy density function and uniform strain hypothesis for arterial mechanics. *Journal of Biomechanics*, 20:7–17, 1987.
- [178] M. Tawhai, J. Bischoff, D. Einstein, A. Erdemir, T. Guess, and J. Reinbolt. Multi-scale modeling in computational biomechanics. *IEEE Engineering in Medicine and Biology Magazine*, 28:41–49, 2009.
- [179] C. A. Taylor and C. A. Figueroa. Patient-specific modeling of cardiovascular mechanics. *Annual Review of Biomedical Engineering*, 11:109–134, 2009.
- [180] *MATLAB. The MathWorks, Inc. MATLAB, Release R2014a, Global Optimization Toolbox User's Guide*, 2014.
- [181] R. N. Vaishnav and J. Vossoughi. Estimation of residual strains in aortic segments. In C. W. Hall, editor, *Biomedical Engineering II*. Pergamon Press, New York, 1983.
- [182] R. N. Vaishnav, J. T. Young, and D. J. Patel. Distribution of stresses and of strain-energy density through the wall thickness in a canine aortic segment. *Circulation Research*, 32:577–583, 1973.

-
- [183] J. P. Vande Geest, M. S. Sacks, and D. A. Vorp. Age dependency of the biaxial biomechanical behavior of human abdominal aorta. *Journal of Biomechanical Engineering*, 126:815–822, 2004.
- [184] J. P. Vande Geest, M. S. Sacks, and D. A. Vorp. The effects of aneurysm on the biaxial mechanical behavior of human abdominal aorta. *Journal of Biomechanics*, 39:1324–1334, 2006.
- [185] M. von Hoegen, S. Skatulla, and J. Schröder. A generalized micromorphic approach accounting for variation and dispersion of preferred material directions. *Computers and Structures*, 2017. doi: 10.1016/j.compstruc.2017.11.013. in press.
- [186] M. von Hoegen, M. Marino, J. Schröder, and P. Wriggers. Direct and inverse identification of constitutive parameters from the structure of soft tissues. Part 2: dispersed arrangement of collagen fibers. *Biomechanics and Modeling in Mechanobiology*, 2019. doi: <https://doi.org/10.1007/s10237-019-01119-3>. in press.
- [187] H. M. Wang, X. Y. Luo, H. Gao, R. W. Ogden, B. E. Griffith, C. Berry, and T. J. Wang. A modified Holzapfel-Ogden law for a residually stressed finite strain model of the human left ventricle in diastole. *Biomechanics and Modeling in Mechanobiology*, 13:99–113, 2014.
- [188] S. A. Wickline, E. D. Verdonk, A. K. Wong, R. K. Shepard, and J. G. Miller. Structural remodeling of human myocardial tissue after infarction. Quantification with ultrasonic backscatter. *Circulation*, 85:259–268, 1992.
- [189] P. Wriggers. *Nonlinear finite element methods*. Springer, 2008.
- [190] G. Xu, P. V. Bayly, and L. A. Taber. Residual stress in the adult mouse brain. *Biomechanics and Modeling in Mechanobiology*, 8:253–262, 2009.
- [191] A. Zahn and D. Balzani. Modeling of anisotropic growth and residual stresses in arterial walls. *Acta Polytechnica CTU Proceedings*, 7:85–90, 2017.
- [192] A. Zdunek, W. Rachowicz, and T. Eriksson. A novel computational formulation for nearly incompressible and nearly inextensible finite hyperelasticity. *Computer Methods in Applied Mechanics and Engineering*, 281:220–249, 2014.
- [193] M. Zemánek, J. Burša, and M. Děták. Biaxial tension tests with soft tissues of arterial wall. *Engineering Mechanics*, 16:3–11, 2009.
- [194] X. Zheng and J. Ren. Effects of the three-dimensional residual stresses on the mechanical properties of arterial walls. *Journal of Theoretical Biology*, 393:118–126, 2016.
- [195] J. Zhou and Y. C. Fung. The degree of nonlinearity and anisotropy of blood vessel elasticity. *Proceedings of the National Academy of Sciences of the United States of America*, 94:14255–14260, 1997.
- [196] O. C. Zienkiewicz. *Method of the finite elements*. Carl Hanser Verlag, München, 2nd edition, 1984.

-
- [197] O. C. Zienkiewicz and R. L. Taylor. *The finite element method for solid and structural mechanics*. Elsevier, 6th edition, 2005.
- [198] O. C. Zienkiewicz, R. L. Taylor, and J. M. Too. Reduced integration technique in general analysis of plates and shells. *International Journal for Numerical Methods in Engineering*, 3:275–290, 1971.

Der Lebenslauf ist in der Online-Version
aus Gründen des Datenschutzes nicht enthalten.

In dieser Schriftenreihe bisher erschienene Berichte:

- Nr. 1 (2004) *Ein Modell zur Beschreibung finiter anisotroper elasto-plastischer Deformationen unter Berücksichtigung diskreter Rissausbreitung*, J. Löblein, Dissertation, 2004.
- Nr. 2 (2006) *Polyconvex Anisotropic Energies and Modeling of Damage applied to Arterial Walls*, D. Balzani, Dissertation, 2006.
- Nr. 3 (2006) *Kontinuumsmechanische Modellierung ferroelektrischer Materialien im Rahmen der Invariantentheorie*, H. Romanowski, Dissertation, 2006.
- Nr. 4 (2007) *Mehrskalen-Modellierung polykristalliner Ferroelektrika basierend auf diskreten Orientierungsverteilungsfunktionen*, I. Kurzhöfer, Dissertation, 2007.
- Nr. 5 (2007) *Proceedings of the First Seminar on the Mechanics of Multifunctional Materials*, J. Schröder, D.C. Lupascu, D. Balzani (Ed.), Tagungsband, 2007.
- Nr. 6 (2008) *Zur Modellierung und Simulation diskreter Rissausbreitungsvorgänge*, O. Hilgert, Dissertation, 2008.
- Nr. 7 (2009) *Least-Squares Mixed Finite Elements for Solid Mechanics*, A. Schwarz, Dissertation, 2009.
- Nr. 8 (2010) *Design of Polyconvex Energy Functions for All Anisotropy Classes*, V. Ebbing, Dissertation, 2010.
- Nr. 9 (2012) *Modeling of Electro-Mechanically Coupled Materials on Multiple Scales*, M.-A. Keip, Dissertation, 2012.
- Nr. 10 (2012) *Geometrical Modeling and Numerical Simulation of Heterogeneous Materials*, D. Brands, Dissertation, 2012.
- Nr. 11 (2012) *Modeling and simulation of arterial walls with focus on damage and residual stresses*, S. Brinkhues, Dissertation, 2012.
- Nr. 12 (2014) *Proceedings of the Second Seminar on the Mechanics of Multifunctional Materials*, J. Schröder, D.C. Lupascu, M.-A. Keip, D. Brands (Ed.), Tagungsband, 2014.
- Nr. 13 (2016) *Mixed least squares finite element methods based on inverse stress-strain relations in hyperelasticity*, B. Müller, Dissertation, 2016.
- Nr. 14 (2016) *Electromechanical Modeling and Simulation of Thin Cardiac Tissue Constructs*, R. Frotscher, Dissertation, 2016.
- Nr. 15 (2017) *Least-squares mixed finite elements for geometrically nonlinear solid mechanics*, K. Steeger, Dissertation, 2017.

- Nr. 16 (2017) *Scale-Bridging of Elasto-Plastic Microstructures using Statistically Similar Representative Volume Elements*, L. Scheunemann, Dissertation, 2017.
- Nr. 17 (2018) *Modeling of Self-healing Polymers and Polymeric Composite Systems*, S. Specht, Dissertation, 2017.
- Nr. 18 (2018) *Proceedings of the Third Seminar on the Mechanics of Multifunctional Materials*, J. Schröder, D.C. Lupascu, H. Wende, D. Brands (Ed.), Tagungsband, 2018.
- Nr. 19 (2018) *Least-squares finite element methods with applications in fluid and solid mechanics*, C. Nisters, Dissertation, 2018.
- Nr. 20 (2018) *A two-scale homogenization scheme for the prediction of magneto-electric product properties*, M. Labusch, Dissertation, 2018.

DuEPublico

Duisburg-Essen Publications online

UNIVERSITÄT
DUISBURG
ESSEN

Offen im Denken

ub | universitäts
bibliothek

Diese Dissertation wird über DuEPublico, dem Dokumenten- und Publikationsserver der Universität Duisburg-Essen, zur Verfügung gestellt und liegt auch als Print-Version vor.

DOI: 10.17185/duepublico/70086

URN: urn:nbn:de:hbz:464-20190423-145950-4

Alle Rechte vorbehalten.